The University of Nottingham

UNITED KINGDOM · CHINA · MALAYSIA

MODELLING OF MULTIPHASE FLOW CONTAINING IONIC LIQUIDS IN A STIRRED TANK REACTOR

Jie Dong, BEng, MSc

Thesis submitted to the University of Nottingham

for the degree of Doctor of Philosophy

May, 2017

ABSTRACT

Stirred tanks are widely used in the chemical reactions and the mixing operations for process industries to enable high product quality and process efficiency. Despite there being a large body of studies on the hydrodynamics of water in the stirred tanks, the understandings of the hydrodynamics of the ionic liquids in the stirred tanks are still very limited. In this study, Computational Fluid Dynamics (CFD) modelling is used to investigate the detailed flow characteristics of the single and multiphase ionic liquid flows in the stirred tanks which are experimentally validated using Particle Image Velocimetry (PIV).

The ANSYS FLUENT was employed in this investigation to carry out the CFD simulation. Initially, the hydrodynamics of single phase flows were numerically studied where the single phase turbulent water flow and single phase transitional ionic liquid flow were modelled using a RANS and LES approach respectively in the three stirred tanks equipped with different bottom shapes and length of baffles. The simulation results indicated that the bottom shape and baffles' length have significant effect on the flow field in a stirred tank when the water was operated in the turbulent state, where a large dead zone region was identified below the impeller. However, the magnitude of the dead zone region reduced a lot when the ionic liquid was operated in the transitional state.

Before carrying out the gas-ionic liquid multiphase flow simulation in a stirred tank, the bubble size needs to be identified as it is crucial information for the accurate gas-ionic liquid multiphase flow modelling. In

order to obtain the bubble size data, a high speed camera and a microscope were employed to experimentally measure the bubble size in the ionic liquid solutions. The correlations between the bubble size in the ionic liquid solutions and the impeller agitation speed were established. It showed that both the bubble breakage and coalescence has significant effect on determining bubble size in the ionic liquid. In addition, it was suggested that the surface tension of the ionic liquid is more important than the liquid viscosity on affecting the bubble size in the stirred tank.

Afterward, the gas-ionic liquid multiphase flow modelling was carried out in the stirred tank at various impeller speeds and gassing rates. The simulation results indicated that the presence of gas phase did not have significant effect on changing the flow of liquid phase under the selected operation conditions due to the small bubble size, low gas flow rate and high viscosity of ionic liquid. The gas phase followed well with the liquid phase and circulated in the majority region of the stirred tank, which implied better gas holdup and mass transfer of the multiphase flow system. A correlation was proposed to predict the impeller power consumption of the gas-ionic liquid transitional flow in a stirred tank agitated by a Rushton turbine impeller.

Finally, in order to validate the above single and multiphase flow CFD models adopted in this study, an experimental rig was established and the advanced visualization technique Particle Image Velocimetry (PIV) was used to measure the single phase water and ionic liquid flows and gas-ionic liquid multiphase flow in a stirred tank. The PIV data showed agreement with the CFD results in terms of the flow pattern and velocity components, which indicates good accuracy of the computational models and approaches presented in this investigation.

ACKNOWLEGEMENTS

I would like to thank the graduate school of the University of Nottingham for the scholarship granted to me to make this PhD possible.

I would like to express my sincerest thanks to my supervisors, Dr. Binjie Hu, Professor Xiaogang Yang and Professor Nick Miles for their supervision, guidance and advice throughout the whole research. This work cannot be done without their help.

I extend my appreciation to:

Professor Andrzej Pacek from the University of Birmingham for his suggestions and guidance on this work.

Yiyang Kong and Rongmeihui Zheng for their help with samples preparation and test.

Jane Zhang, Julian Zhu, Hellen Xu for their help with the installation of the experimental rigs.

Engineers from Dantec Dynamics, Yao Zhang, Chao Jin and Lizi Xu for their help and suggestions on PIV experiments.

The engineer Lu Jiang from ANSYS for her advice on mesh generation.

My friend Guozhen Li, Lele Zhang, Min Hui Yap, Feicheng Wang, Zhaohui Niu, Tingting Ying and Jie Ma who make the hard study time much easier.

Finally, I would like to take this opportunity to express my deep gratitude to my parents for their support, love and encouragement.

TABLE OF CONTENTS

LIST OF FIGURES

LIST OF TABLES

NOMENCLATURE

A	Interfacial area	[m]
A_i	Control volume area at the impeller blade surface	[m^2]
B	Width of baffle	[mm]
C	Distance between impeller and tank bottom	[mm]
C_D	Drag force coefficient	[-]
C_s	Smagorinsky constant	[-]
C_{lift}	Lift force coefficient	[-]
C_{vm}	Added mass force coefficient	[-]
C_w	Constant equals 0.325 in Wall Adapting Local	[-]

	Eddy Viscosity model	
$C_{\varepsilon 1}$	Model constant equals 1.44 in standard *k-ε* and equals 1.42 in *RNG k-ε* model	[-]
$C_{\varepsilon 2}$	Model constant equals 1.92 in standard *k-ε and* equals 1.68 in RNG *k-ε model*	[-]
C_{u}	Model constant equals 0.09 in standard *k-ε* and equals 0.0845 in *RNG k-ε* model	[-]
C_{Smag}	Model constant equals 0.2 in Algebraic Wall-Modeled large eddy simulation	[-]
C_{w}	Model constant equals 0.15 in Algebraic WMLES model	[-]
C_{ε}	Dynamic parameters in Dynamic Kinetic Energy Subgrid-Scale Model	[-]
C_{k}	Dynamic parameters in Dynamic Kinetic Energy Subgrid-Scale Model	[-]
$C_{u,b}$	Model constant equals 1.0	[-]
C_{spa}	Distance between sparger and tank bottom	[mm]
D	Impeller diameter	[mm]
d	The distance from the node to the closest wall	[m]
d_{32}	Sauter mean diameter	[um]
d_{b}	Bubble diameter	[m]
d_{p}	Tracer diameter	[um
d_{w}	The distance from the node to the wall	[m]
G_{b}	Generation of turbulent kinetic energy result from mean velocity gradients	[kg/ms^3]
G_{k}	Generation of turbulent kinetic energy result from buoyancy	[kg/ms^3]
$\vec{g}$	Gravity acceleration	[m/s^2]
H	Height of the ungassed liquid phase	[mm]
H_b	Height of the Baffle	[mm]
h_{max}	Maximum edge length of the cell	[m]
h_{wn}	Wall-normal grid distance	[m]
Fr	Froude number	[-]
$\vec{F}$	Interphase force	[N]

$\vec{F}_D$	Drag force	[N]
$\vec{F}_{D,l}$	Drag force of the liquid phase	[N]
$\vec{F}_{D,g}$	Drag force of the gas phase	[N]
Fl	Flow number	[-]
$\vec{F}_{lift}$	Lift force	[N]
$\vec{F}_{vm}$	Added mass force	[N]
$\vec{f}$	Body force	[N]
q	q=g and q=l represent gas and liquid phase respectively	[-]
$\vec{I}$	Unit tensor	[-]
K	Interphase exchange coefficient	[kg/s]
K_1	Model parameter	[-]
K_2	Model parameter	[-]
K_3	Model parameter	[-]
L_s	Subgrid scales of the mixing length	[m]
N	Impeller speed	[s^{-1}]
N_{Re}	Particle Reynolds number	[-]
N_Q	Flow number	[-]
N_{JS}	Minimum impeller speed to suspend particles	[s^{-1}]
p	Static pressure	[Pa]
$\overline{p}$	Mean pressure	[Pa]
P'	Modified pressure	[Pa]
P	Impeller power input	W/kg]
p'	Fluctuating pressure	[Pa]
Δp	Pressure difference	[Pa]
Q_l	Discharge flow rate	[m^3/s]
r	Radial distance	[m]
R	Radius of stirred tank	[m]
R_{imp}	Radius of impeller	[m]
Re	Reynolds number	[-]
Re_r	Relative Reynolds number	[-]
S	Strain rate	[s^{-1}]
$\bar{S}_{ij}$	Rate of strain tensor for the resolved scale	[s^{-1}]
S_k	User defined term	[kg/ms^3]

S_ε	User defined term	[kg/ms^4]
St	Stokes number	[-]
T	Tank diameter	[mm]
t	Time	[s]
$\vec{u}$	Instantaneous velocity	[m/s]
$\overline{\vec{u}}$	Mean velocity	[m/s]
$\overrightarrow{u'}$	Velocity fluctuation	[m/s]
U_{tip}	Impeller tip velocity	[m/s]
U_{radial}	Radial velocity	[m/s]
V_c	The cell volume	[m^3]
V	Volume of liquid in stirred tank	[m^3]
We	Weber number	[-]
Δx	Length of grid cells	[m]
Δy	Width of grid cells	[m]
Δz	Height of grid cells	[m]
Y_M	Contribution of the fluctuation dilatation in compressible turbulence to the overall dissipation rate	[kg/ms^3]
z	Axial distance	[m]

GREEK LETTERS

α	Volumn fraction	[-]
α_d	Volume fraction of dispersed phase	[-]
ρ	Density	[kg/m^3]
ρ_l	Density of liquid	[kg/m^3]
ρ_p	Tracer density	[kg/m^3]
Δ	Filter cut-off width	[m]
μ_{eff}	Effective viscosity	[N/m^2]
μ	Molecular viscosity	[Pa.s]
μ_t	Turbulent viscosity	[m^2/s]
ν	Kinetic viscosity	[m^2/s]

$\bar{\bar{\tau}}_{eff,i}$	Reynolds stresses	[m^2/s^2]
δ_{ij}	Kronecker delta	[-]
ε	Turbulent kinetic energy dissipation rate	[m^2/s^3]
ε_{avg}	Mean energy dissipation rate	[W/kg]
ε_T	Specific energy dissipation rate	[W/kg]
k	Turbulent kinetic energy	[m^2/s^2]
k_{sgs}	Subgird scale kinetic energy	[m^2/s^2]
∇	Gradient operator	[-]
σ_k	Model constant equals 1.3 in standard k-ε , equals 0.7194 in RNG k-ε model and equals 1.0 in Dynamic Kinetic Energy Subgrid-Scale Model	[-]
σ_ε	Model constant equals 1.0 in standard k-ε and equals 0.7149 in RNG k-ε model	[-]
σ_{ij}	Subgrid-scale (SGS) Reynolds stresses tensor	[kg/ms^2]
σ_{kk}	Isotropic part of the subgrid-scale stresses	[kg/ms^2]
τ_{ij}	Filtered stress tensor	[kg/ms^2]
τ_p	Relaxation time of the particle tracer	[s]
τ_f	Characteristic time of the carrier fluid	[s]
η_l	Kolmogorov length scale	[m]
κ	Von Kármán constant equals to 0.41	[-]
Γ	Torque	[N.m]
η_0	Model constant equals 4.38	[-]
β	Model constant equals 0.012	[-]

ABBREVIATIONS

CFD	Computational fluid dynamics
DBB	Dished bottom stirred tank with baffles reaching to the tank bottom
DBD	Dished bottom stirred tank with baffles reaching to the edge of dish
FB	Flat bottom stirred tank
FPP	Fluorescent Polymer Particles
HGS	Hollow Glass Spheres particles
HWA	Hot-wire anemometry
IA	Interrogation areas

ICEM	Integrated Computer Engineering and Manufacturing
IO	Inner-outer
Pixc	Targe pixel number
RTILS	Room temperature ionic liquids
LES	Large eddy simulation
LDA	Laser Doppler Anemometry
LDV	Laser Doppler Velocimetry
Mic_s	microscope setting
MRF	Multiple Reference Frame
N-S	Navier-Stokes
PIV	Particle Image Velocimetry
PSP	Polyamide Seeding Particles
RANS	Reynolds-averaged Navier-Stokes
RNG	Re-Normalisation Group
SGS	Sub-gird-scale
S-HGS	Silver Coated Hollow Glass particles
SM	Sliding mesh
VOC	Volatile organic compound
VOF	Volume of fluid
WALE	Wall Adapting Local Eddy Viscosity
WMLES	Wall-Modeled large eddy simulation

SUBSCRIPTS

g	Gas phase
l	Liquid phase
t	Turbulent
i	Index of space coordinate
j	Index of space coordinate
radial	Radial direction
axial	Axial direction
tangential	Tangential direction
tip	Impeller tip
imp	Impeller

CHAPTER 1: INTRODUCTION

1.1 General Introduction

Ionic liquids (ILs) are a new class of solvent emerged recently, which are salts that have much lower melting points (at or below 100℃.) than normal salts, and are often fluid at room temperature. Unlike other salts, ionic liquids consist entirely of ionic species. They have extremely low vapour pressures, excellent thermal stabilities, ionic conductivities and are capable of dissolving organic and inorganic species (Dong et al., 2010). Due to these essential characteristics, ionic liquids can be served as an excellent replacement for organic solvents in catalysis, synthesis and biocatalysts (Yue et al., 2011, Olivier-Bourbigou et al., 2010, Yang and Pan, 2005). Research has found that the applications of ionic liquids in chemical industry can greatly reduce the emission of volatile organic compounds (VOCs) (Earle and Seddon, 2000). Therefore, the application of ionic liquids in chemical processes will be an important step toward Green Manufacture.

The strength of the van der Waals forces, Coulombic interactions and the size of the ions affect the viscosity of ionic liquids. The high viscosity of the ionic liquids makes them hard to flow hence affecting mixing, separation, heat and mass transfer and applications in industry (Zhang et al., 2006, Zhang et al., 2015). Besides, compared with research progress on the chemical aspects of the ionic liquids, the literatures on fluid dynamics of the ionic liquids are still very less. The knowledge of the ionic liquid hydrodynamics will provide better design and operation of the chemical process for ionic liquids and therefore is worth investigation.

Despite that some numerical and experimental studies on the ionic liquid hydrodynamics were carried out in the bubble columns with single or limited numbers of bubbles (Dong et al., 2010, Wang et al., 2010a), the hydrodynamics aspects of the gas-ionic liquid multiphase flow in the more complex chemical reactors such as the stirred tanks are still lack of attention. The key features of those reactors are their relative flexibility and simple design control systems, which enable high product quality and process efficiency (Zhanga et al., 2009). Understandings of the hydrodynamics in the stirred tanks will provide considerable insight into designing the reactors, the impellers and for determining the mixing operation conditions (Qi et al., 2012). Stirred tanks are also frequently used in research as they enable detailed study of the relation between the droplet/bubble morphology and the energy dissipation rate (Hu et al., 2005b, Hu et al., 2005a, Hu et al., 2006). Therefore, the stirred tanks are ideally suited for current research.

The computational fluid dynamics (CFD) is a powerful tool for the prediction, design and scale-up of the chemical reactors. In the last two decades, with the advance of computer technology, significant progresses have been achieved on the CFD simulations of the mixing processes. Many simulation methods were developed to understand the details on the flow and bulk mixing. The literatures concluded that the accuracy of the CFD results is highly depended on the individual geometry and on turbulence modelling (Deglon and Meyer, 2006).

Due to the importance of the stirred tanks in processing industry, considerable efforts have been taken to develop the CFD modelling of the stirred tanks (Lanea et al., 2005). CFD has been broadly used in modelling the single phase flow and reasonable success has been achieved in predicting the flow flieds (Lane et al., 2000). Besides the modelling of single phase flow, CFD is also a useful tool for modelling the multiphase flows such as the liquid-liquid, particle-liquid and gas-liquid multiphase flows. CFD has several unique advantages over experiment-based approaches to the fluid systems. For instance, it can substantially reduce time and costs of new designs and has the ability to study systems where controlled experiments are difficult or impossible to perform. In addition, the stirred tanks used in mixing industry are often non-transparent which will limit the application of visualization technology. CFD therefore offers better method to study the detailed flow information in stirred tanks. The CFD method will be employed in the present research to supplement the experimental investigations because of its cost effectiveness and the limitations of the available experimental techniques.

So far, the studies of fluid dynamics are normally carried in the flat bottom stirred tank, whereas the dished bottom stirred tank are frequently used in industry. The effect of the tank bottom shape and the baffles' length on the stirred tank mixing efficiency has not been systematically studied. Besides, due to the considerable additional complexities of the gas-ionic liquid multiphase flow system in the stirred tanks, such as the gas dispersion in the high viscosity liquid, the bubble deformation, the bubble breakup and breakage etc., the CFD investigations on the multiphase flow containing ionic liquid in the stirred tanks are still rare in open publications. Modelling the single phase and multiphase flows in the stirred tanks using CFD will provide an insight into the details of the flow field in single phase and multiphase flow systems especially in areas difficult to examine experimentally. In this research, the single phase water, single phase ionic liquid and the gas-ionic liquid multiphase flows modelling are carried out. The visualization techniques including the high speed camera and Particle Image Velocimetry (PIV) are used to measure the bubble size in the ionic liquid and validate the CFD models respectively.

1.2 Aims and Objectives

At present, the majority of numerical and experimental studies on the flow hydrodynamics in stirred tanks are based on water being the operation medium operated in the flat bottom stirred tanks. And the investigations on ionic liquids are mainly focused on the chemical aspects of the ionic liquids such as the synthesis and chemical properties (Earle Martyn and Seddon Kenneth, 2000). Studies on the effect of the tank bottom shape and baffles' length on the flow mixing and the aspects of hydromechanics of gas-ionic liquid multiphase flow system including the bubble sizes and flow field which relate to mass transfer, stirred tank mixing performance and design are still very rare. The primary focuses of this study are to investigate the effect of the tank bottom shape and baffles' length on the flow hydrodynamics, the bubble size, flow velocities and gas holdup in the gas-ionic liquid multiphase flow system in the stirred vessel, which will provide knowledge for the reactor design and process optimization, and offer unique insights into the application of ionic liquids in the chemical industry.

The intension of the research is to:

- Complete a comprehensive literature review on numerical and experimental studies on the single phase and multiphase flow in the stirred tank reactors. Identify appropriate CFD models and approaches to simulate the turbulent and transitional single phase and multiphase flow in the stirred vessels.
- Apply CFD models to the geometry of stirred tank used in the lab and carry out single phase water turbulent flow and transitional ionic liquid flow modelling. The effect of the tank bottom shape and baffles' length on the flow pattern, velocity profiles, Power number, trailing vortexes at the fully developed turbulent state will be compared and discussed. The effect of the tank bottom shape and baffles' length on the ionic liquid transitional flow pattern will also be compared and discussed.
- Employ digital photography technology to measure the bubble size in a stirred tank. Investigate the effect of the ionic liquid concentration, viscosity, surface tension, impeller speed, gassing rate on the bubble size in the stirred tank. Establish the correlations between the bubble size and stirred tank operation condition.
- Carry out the gas-ionic liquid multiphase flow modelling in the stirred tank where the measured bubble size, the liquid physical properties such as density, viscosity and surface tension will be used in the simulations. The flow pattern, velocity profiles and gas

holdup which are the main concerned parameters in the stirred tank mixing will be systematically studied.

- Establish PIV rig to experimentally validate the single phase water and ionic liquid flows and gas-ionic liquid multiphase flow modelling. The flow pattern, velocity components of single and multiphase flow will be measured. The PIV data will be compared with the CFD data to validate the simulation models and results.

1.3 Research Methodology

The following steps will be taken to carry out this investigation:

Step 1: Carry out literature survey to identify CFD models and approaches for simulating the single phase and multiphase turbulent and transitional flow in stirred tank reactor. Find out proper approaches to simulate the rotation of the impeller which may be the multiple reference frame approach, the sliding mesh approach or other approaches. Identity key parameters affect the mixing performance of stirred tank reactor, which may include agitation speed, flow pattern, velocity field, liquid viscosity, bubble size, temperature, pressure, gas flow velocity, volume fraction of dispersed phase etc.

Step 2: Carry out single phase water and multiphase (gas-water) flow modelling using available operation conditions and geometry from reference. The simulation results can be compared with reference data to verify the CFD approaches and to serve as the bench mark for further water, ionic liquid and gas-ionic liquid flow modelling.

Step 3: Establish the 3D geometry of the stirred tank used in the lab, spatially discretise the geometry using mesh, and carry out the CFD modelling of the single phase water/ionic liquid flows and post-process the simulation data. The selection of suitable grid size, adequate turbulent model, right multiphase model and proper boundary condition settings are the main concerns in this step as they determine the accuracy of CFD simulation.

Step 4: Use the high speed camera to measure the mean bubble size in the ionic liquid, which will be served as a key parameter for the gas-ionic liquid multiphase flow modelling. Identify how the key parameters such as the liquid surface tension, viscosity, ionic liquid concentration, impeller speed, gassing rate etc. affect the bubble size in a stirred tank.

Step 5: Carry out the gas-ionic liquid multiphase flow modelling with special focus on the flow pattern, velocity profiles and gas holdup, which will provide key information for improving the stirred tank mixing efficiency and mixing process optimization.

Step 6: Finally, carry out full experimental investigations using PIV to validate the CFD models.

1.4 Thesis Outline

This thesis consists of eight chapters. The following gives a general description of each chapter contained.

<u>The current chapter, Chapter 1</u> gives a brief introduction of the research background, the aims and objectives of this study, the research methodologies used in this investigation and the outline of the thesis.

Chapter 2 is a literature review focusing on numerical and experimental studies on single phase flow, multiphase flow in the stirred tanks, the investigations on the ionic liquid and flow measurement techniques. Computational Fluid Dynamics (CFD) methodologies used for modelling the flow in the stirred tanks will be introduced which include the governing equations, methods for modelling the rotating impeller, turbulence modelling, multiphase flow modelling, interphase forces, boundary and initial conditions. Available models and methods are reviewed and compared. Applicable models and simulation methodologies are identified, which will be used in modelling the single phase and multiphase flow in the stirred tanks.

Chapter 3 presents the single phase water flow modelling in three different stirred tanks. The three stirred tanks are equipped with different length of baffles and bottom shapes. The flow parameters such as the Power number, Flow number, trailing vortex, turbulent kinetic energy and its dissipation rate and flow pattern are simulated and compared with the experimental data from references. The effects of the bottom shape and baffles' length on these parameters are discussed.

Chapter 4 employs Large Eddy Simulation (LES) method to simulate the single phase water and ionic liquid flows in three stirred tanks. The water flow predicted by the LES is compared with the data obtained by the RANS approaches used in chapter 3 and they showed good agreement. Large Eddy Simulation of single phase ionic liquid flow is carried out. The hydrodynamic behaviour of ionic liquid in terms of the flow pattern, velocity field and velocity components in the three different stirred tanks are compared with the corresponding water cases respectively and showed different behaviours.

Chapter 5 adopts visualization technology to measure the bubble size in ionic liquid solutions in a stirred tank. The effect of impeller agitation speed, gassing rate, liquid viscosity, liquid surface tension, ionic liquid concentration on the bubble size in ionic liquid is analysed and discussed. The bubble size information can be used for the gas-ionic liquid multiphase flow modelling.

Chapter 6 carries out multiphase flow modelling in a stirred tank under various operation conditions. To validate the models and approaches used in the multiphase flow modelling, geometry of a stirred tank from reference is created and used to carry out simulation in this tank. The simulation results in terms of flow pattern and the velocity components of the gas and liquid phase are compared with the PIV data from literature, which proves the accuracy of the current multiphase flow simulation models and approaches. Afterwards, the gas-ionic liquid flow modelling is carried out using the verified simulation models and approaches. The most concerned parameters such as the flow pattern, gas hold-up, velocity components of gas and liquid phase in multiphase flow modelling under various conditions are examined and discussed.

Chapter 7 concerns the experimental validation of the simulation data through the measurement of flow fields using Particle Image Velocimetry (PIV). The flow pattern, velocity components of single phase water and ionic liquid flows, gas-ionic liquid multiphase flow in a stirred tank are measured. The PIV data are compared with the corresponding CFD results and good agreements can be found between them.

Chapter 8 draws together the conclusions from the CFD simulations and the PIV experiments in this thesis and discusses the implications of the present findings for research and practice. Possible future work to advance the present research are suggested and discussed.

CHAPTER 2: LITERATURE REVIEW

2.1 Introduction

In recent decades, the computer technology has been developed at increasing high speed. Computational fluid dynamics (CFD) becomes the most important tool in studying all aspects of hydrodynamics. In chemical industry, CFD is the most cost-effective method to obtain detailed information on flow characteristics in chemical reactors. Furthermore, the actual size of apparatus are effectively dealt with based on CFD simulations, thus scale-up uncertainties can be avoided (Montante et al., 2001b).

In this chapter, the numerical and experimental studies on single phase water flow, water-gas multiphase flow and ionic liquid multiphase flow in chemical reactors including stirred tanks have been reviewed. The methods and models used to simulate the rotating impeller, the turbulent and transitional flow in the stirred tanks are introduced. The potential and applicable CFD models and approaches used in this investigation are identified.

The information of interphase forces and bubble size need to be known prior to carrying out the gas-liquid multiphase flow modelling in the stirred tanks. Investigations on the interphase forces and bubble size in the gas-liquid multiphase flow in stirred vessels are introduced.

Experimental studies are required to carry out to validate the accuracy of the numerical models. Flow measurement equipment such as Pitot tube, Hot-wire Anemometry (HWA), Laser Doppler Velocimetry (LDV) and Particle Image Velocimetry (PIV) are commonly used tools in industry and research to measure the flow fields. The flow field measurement devices including their measuring principles, advantageous and disadvantageous in applications are reviewed in this chapter.

2.2 Principles of the Computational Fluid Dynamics

2.2.1 Reynolds-averaged Navier-Stokes Equations

All CFD models are based on the fundamental governing equations of fluid dynamics which are derived from the law of conservation of mass, momentum and energy. They are continuity equation, momentum equation (Navier-Stokes Equations) and energy equation. Those governing equations are highly non-linear equations, therefore cannot be solved explicitly. The CFD has been established to utilise the numerical algorithms to resolve these equations.

In most engineering cases, the time-averaged flow information (e.g. mean pressures, mean velocities, mean stresses etc.) is good enough to resolve most engineering problems so that it is not required to resolve fluctuation details in turbulent flows. Thus, the majority of turbulent flow simulations has been and for the foreseeable future will continue to be carried out with the methods established based on Reynolds-averaged Navier-Stokes (RANS) equations (Versteeg and Malalasekera, 2007).

In Reynolds averaging, the solution variables in the instantaneous Navier-Stokes equations are decomposed into mean and fluctuating components.

For example, the instantaneous velocities and pressure are substituted by the sum of mean and fluctuation parts:

$$\overrightarrow{u_i} = \overline{\overrightarrow{u_i}} + \overrightarrow{u_i'}$$

(2.1)

$$p = \overline{p} + p'$$

(2.2)

where $\overrightarrow{u_i}$ and p are instantaneous velocity and pressure respectively. $\overline{\overrightarrow{u_i}}$ and $\overrightarrow{u_i'}$ are the mean and fluctuating velocity components (i=1,2,3). $\overline{p}$ and p' are the mean and fluctuating pressure correspondently.

Substituting the Reynolds decomposition for the flow variables into the instantaneous conservation equations of continuity and momentum and taking a time average (and dropping the overbar on the mean velocity) yields the Reynolds-averaged Navier-Stokes equations for incompressible flow as showing in below subsections.

2.2.1.1 Continuity Equation

The flow in stirred tank during agitation process is governed by the continuity equation which the net mass flow out of control volume must be the same as the rate of decrease of mass inside control volume. The differential form of the continuity equation is written as:

$$\frac{\partial \rho}{\partial t} + \frac{\partial (\rho \overrightarrow{u_i})}{\partial x_i} = 0$$

(2.3)

where ρ is the fluid density, t is the time, $\vec{u}$ is the flow velocity vector. In the steady state simulation, the equation 2.3 can be written as:

$$\frac{\partial(\rho\overrightarrow{u_i})}{\partial x_i} = 0$$

(2.4)

2.2.1.2 Momentum Equation

The momentum equation is derived from the fundamental physical principle (Newton's second law) to model the flow:

$$\frac{\partial(\rho\overrightarrow{u_i})}{\partial t} + \frac{\partial\left(\rho\overrightarrow{u_i}\,\overrightarrow{u_j}\right)}{\partial x_j} = -\frac{\partial p}{\partial x_i} - \rho\overline{\overrightarrow{u_i'}\overrightarrow{u_j'}} + \rho\vec{f}$$

(2.5)

where ρ is the fluid density, t is the time, $\vec{u}$ is the flow velocity vector, p is the static pressure, $\rho\vec{f}$ represents the body forces including gravity and buoyancy (ANSYS, 2011a).

However, when this time-averaged Navier-Stokes Equations are applied, the extra term such as Reynolds stress tensor ($\rho\overline{\overrightarrow{u_i'}\overrightarrow{u_j'}}$) appears in the time-averaged (or Reynolds-Averaged) flow equations. The Reynolds stress tensor needs modelling. According to the Boussinesq hypothesis, the Reynolds stress is proportional to the mean strain rate (Shaw, 1992):

$$-\rho\overline{\overrightarrow{u_i'}\overrightarrow{u_j'}} = \mu_t\left(\frac{\partial\overrightarrow{u_i}}{\partial x_j} + \frac{\partial\overrightarrow{u_j}}{\partial x_i}\right) - \frac{2}{3}\rho k\delta_{ij}$$

(2.6)

where μ_t is turbulent viscosity, δ_{ij} is Kronecker delta (if i=j, δ_{ij}=1; if i≠j, δ_{ij}=0). k is the turbulent kinetic energy per unit mass.

The turbulent viscosity (μ_t) is a property of the turbulent flow and can be calculated from:

$$\mu_t = \rho C_\mu \frac{k^2}{\varepsilon}$$

(2.7)

where *k* is the turbulent kinetic energy rate per unit mass and *ε* is the turbulent kinetic energy dissipation rate per unit mass. These two terms require additional modelling to close the RANS equations, which leads to the emergence of various turbulence models such as the standard *k-ε* turbulence model and its variations (e.g. Re-Normalisation Group (RNG) *k*-ε model, Realizable *k-ε* model). C_μ is the model constant equals to 0.09 in the standard *k-ε* turbulence model .

Among these turbulence models, the standard *k-ε* turbulence model is the most widely used one in simulating the turbulent flows in research and industry (Versteeg and Malalasekera, 2007). The form of the standard *k-ε* model is showing below:

$$\frac{\partial}{\partial t}(\rho k) + \frac{\partial}{\partial x_i}(\rho k \vec{u}_i) = \frac{\partial}{\partial x_j}\left[\left(\mu + \frac{\mu_t}{\sigma_k}\right)\frac{\partial k}{\partial x_j}\right] + G_k + G_b - \rho\varepsilon - Y_M + S_k$$

(2.8)

$$\frac{\partial}{\partial t}(\rho \varepsilon) + \frac{\partial}{\partial x_i}(\rho \varepsilon \vec{u}_i) = \frac{\partial}{\partial x_j}\left[\left(\mu + \frac{\mu_t}{\sigma_\varepsilon}\right)\frac{\partial \varepsilon}{\partial x_j}\right] + C_{1\varepsilon}\frac{\varepsilon}{k}(G_k + C_{3\varepsilon}G_b) - C_{2\varepsilon}\rho\frac{\varepsilon^2}{k} + S_\varepsilon$$

(2.9)

The values of semi-empirical constants: $C_{\varepsilon 1} = 1.44$, $C_{\varepsilon 2} = 1.92$, $\sigma_{\varepsilon} = 1.0$, $\sigma_k = 1.3$ were robust in modelling the turbulent flows in engineering applications (ANSYS, 2011b). G_k and G_b represent the generation of k which results from mean velocity gradients and buoyancy respectively. Y_M indicates the contribution of the fluctuation dilatation in compressible turbulence to the overall dissipation rate. S_k and S_ε are user defined terms (ANSYS, 2011a).

Since heat transfer was not of interest in this investigation, the conservation of energy equation was not used in the current simulation and will not be introduced here.

2.2.1.3 Extension of Governing Equations to Multiphase Flow Modelling

There are two distinct alternative kinds of specification to describe the motion of fluid flow: the Lagrangian specification and the Eulerian specification.

The Lagrangian specification of the flow field is a way of looking at fluid motion where the observer follows an individual fluid parcel as it moves through space and time. The Eulerian specification of the flow field is a way of looking at fluid motion that focuses on specific locations in the space through which the fluid flows as the time passes (Lamb, 1994). These two specifications are the bases for the two approaches which are broadly used in the numerical simulation of the multiphase flows: Euler-Lagrange approach and Euler-Euler approach (Lamb, 1994).

In the Euler-Lagrange approach, the primary phase is treated as continuum by solving the N-S equations, while the dispersed phase is solved by tracking every single particle which moving through the flow field. This approach has been used in several applications, such as the modelling of spray dryers, coal and liquid fuel combustion etc. The advantage of this approach is being able to model the motion of particles or bubbles with different sizes. But this method is limited to model relatively dilute flows, since it will bring about vast computational cost and simulation time when there are large numbers of bubbles in the primary phase (Lapin and Lübbert, 1994, Sokolichin et al., 1997, Delnoij et al., 1997, Druzhinin and Elghobashi, 1998). When the Euler-Lagrange method is used in modelling the gas-liquid multiphase flow in the stirred tanks, all the bubbles in the liquid phase will be tracked individually. There are numerous bubbles in a stirred tank generated by means of agitating and sparging, therefore this approach will be highly computational demand in modelling gas-liquid multiphase flow in the stirred tanks and this method is not suitable for the current investigation.

Compared with the Euler-Lagrange approach, the Euler-Euler approach avoids tracking the motion of bubbles with different sizes, hence greatly reducing the computation cost. However, the information of bubble trajectories and bubble size distributions cannot obtain by using the Euler-Euler approach. Since the bubble size distributions and their trajectories are not the main concern of the current stage of investigation and the gas-ionic liquid multiphase modelling is extremely time consuming, the Euler-Euler approach was used in this investigation.

Euler-Euler approach is the most commonly adopted method to model the gas-liquid flow in the stirred tanks. In this approach, the liquid and gas phase are regarded as interpenetrating continua medium which means that both the liquid and gas phase are part of the computational domain and interpenetrating with each other while they are moving (Gimbun et al., 2009). Since the volume of each phase cannot be occupied by the other phase, the volume fraction term is introduced and the sum of volume fraction for each phase equals one (ANSYS, 2011a). When the Euler-Euler approach was employed, the governing equations will be solved for each phase. The continuity (equation 2.3) and momentum equation (equation 2.5) showed previously are changed into below forms respectively:

$$\frac{\partial \alpha_q \rho_q}{\partial t} + \frac{\partial(\alpha_q \rho_q \vec{u}_{q,i})}{\partial x_i} = 0$$

(2.10)

$$\frac{\partial\left(\alpha_q \rho_q \vec{u}_{q,i}\right)}{\partial t} + \frac{\partial\left(\alpha_q \rho_q \vec{u}_{q,i} \vec{u}_{q,i}\right)}{\partial x_j} = -\frac{\partial\left(\alpha_q\, p\right)}{\partial x_i} + \rho\overline{\vec{u}_{q,i} \vec{u}_{q,J}} + \vec{F}_i + \alpha_q \rho_q \vec{f}_q$$

(2.11)

where α is the volume fraction of liquid phase and gas phase. $\alpha_l + \alpha_g = 1$. The subscript q is the phase index, where $q = l$ and $q = g$ indicate the variables of liquid phase and gas phase respectively (ANSYS, 2011a). $\vec{F}_i$ is the interphase forces, which will be introduced in the following section.

2.2.1.4 Forces Acting on Bubbles

The interphase forces mentioned above, which control the bubble movement in the liquid phase, are mainly the drag force, lift force and added mass force (Gimbun et al., 2009).

The drag force of liquid phase ($\vec{F}_{D,l}$) and gas phase ($\vec{F}_{D,g}$) is proportional to the mean relative velocity between different phases. It can be described as:

$$\vec{F}_{D,l} = -\vec{F}_{D,g} = K(\vec{u}_g - \vec{u}_l) \tag{2.12}$$

where K is interphase exchange coefficient.

In general, K is defined as:

$$K = \frac{A}{8}\rho_l C_D \left|\vec{u}_g - \vec{u}_l\right| \tag{2.13}$$

where A is the interfacial area, C_D is the drag force coefficient. By default, A is calculated from the below equation:

$$A = \frac{6\alpha_l \alpha_g}{d_b} \tag{2.14}$$

where d_b is bubble diameter. Thus, equation 2.12 can be written as:

$$\vec{F}_{D,l} = -\vec{F}_{D,g} = \frac{3\alpha_l \alpha_g \rho_l C_D}{4d_b}(\vec{u}_g - \vec{u}_l)\left|\vec{u}_g - \vec{u}_l\right| \tag{2.15}$$

Table 2.1 shows the broadly used expressions for calculating the drag force coefficient from literatures.

Table 2.1 Drag force coefficient in literature

Researchers	**Applications**	**Drag force coefficient**
Schiller and Naumanna (1935)	From laminar flow to turbulent flow	$C_D = \begin{cases} \frac{24\left(1+0.15{Re_r}^{0.687}\right)}{Re_r} & Re_r \leq 1000 \\ 0.44 & Re_r > 1000 \end{cases}$ Re_r is the relative Reynolds number is defined as $Re_r = \frac{d_b \rho_l \lvert\vec{u}_g - \vec{u}_l\rvert}{\mu_l}$
Ishii and Zuber (1979)	Stokes flow	$C_D = \frac{24}{N_{Re}}$, where N_{Re} is particle Reynolds number, $N_{Re} = d_b \rho_l \lvert\vec{u}_g - \vec{u}_l\rvert / \mu_m$, $\mu_m = \mu_l(1-\alpha_g)^{-2.5(\mu_g+0.4\mu_l)/(\mu_g+\mu_l)}$
Ishii and Zuber (1979)	Undistorted bubbles	$C_D = \frac{24(1+0.1{N_{Re}}^{0.75})}{N_{Re}}$
Ishii and Zuber (1979)	Distorted bubbles	$C_D = \frac{2}{3} d_b \sqrt{\frac{g\Delta\rho}{\sigma}} \left\{\frac{1+17.67\left[f(\alpha_g)\right]^{6/7}}{18.67 f(\alpha_g)}\right\}^2$ where $f(\alpha_g) = \sqrt{1-\alpha_g}(\frac{\mu_l}{\mu_m})$

The drag force coefficient proposed by Schiller and Naumanna (1935) is based on the experiment that bubble moving freely in stagnant water and bubble shape is assumed as rigid spherical shape. The drag force coefficient proposed by Ishii and Zuber (1979) considers the distortion of bubble at various Reynolds number. Both of drag force coefficient models were commonly used in modelling the gas-liquid flow in stirred tank. And it has been found that, if the bubble size is small enough (less than 3 mm), the difference is negligible when applying these two drag force coefficient models to the gas-water multiphase flow modelling in the stirred tanks (Gimbun et al., 2009).

Throughout this investigation, only the Schiller-Naumanna drag coefficient model is used because the experiment shows that the mean size of the bubbles in the pure ionic liquid at the investigated operation conditions are less than 1 mm and bubbles are almost in spherical shape.

The lift force is dependent on the relative velocity between gas and liquid phase, the liquid velocity gradient, gas phase volume fraction and liquid density. The lift force is calculated through following equation:

$$\vec{F}_{lift,l} = \vec{F}_{lift,g} = C_{lift}\rho_l\alpha_g(\vec{u}_g - \vec{u}_l) \times \nabla \cdot \vec{u}_l \tag{2.16}$$

where C_{lift} is lift force coefficient, which is the correction to the effect of fluid viscosity and particle shape on flow field. The value of lift force coefficient can be set between 0.01 and 0.5 when bubbles move in the liquid. The value of lift force coefficient equals 0.5 when bubbles move in water, and it decreases with the increase of liquid phase viscosity and with the decrease of the bubble size (ANSYS, 2011a).

The added mass force (virtual mass force) is formed due to the bubble undergoes acceleration different from that of the liquid phase. The equation to express the added mass force is:

$$\vec{F}_{vm} = \alpha_l \rho_l C_{vm} \frac{D}{Dt}(\vec{u}_g - \vec{u}_l)$$

(2.17)

where C_{vm} is added mass force coefficient, which represents the inertial force of moving liquid under the effect of particles. Cook and Harlow (1984) found that the value of added mass force coefficient can be set as 0.25. Lance and Naciri (1991) stated that the added mass force coefficient has relationship with the average gas volume fraction. The correlation is

$$C_{vm} = \begin{cases} \dfrac{1 + 2\bar{\alpha}_g}{2(1 - \bar{\alpha}_g)} & (0 \leq \bar{\alpha}_g \leq 0.5) \\[2ex] \dfrac{3 - 2\bar{\alpha}_g}{2\bar{\alpha}_g} & (0.5 \leq \bar{\alpha}_g \leq 1.0) \end{cases}$$

(2.18)

2.2.2 Large Eddy Simulation

2.2.2.1 Principles of Large Eddy Simulation

Compared with the Reynolds-averaged Navier-Stokes turbulence modelling discussed in section 2.2.1, the Large Eddy Simulation (LES) offers a different approach to simulate the flows. The LES modelling technique assumes that there are different scales of turbulent eddies in the flow fields. The largest eddies are comparable to the characteristic length of the mean flow and the smallest eddies are responsible for the turbulent kinetic energy dissipation (ANSYS, 2011a). The large eddies are anisotropic, which interact with and obtain energy from the mean flow. The behaviour of the large eddies are dependent on the geometry of the computational domain, the boundary conditions and the body forces. Meanwhile, the small eddies were almost isotropic and their behaviour are universal (Versteeg and Malalasekera, 2007).

In the LES, the large turbulent structures in flow field are resolved directly by solving the spatial-averaged Navier-Stokes equations. The information of the small eddies were filtered. The influence of the small eddies on the resolved large eddies are modelled by applying the Sub-Grid-Scale (SGS) model. A spatial filtering operation is used in the LES to separate the large and small eddies. A general process of LES is showing below (Versteeg and Malalasekera, 2007):

- A filtering function and a cut-off width will be selected. All eddies with the length scale larger than the cut-off width will be resolved in the unsteady flow field.

- A spatial filtering process will be executed on the time-dependent flow equations. During this process, the information of turbulent structures of the small and filtered-out eddies will be destroyed.
- Sub-gird-scale (SGS) model will be used to model the sub-gird-scale stresses which are the interaction effect of unresolved small eddies on resolved large eddies.
- If the finite volume method such as FLUENT is used, the unsteady and space-filtered flow equations will be solved on the control volumes along with the SGS model of the unsolved stresses.

The spatial filtering operation used in the LES is defined via a filter function. The form of its function and the cut-off width govern what is retained and filtered out. The filtering functions are showing below (Versteeg and Malalasekera, 2007):

$$\bar{\phi}(x,t) \equiv \int_{-\infty}^{\infty}\int_{-\infty}^{\infty}\int_{-\infty}^{\infty} G(x,x',\Delta)\phi(x,t)dx_1'x_2'x_3' \tag{2.19}$$

where $\bar{\phi}(x,t)$ is the filtered function, $\phi(x,t)$ is the unfiltered function or original function, Δ is the filter cut-off width. The overbear means spatial filtering instead of time-averaging.

The most commonly used forms of the filtering functions in the three-dimensional LES simulations are the Top-hat (or box), Gaussian and the Spectral cut-off. Of which the Top-hat filtering function is used in finite volume implementation. The form of the Top-hat filter function is:

$$G(x, x', \Delta) = \begin{cases} 1/\Delta^3 & |x - x'| \leq \Delta/2 \\ 0 & |x - x'| > \Delta/2 \end{cases}$$

(2.20)

The selection of filter cut-off width (Δ) is important in LES, since it determines which size of the turbulent eddy is retained and which size is rejected in the computational domain. In FLUENT, the filter cut-off width is often taken to be the cube root of the grid volume:

$$\Delta = \sqrt[3]{\Delta x \Delta y \Delta z}$$

(2.21)

where Δx, Δy and Δz are the length, width and height of the grid cells in three-dimensional computational domain respectively.

2.2.2.2 Governing Equations for Large Eddy Simulation

By applying the filtering operation to the governing equations obtains the filtered unsteady state continuity and momentum equations (Bakker et al., 2000):

$$\frac{\partial \rho}{\partial t} + \frac{\partial \rho \bar{u}_i}{\partial x_i} = 0$$

(2.22)

$$\frac{\partial \rho \bar{u}_i}{\partial t} + \frac{\partial}{\partial x_j} \rho\left(\bar{u}_i \bar{u}_j\right) = -\frac{\partial \bar{p}}{\partial x_i} + \frac{\partial \tau_{ij}}{\partial x_j} + \frac{\partial \sigma_{ij}}{\partial x_j}$$

(2.23)

where τ_{ij} is the filtered stress tensor. σ_{ij} is the Sub-Grid-Scale (SGS) Reynolds stresses and its form is $\sigma_{ij} = -(\rho\overline{u_i u_j} - \rho\bar{u}_i\bar{u}_j)$. The SGS stresses are unknown and need to be modelled by the Sub-Grid-Scale model. The Sub-Grid-Scale model will be introduced in the following section.

2.2.2.3 Sub-Grid-Scale Models

Since the SGS stresses (σ_{ij}) arise from the filtering process are unknown, these stresses need modelling. The Sub-Grid-Scale models in FLUENT employ the same Boussinesq hypothesis used in the RANS models (Hinze, 1975), in which the SGS stresses (σ_{ij}) are proportional to the local strain rate (indicate the symbol used equation 2.24) of the resolved flow:

$$\sigma_{ij} - \frac{1}{3}\sigma_{kk}\delta_{ij} = -2\mu_t\bar{S}_{ij}$$

(2.24)

where μ_t is the SGS turbulent viscosity. δ_{ij} is Kronecker delta (if i=j, δ_{ij}=1; if i≠j, δ_{ij}=0). σ_{kk} is the isotropic part of the SGS stresses which is not modelled but added to the filtered static pressure term. $\bar{S}_{ij}$ is the rate of strain tensor for the resolved scale (ANSYS, 2011a):

$$\bar{S}_{ij} = \frac{1}{2}\left(\frac{\partial\bar{u}_i}{\partial\bar{x}_j} + \frac{\partial\bar{u}_j}{\partial\bar{x}_i}\right)$$

(2.25)

FLUENT offers five Sub-Grid-Scale models for calculating μ_t, which are Smagorinsky-Lilly, Dynamic Smagorinsky-Lilly, Wall Adapting Local Eddy

Viscosity (WALE), Algebraic Wall-Modeled LES (WMLES), and Dynamic Kinetic Energy Sub-Grid-Scale model.

In the Smagorinsky-Lilly Sub-Grid-Scale model, the turbulent viscosity is obtained by (ANSYS, 2011a):

$$\mu_t = \rho L_s^2 |\bar{s}| \tag{2.26}$$

where L_s is the subgrid scales of the mixing length. $|\bar{s}| = \sqrt{2\bar{s}_{ij}\bar{s}_{ij}}$. In FLUENT, L_s is calculated from:

$$L_s = \min(\kappa d, C_s V_c^{1/3}) \tag{2.27}$$

where κ is the von Kármán constant, d is the distance to the closest wall, V_c is the cell volume, C_s is the Smagorinsky constant. The von Kármán constant (κ) equals to 0.41 which is a universal value used for flow modelling (ANSYS, 2011a). The Smagorinsky constant (C_s) is an empirical value and its default value in this model equals 0.1. A C_s value of 0.1 has been found to yield the best simulation results for modelling flows in the transitional and turbulent states (ANSYS, 2011a).

Dynamic Smagorinsky-Lilly Sub-Grid-Scale model is a modified version of the Smagorinsky-Lilly Sub-Grid-Scale model proposed by Germano et al. (1991) and Lilly (1992). The Dynamic Smagorinsky-Lilly Sub-Grid-Scale model allows the Smagorinsky constant (C_s) varying in space and time. The value of C_s is dynamically calculated ground on the information offered by the resolved scales of motion and it is not necessary to specify the value of C_s in advance (ANSYS, 2011a).

The WALE Sub-Grid-Scale model used another equation to model the turbulent viscosity (μ_t). The equation is as showing:

$$\mu_t = \rho L_s^2 \frac{(s_{ij}^d s_{ij}^d)^{3/2}}{(\bar{s}_{ij}\bar{s}_{ij})^{5/2} + (s_{ij}^d s_{ij}^d)^{5/4}}$$

(2.28)

where L_s and s_{ij}^d were computed respectively from:

$$L_s = min(\kappa d, C_w V^{\frac{1}{3}})$$

(2.29)

$$s_{ij}^d = \frac{1}{2}\left(\bar{g}_{ij}^2 + \bar{g}_{ji}^2\right) - \frac{1}{3}\delta_{ij}\bar{g}_{kk}^2$$

(2.30)

$$\bar{g}_{ij} = \frac{\partial \bar{u}_i}{\partial \bar{x}_j}$$

(2.31)

C_w is the model constant. Its default value equals 0.325 and this value has been proved to get reasonable simulation results for modelling the wall bounded flows and laminar shear flows (ANSYS, 2011a).

Algebraic WMLES was proposed by Shur et al. (2008). A mixing length model with a modified Smagorinsky model and with the Piomelli wall damping function was combined in the Algebraic Wall-Modelled LES model (ANSYS, 2011a). The turbulent viscosity in this model is calculated:

$$\mu_t = \rho \cdot min\left[(\kappa d_w)^2, (C_{smag}\Delta)^2\right] \cdot S \cdot \{1 - exp[-(y^+/25)^3]\} \tag{2.32}$$

where d_w is the wall distance, S is the strain rate, C_{Smag} is constant equals 0.2. In order to account for the grid anisotropies in the wall-modelled flows, the Algebraic WMLES model employs a modified grid scale:

$$\Delta = min(max(C_w \cdot d_w;\ C_w \cdot h_{max} \cdot h_{wn});\ h_{max}) \tag{2.33}$$

where h_{max} is the maximum edge length of the cell, h_{wn} is the wall-normal grid distance and C_w is a constant equals 0.15.

The Smagorinsky-Lilly and Dynamic Smagorinsky-Lilly Sub-Grid-Scale model are numerical models in which the Sub-Grid-Scale stresses are parameterized by employing the resolved velocity scales. It assumes that a local equilibrium exists between the kinetic energy dissipation at small subgrid scales and the transferred energy through the filter scale of the grid. When the transportation of the sub-grid-scale turbulence kinetic energy is considered, the modelled turbulence in the sub-grid-scale will be more accurate (ANSYS, 2011a).

The Sub-Grid-Scale kinetic energy is defined as:

$$k_{sgs} = \frac{1}{2}(\overline{u_k^2} - \bar{u}_k^2) \tag{2.34}$$

The turbulent viscosity is calculated through k_{sgs}:

$$\mu_t = C_k k_{sgs}^{1/2} V^{\frac{1}{3}}$$

(2.35)

The SGS stresses are calculated by:

$$\sigma_{ij} - \frac{2}{3} k_{sgs} \delta_{ij} = -2 C_k k_{sgs}^{1/2} V^{\frac{1}{3}} \bar{S}_{ij}$$

(2.36)

By adopting the following equation, k_{sgs} can be gained:

$$\frac{\partial \bar{k}_{sgs}}{\partial t} + \frac{\partial \bar{u}_j \bar{k}_{sgs}}{\partial x_j} = -\sigma_{ij} \frac{\partial \bar{u}_i}{\partial x_j} - C_\varepsilon \frac{k_{sgs}^{\frac{3}{2}}}{V^{\frac{1}{3}}} + \frac{\partial (\frac{\mu_t}{\sigma_k} \frac{\partial k_{sgs}}{\partial x_j})}{\partial x_j}$$

(2.37)

The values of C_ε and C_k are calculated dynamically. σ_k is constant equals 1.0 (ANSYS, 2011a).

Among these four Sub-Grid-Scale models, the Smagorinsky-Lilly Sub-Grid-Scale model developed by Smagorinsky (1963) and Lilly (1966) is the most basic and extensively used one in the LES of flow in the stirred tank reactors (Bakker et al., 2000). And this Sub-Grid-Scale model can be used in modelling the turbulent and transitional flow.

2.3 Computational Fluid Dynamics Modelling in the Stirred Tanks

2.3.1 Modelling the Rotating Impeller

Modelling the interactions between the rotating impeller and stationary baffles is one of the key issues in simulating the flow phenomenon in the stirred tanks. The approaches used to model the rotating impeller will be introduced in this section. The generally adopted approaches are (Joshi et al., 2011):

- Impeller Boundary Condition Approach (Black Box)
- Snapshot Approach
- Momentum Source-sink Approach
- Inner-outer Iterative Approach
- Multiple Reference Frame Approach
- Sliding Mesh Approach

2.3.1.1 Impeller Boundary Condition Approach (Black Box)

The impeller Boundary Condition Approach is an earliest and simplest method to simulate the rotating impeller and it has been adopted by researchers such as Ranade and Joshi (1990) and Harvey and Greaves (1982) to model the rotating impeller in the stirred tanks. In this approach, the effect of rotating impeller on the surrounding liquid is modelled by providing boundary conditions which obtained from the experimental data on the cylindrical surface covering the impeller.

The application of the Impeller Boundary Condition Approach is severely limited by the availability of the experimental data. In order to carry out simulation using this method, the flow variables including velocities, pressure, turbulent kinetic energy, and the turbulent kinetic energy dissipation rate have to be determined experimentally. These experimental data will be served as the boundary and initial conditions of the cylindrical surface covering the impeller (Joshi et al., 2011). This method lacks generality, since numerical simulations using this method can at the most be extended to the geometries and operation conditions very much alike to that for which the experimental data are available (Paul et al., 2004). If the operation conditions, impeller design, liquid property or tank geometry have changed, the boundary conditions have to be measured again for simulating the new system. Besides, the Impeller Boundary Condition Approach can only provide the information out of the cylindrical surface, the detailed flow phenomenon such as flow pattern, flow velocity, pressure, turbulent kinetic energy, turbulent kinetic energy dissipation rate etc. around the impeller blade are still unknown. Therefore, this approach is not appropriate to model the rotating impeller in this investigation.

2.3.1.2 Snapshot Approach

The Snapshot Approach proposed by Ranade and Dommeti (1996), a different modelling way from the Impeller Boundary Condition Approach, can be used to model the rotating impeller. This method assumes that the pressure forces formed by the blade rotation will cause ejection of fluid from the front of the blades and suction of fluid at the back side of the blades. If the ejection and suction effect are modelled correctly, a realistic rotational flow in the stirred tank will be well simulated.

In order to achieve this, mass sources and mass sinks were specified on the front of and on the back of the impeller blades respectively. For the flow in the bulk region, this method assumed that the time derivative terms in the transport equations are negligible and removed from the momentum equation. Therefore, the flow in a stirred tank was simulated using steady state framework along with the source terms (Ranade, 1997). The Snapshot Approach can offer detailed flow information around impeller blades. The major limitation of this approach is that this method assumes the baffles have no effect on the flow in and between the impeller blades, which will lead to incorrect simulation results where the baffles and rotating impellers have strong influence on the flows in and between the impeller blades (Joshi et al., 2011).

2.3.1.3 Momentum Source-sink Approach

The Momentum Source-sink Approach was proposed by Pericleous and Patel (1987) and it was further optimized by Xu and McGrath (1996) to model the rotational motion of impeller. In this method, the rotating impeller is treated as the momentum source, whereas the baffles are treated as the momentum sinks. This method assumes that there are two forces namely the drag force and lift force generating the flow in the stirred tanks. The drag force is the force in the fluid resultant velocity direction and the lift force acts in the perpendicular direction to the resultant velocity (Patwardhan, 2001). This method is realized by adding a term, which is corresponding to the drag force and lift force produced by the impeller action, to modify the source terms in the transport equations. However, the Momentum Source-sink Approach is not an available module in commercial CFD software. Certain terms such as the momentum source/sink due to the emergence/decay of the drag and lift force on the impeller blades are required to be experimentally determined prior to carrying out these simulations, which limits its applications in modelling the rotating impeller in industrial scale stirred tanks (Patwardhan, 2001, Chtourou et al., 2014).

2.3.1.4 Inner-outer (IO) Approach

The Inner-outer Approach avoids using empirical or experimental data to model the rotating impeller in the stirred tanks, which makes it a more advantaged method than the Momentum Source-sink Approach in simulating the flow in the stirred vessels (Lane, 2006). When the Inner-outer Approach is employed, the computation domain of the stirred tank is divided into two overlapping zones. The cylindrical region containing the impeller is defined as the inner zone and the bulk of the region in the computational domain is defined as the outer zone. In the modelling procedure, a simulation is firstly carried out in the inner zone in a reference frame rotating with the impeller. Arbitrary boundary conditions will be applied to the inner zone boundary surface. Therefore, a first flow filed in the inner zone is calculated and the information of velocity profiles, turbulent kinetic energy and turbulent kinetic energy dissipation rate on the inner surface of the outer zone can be obtained. This information will be used as the boundary conditions of the outer zone and the simulation will be performed in the inertial reference frame as the Impeller Boundary Condition Approach. And then, the information of velocity profiles, turbulent kinetic energy and turbulent kinetic energy dissipation rate on the outer boundary surface of the inner zone is obtained. These data will in turn used for the second inner zone simulation and so on. The inner-outer interactive procedure will be continued until the simulation reaches satisfactory numerical convergence (Joshi et al., 2011).

This method has been employed by several researchers (Montante et al., 2001a, Brucato et al., 1998) to simulate the flow field in the stirred tanks and agreements were obtained between CFD and experimental data. However, the Inner-outer approach is very time consuming and it is not an available module in current commercial CFD software such as FLUENT and CFX (ANSYS, 2013, ANSYS, 2011b), which may limit its application in modelling the rotating impeller in the stirred vessels.

2.3.1.5 Multiple Reference Frame (MRF) Approach

The Multiple Reference Frame Approach proposed by Luo et al. (1994b) is a steady state simulation approach. Similar to the IO approach, a rotating reference frame is used to simulate the flow in the inner zone and stationary reference frame is used to model the flow in the domain of the outer zone. This method also avoids using any experimental data to model the rotating impeller. Compared with the IO approach, there is no overlap region in the computational domain when the MRF approach is adopted. Instead, an interface is defined and used to bridge the flow variables between the two zones. Thus it makes the MRF approach less computational demand than the IO approach (Joshi et al., 2011).

The MRF method is an available module in many commercial CFD packages and it has been broadly used to model the rotating impeller. For example, Aubin et al. (2004) studied the effect of the impeller modelling methods, discretization schemes and turbulent models on simulating the mean velocities, turbulent kinetic energy, flow pattern and power numbers etc. The simulation adopting MRF method showed good prediction of the flow pattern and turbulent kinetic energy in a stirred tank. Scargiali et al. (2007) employed the MRF method with the Eulerian–Eulerian multiphase flow approach and the standard k–ε turbulence model to study the gas-liquid flow in stirred tank. The simulated gas and liquid flow field and gas holdup showed agreement with experimental data.

2.3.1.6 Sliding Mesh (SM) Approach

Like the MRF approach, the Sliding Mesh is also a suitable method to simulate the rotating impeller in the stirred tanks. The Sliding Mesh is an available module in most commercial CFD packages. By applying this method, full transient simulation can be carried out using two grid zones: an inner rotating zone and outer stationary zone. The inner rotating zone includes the impeller. Region out of the inner zone in the computational domain is treated as the outer stationary zone. During the simulation, the grid in the inner zone rotates with the impeller while the grid in the outer zone keeps stationary. The two zones slide with each other at a cylindrical interface. The standard conservation equations will be solved in the outer zone and acceleration terms which consider the rotating impeller will be added to the conservation equations to calculate the flow in the inner zone. These two regions are coupled at the sliding interface via sliding-grid algorithm (Joshi et al., 2011). The Sliding Mesh Method is an accurate approach to model the impeller rotation, but it is more computational demand than the MRF approach (ANSYS, 2011b).

The Sliding Mesh has been broadly used to study the transient flow field in the stirred tanks. For example, Bakker et al. (1997) employed the Sliding Mesh method to study the time dependent laminar flow in a stirred tank. They concluded that the Sliding Mesh method can well predict the laminar flow pattern, velocity magnitude and pumping number without any experimental data for the impeller boundary conditions. Fan et al. (2007) stated that good agreements were obtained between the PIV data and simulation results applying LES together with the Sliding Mesh.

2.3.2 Boundary and Initial Conditions

The boundary and initial conditions need to be applied to the flow problems being simulated when numerically solving the governing equations. Based on the FLUENT package, those types of boundary conditions could be used to model the single phase and multiphase flows in the stirred tank are:

- Wall boundary conditions: the wall of tank, impeller, agitating shaft.
- Interface boundary conditions: the boundaries between rotational zone and stationary zone which enable flow variables in one zone to be used to calculate fluxes at the boundary of the neighbouring zone.

- Velocity inlet boundary conditions: the specification of the gas inlet velocity at the sparger where gas is introduced into the gas-liquid multiphase flow stirred tank.
- Degassing boundary conditions: the top of the tank in which the dispersed gas phase is allowed to escape while the liquid phase stays in the gas-liquid multiphase flow stirred tank.

And the following initial conditions must be provided:

- The physical properties of fluid such as viscosity, density, surface tension.
- The speed of the agitator in the rotational zone.
- The volume fraction of the gas phase at the inlet in the gas-liquid multiphase flow stirred tank.
- The velocity of the inlet gas and bubble size in the gas-liquid multiphase flow stirred tank.

2.3.3 RANS Modelling of the Single Phase Flow in the Stirred Tanks

In order to apply the CFD to simulate the real flow fields in the stirred tanks as much as possible, accurate numerical models should be built up. The CFD studies on single phase turbulent and transitional flows in the stirred tanks will be reviewed in this section.

2.3.3.1 Modelling the Turbulent Flow in the Stirred Tanks

A novel grid disc impeller (see Figure 2.1) has radial flow characteristic was designed by Buwa et al. (2006), and this impeller was used for their study of single phase flow mixing in a stirred tank. In their investigation, the MRF method and the standard *k*-*ε* model were applied to model the flow field. The mixing time and power consumption were numerically and experimentally studied. They found that this novel disc has good mixing performance and requires less power consumption. The simulated mean velocities, power consumption and mixing time showed good agreement with their experimental results.

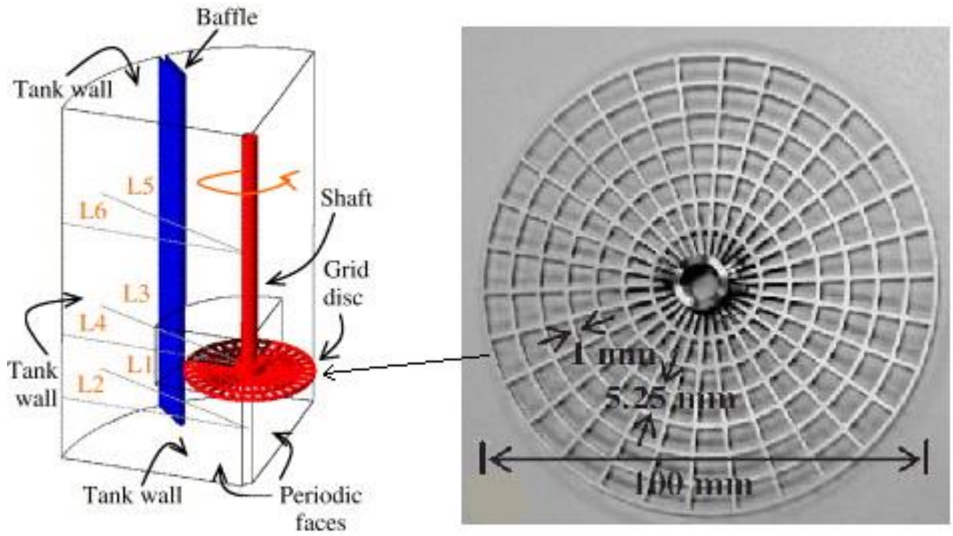

Figure 2.1 Grid disc impeller (Source: Buwa et al. (2006))

Bakker and Van den Akker (1994b) used the standard *k*–*ε* model to simulate the turbulent flow in a stirred tank equipped with a Rushton turbine impeller. The results showed the characteristic turbulent flow pattern in a flat bottom vessel agitated by a Rushton turbine. The liquid around the impeller was thrust toward the wall of tank with radial jet flow reaching the tank wall and forming two circulation loops: the upward circulation loop and the downward circulation loop. The impeller was located at an impeller to bottom clearance of one third of tank diameter, thus the size of the downward circulation loop is smaller than the upward circulation loop.

Deglon and Meyer (2006) investigated the effect of the different turbulent models, rotating impeller modelling methods and discretization schemes on the accuracy of simulations in a flat bottom stirred tank fitted with a Rushton turbine impeller. They showed that the Multiple Reference Frames (MRF) method and the standard *k-ε* model accurately predict the flow in the trailing vortexes regions. The MRF method and the standard *k-ε* model enable accurate simulation of the Power number if very fine girds and higher-order discretization schemes are employed. Due to the deficiencies of the *k-ε* model, the turbulence kinetic energy near the impeller region was over or under estimated even very fine gird and higher-order discretization were used in the simulations.

Aubin et al. (2004) simulated the flow field generated by a down and an up-pumping pitched blade turbines in a dished bottom stirred tank. The standard *k–ε* and RNG *k–ε* models were used to model the turbulence. The Sliding Mesh and MRF methods were adopted to model the rotating impeller. They observed that the secondary circulation loop below the impeller is more radially far away from the axial centre and the vorticity was also larger than the that of secondary loop observed in a flat bottom stirred tank agitated by a down pumping pitched blade (Gabriele et al., 2009). Aubin et al. (2004) concluded that for simulation of the flow in a dish bottom vessel, the numerical scheme was important in predicting turbulent kinetic energy. However the choice of turbulence models: standard *k-ε* and the RNG *k–ε* models have little effect on predicting the mean flow pattern and turbulent kinetic energy. Their simulated turbulent kinetic energy showed better agreement with experimental data for up-pumping pitched blade turbine. The latter conclusion contradicts the results obtained in flat bottom vessel, where the standard k-ε model can predict the turbulence kinetic energy with smallest deviations than other turbulence models such as the RNG k–ε model and Realizable k–ε model (Jaworski and Zakrzewska, 2002).

Haque et al. (2011) adopted four turbulence models: the standard k–ε model, shear-stress transport model and two Reynolds-stress turbulence models with variant of the pressure-strain correlations to simulate the turbulent flow in an unbaffled dished bottom stirred vessel fitted with a Rushton turbine impeller. They found that an inner vortex below the impeller was formed which was not observed in a fully baffled flat bottom stirred vessel. They concluded that all four turbulence models can predict very similar flow field, but the Reynolds stress model is more accurate in predicting the mean axial velocity. All turbulence models give accurate estimation of the turbulent kinetic energy below the impeller, but underestimate its level in the impeller region and in the areas close to the tank walls.

Deen et al. (2002) adopted the standard k–ε model and the sliding mesh method to study the turbulent flow in a stirred tank. They reported that the shape of tank bottom has practically no significant effect on the flow pattern in the Rushton turbine impeller region. However, this conclusion was based on the comparison of the simulation of the water turbulent flow in a flat bottom stirred tank with PIV experimental data obtained in a dished bottom stirred vessel. Detailed analysis of their results indicates that the experimentally observed jet from the impeller was slightly inflected downward in the dished bottom stirred tank, whilst it was almost horizontal in simulation carried out in the flat bottom stirred tank. This study is mainly focused on the flow field in the region near the impeller (in Figure 2.2). The flow pattern outside the region was not discussed.

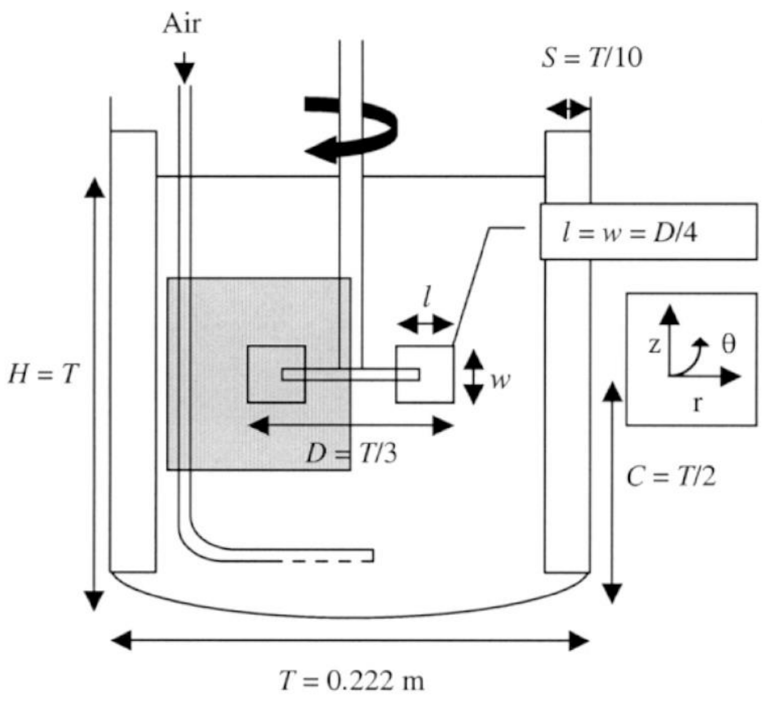

Figure 2.2 The investigated region in the stirred tank (Source: Deen et al. (2002))

According to the above literatures, the single phase flows in the stirred tanks are often operated in the fully developed turbulent state. The standard *k*–*ε* model is the generally used turbulence model in modelling the turbulence in the stirred tanks. The MRF and SM method can be used in simulating the rotating impeller in the steady and transient simulation respectively. The most concerned flow parameters such as the flow pattern, flow velocities, power number, turbulent kinetic energy and its dissipation rate etc. can be well predicted by adopting the standard *k*–*ε* model combined with MRF or SM method. The effect of impeller type, impeller combinations on flow pattern, power number are generally studied in literatures. Majority of investigations are carried out in the flat bottom stirred tanks in lab scale. However, dished bottom stirred tanks are commonly used in industry. The flow in the dished bottom stirred tanks may show different flow patterns when water or ionic liquid is served as the operation liquid. The effect of the stirred tank bottom shape and baffles' length on water and ionic liquid flow pattern will be studied in chapter 3 and chapter 4.

2.3.3.2 Modelling the Transitional Flow in the Stirred Tanks

Since the viscosity of the ionic liquid ($BmimBF_4$) is 0.07 Pa.s, the flow will be in the transitional state ($10 \leq Re \leq 10{,}000$) if the pure ionic liquid is served as the operation liquid in the stirred tanks (Paul et al., 2004). However, compared with the turbulent flow modelling, investigations on the CFD modelling of the transitional flow in the stirred tanks are still very rare.

Jaworski et al. (1996) simulated the transitional flow of a non-Newtonian liquid (*Re*=430) in a fully baffled flat bottom stirred tank agitated by a Rushton turbine. The sliding mesh method was used to model the rotating impeller. The power law equation was defined to describe the rheological behaviour of the shear thinning operation fluid. The RNG *k*-*ε* model, which includes a differential formulation of the turbulent viscosity that is supposed to account for the low Reynolds number effects, was used to closure the Reynolds-averaged N-S equations. The flow pattern, mean velocity components, effective viscosity, turbulent kinetic energy and energy dissipation rate were simulated in their study. The typical radial jet flow from the impeller was found. The magnitude of the radial-axial circulation loops diminished a lot when the viscous liquid was agitated in the stirred tank. High level of turbulent kinetic energy and lowest apparent viscosity was found in the impeller discharge region. The simulated mean velocity components including axial, radial and tangential velocities showed agreement with the LDV data. The authors stated that the RNG k-ε model can predict better results than the two-equation model (such as the standard k-ε model) when it is adopted for simulating transient, high swirl, transitional flows.

Murthy Shekhar and Jayanti (2002) employed two different turbulent models (standard k-ε model and low Reynolds k-ε model) to simulate the transitional flow field in a stirred tank. Different flow patterns were observed in the upper bulk region when those models were employed in the simulation. A secondary circulation flow was found in the corner region close to the tank top when the low Reynolds k-ε model was employed. The species transport equation was then solved to investigate the mixing time in the stirred tank. They found different mixing times when the species transport equation was solved based the initial flow fields simulated by the standard k-ε model and low Reynolds k-ε model respectively. The additional recirculation zone around the main circulation loop, predicted by the low Reynolds k-ε model, will impede the stirred tank fast mixing and increase the stirred tank mixing time.

Kelly and Gigas (2003) carried out CFD simulation to model the flow in a stirred tank agitated by an axial-flow impeller using viscous liquids (glycerin and Carbopol polymer solutions). The flow pattern investigated is in the transitional state ($50 \leq Re \leq 400$). The laminar flow modelling equation was adopted to close the RANS equations. The MRF method was used to model the rotating impeller. The Power law model was used to model the shear-thinning behaviour of the liquid. They found that the power number of the operation liquid depends on the Reynolds number as well as on the flow behaviour index of the power law model. The simulated impeller power number and flow velocities showed good agreement with the experimental data.

Sossa-Echeverria and Taghipour (2015) numerically and experimentally studied the flow velocities in the cylindrical tanks agitated by three different side-entry impellers. The operation liquids (carbopol solutions) were shear thinning fluids and operated in the laminar-transitional regimes. The MRF method was used to model the rotating impeller. The Herschel-Bulkey model and Bingham model were used to describe the non-Newtonian property of operation liquids. They found that the impeller with smaller pitch ratio has lower power requirements and pumping capacities. Impeller with large pitch ratio offers larger high shear rate areas. The predicted flow fields showed agreement with the PIV results

It can be concluded that the models designed for modelling the transitional flows are less developed than the models used to simulate the fully development turbulent flows. The commonly used standard *k*-*ε* model is more appropriate for modelling the flow in the fully development turbulent state. However, it may not provide accurate simulation results such as the flow pattern, flow velocities etc. when the flow is in the transitional state. The RNG *k*-*ε* model and low Reynolds *k*-*ε* model are more suitable to simulate the transitional flow. Agreements between CFD and experimental data have been obtained by adopting these two models.

2.3.4 Large Eddy Simulation of the Single Phase Flow in the Stirred Tanks

As it was mentioned in section 2.2.2, compared with the RANS modelling, the Large Eddy Simulation (LES) adopts a different modelling method to simulate the flows. Since the detailed information of flow structures and turbulence can be captured by adopting the LES, this method has been gained much attention in recent years to model the flows operated at various operation conditions (from the laminar to turbulent regimes). The investigations of the LES of the single phase flow in the stirred tanks will be reviewed in this section.

Bakker and Oshinowo (2004) employed the large eddy simulation to model the large-scale chaotic structures of the turbulent flow field agitated by a Rushton turbine impeller in a flat bottom stirred tank. The Sliding Mesh method was applied to model the rotational motion of the impeller. The trailing vortexes formed behind each blade tips of Rushton turbine were also numerically studied. Both the numerical and experimental results indicated that the trailing vortexes were formed behind each blade and moved radially toward the tank wall. This phenomenon was also verified by the numerical study carried out by Derksen and Van den Akker (1999) and Eggels (1996).

Zadghaffari et al. (2010) carried out the large eddy simulation to study the turbulent water flow in a stirred tank agitated by a Rushton turbine impeller. The Smagorinsky-Lilly Sub-Grid-Scale model was used to model the SGS stresses. The flow pattern, power number, mixing time, turbulent kinetic energy and its dissipation rate were simulated. The simulation results showed agreement with the LDV results obtained by Wu and Patterson (1989). Zadghaffari et al. (2010) concluded that the LES simulation can predict the flow field, power number, mean velocity components and mixing time accurately. The variation trend of turbulent kinetic energy at radial direction can also be captured. Obvious deviations with experimental data were found in predicting the turbulent kinetic energy dissipation rate close to the wall and impeller.

Hartmann et al. (2004) performed the LES and Reynolds-averaged Navier-Stokes (RANS) simulations to model the flow field in a fully baffled stirred tank. The Reynolds number (*Re*) equals 7300, which indicates that the flow is in the lower limit of the turbulent regime. The Sliding Mesh method was applied to model the rotating impeller. Laser Doppler Velocimetry (LDV) was used to verify the simulation results. They noted that the LES is more advantageous than the RANS, in which the velocity fluctuations, Reynold stresses, turbulent kinetic energy are resolved down to the numerical grid scale. The predicted flow field showed good agreement with the LDV data, whereas deviations can be identified in the tangential velocities predicted by the RANS. The development of trailing vortexes was well predicted by adopting the LES and RANS simulation. The LES is better than the RANS simulation in simulating the turbulent kinetic energy and its dissipation rate.

Delafosse et al. (2008) employed the large eddy simulation to study the turbulent flow in a mixing tank agitated by a Rushton turbine impeller. Comparisons were made in the key parameters in terms of the turbulent kinetic energy, turbulent kinetic energy dissipation rate and velocity profiles which were predicted by the LES and the standard k-ε model. The default Smagorinsky-Lilly Sub-Grid-Scale model was used to model the Sub-Grid-Scale stresses. They concluded that both the LES and the standard k-ε model offer good result of the mean flow field. However, the LES was better in predicting the flow in the impeller discharge region.

Li et al. (2011) investigated the single loop flow patterns agitated by the Rushton turbines with different diameters. The phase-averaged and phase resolved velocities, turbulent kinetic energy, trailing vortices and their behaviours were simulated and validated by PIV experiments. Comparisons were made between the simulation results obtained from standard k-ε model and LES. The different SGS models in terms of Smagorinsky-Lilly, Dynamic Smagorinsky-Lilly and Dynamic Kinetic Energy model were used in LES. The simulated flow parameters including velocity components and turbulent kinetic energy were compared. They concluded that regions with high levels of turbulent kinetic energy are consistent with the trailing vortexes and the vortexes transfer the energy from the blade to the bulk region of the stirred tank. The LES with all the tested SGS models can give accurate results. They found that the flows in the trailing vortexes regions are anisotropic, thus the standard k-ε model based on isotropic assumption is less accurate in simulating the flow phenomenon in this area.

Fan et al. (2007) compared the flow fields predicted by the LES and the standard *k-ε* model. The Smagorinsky-Lilly Sub-Grid-Scale model was used in LES. They found that the flow patterns predicted by the LES are asymmetric, chaotic, complex and detailed.

Preliminary series of LES of single phase water turbulent flow in a flat bottom stirred tanks (geometry and operation condition are the same as shown in section 3.2) were carried out to estimate the effect of Sub-Grid-Scale models on the simulation results. The simulation data were sampled and compared at a horizontal plane 40 mm above the tank bottom, which indicates that there is no significant among the simulation results when different Sub-Grid-Scale models used in this study (Appendix 2.1 Velocity Magnitudes Predicted by Different SGS Models).

According the literatures in this section, the LES showed more detailed and accurate simulation results than that predicted by the RANS modelling. The Smagorinsky-Lilly model was the economic and widely used Sub-Grid-Scale model in the LES. The LES avoids the limitation of the standard *k-ε* model that can only be used in the fully developed turbulent flow. Therefore, the LES together with the Smagorinsky-Lilly Sub-Grid-Scale model will be used to model the single phase water and the ionic liquid transitional flows in the stirred tank.

2.3.5 Modelling the Gas-liquid Multiphase Flow in the Stirred Tanks

The term multiphase flow is used to describe any fluid flow consisting of more than one phase or component (Brennen, 2005). A phase refers to the solid, liquid or vapour state of the matter. A component is a chemical species such as hydrogen, oxygen, water or Freon (Schwarzkopf. et al., 2012). Multiphase flows can be divided into four categories: solid-liquid, gas-solid, gas-liquid and three phase flows (Schwarzkopf. et al., 2012). By definition, the dispersed phase is termed as the particles, droplets or bubbles in solid-liquid flow, liquid-gas flow and gas-liquid flow respectively. The continuous phase is referred to the medium around the dispersed phase (Clift et al., 2005). In this study, we focus on modelling of the gas-liquid dispersion in the stirred vessel. The essential information required for the gas-liquid multiphase flow modelling in the stirred tanks in terms of bubble size, interphase forces, turbulence model are reviewed and discussed in this section.

2.3.5.1 Experimental Studies on the Bubble Size in the Stirred Tanks

The knowledge on bubble size and its distributions in the stirred tanks are important in determining both the mass transfer rate and the gas-liquid interfacial area in the gas-liquid stirred vessels (Paul et al., 2004). And the bubble size data is required to carry out multiphase modelling in the stirred tanks. Accurate bubble size information is a key factor towards successful gas-liquid multiphase flow simulation (Khopkar and Ranade, 2006).

A number of techniques such as the capillary and digital photography are generally used for measurement of the bubble size and its distributions in the stirred tanks. Capillary suction probe is an intrusive point wise technology to measure the bubble size. In this method, a capillary will suck bubble and the photoelectric probes are used to calculate the size of the bubble inside the capillary (Moilanen, 2009). Greaves and Barigou (1988) used capillary probe technique measured the bubble size and its distribution at several positions in stirred tank. They concluded that the bubble size distribution was dependent on the intensity of impeller rotation and its location in the stirred tank.

Barigou and Greaves (1992) carried out several experiments to investigate the bubble size distributions in stirred tank using capillary suction probes. Data were sampled at the bulk of the tank, impeller region and area below the impeller. The twenty-two measuring points were plotted in the mid-plane between two adjacent baffles as shown in Figure 2.3. They found that smallest bubbles were found mainly near the impeller tips region due to the high level of turbulence, and the bubble sizes are relative larger at other sampling positions. At low agitation speed around 100 rpm, bubbles were not found in the centre zone below impeller due to the uncompleted flow circulation. By increasing the impeller speed, the lower circulation loop was enlarged causing more gas circulated in this area. Compared with the bubble size in the impeller region, the bubble sizes are larger in the lower circulation loop. The bubble diameter rises from the impeller tips towards the tank wall due to the increasing number of bubbles and gas holdup which enhance the bubble collision and coalescence.

The effect of the impeller speed on the overall Sauter mean diameter in the bulk region was found to be insignificant. Barigou and Greaves (1992) stated that the increased turbulence intensity by increasing the impeller speed was balanced by the increase in bubble coalescence due to the rise of gas holdup. The gas holdup in the downward flow region is higher than that in the upward flow region.

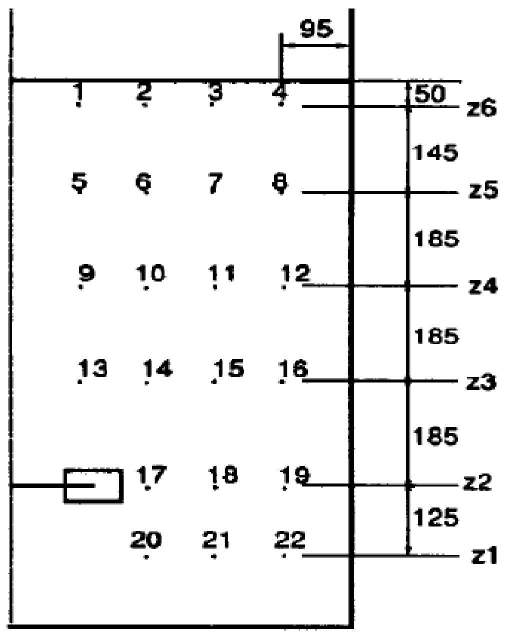

Figure 2.3 Measuring points in mid-plane between two baffles (dimensions in mm) (Source: Barigou and Greaves (1992))

The digital photography is a non-intrusive, optical and the most informative measurement technique. The experimental results can be visually evaluated by adopting this method. Koji Takahashi and Nienow (1993) used this technique successfully measured the bubble size distributions in a stirred tank. They found that the bubble sizes close to the vessel wall (especially near the baffles) or in the upper levels of the vessel were more than four times larger than those in the impeller discharge region.

Martín et al. (2008) used high-speed video technique to study the formation of the bubbles in a stirred tank equipped with different impellers and with impellers fixed at different positions. They found that the bubbles are smaller under stirring condition than those formed in stagnant fluids. The initial bubble size at the orifice controls the contribution of the impeller to the bubble diameter. The location of the impeller, impeller rotation speed and the gas flow rate control the bubble size in the stirred tank.

Montante et al. (2008) used digital camera studied the mean bubble size in a stirred tank agitated by a Rushton turbine impeller. The stirred tank was divided into thirteen investigation areas as shown in Figure 2.4. Figure 2.5 shows the mean bubble size in these thirteen areas. As can be seen from Figure 2.5, the smallest bubbles appear in the impeller region (area marked A). Due to the effect of the downward flow in the lower B and C region, the bubble resident time is longer in lower B and C region, which forms large bubbles in these areas. In the upper and lower central G zones, the differences in bubble size are not evident. They also mentioned that the bubbles diameter in the upper and lower D zones are relative the same due to the apparent coalescence below and above the impeller. Due to the entrainment of bubbles from the liquid surface, an increase in bubble size can be found in the upper zone E. While in the lower E zone, attribute to the jet of the circulation flow, the bubbles are smaller than upper zone E (Montante et al., 2008).

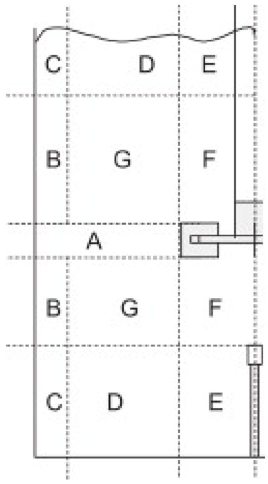

Figure 2.4 Investigation areas (Source: Montante et al. (2008))

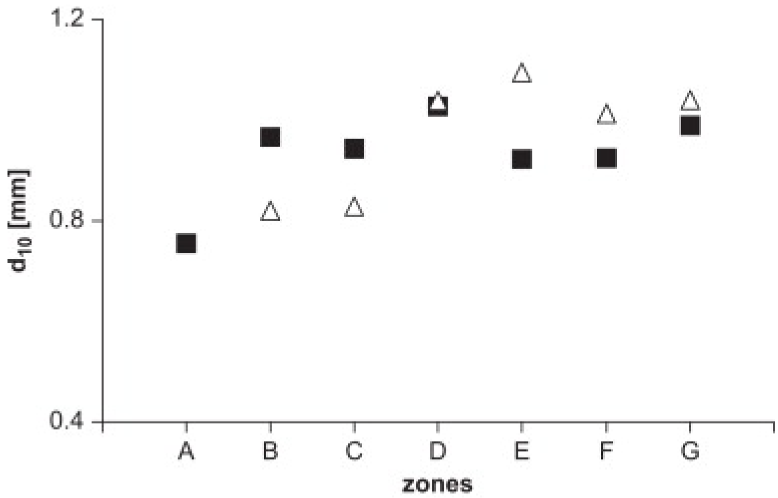

Figure 2.5 Mean bubble diameter in different areas. Solid symbols: lower half vessel; empty symbols: upper half vessel (Source: Montante et al. (2008))

However, there is difference between the experimental results from Barigou and Greaves (1992) and Montante et al. (2008). For example, Montante et al. (2008) found that the bubble size in the upper and lower D zones are relatively the same, and negligible discrepancies can be found in lower and upper G zones. But in Barigou and Greaves' study, the bubble size in the area near the bottom (point 21 in Figure 2.3 corresponding to lower D zone in Montante et al.'s study) is smaller than the area near liquid surface (point 2,3,6,7 in Figure 2.3 corresponding to upper D zone in Montante et al.'s study).

Several studies correlated bubble/droplet size in stirred tank with operation conditions, which can be used to estimate the bubble/droplet size in the stirred vessels. Early researchers such as Shinnar (1961) proposed equations to predict bubble/droplet size in the stirred tanks. The equation, $d_{32} \approx N^{-1.2}$, can be used to estimate the droplet size for systems where droplet size is controlled by the bubble/droplet breakup. The equation, $d_{32} \approx N^{-0.75}$, is applicable for systems where the bubble/droplet size is controlled by the coalescence. Peters (1992) correlated Sauter mean diameter with impeller diameter (D) and Weber number (We), as showing below:

$$\frac{d_{32}}{D} = K_1 We^{-0.6} \tag{2.38}$$

Above equation can be used to estimate the bubble/droplet size for dilute systems. For more concentrated systems, the coalescence will be important and this equation may not applicable. The following equation was established:

$$\frac{d_{32}}{D} = K_2(1 + K_3\alpha_d)We^{-0.6} \tag{2.39}$$

where α_d is the volume fraction of dispersed phase. $K_3\alpha_d$ is considered to allow for either the damping of turbulence when the concentration of dispersed phase is relatively low with $K_3 = 3$; or owing to coalescence with value of K_3 from 3 to 10 (Pacek et al., 1998).

Pacek et al. (1998) proposed correlation between operation conditions and *d₃₂* where breakup controls the droplet/bubble size as following:

$$\frac{d_{32}}{D} = K_2 We^{-0.6} = K_3 {\varepsilon_T}^{-0.4} = K_4 N^{-1.2} \tag{2.40}$$

where ε_T is specific energy dissipation rate. K_2, K_3 and K_4 are equation variables and they varies in different systems.

Equation 2.40 has been usually used to correlate the bubble/droplet size in the gas-liquid/liquid-liquid multiphase flow stirred tanks. However, this equation was found to be unsatisfactory to predict the mean bubble size in some cases where different operation mediums (such as the mixtures of water and isopropanol) were involved (Hu et al., 2003, Hu et al., 2006). So far, there has been no report on whether this equation can be used to predict the bubble size in the ionic liquids in the stirred tanks. The knowledge of bubble behaviour in the ionic liquids operated in the stirred tanks is still a research gap in literature.

2.3.5.2 Interphase Forces Considered in the Gas-Liquid Multiphase Flow Modelling in the Stirred Tanks

Since the interphase forces determine the bubble behaviours in the gas-liquid multiphase flow in the stirred tanks, the inclusion of those interphase forces in simulation is the key factor towards a successful multiphase flow modelling. As it was introduced in section 2.2.1.4, there are many forces acting on the bubbles moving in the liquid phase. These forces can be categorised as the drag force, lift force and added mass force (Morud and Hjertager, 1996). However, the inclusion of all the forces will not only bring about vast computation demand, but also cause convergence difficulty. Therefore, the interphase forces considered in the gas-liquid multiphase flow modelling in the stirred tanks will be reviewed and determined in this section.

The drag force equation is showed in section 2.2.1.4. This force is caused by the relative velocity between the gas and liquid phase. The particles (or droplets or bubbles) with low density can response much faster to the liquid phase and high-density particles (or droplets or bubbles) response much slower to the flow around them. The low-density particles (or droplets or bubbles) will have smaller relative velocity than particles (or droplets or bubbles) with high density. Therefore, the drag force will become dominant for high density particles (or droplets or bubbles) and relative smaller as the density of particles (or droplets or bubbles) decreases (ANSYS, 2011a).

The lift force results from liquid velocity gradient and the relative velocity between the particles (or droplets or bubbles) and surrounding liquid. The lift force equation is displayed in section 2.2.1.4. The lift force acts perpendicularly to the direction of main flow. The lift force appears very small compared with the drag force. Sometimes, the lift force can be ignored when computes the particles (or droplets or bubbles) trajectory (ANSYS, 2011a).

Added mass force was formed when the particles (or droplets or bubbles) undergo acceleration different from that of the liquid phase (Scargiali et al., 2007). This additional force contribution is added mass force. The equation of the added mass force is displayed in section 2.2.1.4. The added mass force has constant influence and plays a key role when computing the trajectory of particles (or droplets or bubbles) (Martin, 2011).

Compared with the drag force and the lift force, the effect of the added mass force on bubbles' behaviour is much smaller. This force is ignored in most studies and including this force has negligible effect on simulation results such as flow pattern, velocity profiles, gas holdup etc. in the stirred tanks. For example, Scargiali et al. (2007) stated that the effect of added mass force is insignificant when modelling the gas-liquid flow in the stirred tanks. Gimbun et al. (2009) found that there is only a little increase in the overall gas hold-up in aerated stirred tank from 4.36% to 4.60% and from 4.36% to 4.67% by adding the effect of virtual mass and lift force respectively.

Among the drag force, lift force and added mass, the drag force is the dominated interphase force and it needs to be considered in modelling the gas-water turbulent flow in the stirred tank (Scargiali et al., 2007). For example, Petitti et al. (2013) stated that velocity field is dominated by the liquid phase motion agitated by the rotational turbine in the stirred tanks, thus other forces can be neglected compared with the drag force in the gas-water turbulent flow in the stirred tank. The Lift force will be more significant for larger the bubbles, the inclusion of the lift force is not appropriate for closely packed bubbles or for very small bubbles (ANSYS, 2011b). In this investigation, it has been observed that the measured mean bubble size in the gas-ionic liquid multiphase flow system in the stirred tank (bubble size is less than 1 mm) is much smaller than that in the gas-water multiphase flow system (bubble size is larger than 2 mm) by adopting the visual technology. And the viscosity of the ionic liquid is 77 times larger than that of water, which means that the lift force coefficient would be at least one order smaller than that in the gas-water multiphase flow system in the stirred tank (ANSYS, 2011a). Therefore, effect of the lift force on the bubble motion is insignificant in modelling the gas-ionic liquid multiphase flow system in the stirred tank. It has been found that the inclusion of lift force and added mass force in gas-water multiphase flow modelling in the stirred tank will bring out convergence difficulties and highly computational demand (Wang et al., 2014). Due to the above reasons, the drag force can be considered as the dominated interphase force in modelling the gas-ionic liquid multiphase flow in a stirred tank. The effect of lift force on bubble motions in the highly viscous fluid such as the ionic liquid is neglected in this investigation.

2.3.5.3 Modelling the Air-water Turbulent Flow in the Stirred Tanks

Apart from the information of the bubble size, the interphase force models, the rotating impeller modelling method, the two phase model and the turbulence model are also the key factors towards the successful gas-liquid flow modelling in the stirred tanks. The numerical and experimental studies on the air-liquid multiphase turbulent flow in the stirred tank reactors will be introduced in this section.

Deen et al. (2002) used Eulerian-Eulerian method to describe the continuity and momentum equations of multiphase flow. The standard k-ε model was used to model the turbulence. The drag force was the only interphase force considered in their study. Sliding mesh method was used to model the rotating impeller. Since the liquid phase was water, they assumed that the bubbles have the same diameter of 4 mm or 2 mm in the stirred tank and applied it into gas-liquid simulation. Free surface boundary condition was user-defined on the liquid surface, in which only the gas phase is allowed to escape from the liquid surface. A source term was defined to describe the gas inflow velocity at the sparger. They reported that the trailing vortexes formed behind each impeller blade in single phase flow were disappeared and the flow is less periodic when gas was introduced from the sparger. The measured liquid velocities showed agreements with PIV data. They found that the liquid velocities reduced around 30% in the impeller region with the existence of gas. The presence of the gas phase has large impact on the liquid velocity field.

Ranade et al. (2001b) applied Eulerian-Eulerian model to simulate the turbulent gas-water flow in a stirred tank. The standard k-ε model was used to model the turbulence. The Snapshot method was used to simulate the rotating impeller. The drag force was the only interphase force considered in their simulation. By defining a source term at the sparger, the gas injection into the stirred tank was realized. The tank top was treated as a wall for the liquid phase, in which water was not allowed to escape from here. A sink term was specified at the tank top for the gas phase, where the exiting of bubbles was simulated. They found that the location of the gas accumulation behind each impeller blade is in the region where trailing vortexes exist. The gas accumulation region can keep their structure up to 30 degrees behind each impeller blade. The current CFD models used in their investigation can well predict the gas accumulation behind the impeller blades and the CFD results showed good agreement with the PIV data.

Wang et al. (2014) carried out series of simulations to study the hydrodynamic behaviours of the gas-liquid multiphase flow agitated by two six-blade impellers in a stirred tank. The Eulerian-Eulerian model was adopted to simulate the turbulent flow of the gas and liquid phases. The standard k-ε model was applied to model the turbulence. The drag force and lift force were considered in the simulation. They noted that the adding of virtual mass force did not bring any improvement of simulation results and cause convergence difficulties.

According to the above literature review on the air-water turbulent flow modelling in the stirred tanks, the current CFD and experimental multiphase flow studies are usually carried out in the gas-water system in stirred tanks. The Eulerian-Eulerian model, the standard k-ε model and the MRF or SM method are combined to simulate the multiphase flow in the stirred tanks. The drag force is generally considered as the dominated interphase force in the gas-water multiphase flow modelling in the stirred tanks. These modelling methods may be moved to model the gas-water turbulent flow or gas-ionic liquid multiphase flow in a stirred vessel. The flow pattern and velocity profiles of each phase, gas holdup, bubble size etc. are the most concerned parameters in the gas-liquid multiphase flow in the stirred tanks. These key parameters are worth studying in the gas-ionic liquid multiphase flow system in a stirred tank.

2.3.5.4 Modelling the Gas-Ionic Liquid Multiphase Flow

As it has been discussed in section 2.3.5.3, the most numerical and experimental studies are carried out in the gas-water multiphase flow system in the stirred tanks. The studies on the gas-ionic liquid multiphase flow in the stirred tanks are still very rare. In this section, the property of the ionic liquid and studies of gas-ionic liquid system in the chemical reactors were introduced, which will provide insight to model the gas-ionic liquid multiphase flow in the stirred tanks.

The Property of Ionic Liquid

According to current common definition, the ionic liquids are materials that are consisted of cations and anions with melting point at or below 100℃. Some of them are called room temperature ionic liquids with melting point at room temperature (Plechkovaa and Seddon, 2008). The person discovered and identified ionic liquid is controversial. Gabriel and Weiner discovered ethanolamminium nitrate which has melting point between 52℃ and 55℃ (Gabriel and Weiner, 1888). The first report of the room temperature ionic liquids can be tracked to 1914 when a scientist called Paul Walden synthesized ethylammonium nitrate which has a melting point of 12℃ and was the product of neutralisation of ethylamine with concentrated nitric acid (Plechkovaa and Seddon, 2008). However, their findings did not cause any significant interest to other researchers at that time. But this study area is becoming prosperous in recent years.

Ionic liquids are salts in liquid form. They have high boiling points, low vapour pressure. Due to the nature of the anions and cations, the polarity of ionic liquid varied (Dumitriu et al., 2010). Ionic liquids have been chosen as preferable solvents in several cases of chemical industry. The properties of ionic liquid can be adjusted based on requirements of particular cases of application. Therefore, researchers described ionic liquids as designer solvents (Freemantle, 1998).

Generally, for traditional liquid, the degree of hydrogen bonding greatly affects the viscosity of liquid hence influencing the flow behaviour in the stirred tanks (Sawamura et al., 1992). By reducing the degree of hydrogen bonding, the viscosity of water and corresponding solutions can be reduced, which makes the liquid easier to flow (Sawamura et al., 1992). By adding the electrolytes, the extent of the structure of hydrogen bonding will be disrupted and the viscosity of aqueous solution will be reduced (Briscoe et al., 2000).

Compared with the traditional liquid, the strength of the van der Waals forces, Coulombic interactions and the size of the ions affect the viscosity of ionic liquids and make the ionic liquids more viscous. For example, Zhang et al. (2006) stated that the increase in van der Waals interactions will result in the alkyl chain lengthening or fluorination, which makes the ionic liquid more viscous. However, by increasing the alkyl chain length, the columbic interactions between anions and cations will be reduced. But, the increasing alkyl chain length has stronger effect on ionic liquid viscosity than that of decreasing the Coulombic interactions of anions and cations (Zhang et al., 2006). Shirota and Fukazawa (2011) noted that the charge localization in the ions has a stronger interaction with a counter ion than the ions with the delocalized charge distribution, and the stronger Coulombic interaction between the cation and anion provides the larger shear viscosity in fluids. Ohno (2005) stated that smaller the ions, the higher the cohesion is. And the high cohesion means high viscosity. Shirota and Fukazawa (2011) noted that the high cohesion of molten salts combined with electrostatic forces make ionic liquid more viscous.

Researchers also found that by increasing the alkyl chain length, the nonpolar regions will increase and take up more and more space, hence decrease the density of ionic liquid (Kolbeck et al., 2010). For the longer alkyl chain the Coulombic interactions contribute less to the surface tension (Kolbeck et al., 2010).

Hydrodynamics Studies of the Ionic Liquids

As a new class of solvent, ionic liquids possess several unique properties, such as high boiling points, low vapour pressure, high viscosity etc., are worthy of scientific research. Knowledge of the bubble behaviour in the ionic liquids will offer beneficial and fundamental information for design and scale-up the reactors and the optimization of the mixing process for these new class of solvents. However, studies related to hydrodynamics of gas-ionic liquid system in stirred tank are still very rare in literatures. Limited studies on the bubble behaviour in the ionic liquids in the bubble columns are available, which can provide knowledge for researching the gas-ionic liquid multiphase flow in the stirred tanks.

Bubble column is a type of chemical reactors normally used in chemical process industry. The study of bubble behaviour in the bubble columns will provide valuable information for design and optimization of these reactors. The drag force, surface tension, viscosity and density of the ionic liquids and gas can be used in simulation to describe the interphase forces and physical properties of the gas-ionic liquid multiphase flow systems (Wang et al., 2010b).

Wang et al. (2010a) studied the bubble behaviour in the ionic liquids in a bubble column. They stated that drag force is the dominated force which determines the bubble velocity in the ionic liquids in the bubble column, while other forces such as the lift force and added mass force are ignored because of their small magnitude compared with the drag force. Among the interphase forces, only the drag force is considered and drag coefficient correlation considering the properties of ionic liquid such as high viscosity and non-molecular structure is proposed. When the proposed drag force coefficient coupled with the PBM (Population Balance Model), the simulated gas holdup in the bubble column agreed well with the experimental data than the default one in the FLUENT. However, the drag force coefficient is applicable in cases operated at low Reynolds number ($0.5 \leq Re \leq 50$). The application of this drag force coefficient may be limited in modelling the gas-ionic liquid system operated at high Reynolds number.

Wang et al. (2010b) adopted an improved volume of fluid (VOF) method combined with the modified drag force and drag force coefficient to simulate the bubble's motion in the ionic liquid. The predicted bubble velocity agreed well with experimental data. However, the VOF model is appropriate for the multiphase flow with the dispersed phase volume fraction less than 10%. Besides, the improved VOF model is proposed based on the assumption that the bubbles move with the same speed as the liquid around them. Therefore, the improved VOF method may be not suitable to model the bubble behaviour in the stirred tanks.

At present, available numerical and experimental studies on the bubble behaviour in the ionic liquids were mainly carried out in the bubble columns. The density and viscosity were used to describe the physical property of the ionic liquid. The drag force plays a leading role in determining the bubble behaviour in the gas-ionic liquid multiphase flow system. As another commonly used chemical reactor, stirred tank, open publications on the gas-ionic liquid flow in these vessels are still very rare. Both the numerical and experimental investigations need to carry out to fill this research gap.

2.4 Flow Measurement Techniques

The applications of the flow measuring techniques in industry will provide information to develop novel configurations of the equipment and expand present knowledge. These measuring techniques can also be served as the validation tools for CFD models, which are essential for reactor design and process optimization in this investigation. The frequently used flow measurement techniques are listed below and will be reviewed in this section:

- Pitot Tube
- Hot-wire Anemometry
- Laser Doppler Velocimetry
- Particle Image Velocimetry

Pitot Tube

The Pitot tube was invited by Henri de Pitot in 1724, to measure the water velocity in rivers, and then this device was modified for measuring flows in closed channel and vessels etc. Henri de Pitot gave his name to this device. The typical Pitot tube consists of a right-angled tube with an open tip direct against the fluid flow and small taps placed perpendicular to the upcoming flow (see Figure 2.6). By measuring the total pressure (at tube tip) and static pressure (at small taps), the local velocity can be calculated from the Bernoulli's equation.

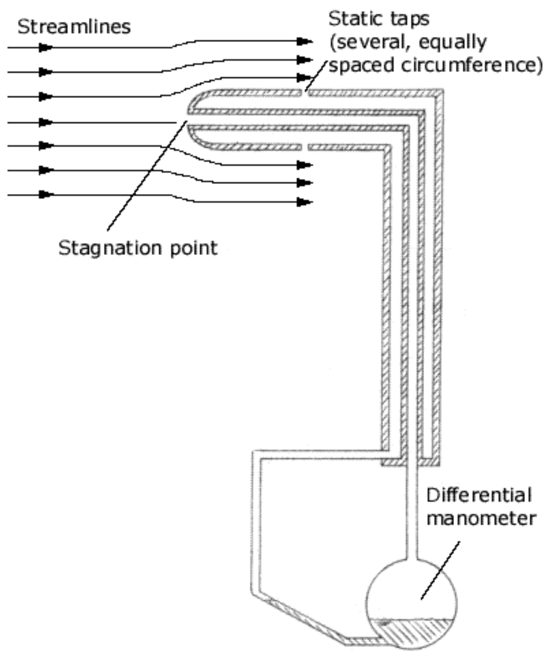

Figure 2.6 Pitot tube (Source: Ahmad (2012))

This measuring tool has been used to measure the velocity of different fluid flows for many years (Chevula et al., 2015). In early years, it was used by Wang and Qian (1989) and Jaworski and Fořt (1991) to measure the velocities in the stirred tanks. This method has its disadvantage: the Pitot tube is intrusive tool which needs to be placed inside the flows. Therefore, the flow pattern will be affect a lot by the inside probes especially for the measuring carried out in the small sized vessels. Besides, it has substantial dynamic resistance to the changing conditions, thus this device cannot precisely measure the accelerating, unsteady or fluctuating flows (Ahmed and Alam Uzzal, 2012).

Hot-wire Anemometry

The hot-wire anemometry (HWA) is another point measurement technique for measuring the flow velocity. The vital part of HWA is a hot wire exposed in the flow, which is either heated by a constant current or retained at a constant temperature (see Figure 2.7). The wire is usually made of tungsten, platinum or platinum-iridium with diameter on the order of several micrometres. When there is flow passing through the hot wire, it will cause cooling effect on this wire. The HWA is based on sensing and measuring the rate of cooling of the hot wire. Since the electrical resistance of the fine wire is dependent on the temperature of the metal, a relationship between the electrical resistance and flow velocity can be made when the fluid passing through the wire (Sun et al., 1992). It is possible to detect the velocity components at this point in the flow field by combining several wires on the same probe.

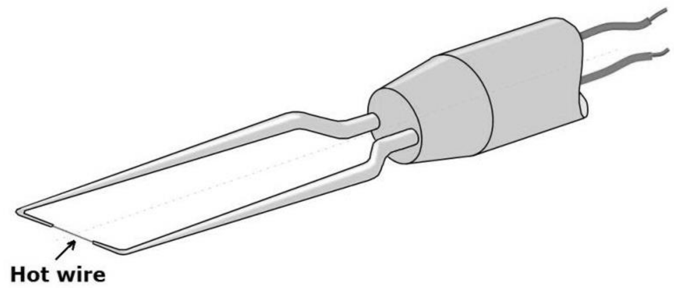

Figure 2.7 Hot-wire (Source: Mars (2015))

HWA has been frequently used to study the flow field (Sherif, 1998, Amini and Hassan, 2014). Beforehand knowledge of the functional dependence of the heat loss from the hot wire on the flow velocity, density, temperature and the flow angle will guarantee more accurate test results. Precise measurement data can be attained in variety of flows: liquids, gasses, conducting liquid metals etc. under a wide range of environmental conditions (Mavros, 2001). But HWA has usage limitation in industry, e.g. for industrial applications contain dirt and pollutants which will cause severe damage to the hot-wire anemometer. Besides, the HWA is an intrusive measurement technique which will cause modification of the local flow field (Paul et al., 2004).

Laser Doppler Velocimetry

Laser Doppler Velocimetry (LDV) also known as the Laser Doppler Anemometry (LDA), which is a nonintrusive tool to measure the velocities of the transparent or semi-transparent fluid flows. The fluids are seeded with particle tracers. If the size of these particle tracers is pretty small, in the order of micrometres, they can be treated as good tracers following the flow field with their velocity corresponding to the fluid velocity (Paul et al., 2004).

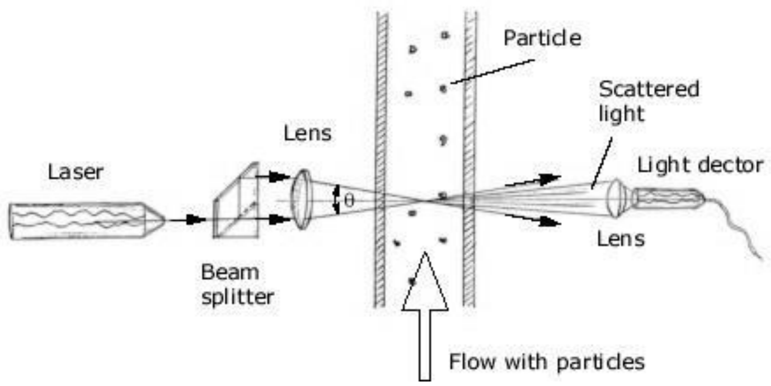

Figure 2.8 LDV setup (Source: Doda (2008))

Figure 2.8 illustrates a LDV system. The LDV adopts splitter to generate two laser beams which cross at some place in the flow of the fluid being measured. The tracer particles suspended in the flow are illuminated by the laser beams and at the same time, these two beams interfere and generate a set of parallel straight fringes in the intersection area. When the seeded particle tracers in the fluid pass through the fringes, they scatter laser light that is then captured by a photodetector. The frequency of the scattered light from the particles is different from that of the incident beam from the laser, which is called the Doppler shift, is linearly proportional to the tracer velocity. Therefore, it is possible to determine the particle velocity at the cross area by analysing the change in the scattered laser intensity fluctuations on the photodetector.

LDV has been broadly used to measure the velocity profiles in the stirred tank reactors and good experimental results were obtained by researchers such as Bittorf and Kresta (2000) and Schäfer et al. (1997). Like other velocity measuring tools such as the Pitot tube and Hot-wire Anemometry, LDV is single point measuring device. It can only measure the velocity at a set point in the flow field.

Particle Image Velocimetry

The Particle Image Velocimetry (PIV) is also a nonintrusive optical flow measurement and visualization technique used in research. It can be used to investigate the flow field and turbulent quantities in the single phase flow and the multiphase flow systems. PIV measures the instantaneous velocity for an entire plane of a flow field directly. Therefore PIV has obvious advantages over point wise measurement such as the capillary suction probe and the laser Doppler anemometry (Oakley et al., 1997).

PIV measures the flow velocities and flow related properties if the fluid is seeded with tracer particles. Like the tracers used in the LDV, the tracers should be assumed to faithfully follow and do not alter the operation liquid. When a powerful laser sheet is passing the seeded fluid, these tracers are illuminated and become visible. Pictures of the tracers at the test area will be taken by a high speed camera at short intervals. A map of the instantaneous velocity field can be gained by analysing the displacement of each tracer at the time interval if sufficient tracer particles are present.

Generally, as shown in Figure 2.9, the PIV system consists of a laser source to illuminate the test area, a high speed digital camera to record the images of tracers, a synchronizer to serve as a trigger for controlling the laser source and camera, a cylindrical lens to convert a laser beam to a laser sheet, a traverse to control the position of the camera, a computer and the image sampling and processing software.

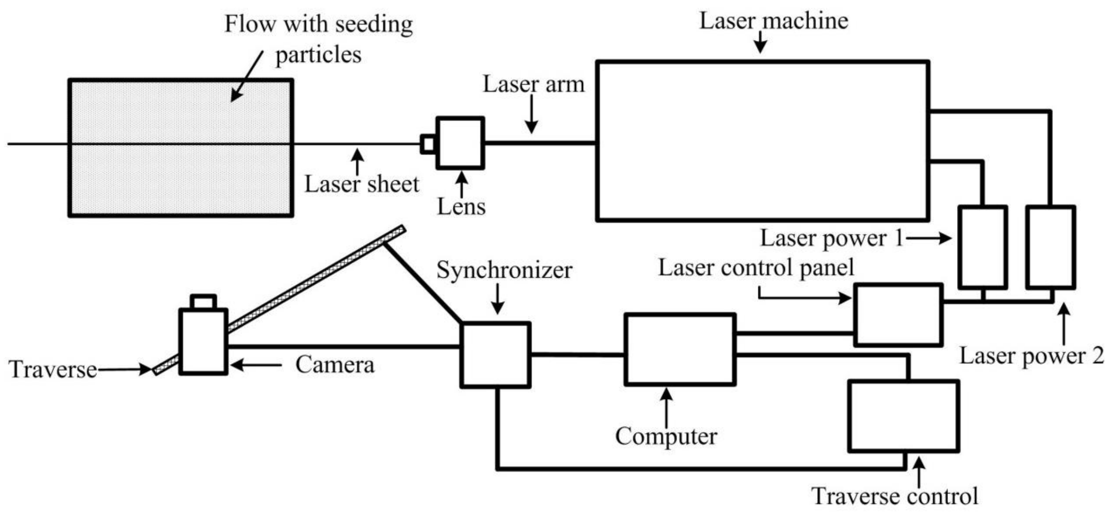

Figure 2.9 Sketch of the PIV system

The sampled images of traces are divided into small regions named as the interrogation areas (IA). The interrogation areas from each image frame are cross-correlated with each other, pixel by pixel. The correlation produces a signal peak and detects the particle's displacement. An accurate measurement of the tracer's displacement obtains the velocity vector. A detailed velocity vector map over the whole test area can be gained by repeating the cross-correlation for each IA over the two image frames taken by the high speed camera (Dynamics, 2013).

The PIV system has been served as a useful tool in research and used in flow measurement in the stirred tanks. Li et al. (2011) applied the PIV to study the single-loop flow pattern generated by a Rushton turbine fixed close to tank bottom in a stirred tank. They found that the areas with high level of turbulent kinetic energy were affected by the movement of the trailing vortexes formed behind the impeller blades. The single-loop flow pattern was altered into the double-loop one if the impeller dimeter increased from T/3 to T/2.

Montante et al. (2008) adopted two-phase PIV technique to measure the bubble and liquid velocity profiles in a gas-liquid multiphase flow system in a stirred tank. They found that there are very small differences between the liquid and bubble mean radial velocities for all testing locations (above, near and below the impeller). Expect for the impeller discharge region, there were obvious slip velocities in the axial direction along the tank wall. They also found that presence of bubbles has little on affecting the liquid turbulent characteristics.

Ranade et al. (2001b) used PIV to study the effect of the gas flow on the trailing vortexes structure which are formed behind a Rushton turbine impeller blade. They discovered that the location of the gas cavities coincides with the location of the trailing vortexes identified in the single phase water flow. The areas of gas accumulation were found to maintain their coherent structure up around 30 degrees behind the impeller blade.

Bakker et al. (1996) used this technology to study a flow field at a vertical plane along a baffle in a stirred tank. Their study revealed the nature of the chaotic flow field in a stirred tank.

Honkanen and Saarenrinne (2002) measured a bubbly flow field using the PIV technology. The PIV measuring methods were compared. They mentioned that the PIV cameras installed with the optical filters together with the flow seeded with the fluorescent tracers can offer a good gas-liquid multiphase flow measuring results.

Among the widely used flow measurement devices, the PIV system due to its non-intrusive optical flow measurement ability and obtaining the entire plane of flow data, it is the best tool to measure the flow fields. The PIV system will be used to measure the single phase and multiphase flow fields in the stirred tanks, and adopted to validate the CFD models used in this investigation.

2.5 Conclusions

The CFD simulation methodology for single phase and multiphase flow, and flow measurement techniques were introduced in this chapter. The models and approaches used for simulation and the research gaps for this investigation have been identified.

The standard *k-ε* turbulence model is more appropriate to model the turbulent flow in the stirred tank. The RNG *k-ε* turbulence model and LES can be adopted to model the transitional flow in the stirred tank. The MRF or SM approach can be used to model the rotating impeller when the steady or transient state simulation is carried out respectively. Among the interphase forces, the drag force is the dominated force and other forces could be ignored when simulating the gas-ionic liquid multiphase flow in the stirred tanks.

The flat bottom stirred tanks are widely used in the CFD and experimental studies, whereas the dished bottom stirred tank are frequently used in industry. The flow hydrodynamics may be different when the flow is operated in a dished bottom stirred tank. The effect of bottom shape on the hydrodynamics in the stirred tank still needs investigation.

The Experiments need to be carried out to obtain the bubble size information which is an essential data used for the gas-ionic multiphase modelling. The high speed camera can be adopted to measure the bubble size in the stirred tank. The correlations between the bubble size in the ionic liquid and the stirred tank operation conditions are not published in openly literatures. These correlations will be established in this research, which provides information for estimating the bubble size in gas-ionic multiphase flow systems.

Literature review on studies of single phase and multiphase flow in the stirred tanks suggest that current investigations are normally focused on water or water-gas turbulent flow in the stirred vessels. The flow is in transitional state when the pure ionic liquid is served as the operation liquid. The single phase ionic liquid and the gas-ionic liquid multiphase flows in transitional state in the stirred tanks are still very rare in literatures.

The Particle Image Velocimetry (PIV), due to its non-intrusive and entire plane measurement abilities, is used to study the hydrodynamics in the stirred tanks. The PIV can also be served as the best tool to validate the simulation models and results in this investigation.

CHAPTER 3: SINGLE PHASE WATER FLOWS MODELLING IN THE STIRRED TANKS

3.1 Introduction

Stirred tanks are broadly used in process industry with these processes typically involving solids dissolution, fermentation, gas absorption, extraction etc. (Paul et al., 2004). The performance of a stirred tank can be optimised by adjusting of the operation parameters including reactor and impeller shapes, aspect ratio of the stirred tank, type, number, location and size of impellers and baffles (Joshi et al., 2011).

As mentioned in the literature review in chapter 2, in order to optimize the mixing performance of the stirred tanks, several investigations on stirred tanks were carried out in fully baffled flat bottom vessels in lab scale and the effect of the type of the impeller on the overall flow pattern and the distributions of the energy dissipation rate in a single phase reactors (Bakker and Van den Akker, 1994b, Ng and Yianneskis, 2000, Kumaresan and Joshi, 2006) and in multiphase reactors (Bakker and Van den Akker, 1994a, Gimbun et al., 2009) were investigated. However, in many industrial applications, especially in the processes carried out at the elevated pressurised stirred tanks, the dished bottom tanks are frequently used. Investigations carried out in such dished bottom stirred tanks are still rare (Roy et al., 2010).

The dished bottom tanks with baffles reaching to the edge of dish level are normally used in pressurised processes in industrial applications.

However the effect of length of baffles and the shape of tank bottom on the flow field were not discussed in open literatures. The effects of the bottom shape and baffles' length on the real stirred tanks' operation especially the mixing efficiency might be significant. Therefore, this chapter investigates the effects of bottom shape and baffle length on the mixing performance in stirred tanks, which is helpful to obtain further insights for the design and optimisation of stirred vessels.

Series of numerical simulations were carried out in the agitated stirred tanks which contain water as the liquid medium. The flow was operated in the fully development turbulent state. The Rushton turbine impeller was used in this investigation due to its strong ability of dispersion in the single phase and gas-liquid multiphase flows and a large number of available experimental and CFD data in literatures (Joshi et al., 2011). The stirred tanks with different bottom shape and baffles length were selected to evaluate the key parameters affecting the mixing efficiency in terms of the Power number, Flow number, trailing vortex, turbulent kinetic energy, turbulent kinetic energy dissipation rate and flow pattern.

3.2 Geometries of the Stirred Tanks and Flow Operation Conditions

3.2.1 Geometries of the Stirred Tanks

The flows in the following three types of stirred vessels were simulated namely the fully baffled flat bottom stirred tank (FB tank in Figure 3.1), the dished bottom stirred tank with baffles reaching to the dish level (DBD tank in Figure 3.2), and dished bottom stirred tank with baffles extending to the tank bottom (DBB tank in Figure 3.3). These tanks are equipped with four baffles on the tank wall, and a Rushton turbine impeller is fixed in the tank centre with ½ clearance from the tank bottom. The detailed dimensions of the three tanks used in simulation are shown from Figure 3.1 to Figure 3.3.

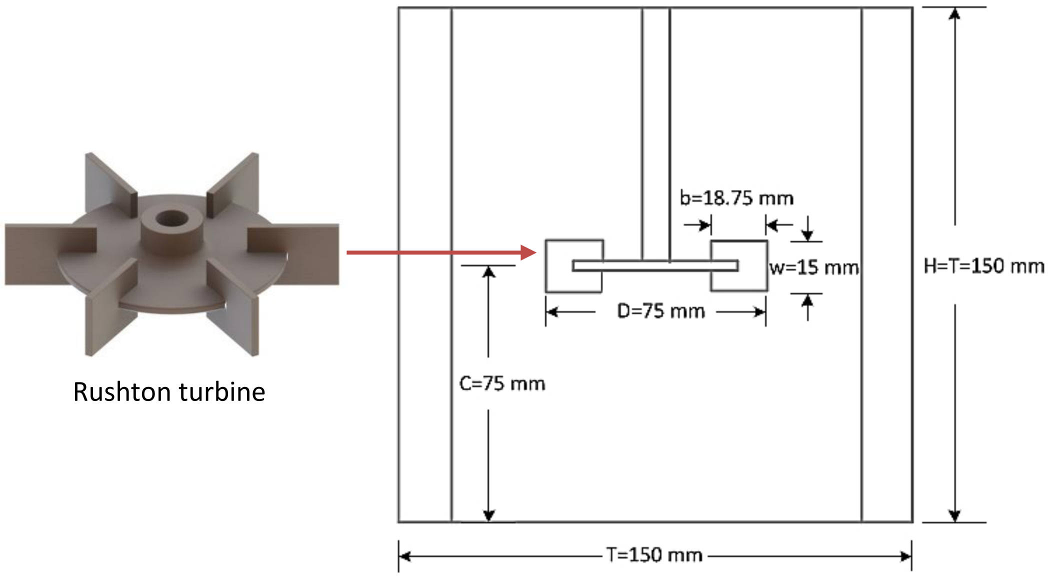

Figure 3.1 Geometry of the fully baffled Flat Bottom stirred tank (FB tank)

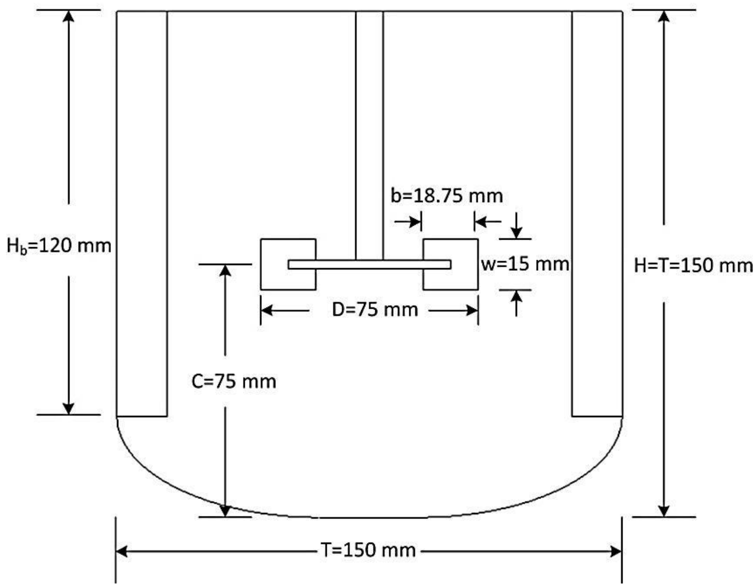

Figure 3.2 Geometry of the Dished Bottom stirred tank with baffles reaching to the Dish level (DBD tank)

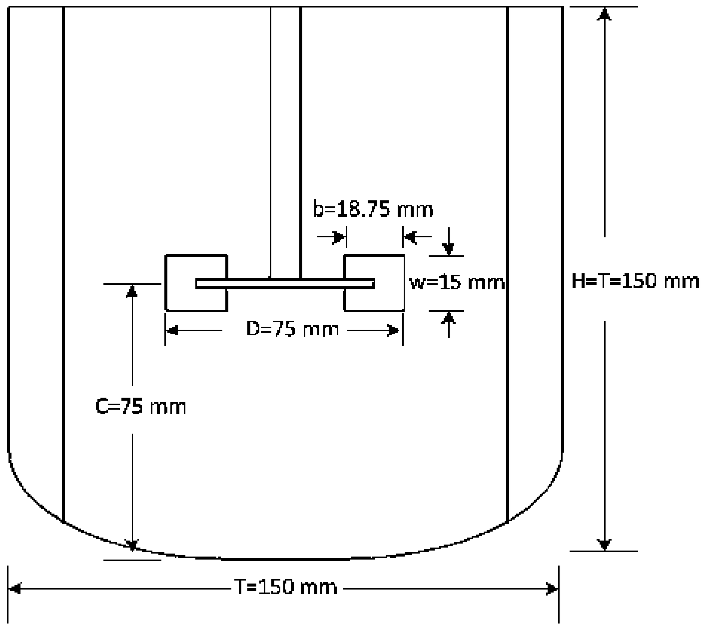

Figure 3.3 Geometry of the Dished Bottom stirred tank with baffles extending to the tank Bottom (DBB tank)

3.2.2 Flow Operation Conditions

The simulations were carried out with water as the working fluid and with an impeller speed of 150 rpm. The Reynolds number (Re) is used to define the flow regime as showing:

$$Re = \frac{\rho N D^2}{\mu} \tag{3.1}$$

where ρ is the density of the operation liquid, N is the impeller rotation speed, D is the impeller diameter and μ is the viscosity of the operation liquid.

For Reynolds numbers below 10, the flow in a stirred vessel is laminar. The fully development turbulent flow is achieved at Reynolds numbers higher than 10,000 in a stirred tank, and the flow is considered transitional with Reynolds number between 10 and 10,000 (Paul et al., 2004). According to the equation 3.1, the Reynolds number (*Re*) is about 14,000 and the fully developed turbulent states were achieved in the stirred vessels.

3.3 Numerical Modelling Methods

3.3.1 Turbulence Modelling

The ANSYS FLUENT (Version 14.5) was employed to simulate the flow in the stirred tanks by solving continuity and momentum equations for the incompressible, steady state turbulent flow. FLUENT adopts finite volume method (FVM). The used solver was velocity-pressure coupling with second-order numerical schemes for the spatial and temporal discretization.

As discussed in the chapter 2, the standard k–ε model has robust applications in modelling the turbulent flow. Therefore, it was used to close the RANS equations and simulate the turbulence in the stirred tanks. The detailed RANS equations and the standard k–ε model were introduced in the chapter 2 and they will not show here again.

3.3.2 Modelling the Rotating Impeller

The Multiple Reference Frame (MRF) method is less computationally demanding than the Sliding Mesh (SM) method whilst there is practically no significant difference in the accuracy between those methods (Luo et al., 1994a, Tabor et al., 1996). Thus, the MRF was used here to model the steady-state simulation of the flow fields in the stirred tanks. In the MRF method, the computational domain is divided into two zones: the rotational zone and the stationary zone (as indicates from Figure 3.4 to Figure 3.6). The rotational zone includes the impeller, whereas stationary zone includes the domain outside rotational zone. An interface was used to bridge the flow variables between the two zones as shown in Figure 3.4 to Figure 3.6 (purple faces that cover the rotational zone are the interface).

3.3.3 Meshing the Stirred Tanks

Before the governing equations can be numerically solved, the flow domain and the surface of all the boundaries need to be discretised into a finite number of elements known as control volumes by the regular or irregular arrangement of nodes, namely the mesh. The software, named Integrated Computer Engineering and Manufacturing Code for Computational Fluid Dynamics 14.0 (ICEM CFD 14.0), was used to mesh the geometries of the stirred tanks. The structured hexahedral mesh, which enables simple data handling to speed up the calculations, was employed (Shaw, 1992). Figure 3.4, Figure 3.5, Figure 3.6 show the meshes of the FB, DBD and DBB stirred tank respectively.

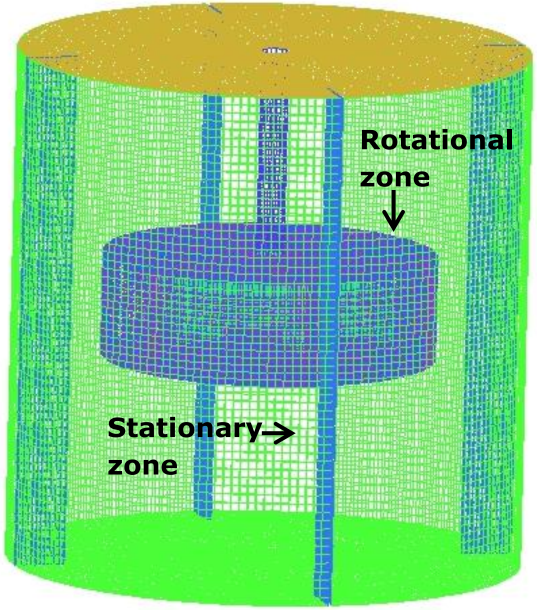

Figure 3.4 Mesh of the FB tank

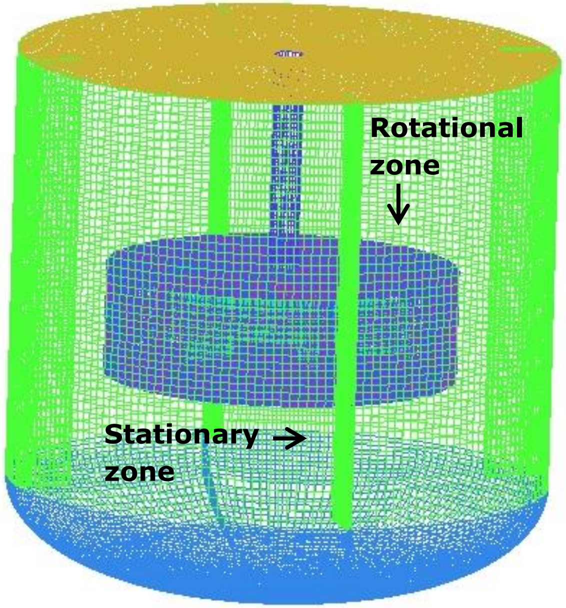

Figure 3.5 Mesh of the DBD tank

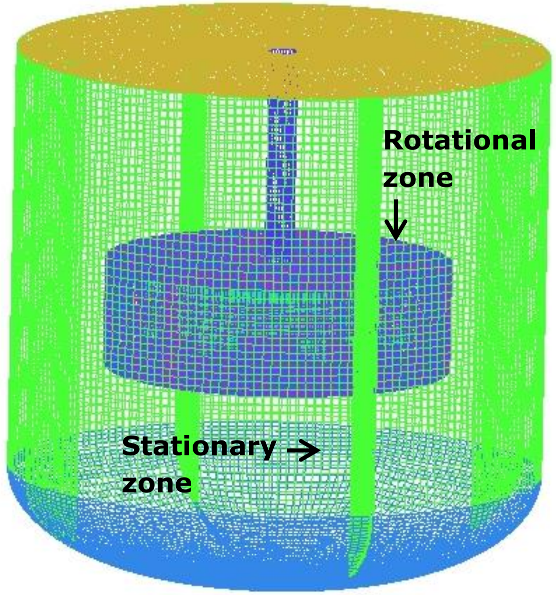

Figure 3.6 Mesh of the DBB tank

To make sure that the simulation results are not affected by the size of grid, the mesh independence test needs to be carried out. The mesh independence test is used to determine an optimum number of nodes of the computational domain, where a fairly accurate solution for the problem is found at the expense of the least computational resources (Mat and Kaplan, 2001). The coarse grids with nodes number of 440 k, 650 k and 660 k were used for the initial flow modelling in FB tank, DBD tank and DBB tank respectively. The velocity magnitudes at a horizontal plane 40 mm above the tank bottom were monitored in each simulation. The simulated velocity magnitudes did not significantly change as the grids number increased to 920 k, 860 k and 880 k for the FB tank, DBD tank and DBB tank respectively (Appendix 3.1 Mesh Independence Tests of the Grids of Stirred Tanks). And the solutions can be considered mesh independent for the three stirred tanks.

The simulated flow parameters including the Power number, Flow number, trailing vortex, turbulent kinetic energy, turbulent kinetic energy dissipation rate and flow pattern in the FB tank, DBD tank DBB tank were compared and discussed in the next section 3.4.

3.4 Effect of the Bottom Shape and Baffles' Length on the Flow Parameters

3.4.1 Power Number and Flow Number

In the stirred vessels design, the Power number (P_o) and Flow number (N_Q) are the key parameters used in describing the impeller energy consumption and impeller pumping ability of the stirred tank reactors respectively (Lane, 2006).

3.4.1.1 Power number

The Power number (P_o) is defined as following equation (Paul et al., 2004):

$$P_o = \frac{P}{\rho N^3 D^5}$$

(3.2)

where *P* is the power applied to the impeller. *N* is the impeller speed and *D* is the impeller diameter. The power conveyed to the operation liquid is the product of the impeller rotating speed and torque (Γ) :

$$P = 2\pi N\Gamma$$

(3.3)

Since the surfaces of the impeller blades have been discretised into a finite number of elements known as the control volumes, the torque can be obtained by integrating of the pressure differences between the front and back side of the nodes of the control volumes at the impeller blades:

$$\Gamma = \sum_i (\Delta p)_i A_i r_i$$

(3.4)

where the summation is over the control volumes i corresponding to each impeller blade surface. Δp is the pressure difference between the back and front side of each blade at the blade surface element (A). r is the radial distance from the impeller shaft centre to the impeller blade surface element (Zadghaffari et al., 2010).

The Power number is a measure of the power requirements in a flow field for a fixed geometry of impeller. It also gives important information regarding the energy requirement, heat and mass transfer performance and stirred tank scale-up (Markopoulos et al., 2004). A large number of numerical and experimental investigations have been carried out to study the Power number and how it is affected by the operation conditions, the geometry of stirred tank and the impeller (Zadghaffari et al., 2010, Nienow et al., 1983, Rutherford et al., 1996, Qi et al., 2010). It has been found that the value of Power number sharply decreases with the increasing Reynolds number if the flow is operated in laminar condition ($Re \leq 10$). Whereas, the P_o is almost constant when the flow is in fully developed turbulent state ($Re \geq 10{,}000$) (Paul et al., 2004).

In order to verify the simulated Power number, the Power numbers of FB tank under various operation conditions (*Re*=1, 5, 10, 50, 100, 500, 1000, 5000, 10000, 50000, 100000 respectively) were simulated and calculated based on equation 3.2 to 3.4. The simulation results were compared with the available experimental data obtained by Nienow et al. (1983) with the same Rushton turbine impeller as shown in Figure 3.7. Both the simulated and experimental results showed sharp decrease of the Power number with the increasing Reynolds number at the laminar regime ($Re \leq 10$), and the Power number is almost constant with the rising Reynolds number if the flow is in the fully developed turbulent state ($Re \geq 10{,}000$). The predicted Power number is generally in good agreement with the experimental data under all operation conditions. However, the predicted values are slightly smaller than the experimental ones. For instance, at the Reynolds number of 10,000 when the flow is fully developed turbulence state, the simulated Power number is 4.6 while the reported experimental data is 5.0.

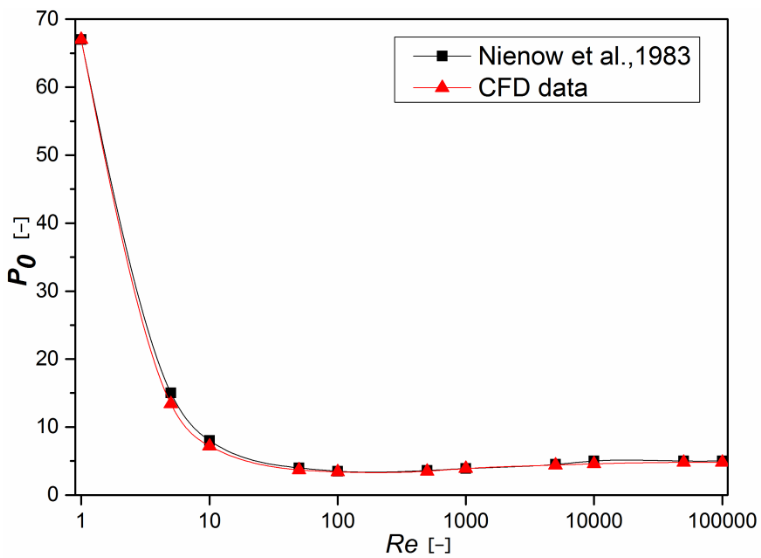

Figure 3.7 The predicted and measured Power number of FB tank

As has been shown in Figure 3.7, the predicted Power numbers are slightly smaller than the experimental ones. The discrepancy may attribute to the following reasons.

The first reason may be due to the difference in the thickness of the impeller used in the modelling and experiment. Rutherford et al. (1996) carried out experimental study to investigate the effect of the thickness of the Rushton turbine impeller blade on the Power number in the turbulent flow. They found that the Power number is dependent on the thickness of the impeller blade. The measured torque on the impeller would be decreased with the increasing blade thickness. The measured torque was found up to 33% reduction when the ratio of the blade thickness and impeller diameter was increased from 0.008 to 0.033. Similar conclusions were also obtained by Chapple et al. (2002). The impeller blade used in this investigation has a ratio of the blade thickness and the impeller diameter being 0.027, according to Chapple et al. (2002)'s study, the corresponding experimental measured Power number in the turbulent flow is about 4.9. However, it is not clear under which blade thickness Nienow et al. (1983) obtained the experimental data as this information was not included in their paper. Therefore, the potential difference in the thickness of impeller may contribute to the slight discrepancy between the experiment and simulation results.

Another reason that contributes to the discrepancy might be the grid resolution used for modelling the impeller. Lane (2006) stated that high resolution gird is needed to mesh the impeller blade for modelling. By using dense grid resolution, the actual pressure difference between the front and back side of each blade can be well predicted. Deglon and Meyer (2006) also noted that very fine grid resolution is required to predict the accurate Power number. However, much higher grid density near the impeller blade will give rise to excessive computation demand and cause converge difficulty for flow modelling. It is also not practical to use very dense grid near the impeller blade where there were software limitations on the number of nodes in the computational domain.

In order to investigate the effect of the bottom shape and baffles' length on the impeller Power number, the simulated results for Power number as a function of Reynolds number, ranging from 1 to 10,000 at different geometries of stirred tank, i.e. FB tank, DBD tank and DBB tank, are illustrated in Figure 3.8. The simulated Power number curve of the FB tank is almost consistent with the curve of DBB tank under various operation conditions. The shape of the tank bottom does not have significant effect on the Power number at current investigated conditions. Compared with the FB and DBB tank, the DBD tank has a slightly reduction of the Power number under turbulent state. For example, the simulated Power number for FB and DBB tank are 4.6 and 4.5 respectively (Re=10,000), whereas the Power number for DBD tank is 4.0.

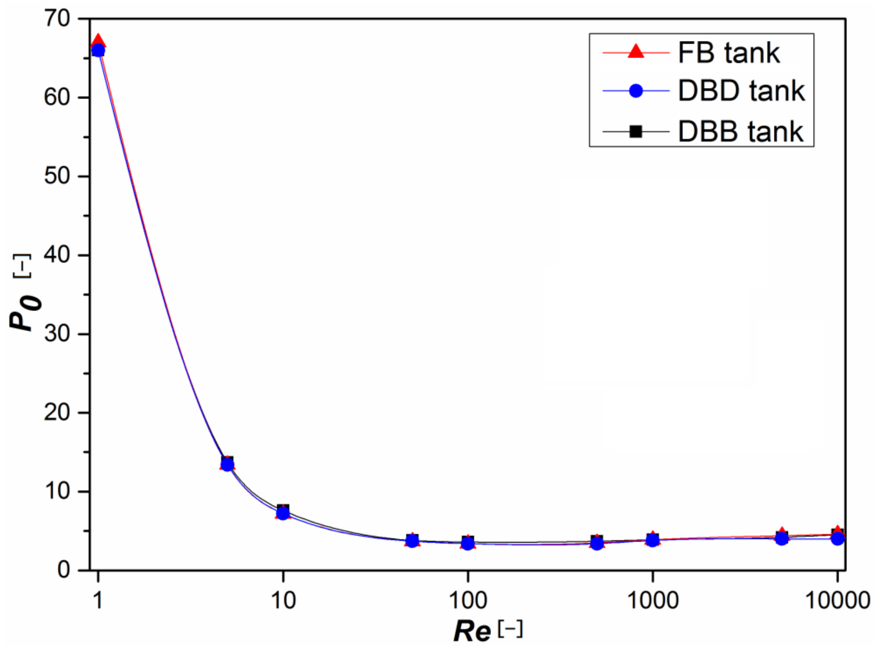

Figure 3.8 The Power number curves of three stirred tanks

The FB tank, DBD tank and DBB tank equipped with the same geometries of the impellers, and the same numbers of nodes were adopted in the impeller rotation region in the three stirred tanks. Therefore, the thickness of the impeller blades and the number of nodes near the impeller blades are not the key reasons caused the difference in the Power number prediction in the three stirred tanks. The baffles' length in the DBD tank is shorter than that in the FB tank and DBB tank. For a Rushton turbine impeller, the decreased Power number for DBD tank is mainly caused by the shorter baffles equipped in this vessel. Karcz and Major (1998) carried out investigations to study the effect of baffles' length on Power number and found that the Power number of flat bottom stirred tank fitted with Rushton turbine decreases with the decreasing length of the baffles. Similar phenomena can also been found in the study carried out by Markopoulos et al. (2004) where dual Rushton turbines were used in a flat bottom stirred tank. Therefore, under the same operation condition, slight reduction of the Power number can be identified in the DBD tank. And compared with the DBD tank, more power was required to operate the liquid in the FB and the DBB tank by means of the impeller agitation.

3.4.1.2 Flow number

The Flow number (N_Q) is a measurement of the pumping ability of an impeller in a given geometry. The Flow number offers information for impeller design for circulating the fluid in the stirred vessels (Lane, 2006). The equation used for the Flow number is defined as (Paul et al., 2004):

$$N_Q = \frac{Q_l}{ND^3}$$

(3.5)

where Q_l is the discharge flow rate produced by the impeller. The subscript (l) means that only the liquid flow rate is used in this calculation.

The discharge flow rate was calculated by creating a cylindrical surface spanning the width of the impeller blades and applying mathematical summation over this area as following:

$$Q_l = \sum_{i=1}^{n} U_{radial,i} A_i$$

(3.6)

where $U_{radial,i}$ is the radial velocity obtained by solving the governing equations and the turbulent models at the *i*th node. A_i is the area of the radial flow of the *i*th node.

The FLUENT offers a function which employs the equation 3.6 to calculate the volumetric flow rate through a given surface. The simulated Flow number (N_Q) for FB and DBB tanks were calculated to be 0.71 and 0.70 respectively. These values are very close to the reported experimental data of 0.73 when the flow is agitated by a Rushton turbine in the turbulent status in a fully baffled flat bottom stirred tank (Costes and Couderc, 1988). The Flow number for DBD tank was calculated to be 0.66 which is slight smaller than that in the FB and DBB tanks. Therefore, under the same operation condition, the impeller pumping ability was slightly reduced when liquid was operated in a tank with shorter baffles (DBD tank) hence decreasing the impeller pumping efficiency for circulating the operation liquid inside this tank.

The investigations in terms of the effects of the tank bottom shape and baffles' length on the Flow numbers are very rare in the literatures. According to equation 3.5, this reduction in the Flow number in the DBD tank is mainly caused by the decreased liquid discharge rate (Q_l). The decreased Q_l maybe casued by a large dead zone region, which will be illustrated in section 3.4.4, is identified below the impeller disk in DBD tank when water is served as the operation liquid. This dead zone starts from the tank bottom and reaches to the impeller. The liquid velocity in this dead zone is almost zero. Probably it is the existence of the large dead zone area below the impeller, which inhibits the amount of liquid flow axially back to the impeller and discharge from the blades, that causes the slight reduction in the impeller pumping ability and the Flow number in DBD tank.

3.4.2 Trailing Vortex

An important feature of the flow in the immediate vicinity of the impeller blades is the presence of trailing vortexes, which are strongly swirling structures produced on the trailing sides of impeller blades due to the flow separation (Lane, 2006). The vortexes are the primary sources of the turbulence in the stirred tanks, fully understanding the trailing vortex behaviour is vital in the improvement of the mixing efficiency of the stirred tanks (Gabriele et al., 2009, Li et al., 2011, Ranade et al., 2001a). Therefore, the information of the trailing vortexes offers knowledge for the optimization of the stirred tank design and the mixing operations in mixing industry.

The trailing vortexes were found forming behind the impeller blades when the Rushton turbine was used in a stirred tank (see Figure 3.9). These vortexes are caused by the pressure differences between the high pressure in the front and the low pressure behind each impeller blade and the radial jet flow induced by the passage of the impeller blades. A pair of trailing vortexes can be observed behind each blade disk of a Rushton turbine.

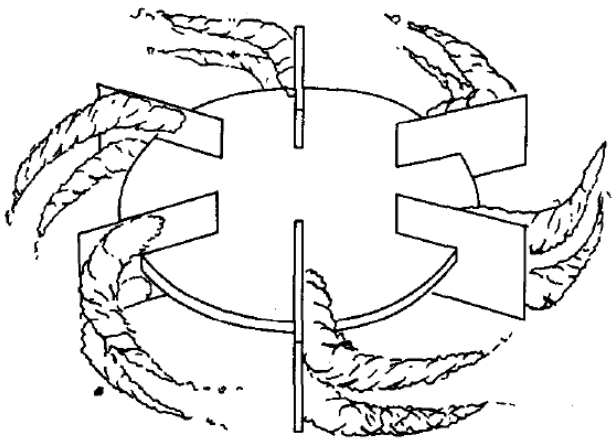

Figure 3.9 Trailing vortexes behind impeller blades (source: Nienow and Wisdom (1974))

In order to show the more detailed pressure differences near the impeller blade, the simulated pressure field at a horizontal plane passing through the impeller in the FB tank was simulated and results are showed in Figure 3.10. The impeller is rotating at the anti-clockwise direction at 150 rpm. It has been found the high pressure region (red) formed in front of each blade, and low pressure region (green) formed behind every blade where trailing vortexes exist.

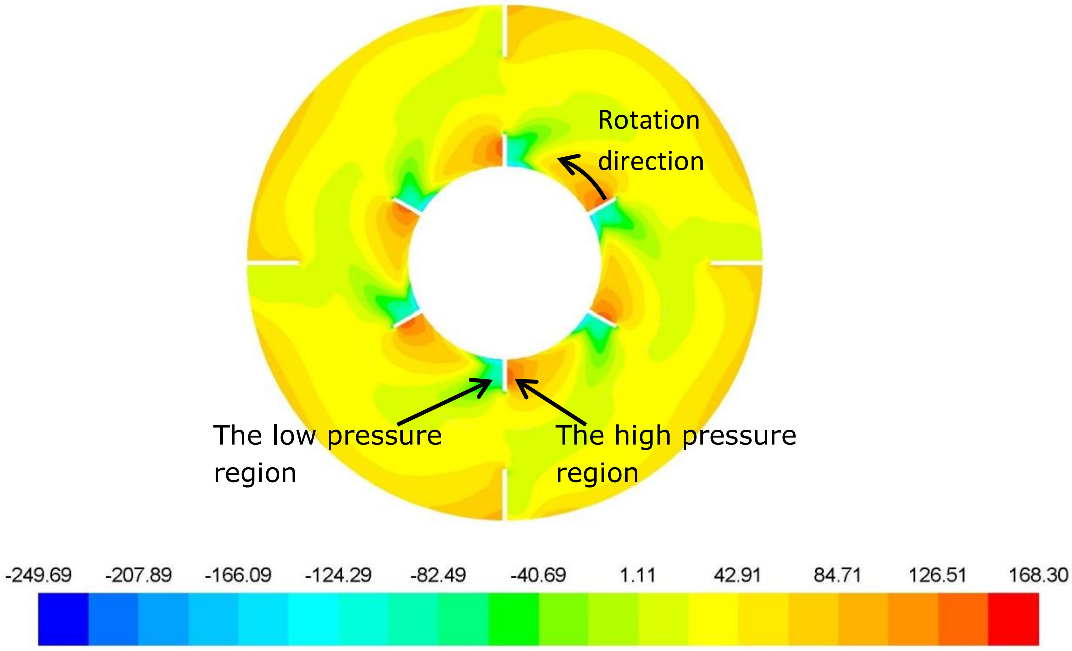

Figure 3.10 Simulated pressure distributions around impeller blades in FB tank (unit: Pa)

For each pressure contour at the rear of the impeller blades, the point furthest out from the impeller is roughly aligned with the outflow from the impeller (Lane, 2006), Figure 3.10 was used to predict the movement locus of the trailing vortexes behind the impeller blades. As has been noted that the trailing vortexes of a Rushton turbine are noticeable for angles up to about 30^{o} behind the impeller blade and beyond that range these vortexes start to dissipate and merge with the flow in the discharge region (Lane, 2006), the locus of the trailing vortex was displayed at the angles from 0^{o} to 30^{o} behind one impeller blade.

Since it has been found that the effect of the ratio of the impeller diameter to tank diameter (D/T) on the trailing vortexes is insignificant (Zhao et al., 2011). The simulated locus of the trailing vortex behind one Rushton turbine blade in the FB tank (D/T=1/2) was showed and compared with the experimental data obtained by Stoots and Calabrese (1995) where the D/T=1/3 was used in their investigation. As shown in Figure 3.11, both the simulated trailing vortexes in the FB tank and experimental measured trailing vortexes by Stoots and Calabrese (1995) are formed behind impeller blade and move radially toward the tank wall. The simulation data in the FB tank shows good agreement with the experimental results carried out by Stoots and Calabrese (1995), which indicates that the current CFD models and methods i.e. the MRF approach, turbulence model, grid resolution etc. can be used to accurately simulate the track of the trailing vortex behind the Rushton turbine blade.

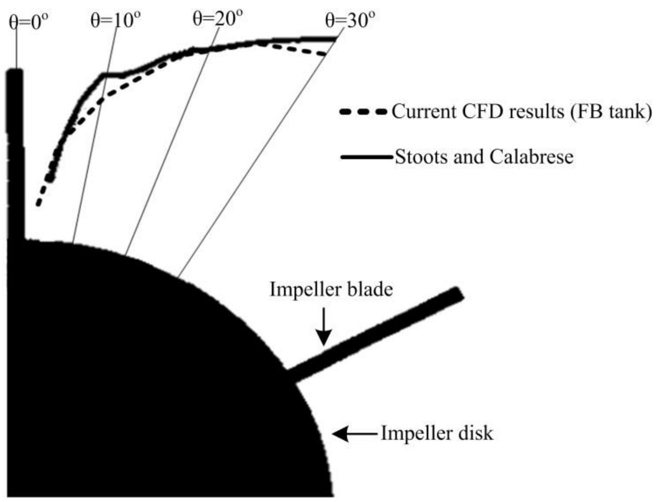

Figure 3.11 Comparison of the simulated locus of the trailing vortex with the experimental one obtained by Stoots and Calabrese (1995)

In order to investigate the effect of the baffles' length and tank bottom shape on the behaviour of the trailing vortex, the trailing vortex trajectories behind one impeller blade in the FB tank, DBD tank and DBB tank were simulated and displayed in Figure 3.12. As can be observed from Figure 3.12, the trailing vortex in all three stirred tanks have shown similar locus behind one Rushton turbine blade, which indicates that the bottom shape as well as the length of baffles do not have significant effect on the movement of the trailing vortex in these stirred vessels.

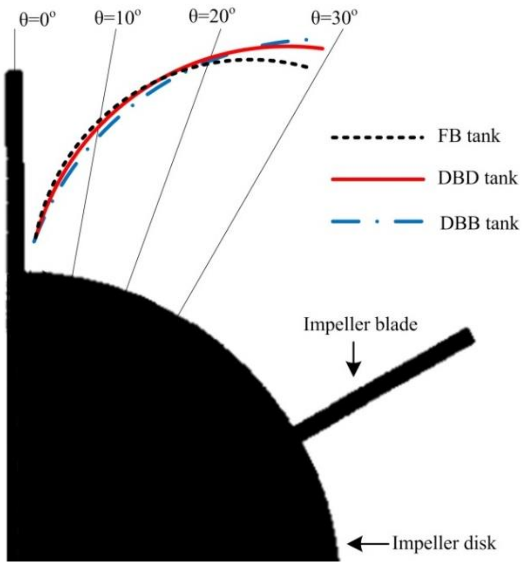

Figure 3.12 Comparisons of the trailing vortexes in the FB, DBD and DBB tank

3.4.3 Turbulent Kinetic Energy and Its Dissipation Rate

In most conditions, the liquids in the stirred tanks are normally operated in a fully developed turbulent state. An insight into the detailed time-averaged turbulent flow parameters i.e. flow pattern, flow velocity, turbulent kinetic energy and its dissipation rate in the stirred tanks are necessary for the design of the stirred vessels under required operation conditions (Lane, 2006). Besides, the turbulent kinetic energy (k) and turbulent kinetic energy dissipation rate (ε) are important turbulence parameters for CFD models, since the value of k and ε are needed to calculate the turbulent viscosity which in turn models the Reynolds stress term in the momentum equation (equation 2.7 in chapter 2) (Lane, 2006). Therefore, accurate prediction of the value of *k* and *ε* are vital for the stirred tank design and precise CFD modelling.

In order to facilitate the scale-up or scale-down of the obtained results to the real flow conditions, the flow variables are normally compared and shown in the dimensionless forms. The dimensionless flow variables often include velocity, turbulent kinetic energy and its dissipation rate. Rules like geometric similarity, same energy dissipation and equal impeller tip velocity make the dimensionless flow variables comparable between different investigations (Bashiri et al., 2014). In most literature, the stirred tanks investigated had a D/T (impeller diameter/tank diameter) ratio of 1/3. However, in this study, a tank with a D/T ratio of 1/2 is used for lab experiments and CFD simulation, this makes it difficult to compare the normalized CFD data with the experimental results from references at the normalized positions near the impeller blades. For this reason, another geometry of a flat bottom stirred tank from Lane (2006) with tank diameter T=150 mm, impeller radius R_{imp}=25 mm, and with a D/T ratio of 1/3 was created to validate the current CFD results in terms of *k* and *ε*.

Since the high level of *k* and *ε* can be found in the Rushton turbine impeller discharge region which is the area most experimental and numerical studies focused on (Delafosse et al., 2011, Zhao et al., 2011), a special attention has been paid to the simulation of these two variables in this location. The simulated turbulent kinetic energy (*k)* and its dissipation rate (*ε)* at impeller centre line from impeller blade (r/R_{imp}=1) to region close to the baffle (r/R_{imp}=2.4) were compared with the available LDV data obtained by Wu and Patterson (1989) and CFD results obtained by Lane (2006) respectively.

The impeller speed is 300 rpm which is the same speed used by Lane (2006). Water is served as the operation liquid. The comparisons in terms of *k* and *ε* are shown in Figure 3.13 and Figure 3.14 respectively, where the radial distance (*r*) was normalized by the radius of impeller R_{imp} (25 mm), the *k* was normalized by the square of impeller tip velocity (U_{tip}=0.79 m/s) and the *ε was* normalized by the average energy dissipation rate (ε_{avg}=0.073 m^2/s^3) which is obtained from below equation:

$$\varepsilon_{avg} = \frac{P}{m} = \frac{P_0 N^3 D^5}{V} \tag{3.7}$$

where $P_0 = 5.0$, *N*=5 rps, *D*=0.05 m and *V* is the volume of the operation liquid equals to 0.00265 m^3. The flow was in fully developed turbulent state with the Reynolds number of being 12500.

The comparison of the CFD and LDV results of the turbulent kinetic energy distributions at the impeller centre line are displayed in Figure 3.13. As can be seen from Figure 3.13, both the Lane (2006)'s and this work's CFD results show high level of turbulent kinetic energy close to the impeller blades ($R_{imp} \leq r \leq 1.3R_{imp}$), and the values of turbulent kinetic energy are decreasing away from the impeller blades ($r \geq 1.3R_{imp}$). Both the Lane (2006)'s and this work's CFD models show peak value of *k* at radial distance around $r=1.3R_{imp}$. And the LDV data obtained by Wu and Patterson (1989) shows the peak at the distance $r=1.4R_{imp}$. There is a large discrepancy between the experimental LDV data and the CFD results at the radial distance from $r=R_{imp}$ to $r=1.2R_{imp}$. This discrepancy is might due to the experimental error caused by Wu and Patterson (1989)'s LDV measurements. In the LDV results obtained by Hartmann et al. (2004), showed that the value of k/U_{tip}^2 at the impeller centre line near the impeller blade (r/R_{imp} =1.1) is about 0.06, however as shown in Figure 3.13, the experimental value of normalized k by Wu and Patterson is around 0.04 at corresponding positon which is lower than the one measured by Hartmann et al. (2004). Nevertheless, the CFD results in this study showed good agreement with the CFD results by Wu and Patterson (1989) in the position away from the impeller tips. And the CFD models used in this investigation provide better results than the CFD models used by Lane (2006) as they are more close to the LDV results.

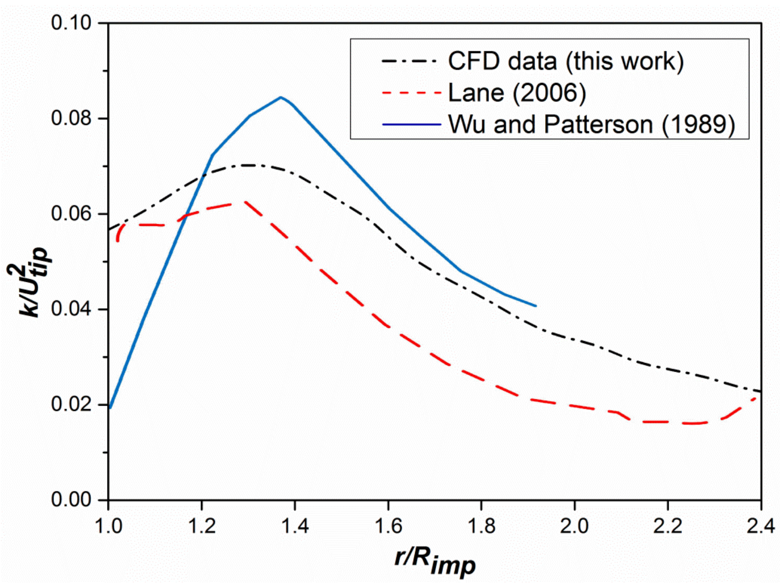

Figure 3.13 Comparison of the CFD and LDV results of the turbulent kinetic energy distributions at the impeller centre line

Figure 3.14 illustrates the distributions of the turbulent kinetic energy dissipation rate at the impeller centre line obtained by Lane (2006)'s CFD simulation, this work's CFD prediction and the LDV results from Wu and Patterson (1989). As can be observed from Figure 3.14, high level of turbulent kinetic energy dissipation rates can be found in regions close to the impeller blades ($r=R_{imp}$), and the values of the turbulent kinetic energy dissipation rates are decreasing away from the impeller blades ($r\geqslant R_{imp}$). Again, the current CFD models provide better simulation results than the models used by Lane (2006). Large differences can also be found between the LDV and the CFD data in the regions from $r=R_{imp}$ to $r=1.2R_{imp}$. This low level of energy dissipation rate in the LDV experiment may be also caused by the measuring error using LDV, since it was indicated by Wu and Patterson (1989) that there were obvious difference among literatures in measuring the values of ε in the region close to the impeller blade. And Hartmann et al. (2004) mentioned that due to the high shear of the impeller blade, high level of ε are always found around the impeller blades which decay to lower value toward the bulk region. This trend shown in Figure 3.14 is in good consistency as suggested by Hartmann et al. (2004).

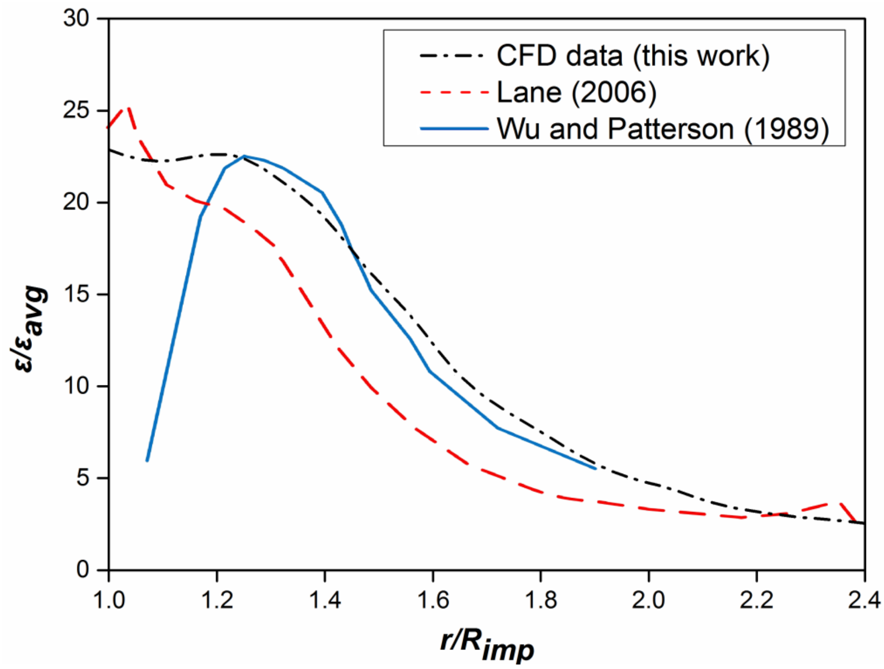

Figure 3.14 Comparison of CFD and LDV results of turbulent kinetic energy dissipation rate distributions at impeller centre line

Generally, the CFD models used in this study underestimated or overestimated the values of the *k* and *ε* in the impeller discharge region, which may attribute to the below two reasons.

- Numerical errors due to the spatial discretisation

The accuracy of the CFD model is affected by the number of nodes. Deglon and Meyer (2006) investigated series of models with various grid resolutions to study the effect of grid number on prediction of *k*. It was found that the accuracy of simulation of *k* can be improved when the very fine grid was used, since if the flow is in turbulent condition, the trailing vortexes around the impeller blades cause large velocity gradients near the impeller blades. A very find grid is required to resolve the gradients in this area. As it has been discussed previously that very fine mesh would greatly increase the calculation time and may lead to divergence of the simulation, therefore, very fine grid was not attempted in this study.

- Errors due to the isotropic assumption used in the standard k-ε model

Due to the high shear and swirl caused by the impeller, the flow especially in the impeller discharge region is anisotropic turbulence, which contradicts the isotropic assumption of the standard k-ε model that the turbulent stresses are proportional to the mean rate of strain. Anisotropic turbulence model such as the Reynolds stress model and LES would give more accurate predictions of the turbulence parameters such as the turbulent kinetic energy and turbulent kinetic energy dissipation rate (Hartmann et al., 2004). However, the problem of underestimating or overestimating the turbulent kinetic energy and its dissipation rate is still unavoidable so far (Lane, 2006).

- Errors due to the experimental rig

The geometry of the stirred tank, impeller and baffles used in the lab are normally made by hand, therefore these components are not exactly the same as that made by the software. And it has been noted that the geometry of the stirred tank, impeller and baffles have significant effect on the flows inside the stirred vessels (Kumaresan and Joshi, 2006) hence causing the difference between the CFD and experimental results.

The LDV and PIV, which laser is served as the light source to illuminate the flow domain, are broadly used to measure the flow parameters inside the stirred tank. In this investigation, it has been found that there were very strong reflective laser lights at the surfaces of the impeller blades when the laser beam reached to the impeller blades. The very strong reflective laser light will disturb the scattered laser light from the particle tracers and form glare near the impeller tips hence affecting the accuracy of the LDV or PIV measurement (Petrosky et al., 2015).

Despite the slight underestimation or overestimation of the k and ε, the CFD models used in this study showed good agreement with available numerical and experimental results from the literatures. These validated CFD models will therefore be used to investigate the effect of bottom shape and baffles' length on the turbulent kinetic energy and its dissipation rate in the stirred tanks. The numerical simulations were carried out in the FB tank, DBD tank and DBB tank with tank diameter T=150 mm and D/T=1/2. The impeller speed is 150 rpm for all stirred tanks, corresponding to Reynolds number equals 14,000. The impeller was fixed at the height 0.45≤z/H≤0.55. The data were sampled close to the impeller blade (at r=0.26T). The turbulent kinetic energy was normalized by the U_{tip}^2 (U_{tip}=0.59 m/s). The axial distance (z) was normalized by the tank height (H).

Figure 3.15 illustrates the averaged turbulent kinetic energy distributions at the axial distance from 0.42T to 0.58T for the three tanks. As can be seen from this figure, the distribution of k showed similar trend for the FB, DBD and DBB stirred tanks where the turbulent kinetic energy shows peak value around the impeller blade centre line area (z/H=0.5) and relative small values away from this region. The FB and DBB tank show similar peak values in region 0.45≤z/H≤0.55. However a slight reduction of k can be found in this region when water is agitated in the DBD tank. This implies that the shape and length of baffles slightly affect the value of k at this area.

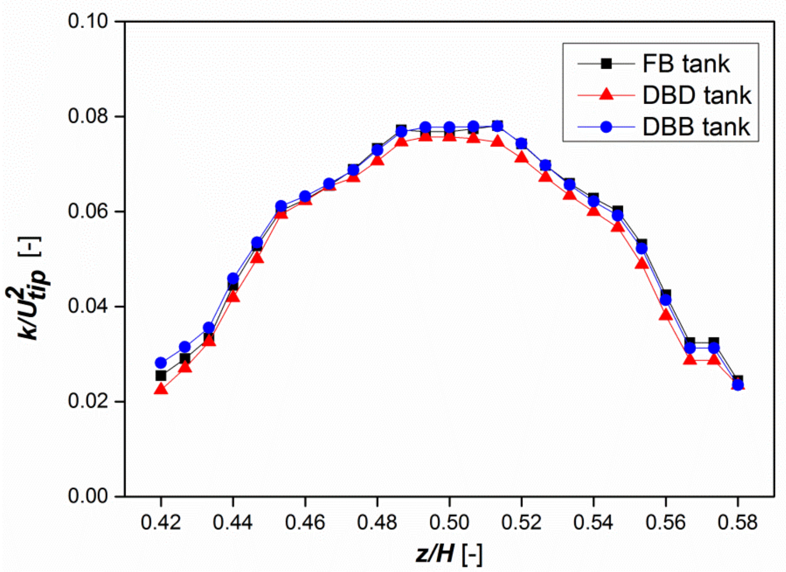

Figure 3.15 Turbulent kinetic energy distributions near the impeller blade in FB, DBD and DBB tank

Figure 3.16 illustrates the distributions of the turbulent kinetic energy dissipation rates at the axial distance from 0.42T to 0.58T for the three tanks. The turbulent kinetic energy dissipation rate ε is normalized by the average energy input per unit volume (ε_{avg}=0.066 m^2/s^3). As can be found from Figure 3.16, there is no significant difference in ε value when water was agitated in the FB and DBB stirred tanks, except slight decrease of ε in $0.45 \leq z/H \leq 0.50$ in the DBD tank. Figure 3.16 implies that the short length of baffles slightly weakens the turbulent kinetic energy dissipation rate in the flow close to the impeller blade.

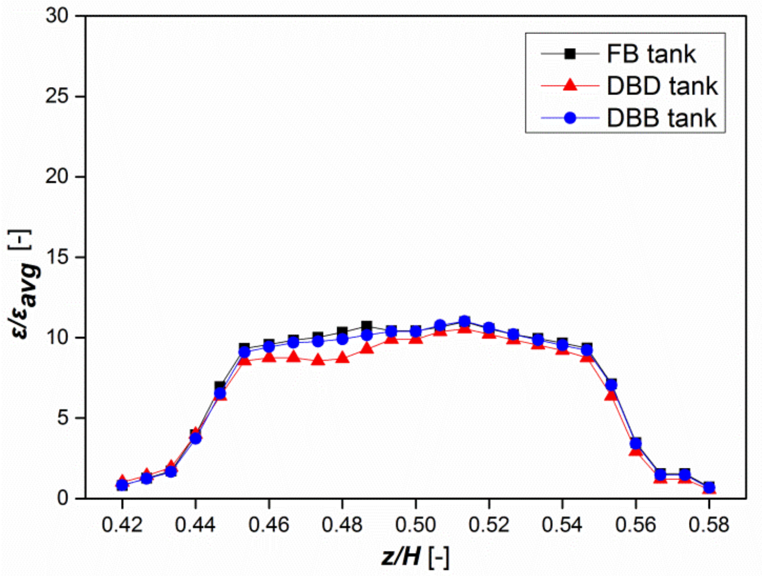

Figure 3.16 Turbulent kinetic energy dissipation rates near the impeller blade in the FB, DBD and DBB tank

According to Figure 3.15 and Figure 3.16, the distributions of k and ε in the FB tank and DBB tank showed similar values, however slight reductions in k and ε can be observed in the impeller blade sweeping area ($0.45 \leq z/H \leq 0.55$) when water was agitated in DBD tank. Since the length of the baffles is the main geometry difference between the DBD tank and the DBB tank, the baffle length slightly affects the turbulent kinetic energy and its dissipation rate in the region close to the impeller blade. Though the overall trend is same, the full baffle length stirred tank give higher $\varepsilon/\varepsilon_{avg}$ hence giving better mixing performance (Zhao et al., 2011, Kumaresan and Joshi, 2006). To sum up, the CFD modelling suggests that the FB and DBB tank have better mixing performance than the DBD tank in agitating water in fully developed turbulent state.

3.4.4 Flow Pattern and Flow Velocity

It has been mentioned in section 3.4.3 that except for the turbulent kinetic energy and its dissipation rate, the flow pattern and the flow velocity also provide the information for the stirred tank design and process optimization. For example, it has been found that the additional circulation zones and dead zone in the flow filed of stirred tank will impede the mixing efficiency in the stirred vessels hence reducing the quality of the final products and cause the waste of energy (Murthy Shekhar and Jayanti, 2002). Therefore, this section explores the effect of the tank bottom shape and baffle length on the flow pattern and the flow velocity in the stirred tanks, which provide the information for the stirred tank design and process optimization.

The flow pattern in a flat bottom, fully baffled stirred tank fitted with a Rushton turbine impeller has been extensively studied and it has well understood. As shown in Figure 3.17 to Figure 3.19, the flow patterns in the stirred tanks are characterised by the axial symmetry and the presence of the symmetrical circulation loops with the similar intensity below and above the impeller. It has been found that the shape of the bottom and the extension of baffles have a strong effect on the flow field below the impeller, but they have very little effect on the flow field in the top part (above the impeller) of the vessel. The most striking difference among the three geometries is the very large volume of nearly stagnant liquid (dead zone) just between the impeller disk and vessel bottom in the DBD tank as shown in Figure 3.18.

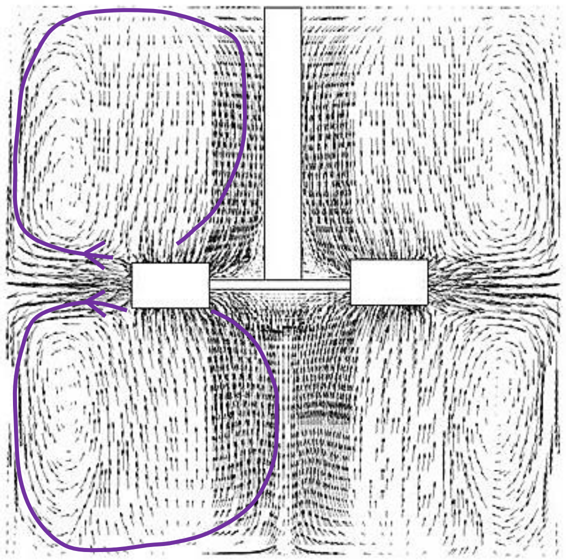

Figure 3.17 Velocity vectors in the FB tank

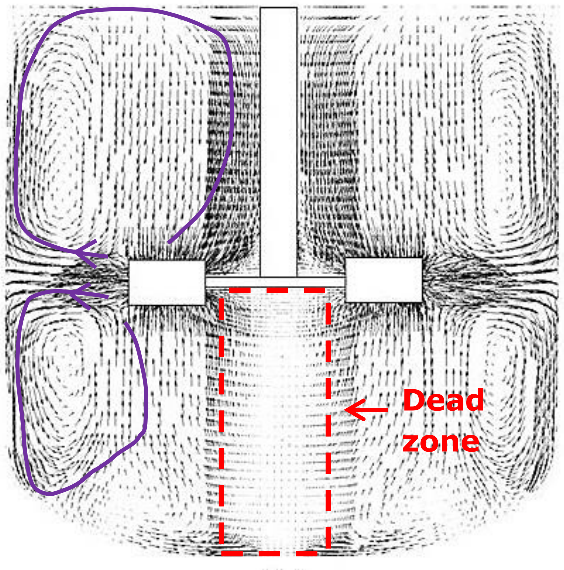

Figure 3.18 Velocity vectors in the DBD tank

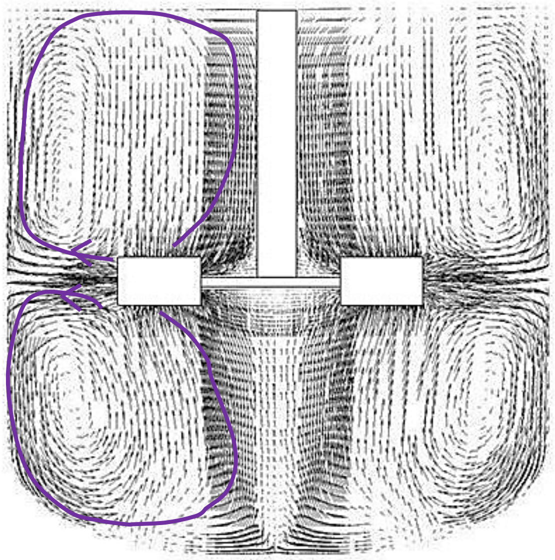

Figure 3.19 Velocity vectors in the DBB tank

Figure 3.18 depicts the vectors plot of the flow field in the DBD tank in a vertical plane between two adjacent baffles which clearly show that the intensity of the axial flow is reduced in a dish bottom vessel with baffles reaching to the edge of the dish. This leads to the reduction of the downward circulation loop which becomes much smaller than the upward circulation loop and forms a large dead zone. Such large dead zone was not observed in a flat bottom fully baffled (FB) stirred tank. In the DBB tank, the size of the dead zone was reduced by the longer baffles that reach to the very bottom of the vessel as shown in Figure 3.19. With the help of these longer baffles, the downward axial flow moves along the dished wall, and then flows towards the impeller when it reaches the stagnation point close the tank bottom. This results in larger circulation loop and the increase of velocity magnitude below the impeller leading to improvement of mixing efficiency.

Figure 3.17 to Figure 3.19 show that the velocity profiles in and above the impeller discharge region are nearly the same in all three geometries. However, there are pronounced differences in the velocity distributions below the impeller indicating a very strong effect of the dish shape and length of the baffles on the flow below the impeller and close to the bottom. The details of the flow vectors and contours below the impeller enabling better comparison of the effect of dish shape and baffles' length on the flow field are shown from Figure 3.20 to Figure 3.22.

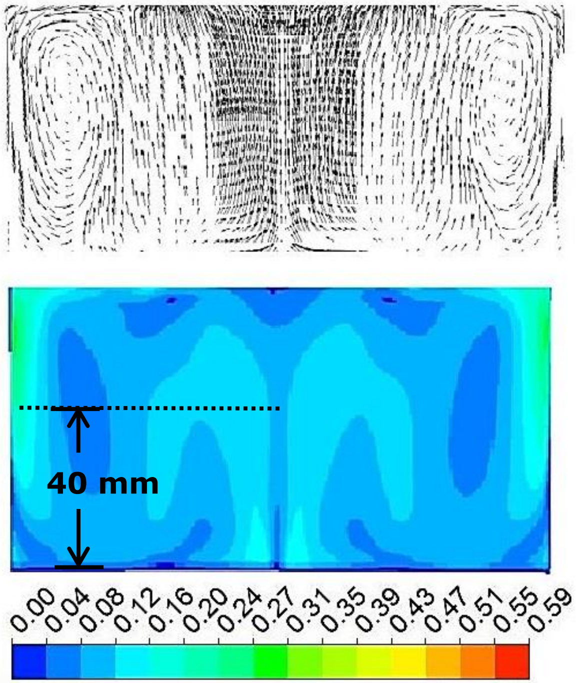

Figure 3.20 Flow velocity contours of the FB tank (unit: m/s)

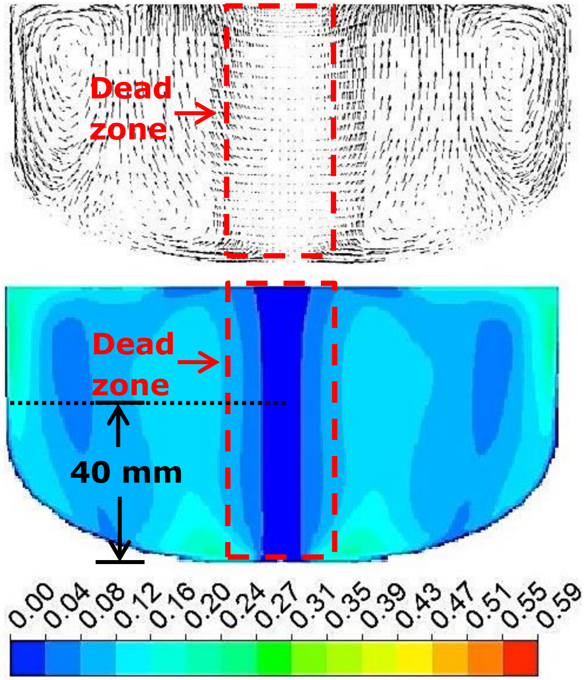

Figure 3.21 Flow velocity contours of the DBD tank (unit: m/s)

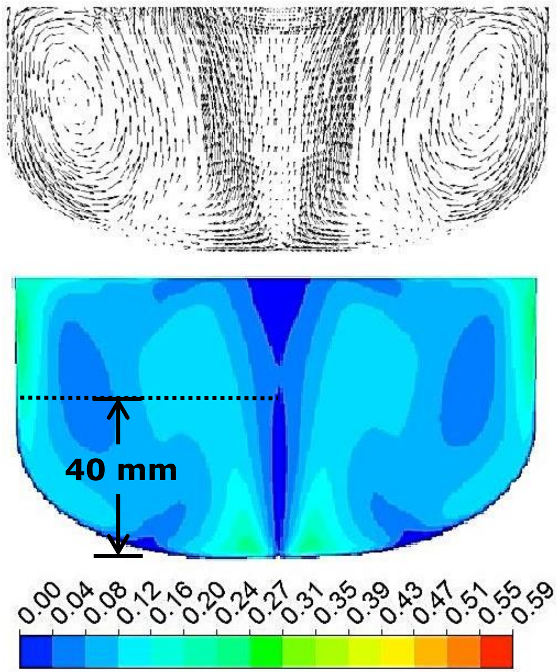

Figure 3.22 Flow velocity contours of the DBB tank (unit: m/s)

In a fully baffled flat bottom vessel (FB tank as shown in Figure 3.20), the stagnation zones exist at the bottom and near the corners between the bottom plane and the cylindrical walls whilst there is a very intensive axial flow directly below the impeller. In the dished bottom vessel with baffles reaching the edge of the dish (the DBD tank as shown in Figure 3.21) the stagnation zones at the bottom have disappeared. However, a very large, cylindrical dead zone separating the circulations loops is formed directly below the impeller. The diameter of this dead zone is almost one fifth of impeller diameter and it extends from the impeller to the bottom of the vessel. Such a large dead zone in the dished bottom vessels has not been reported in the numerical and experimental studies on flow hydrodynamics in the stirred tanks.

The presence of such a large dead zone does not only has a negative effect on mixing in single phase systems, but also causes problems of suspending solid particles in the liquid in the multiphase flow systems. The minimum impeller speed N_{JS} (Paul et al., 2004) which is necessary to suspend the particles is calculated from the empirical correlations based on the experimental data obtained in a fully baffled flat bottom tanks. The above simulation results with the DBD tank may rise up a question on the applicability of such correlations to the dish bottom tanks where a dead zone region exists below the impeller.

The size of the dead zone can be reduced by extending the baffles to the very bottom of the vessel as shown in Figure 3.22, which results in higher intensity of the downward flow circulations and the increase of flow velocity magnitude between the impeller and the tank bottom (compare with Figure 3.21 and Figure 3.22). The increased intensity of the downward flow circulations and the decreased dead zone region below the impeller can reduce the mixing time in the single phase systems (Murthy Shekhar and Jayanti, 2002), and might also lead to the decrease of the minimum velocity of the particles suspension in the solid/ liquid systems in the stirred tanks.

In order to show more detailed information of the dead zone below the impeller disk and which velocity components lead to the formation of the dead zone region, the velocity components were sampled at a horizontal plane 40 mm above the tank bottom passing through the dead zone (as indicates in Figure 3.20 to Figure 3.22). The radial distributions of all velocity components at this plane are normalized by the impeller tip velocity (U_{tip}=0.59 m/s). The results obtained from different shape of stirred tanks and length of baffles are shown in Figure 3.23 to Figure 3.25 respectively. As can be observed from Figure 3.23, the normalized radial velocities show little change along the *r/R* ranging from 0 to 1.0. And the radial velocities are almost zero at this cross section, due to the flows in this region (between impeller and the bottom) is mainly axial/ tangential.

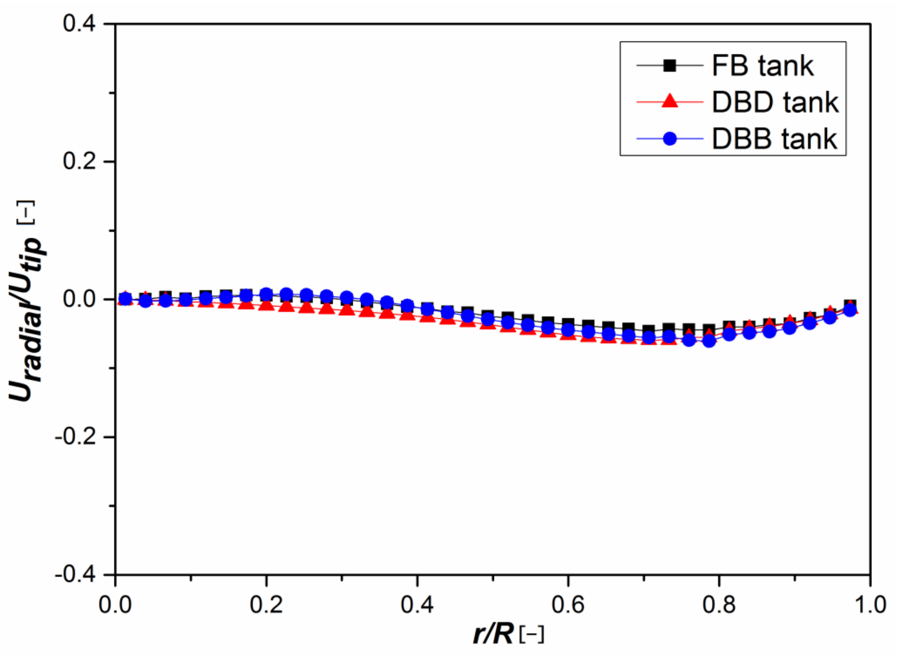

Figure 3.23 Radial velocities at a horizontal plane 40 mm above the tank bottom

There is however a strong effect of the shape of the tank bottom and length of baffles on both tangential and axial velocities in the region below the impeller (in Figure 3.24 and Figure 3.25). As can be observed in Figure 3.24, there is a significant reduction of axial velocities in the axis of the vessel from $0.2U_{tip}$ in the FB tank to $0.06U_{tip}$ in the DBB tank and to almost 0 in the DBD tank, and they followed by a gradual increase to the positive maximum at r=0.19R in the FB tank, r=0.41R in the DBD tank and to r=0.28R in the DBB tank. From the range r=0.6R to r=R, the axially velocity gradually increases to its negative maximum as it approaches the wall of the tank with the difference between the three tanks are very small. Since the mixing efficiency of the stirred tank equipped with the Rushton turbine can be significantly improved by increasing the axial flow rate (Lamarque et al., 2010), the FB tank provides better mixing performance than the DBD and DBB tank especially in the region below the impeller. The majority volume of liquid below the impeller in the DBD tank is poorly mixed in the axial direction.

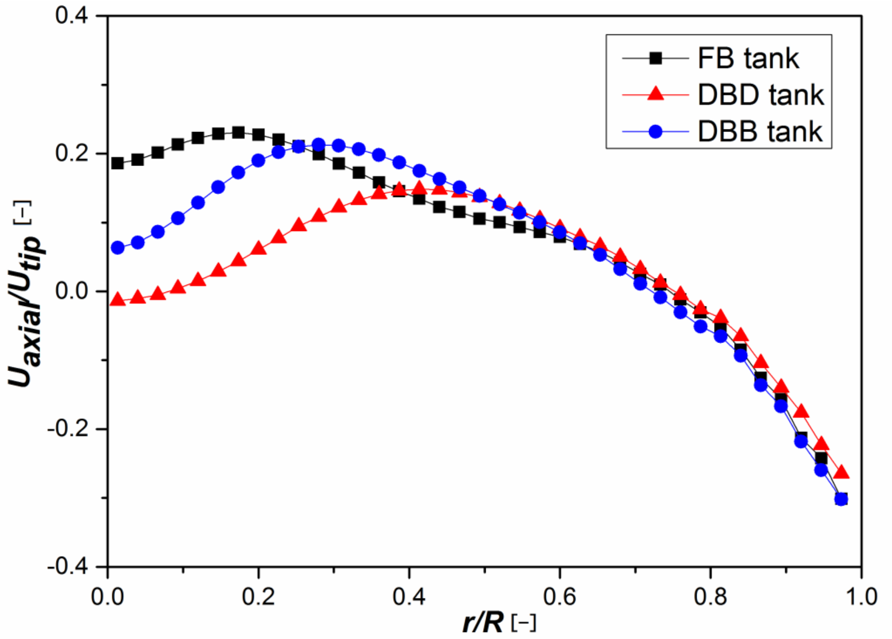

Figure 3.24 Axial velocities at horizontal plane 40 mm above the tank bottom

Compared with the radial velocity distributions, the tangential velocities shown in Figure 3.25 are also sensitive to the bottom shape and baffle length. In the DBD tank, it can be noticed that almost zero tangential velocity in the dead zone centre (r/R=0) and a peak value of the tangential velocity at the edge of the dead zone (r/R=0.3). This distribution of tangential velocities indicates a forced vortex is formed here. Due to the short baffles in DBD tank, high level of tangential velocities can be observed at this data sampling plane. Majority volume of the liquid in the vortex region is rotating in the tangential direction without efficient mixing in the axial direction. Figure 3.23 to Figure 3.25 clearly indicate that reduction of the axial velocity below the impeller

($0 \leq r/R \leq 0.25$) causes the reduction of the magnitude of the resultant velocities in this region.

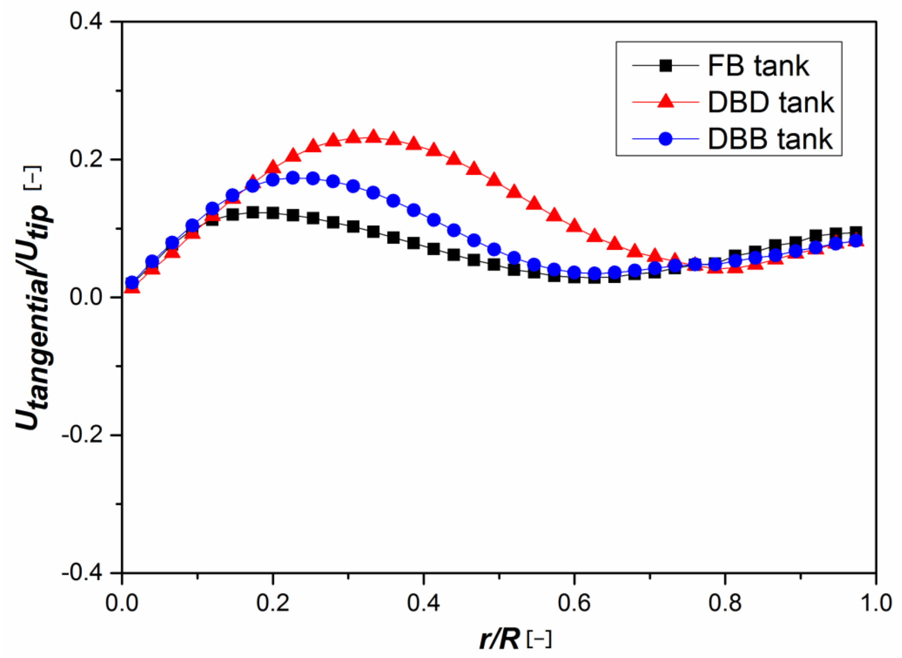

Figure 3.25 Tangential velocities at a horizontal plane 40 mm above the tank bottom

It is well known that the presence of baffles prevents swirling and vortexing (Lu et al., 1997, Haque et al., 2011). The relative tangential velocities between the impeller and liquid were small without baffles, which results in the reduction of the downwards pumping and poor mixing (Busciglio et al., 2013). In the DBD tank, a forced vortex is formed below the impeller with low tangential velocity at the vortex centre and high tangential velocity at the vortex edge. Since the mixing could be drastically improved when the baffles reach to the tank bottom, which breaks the tangential rotation of the liquid and increases the axial flow rate (Lamarque et al., 2010), the extending baffles to the tank bottom (the DBB and FB tank) can reduce the magnitude of the forced vortex and decrease the intensity of rotation liquid below the impeller. As a result, the mixing efficiency in the region below the impeller in the dished bottom stirred tanks can be greatly improved.

3.5 Conclusions

The effects of the stirred tank bottom shape and baffles' length on the single phase water turbulent flow in the stirred tanks were studied. The most concerned flow parameters such as the Power number, Flow number, trailing vortex, turbulent kinetic energy, energy dissipation rate and flow pattern in the stirred vessels were simulated and compared with available data in open literatures.

The simulated Power number of the Rushton turbine impeller in the FB tank showed good agreement with the reference data. At the same operation condition, due to the short baffles, slight reduction of the Power number can be found when water was operated in the DBD tank in the fully developed turbulent state (Re>10,000). The impeller Flow number was slightly affected by the baffles' length. The Flow number was very similar in the FB tank and the DBB tank with being 0.71 and 0.70 respectively. When flow is operated in the DBD tank, the Flow number was reduced to 0.66. The slight reduction of the Flow number might be attributed to the dead zone area formed below the impeller, which reduces the amount of liquid flow back to the impeller and discharge from the impeller blades.

The simulated trailing vortexes trajectory behind one Rushton turbine impeller blade was compared with the reference data. The simulation results in the FB tank showed good agreement with the data from the reference. According to the simulation, the trailing vortexes trajectory behind impeller blade showed similar trend in the FB, DBD and DBB tank. The bottom shape and baffles' length have little effect on trailing vortex behaviour behind the impeller blade.

Simulations of the turbulent kinetic energy (k) and energy dissipation rate (ε) were carried out in a flat bottom stirred tank with a same geometry from reference. Due to the grid resolution, the drawback of the standard k–ε model and experimental errors, under or over estimation of these two parameters were identified. Generally, the simulated k and ε were closer to the experimentally obtained LDV data than the CFD results gained from other researchers. The same CFD models and approaches were used to model the k and ε values in the FB tank, DBD tank and DBB tank though out this study. The CFD results indicated that the distributions of k and ε were very similar near impeller tips in the FB and DBB tank. At the same operation conditions, compared with the FB and DBB tank, slight reduction of k and ε can be found in the regions close to the impeller blade in the DBD tank. This finding suggests that the FB and DBB tank provide better mixing performance than the DBD tank in mixing the flow in turbulent state at the same condition compared with the DBD tank.

Finally, the flow patterns and the flow velocities in the FB, DBD and DBB stirred tanks were numerically investigated. The simulation results showed that both the bottom shape and baffles' length has significant effect on the flow field in the stirred tanks especially in the region below the impeller. The flat bottom stirred tank, due to its minimum magnitude of the dead zone region below the impeller when the liquid was operated in the fully developed turbulent flow, has better mixing performance than the DBD and DBB tank at the same operation condition. A large dead zone area was formed below the impeller in the DBD tank, which makes it inefficient to mix the liquid below the impeller in the turbulent flow. The DBB tank could greatly reduce the magnitude of this dead zone, which improves the mixing efficiency in the dished bottom stirred tanks. Since dished bottom tanks are more widely used in mixing industry, similar stirred tank geometries like the DBB tank will provide better mixing for the industries.

CHAPTER 4: LARGE EDDY SIMULATION OF SINGLE PHASE WATER AND IONIC LIQUID FLOWS IN STIRRED TANKS

4.1 Introduction

Fundamental information of the flow fields in stirred vessels in terms of flow pattern, velocity profiles etc. are essential for optimizing engineering design and assessing practical performance of stirred tanks (Li et al., 2011). The flow pattern and velocity profiles in the stirred tank have significant impact on the processes carried out in these vessels. Especially for the flow pattern and axial velocity profiles below the impeller which has substantial effect on solids suspension behaviour (Montante et al., 2001a, Armenante et al., 1998). Besides, the mean velocities as well as flow pattern are important parameters since they are significant in preventing the dead zone formation and ensuring homogeneity in stirred tanks (Xuereb and Bertrand, 1996).

It has been discussed in chapter 3 that one of the major differences among the three investigated tank geometries is the magnitude of the forced vortexes formed below the impeller. Since the Large Eddy Simulation (LES) is better suited for simulating large dynamic structures, it was employed here to predict the magnitude of this forced vortex in this chapter. Since the detailed information of the LES and the justifications of the model parameters have been discussed in section 2.2.2 and 2.3.4 in chapter 2, the LES models will not show here.

The LES results of water turbulent flow in stirred tanks are compared with the velocity profiles obtained from RANS modelling in chapter 3. The main focus is on the dead zone regions below the impeller disk. The LES is then applied to simulate the ionic liquid transitional flow in flat and dished bottom stirred tanks. The main attention is paid to the areas below the impeller. Comparisons are made between water turbulent flow and ionic liquid transitional flow in stirred vessels to show the effect of the flow regime on the dead zone area below the impeller.

4.2 LES of Single Phase Water Flow

4.2.1 Numerical Modelling Methods

The detailed geometries of the stirred tanks used in this investigation are the same as these introduced in the chapter 3. The operation liquid is water and impeller speed is 150 rpm. As it was showed in chapter 3, the flow in the stirred tanks was in the fully developed turbulent state (Re=14,000) under current impeller agitation speed. The meshes of the stirred tanks were refined and the nodes number of 1.62 million, 1.60 million and 1.65 million were used for DBD tank, DBB tank and FB tank respectively. The value of Y plus near the tank wall and impeller surface is less than 5 when the maximum grid size of 2 mm used in the LES, which means that this size of grid is fine enough to solve the flow in the near-wall region and in the flow domain in the LES.

FLUENT (Version 14.5) was used to solve the spatial filtered continuity and momentum governing equations in the finite volumes. The Smagorinsky-Lilly subgrid-scale model was used to close the space-filtered governing equations and to simulate the effect of the small scale eddies on the large scale eddies.

Since the LES is required to carry out on a basis of a preliminary steady state flows, the standard *k–ε* model and MRF approach were used to get a converged steady state flows as the initial condition for LES. And then, the LES and the sliding mesh (SM) approach were adopted to carry out the transient simulation in the stirred tanks.

4.2.2 Judging Convergence

For a transient simulation, the choice of the time step is critical. For a rotary mechanical device consists of a rotor (the rotating part) and a stator (the stationary part), around 20 time steps between each blade passing is recommended (ANSYS, 2011b). For the impeller agitation speed at 150 rpm, a time step of 0.003 s was sufficient enough for this transient simulation. 20 iterations were performed at each time step.

As it was suggested by ANSYS (2011b) and Hartmann et al. (2004), a good level of convergence can be achieved at each time step if the residual values of the velocity components and continuity at the end of each time step showed three orders of magnitude smaller than that at the beginning of the time step. The residual values of velocity components and continuity were monitored during the simulation. These data were found dropped within three orders of magnitude at the end of each time step, which implies good convergence of simulations.

Since the torque and velocities are normally served as the indications to show whether the steady state flows are achieved in the stirred tanks, their values were monitored in each simulation (Gimbun et al., 2012, Li et al., 2011, Li et al., 2013). As the simulation continued, after 12 seconds of impeller rotation time, the torque and velocities were more stable and periodic which indicates the steady state flows were achieved in the stirred tanks. The simulation data was then sampled when the flows were in the steady state. The simulation data over 30 seconds of the stirred tank running time corresponding to 75 rounds of impeller rotation was collected and this amount of gathered information was believed to be able to get reasonable mean velocity profiles.

4.2.3 Comparisons of Flow Fields Predicted by RANS and LES

In order to compare the flow velocities obtained by RANS and LES, the times-averaged velocity profiles were obtained at a plane 40 mm above the bottom of the stirred tanks (the plane was indicated in section 3.4.4 in chapter 3) for both RANS and LES. The axial velocity (U_{axial}), radial velocity (U_{radial}), and tangential velocity ($U_{tangential}$) were normalized by the impeller tip velocity (U_{tip}=0.589 m/s). The radial distance (r) was normalized by the tank radius (R=75 mm). The detailed velocity components distributions in DBD, DBB and FB tank obtained by the standard k–ε model and LES were compared at this area and showed in this section.

Figure 4.1 to Figure 4.3 display the axial, radial and tangential velocity profiles at the data sampling plane for RANS and LES in DBD tank. Very low velocities were found near the centre of this plane (r/R=0) in each figure indicating that a dead zone is formed in this region. The axial velocity is almost zero at the centre of this plane which means poor mixing in axial direction in this area (in Figure 4.1). As shown in Figure 4.3, the trend of the tangential velocity distributions, with zero tangential velocity at the plane centre and a peak tangential velocity at $r=0.3R$, below the impeller disk indicates that a forced vortex is formed here. Majority of the liquids at this plane are rotating without efficient mixing in axial direction. LES predicts slightly higher values in terms of the axial velocity near the tank wall ($0.8R \leq r \leq R$) and tangential velocity in the range from $r=0.6R$ to $r=0.8R$ than the results obtained by the standard k–ε model.

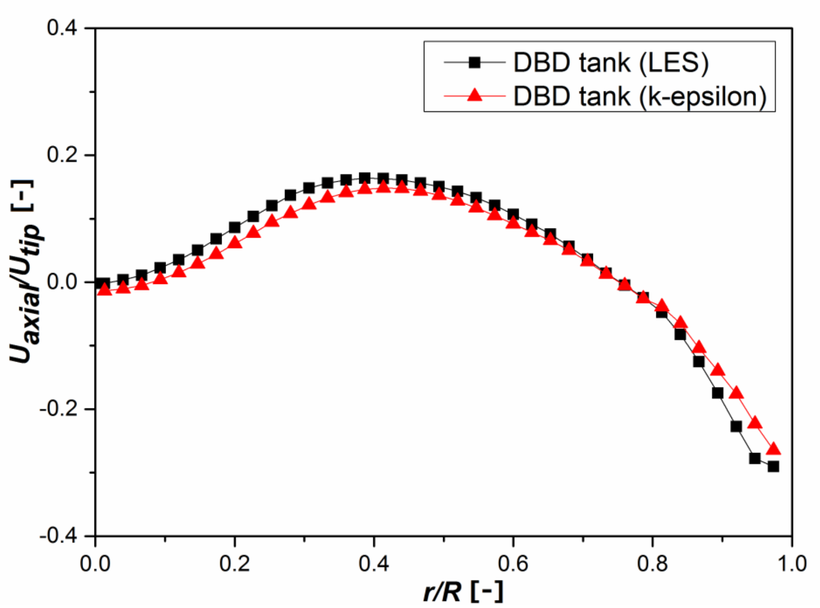

Figure 4.1 Distributions of axial velocity (DBD tank)

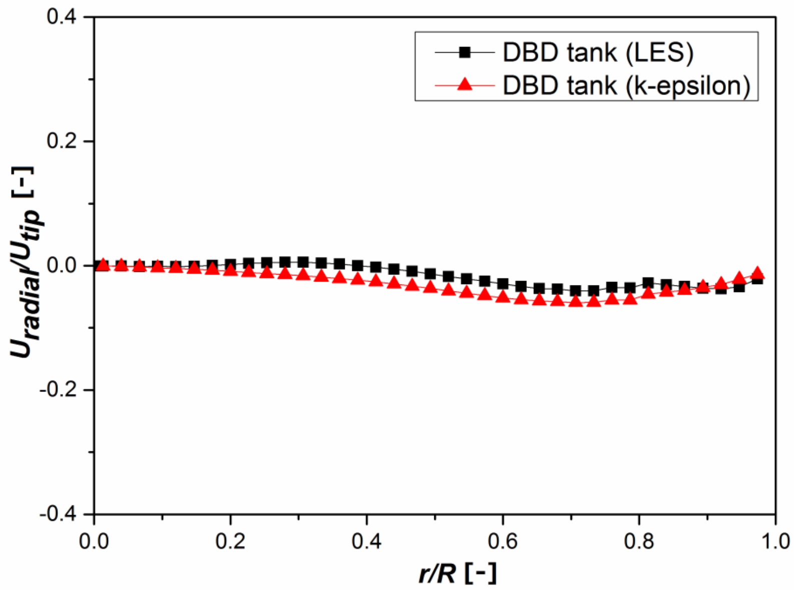

Figure 4.2 Distributions of radial velocity (DBD tank)

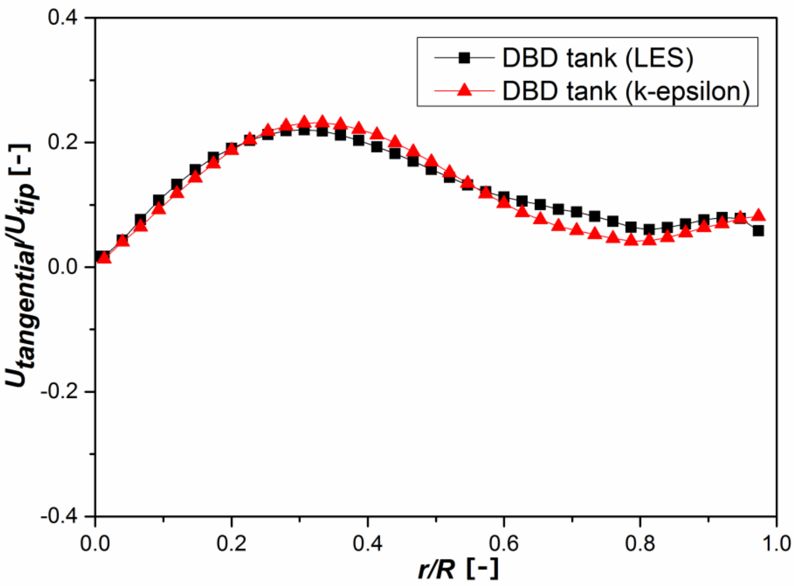

Figure 4.3 Distributions of tangential velocity (DBD tank)

Followed by the comparisons made in the DBD tank, the velocities distributions at the data sampling plane in DBB tank are showed from Figure 4.4 to Figure 4.6. As can be observed from these figures, both the k–ε model and LES show the similar trends of velocity components distributions at the data sampling plane in the DBB tank. As shown in

Figure 4.4, the LES predicts a little higher axial velocity component near the plane centre (0≤r≤0.2R) than that predicted by the *k*–*ε* model, however lower in the area close to the tank wall (0.85R≤r≤R). Figure 4.5 shows that the predicted radial velocities are similar for both *k*–*ε* model and LES except in the region of 0.7*R*≤r≤0.9*R*. Figure 4.6 depicts that the LES gives a slightly higher tangential velocity component than the *k*–*ε* model in the radial direction from 0.5*R* to 0.8*R*. Generally, the predictions given by *k*–*ε* model and LES are of good consistency.

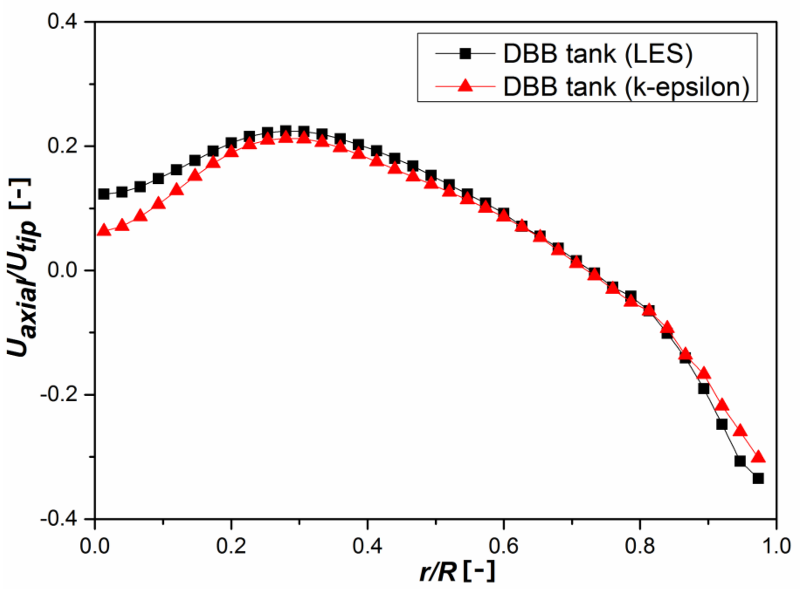

Figure 4.4 Distributions of axial velocity (DBB tank)

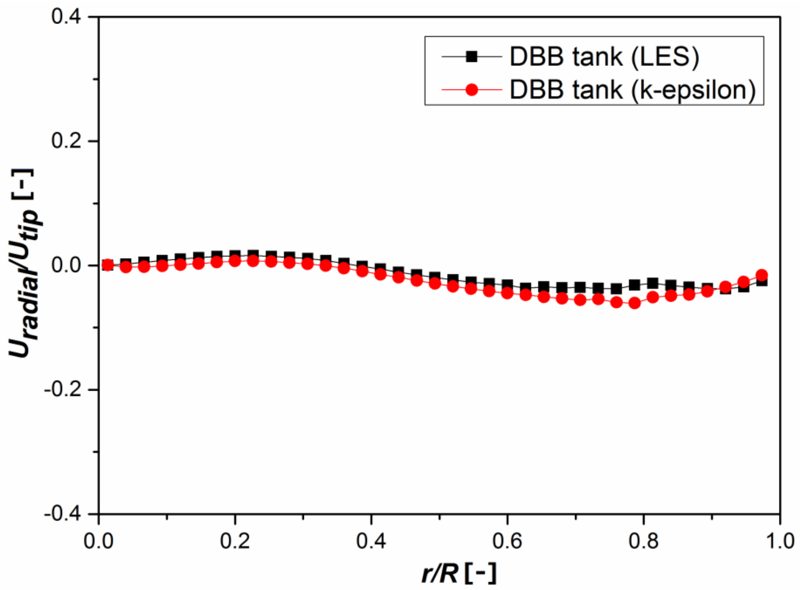

Figure 4.5 Distributions of radial velocity (DBB tank)

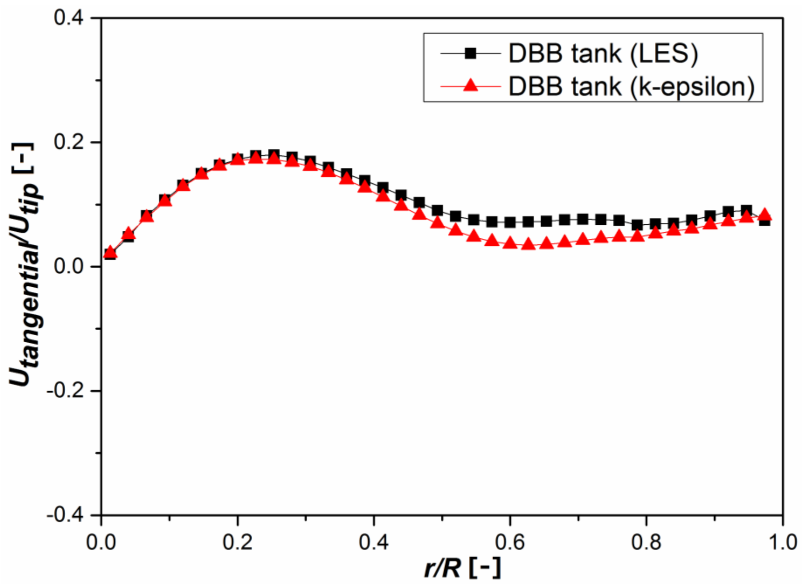

Figure 4.6 Distributions of tangential velocity (DBB tank)

Followed by the comparisons made in the DBD and DBB tank, the velocity profiles in the flat bottom stirred tank at the data sampling plane obtained by LES and k–ε model are displayed from Figure 4.7 to Figure 4.9. As can be seen from these figures, there is no significant difference in axial and radial velocity components predicted by LES and k–ε model. However, differences in the predicted tangential velocity can be observed that LES predicts lower tangential velocities from plane centre to 0.25*R* and higher tangential velocities from 0.3*R* to 0.7*R*. The peak value of the tangential velocity predicated by LES is at 0.25*R*, while the *k*–*ε* model predicates the peak value at around 0.19*R* indicating smaller forced vortex simulated by the *k*–*ε* model. Despite the difference, their trends are similar.

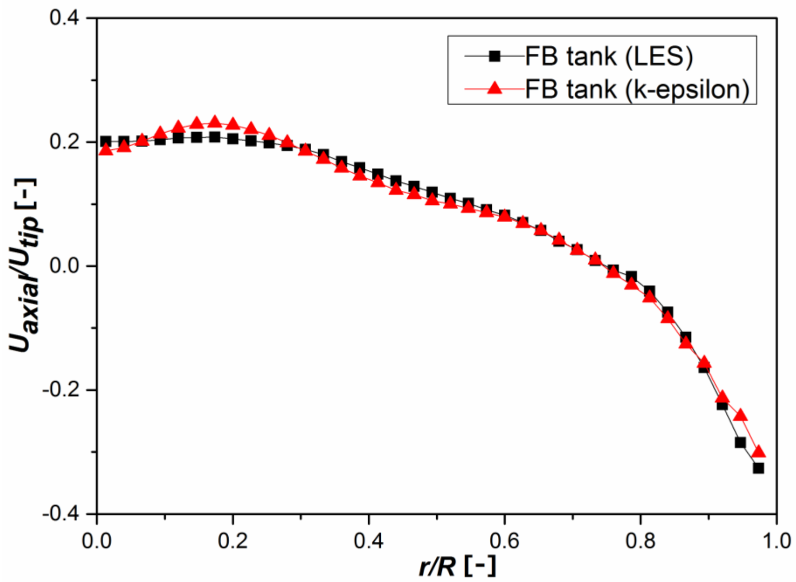

Figure 4.7 Distributions of axial velocity (FB tank)

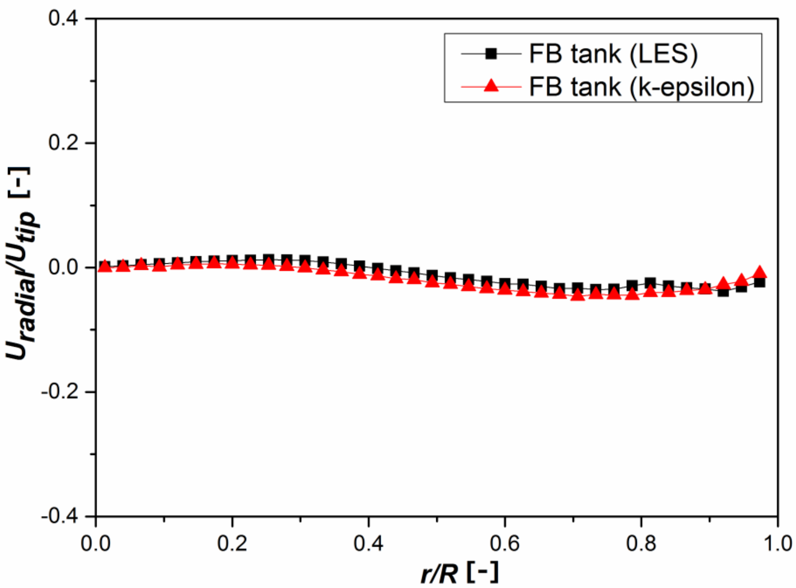

Figure 4.8 Distributions of radial velocity (FB tank)

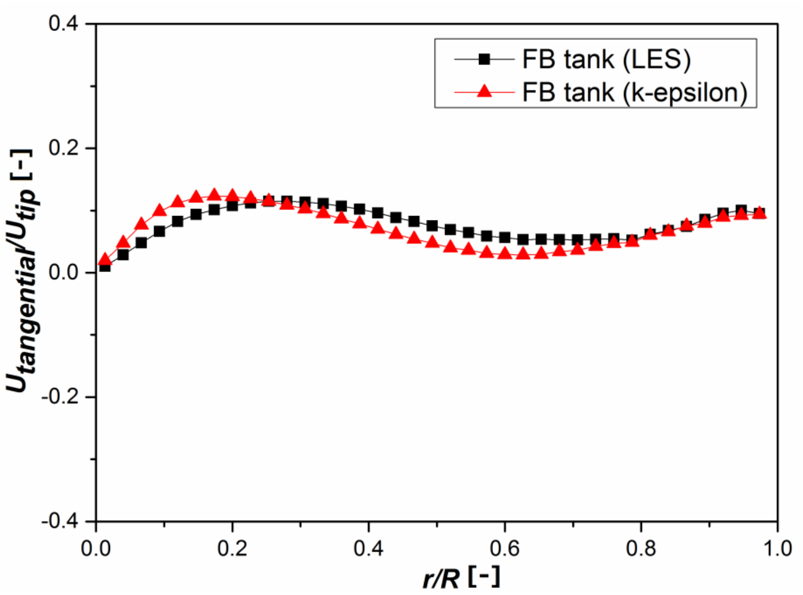

Figure 4.9 Distributions of tangential velocity (FB tank)

To sum up, it appears that the tangential velocity distributions (the structure of forced vortex) predicted by the LES and standard k-ε model have similar trend for the three stirred tanks. However, in the FB tank, the size of the vortex predicted by standard k-ε model is slight smaller than that gained by LES. Figure 4.3 and Figure 4.6 show that the water tangential velocity profiles predicted by both methods are similar in DBD and DBB tanks and minor differences can only be observed away from the vortex edge. Therefore, the existence of the dead zone was proved by two different CFD models.

Generally, velocity profiles obtained by the standard k-ε model agree well with the LES results, which confirm the presence of the large dead zone area below the impeller in DBD tank. The bottom shape and baffles' length have significant effect on flow patterns and the mixing efficiency in the region below the impeller.

4.3 LES of Single Phase Ionic Liquid Flows in the Stirred Tanks

The report on the mixing of highly viscous fluids, such as ionic liquids, in transitional state is rather limited in open literature. To fill this research gap, systematic numerical studies on mixing in stirred vessels were undertaken. The transitional state flow pattern of ionic liquid agitated by Rushton turbine was modelled by adopting LES as the standard k–ε model is only suitable to model the fully developed turbulent flows. Since the tank bottom shape and baffles' length have significant effect on flow dynamics in the lower bulk region, attention was paid to the flow pattern and velocity components below the impeller disk. The simulation results would not only offer knowledge for design and optimization of the ionic liquid mixing operations, but also provide information for investigating mixing efficiency of gas-ionic liquid multiphase flow in stirred vessels.

4.3.1 Operation Conditions

The FB, DBD and DBB stirred tanks used in this investigation have been introduced in detail in chapter 3. The ionic liquid ($BmimBF_4$) with μ=0.07 Pa.s, ρ=1210 kg/m^3 (at 25℃) was used as operation liquid. For single phase flow study, the impeller speed was kept at 440 rpm (Re=650) in simulation, which was determined experimentally to guarantee liquid flow without entrainment of bubbles in PIV measurement of velocity distributions. Similar conditions are used in the PIV measurement for validation and the results will be discussed in chapter 7.

4.3.2 Numerical Modelling Methods

The same mesh files of stirred tanks used in section 4.2 were adopted here. The standard k–ε model was used to get the initial flow fields. And then, LES was carried out based on the flow fields. A time step of 0.0016 s was used in this transient simulation which is small enough to enable around 20 time steps between each blade passing. The torque of the impeller and the velocities in the region below the impeller were monitored. The torque and velocities showed regular periodic fluctuations after 12 seconds of impeller rotating time, which indicates the flows in stirred tank were in the steady state (Gimbun et al., 2012, Li et al., 2011, Li et al., 2013). The velocity profiles data were sampled after 12 seconds of mixing in stirred tanks. Around 30 seconds of simulation data was collected corresponding to 75 rounds of impeller rotation and this amount of data was believed to give reasonable mean velocity profiles.

4.3.3 Transitional Flow Fields in Stirred Tanks

The effects of the tank bottom shape and baffles' length on the ionic liquid flows in stirred tanks were discussed in this section. The ionic liquid is agitated in the FB, DBD and DBB tanks respectively with the operation conditions mentioned in section 4.3.1. The ionic liquid was agitated at 440 rpm. The Reynolds number (*Re*) is 650 which indicates that the flow is in transitional flow regime at these operation conditions (Paul et al., 2004).

Figure 4.10 to Figure 4.12 show the time-averaged flow vectors and the contours of velocity magnitude of ionic liquid below the impeller for FB, DBD and DBB tanks respectively. It can be observed in Figure 4.10 to

Figure 4.12, the volume of dead zone below the impeller in DBD tank (Figure 4.11) is significantly smaller than the one found in water fully turbulent flow mixing. The extent of radial-axial circulation is greatly reduced with its extent being similar to the results reported by (Jaworski et al., 1996). Meanwhile, secondary circulation flows are formed below the downward circulating loops in each stirred tank with the strongest ones being observed in flat bottom stirred tank as shown in Figure 4.10. It is reported that the weak turbulence and secondary circulation loops have significant effect on mixing performance in that additional recirculation zone and weak turbulent circulation flow will prolong the mixing time in stirred vessels (Murthy Shekhar and Jayanti, 2002, Sano and Usui, 1985). The secondary circulation loops identified in the stirred tanks may weaken the mixing efficiency of ionic liquid at the region.

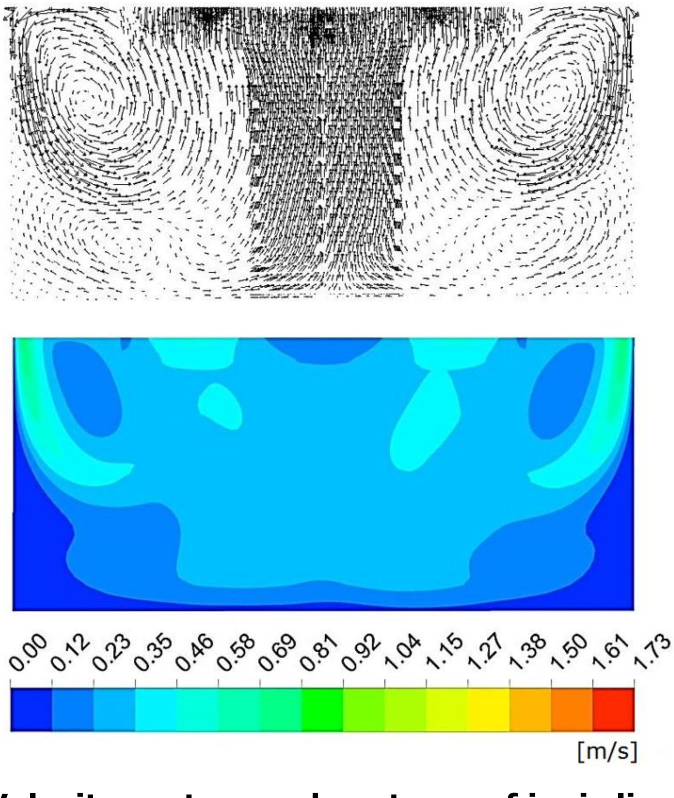

Figure 4.10 Velocity vectors and contours of ionic liquid below the impeller in FB tank

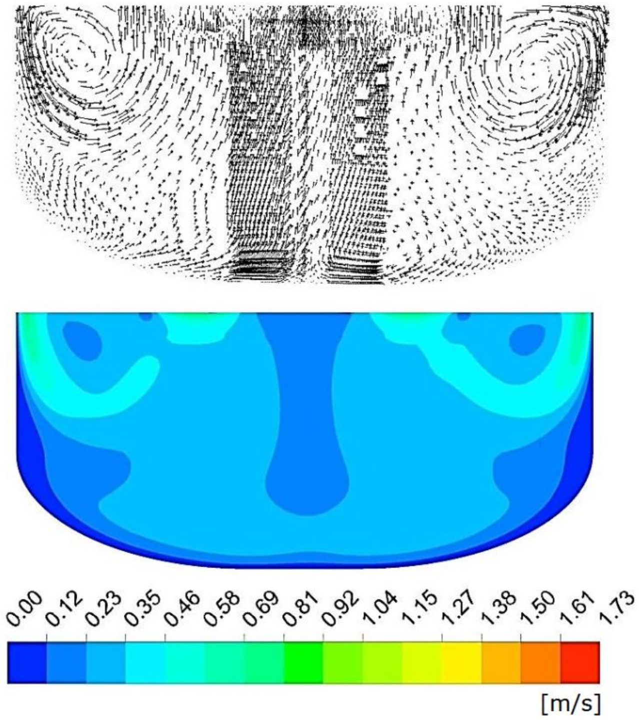

Figure 4.11 Velocity vectors and contours of ionic liquid below the impeller in DBD tank

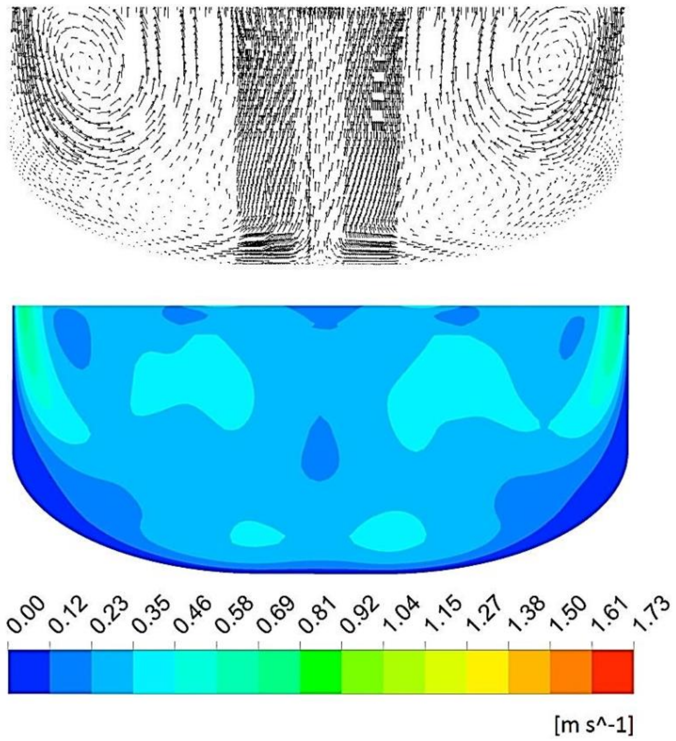

Figure 4.12 Velocity vectors and contours of ionic liquid below the impeller in DBB tank

In order to provide more detailed information of the effect of the bottom shape and baffles' length on the flows in the region below the impeller, the radial distribution of radial, axial and tangential velocities at the plane 40 mm above the tank bottom in all three geometries are shown from the Figure 4.13 to Figure 4.15. The data of velocity components were normalized by impeller tip velocity of 1.73 m/s here. Since this plane passes through the downward circulation loops, the radial velocity is negative between 0.3*R* and 0.9*R*. Figure 4.13 shows that the radial velocity at the plane are close indicating that neither the bottom shape nor baffles' length has significant effect on radial velocity at this plane. However, as shown in Figure 4.14, the axial velocity in dished bottom tanks, especially in the DBD tank, is decreased in the regions below the impeller. The axial velocity in the baffle region (around r/R=0.9) was also reduced in DBD tank where short baffles were employed. Since the mixing efficiency of stirred tank equipped with the Rushton turbine can be improved significantly by increasing the axial flow rate (Lamarque et al., 2010), the FB and DBB tank provide better mixing than the DBD tank in regions close to the tank wall. And the FB tank provides better mixing than the DBD and DBB tank in the region below the impeller disk when the ionic liquid is served as operation liquid.

Figure 4.15 shows the tangential velocity distributions below the impeller in each stirred tank. As it was mentioned in chapter 3, this distribution of the tangential velocities indicates a forced vortex is formed below the impeller. The tangential velocities of ionic liquid in the three tanks show very similar variation trend suggesting that the change of bottom shape and extension of baffles do not cause significant change on the magnitude of forced vortex. This is very different from the phenomenon observed in the water turbulent flows that the bottom shape and baffle length have a clear effect on the magnitude of the forced vortex.

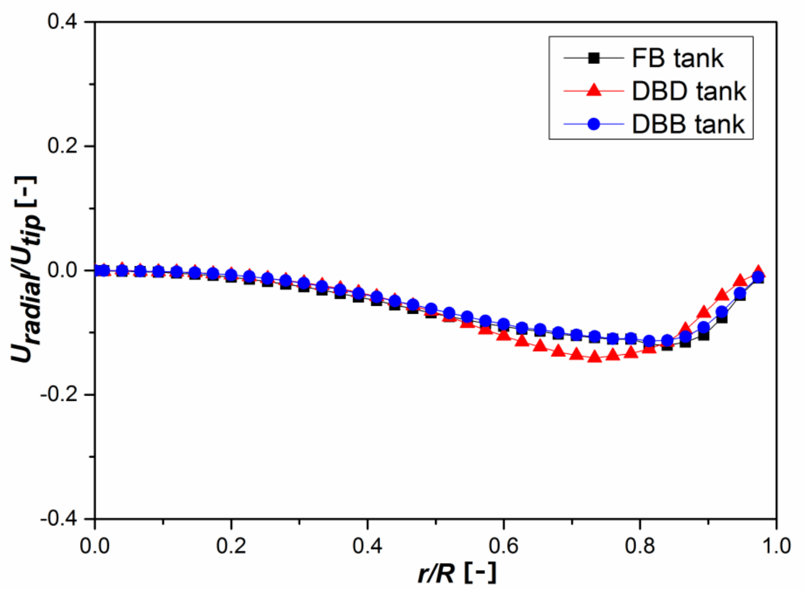

Figure 4.13 Radial velocity distributions of ionic liquid in stirred tanks

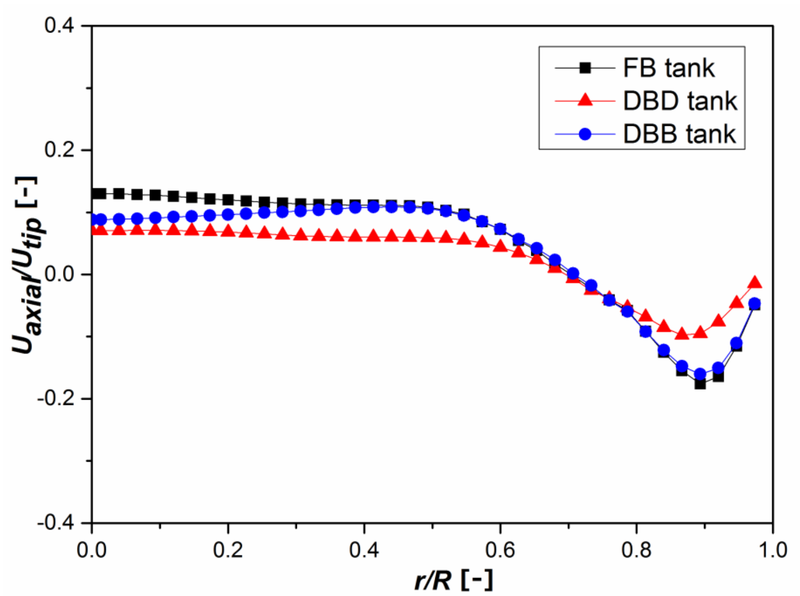

Figure 4.14 Axial velocity distributions of ionic liquid in stirred tanks

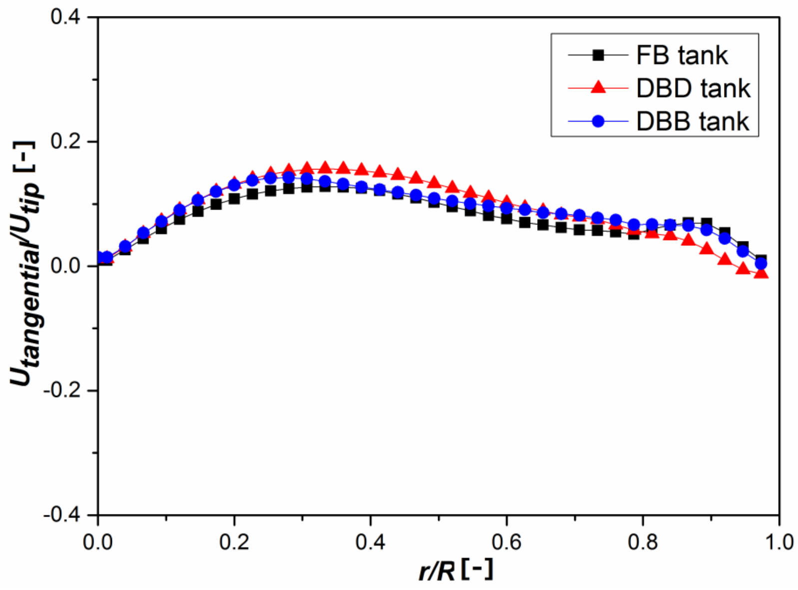

Figure 4.15 Tangential velocity distributions of ionic liquid in stirred tanks

4.3.4 The Effect of the Flow Regime on the Flow Fields

In order to study the effect of the flow regime on the flow filed. The LES of water turbulent flow simulation results showed in section 4.2.3 were compared with the LES of ionic liquid transitional flow modelling results in section 4.3.3. The focus was on the region below the impeller and the detailed differences are showed in Figure 4.16 to Figure 4.24. The simulations will show the different flow behavers of ionic liquid from conventional solvent like water which will offer insights into stirred tank design for mixing ionic liquids.

Figure 4.16 to Figure 4.24 show the comparison of velocity components of ionic liquid in transitional state (highly viscous ionic liquid) and water in turbulent state in the three stirred tanks. The time-averaged data were all sampled at the horizontal plane 40 mm above the tank bottom in all LES cases. As shown in Figure 4.16, the radial velocity of water in turbulent flow is practically zero in the flat bottom tank. However, in the ionic liquid transitional flow, the radial velocity is negative away from this plane centre, and the axial (in Figure 4.17) and the tangential velocities (in Figure 4.18) near the tank wall (*0.9R≤r≤R*) are quite low due to the high viscosity of the ionic liquid, all of which implies that the intensity of the downward circulation has reduced and the liquids start to flow towards the impeller before they reach the tank bottom. The Figure 4.17 depicts that the axial velocities of ionic liquid just below the impeller and in the baffle region in FB tank are lower than the water in turbulent flow. At the plane centre (r/R=0), the axial velocity of ionic liquid is 0.13Utip which is smaller than the axial velocity of water of 0.2Utip implying that the intensity of mixing in ionic liquid system is decreased (Lamarque et al., 2010). The tangential velocity profiles in both ionic liquid and water flow in FB tank are practically overlapping as shown Figure 4.18. It seems that the difference in liquid viscosity does not cause significant effect on the tangential velocity component below the impeller at this plane.

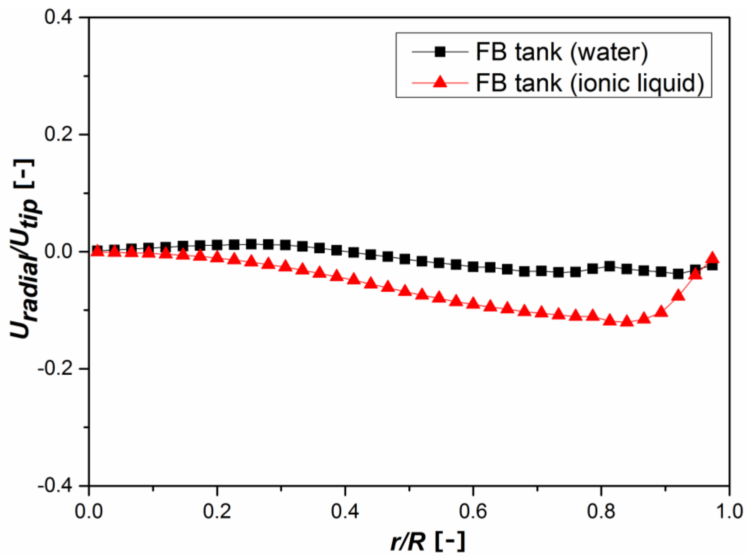

Figure 4.16 Radial velocity distributions of water and ionic liquid flow in FB tank

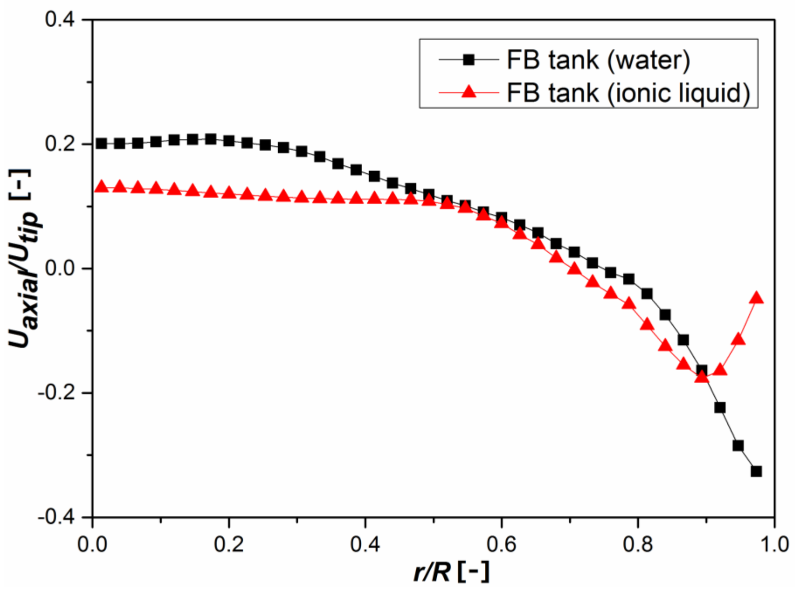

Figure 4.17 Axial velocity distributions of water and ionic liquid flow in FB tank

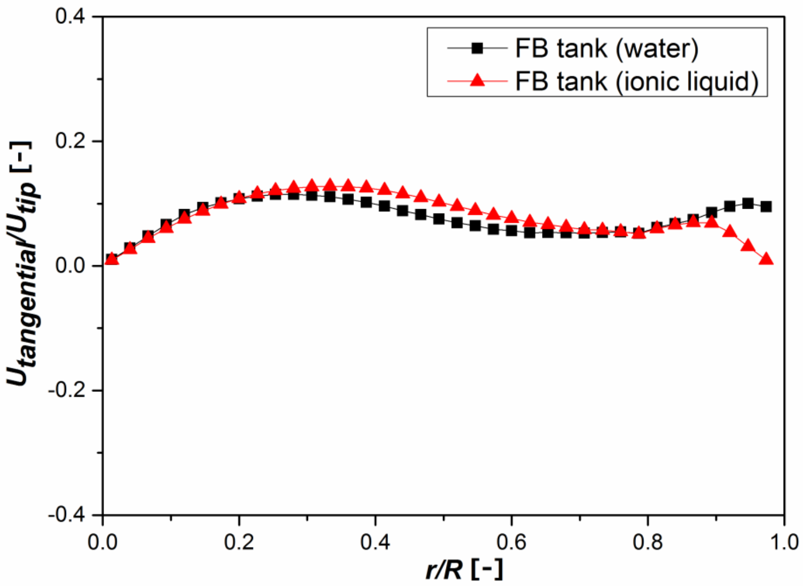

Figure 4.18 Tangential velocity distributions of water and ionic liquid flow in FB tank

Followed by the comparisons made in the FB tank, Figure 4.19 to Figure 4.21 show the velocity components of water turbulent flow and ionic liquid transitional flow in the DBD tank. As mentioned earlier, the bottom shape and baffles length did not have significant effect on the radial velocity profiles as the radial velocity components showed similar trend in all tested tanks when water and ionic liquid were operated in turbulent or transitional status respectively. The effect of flow regime on radial velocity distributions in DBD and DBB tank was very similar as it identified in FB tank in Figure 4.16. Therefore, Figure 4.19 and Figure 4.22 which compare the radial velocity components will not further discussed here.

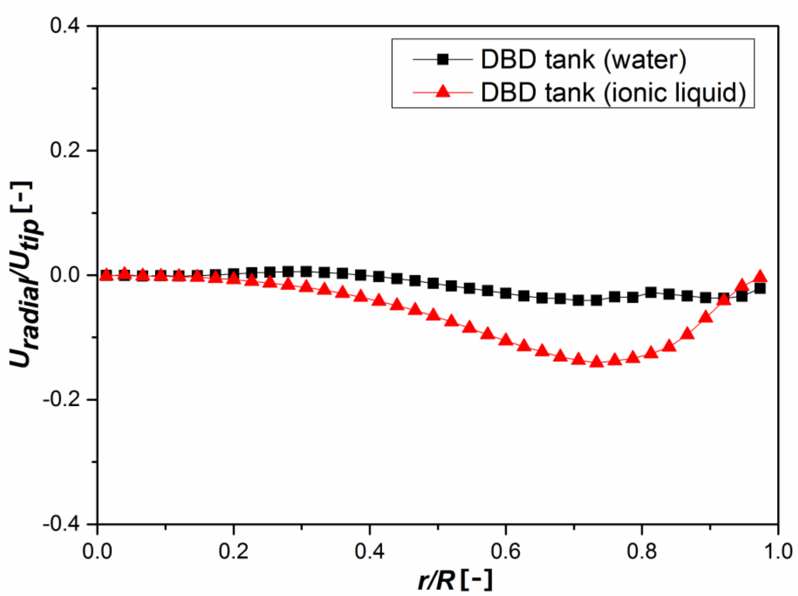

Figure 4.19 Radial velocity distributions of water and ionic liquid flow in DBD tank

As can be observed in Figure 4.20 and Figure 4.21, there is strong effect of flow regime on the axial and tangential velocity profiles. In the water turbulent flow, the axial velocity at the centre of this plane is practically zero whilst at the same point the axial velocity of ionic liquid is approximately $0.07U_{tip}$ as shown in Figure 4.20. Figure 4.20 also shows that the axial velocities of ionic liquid transitional flow is more uniform than that in the turbulent flow, and it only goes through weak minimum value around the baffles (r=0.9R). Figure 4.21 shows a lower peak value of tangential velocity of ionic liquid than water in the DBD tank below the impeller, which decreases from 0.22U_{tip} to 0.15U_{tip}. This reduction implies that a reduced intensity of the forced vortex at this region.

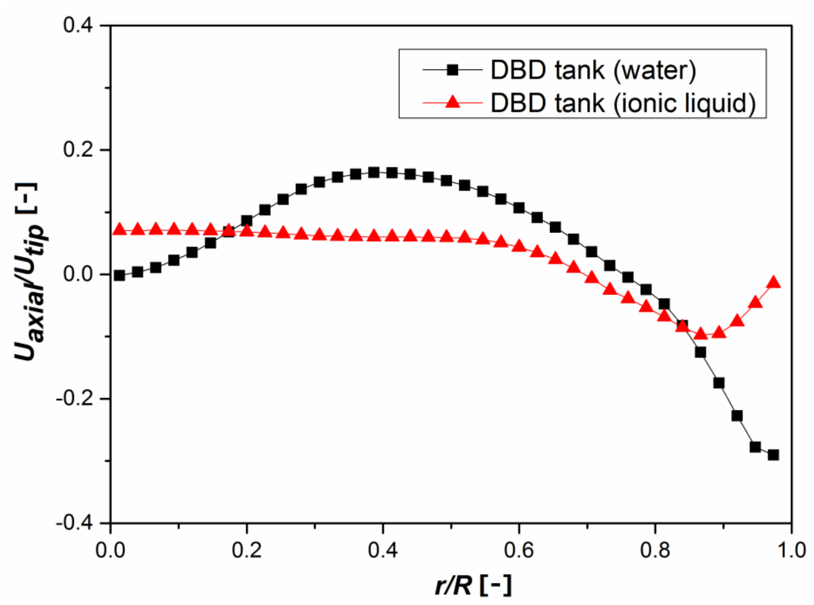

Figure 4.20 Axial velocity distributions of water and ionic liquid flow in DBD tank

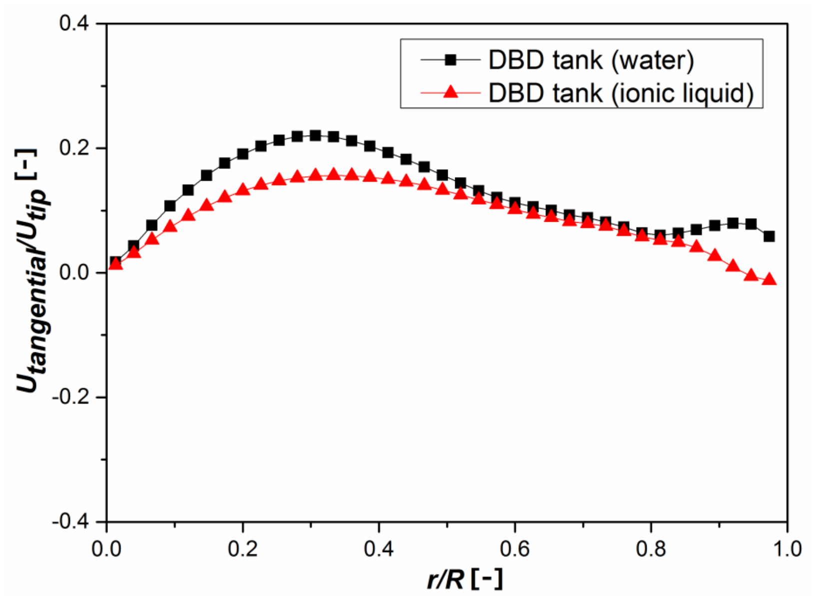

Figure 4.21 Tangential velocity distributions of water and ionic liquid flow in DBD tank

Figure 4.22 to Figure 4.24 show the velocity components of water in turbulent flow and ionic liquid in transitional flow in DBB tank at a horizontal plane 40 mm above tank bottom.

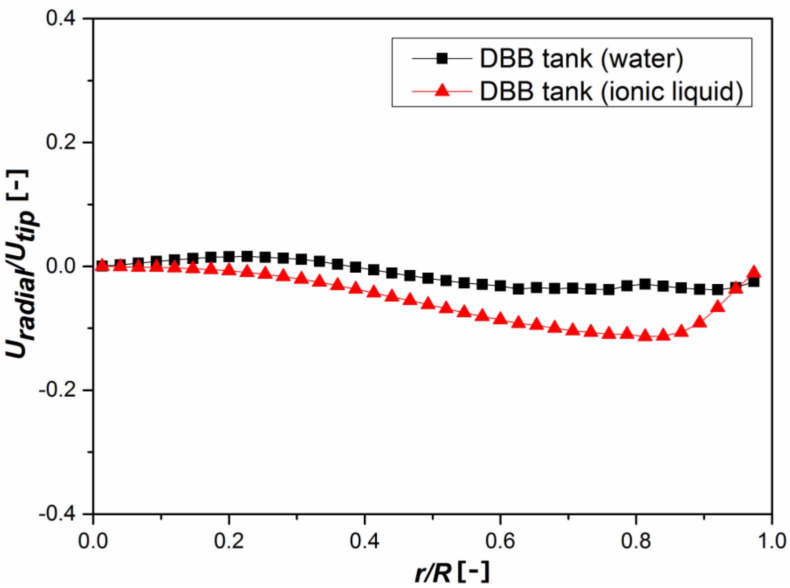

Figure 4.22 Radial velocity distributions of water and ionic liquid flow in DBB tank

As can be seen in Figure 4.23 and Figure 4.24, slightly decrease of the axial and tangential velocities at this plane centre can be found when the ionic liquid is used as operation liquid. While a more obvious reduction of axial and tangential velocities of ionic liquid can be observed away from the plane centre. The peak tangential velocity below the impeller has reduced a lot (from $0.18U_{tip}$ to $0.14U_{tip}$) which implies that the magnitude of the forced vortex has reduced in this area. Like Figure 4.17, the reduction of the axial velocities at this plane is observed and the effect of baffles on promoting the flow in axial direction below the impeller is weakened when the ionic liquid is agitated in the DBB tank. The peak axial velocity below the impeller decreased from $0.23U_{tip}$ to $0.1U_{tip.}$ Therefore, compared with water turbulent flow, the mixing in axial direction below the impeller is weakened when the ionic liquid is operated in the DBB tank

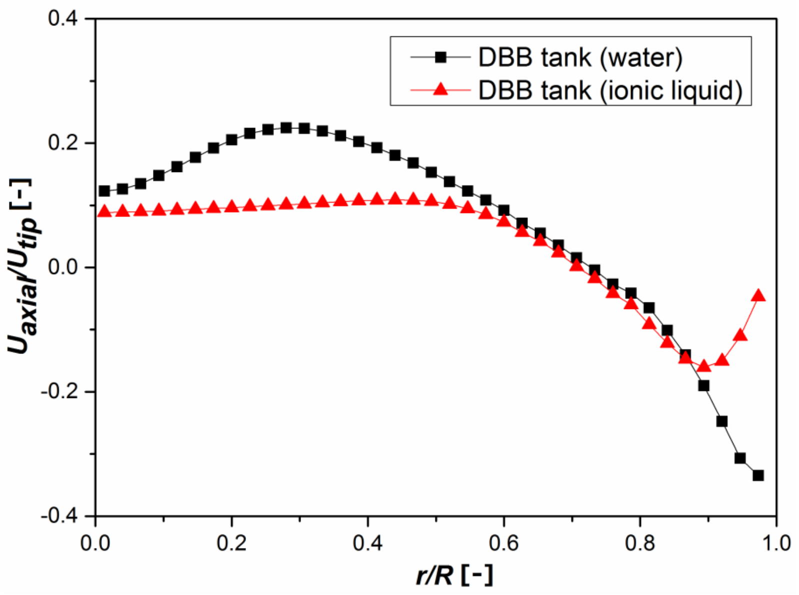

Figure 4.23 Axial velocity distributions of water and ionic liquid flow in DBB tank

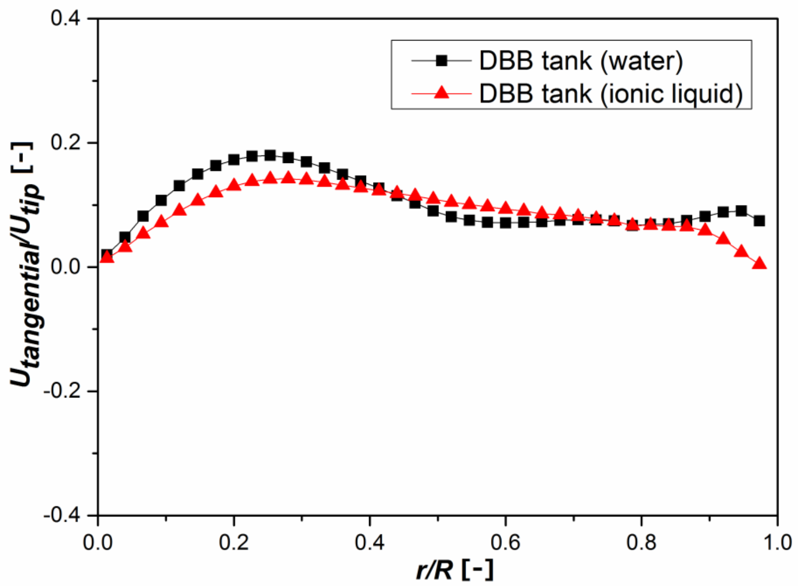

Figure 4.24 Tangential velocity distributions of water and ionic liquid flow in DBB tank

Figure 4.16 to Figure 4.24 clearly show that the flow regime, the shape of the tank bottom and the baffles' length have significant effect on the flow fields in the stirred tank. For example, in the transitional ionic liquid flow, flow velocity that closes the tank wall is almost zero in all geometries, which indicates that ionic liquid in this region is almost stagnant. The stagnant area near wall region in stirred tank has significant effect on mixing performance of stirred tank, since it may cause concentration gradients close to the wall and persist for a relative long time during mixing process hence prolonging the mixing time (Lamberto et al., 1999).

Unlike the characteristic water turbulent flow pattern agitated by Rushton turbine, the ionic liquid viscosity weakened the magnitude of the upward and downward circulation loops in all stirred tanks, and reduced the effect of baffles on generating flow in axial direction in FB tank and DBB tank. Maybe due to the effect of the high viscosity of ionic liquid and secondary circulation loops near the tank bottom, the short baffles have slight effect on forming the dead zone in the area below the impeller disk in DBD tank where large and obvious stagnant region can be observed in water turbulent flow.

In the water fully turbulent condition, the extension of baffles' length has a clear effect on reducing the magnitude of the forced vortex below the impeller and increasing the flow velocities in axial direction, hence enhancing the mixing efficiency in this area in the dished bottom stirred tank. This dead zone has reduced a lot when the ionic liquid is used as the operation liquid in the DBD tank.

The DBD and DBB tank have similar performance in mixing the viscous fluids such as the ionic liquid in the transitional state, but the DBB tank provides better axial mixing near the baffles region. Therefore, for dished tanks, the DBB tank offers better mixing for viscous fluids such as ionic liquid than the DBD tank.

4.4 Conclusions

Since LES provides more accurate simulation results than RANS modelling, the LES was used in this chapter to simulate the water turbulent flow and ionic liquid transitional flow in the FB, DBD and DBB stirred tanks. Comparisons were made between simulated data obtained by LES and RANS modelling. The LES results of velocity components in stirred tanks showed agreement with data predicted by the RANS modelling in chapter 3, which once again confirmed the formation of the large dead zone area in DBD tank.

In the modelling of the ionic liquid transitional flow fields in the stirred tanks, attention was paid to regions below the impeller. The intensity of the upward and downward circulation loops induced by the rotating impeller were greatly reduced when the ionic liquid was served as the operation liquid, and secondary circulation loops were formed around tank bottom. Ionic liquid velocities in the near tank bottom region were quite low, which would cause the existence of concentration gradients for a relative long time hence affecting the mixing efficiency in this region.

The flow pattern and velocity components were similar in DBD and DBB tank below the impeller region when the ionic liquid was agitated in these vessels. The dead zone found in the water turbulent flow in the DBD tank was reduced clearly when the ionic liquid was used as the operation liquid. Therefore, the disadvantage of the DBD tank in mixing performance was reduced when liquid with high viscosity such as ionic liquid was mixed in this vessel. Since the DBB tank provides better axial mixing near baffle region, the DBB tank offers better mixing for viscous fluids such as ionic liquid.

CHAPTER 5: EXPERIMENTAL INVESTIGATION ON THE EFFECTS OF MIXING PARAMETERS AND PHYSICAL PROPERTIES OF IONIC LIQUID ON THE BUBBLE SIZE IN A STIRRED TANK

5.1 Introduction

The multiphase (gas-liquid flow) stirred tanks are broadly used in the mixing industry, since they enable high levels of back mixing for efficient contacting between the gas and liquid phase to undertake good mass transfer and improve the reaction rates (Paul et al., 2004). And a good design of the multiphase stirred tanks and the optimized mixing process can improve the quality of the final products, reduce the amounts of the excessive by-products and cut down the operational cost (Mueller and Dudukovic, 2010). Therefore, the contact area of the gas and liquid phase is the most important parameter for the gas-liquid multiphase flow reactor design and mixing process optimization.

The distribution of bubble size in the multiphase stirred tanks is crucial in determining both the gas-liquid interfacial area and the mass transfer and reaction rates in the gas-liquid multiphase flows in the stirred vessels. The experimental and numerical investigations on the bubble size in the stirred tanks have been reviewed in Chapter 2. It has been recognised that the impeller type, agitation speed, gas flow rate and physical properties of the operation liquids are the key factors affecting the bubble size distribution (Puthli et al., 2005). This chapter focuses on the effects of the impeller speed, gas flow rate and physical properties of the ionic liquid solutions on the bubble size in the gas-ionic liquid system.

5.2 Experimental Setup and Camera Calibration

5.2.1 Experimental Setup

The bubble size measurement was carried out in a dished bottom stirred tank with four baffles reaching to the edge of dish (DBD tank). This stirred vessel is equipped with a standard Rushton turbine impeller placed at the halfway between the tank bottom and top. The detailed geometry of the stirred tank was introduced in Chapter 3 (in Figure 3.2). The nitrogen was served as gas source and ionic liquid ($BmimBF_4$) aqueous solutions with various concentrations were served as the liquid phase. A gas tube with an inner diameter of 2 mm was inserted into the stirred tank via the tank cover and was fixed below the impeller. The clearance between the gas outlet and tank bottom is T/4 where T is the tank diameter which equals 150 mm. A porous filter was fixed on the top of the tube to break the incoming gas into small bubbles. The gas phase was introduced into the stirred tank through this tube. The gas flow rate was controlled by adjusting a gas flow meter.

Experimental investigations were carried out to study the effect of the ionic liquid physical properties, impeller agitation speed and gas flow rate on the bubble size in the stirred tank respectively. The operation liquids were 0 wt.%, 1 wt.%, 5 wt.%, 10 wt.%, 30 wt.%, 50 wt.%, 100 wt.% ionic liquid ($BmimBF_4$) aqueous solutions. The aqueous solutions were prepared beforehand in the 3L measuring cups. Before the injection of the gas, the level of the operation liquid inside the stirred tank was maintained at the height equals to the tank diameter. The Room temperature was kept at 25 ℃ during the experiments with the help of air conditioning.

A high speed camera (2048×2048 pixels CCD) was connected to a microscope (Nikon-SM) to capture the images of bubbles in the stirred tank.

The impeller speed was controlled at 150 rpm, 200 rpm and 250 rpm respectively. The gas flow rate was controlled by a gas flowmeter. The flow rate was controlled at 0.1 L/min, 0.2 L/min and 0.3 L/min respectively for each impeller agitation speed. The impeller speed greater than 250 rpm was not considered to avoid significant air entrainment from the liquid surface into the stirred tank. In addition, the gas flow rate was restricted less than 0.3 L/min to make sure that the images of bubble's boundary were detectable in post-processing. The minimum impeller agitation speed of 150 rpm and the maximum gassing rate of 0.3 L/min were employed to guarantee that complete dispersion of the gas phase can be achieved in the stirred tank.

5.2.2 Camera Calibration

In order to accurately measure the bubble size in the stirred tank by means of measuring the number of image pixels of each bubble, the camera used in this investigation needs to be calibrated prior to the measurement. During the calibration, a relationship between the measured pixels of the calibration target (Pix_c) and the microscope settings (Mic_s) can be obtained at a focal plane. Since the diameter of the calibration target is known, a correlation between the distance and the pixel numbers in the image can be obtained. It is possible to get the data of the bubble size by measuring the pixel numbers of the bubble diameter at the focal plane at different microscope settings marked on the microscope.

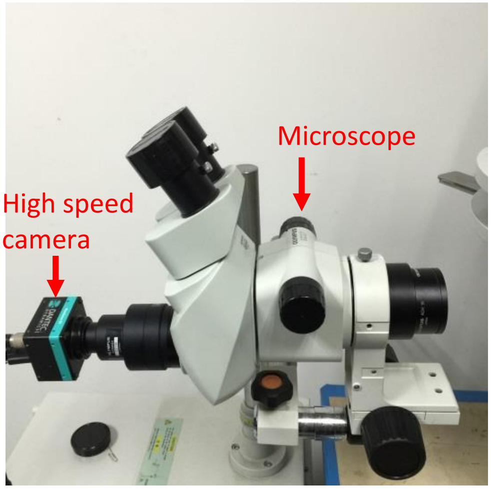

(a) Camera mounted at the microscope

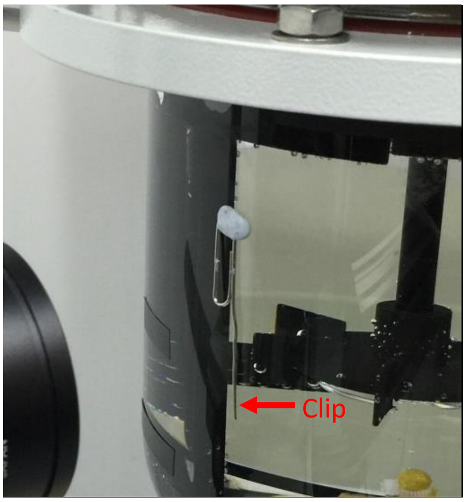

(b) Calibration target fixed at tank wall

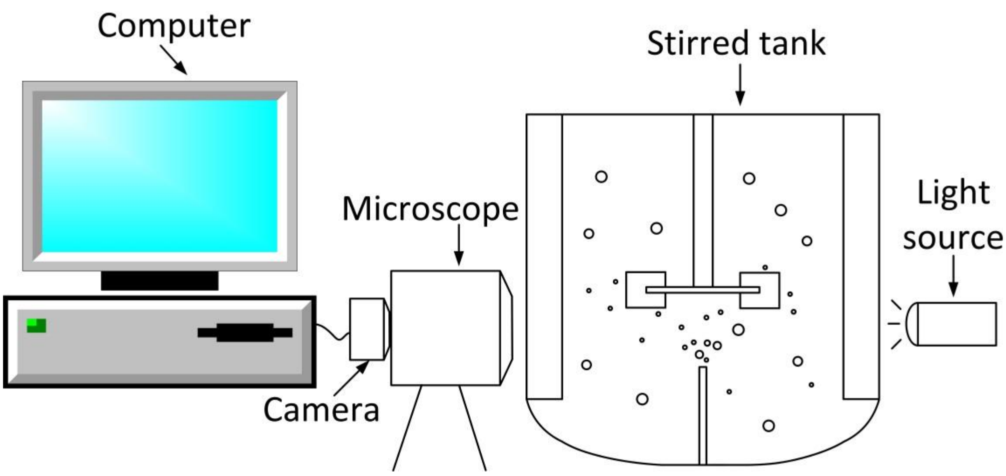

(c) Sketch of the experimental rig

Figure 5.1 Experiment setup

Figure 5.1 shows the experiment setup. A clip with diameter of 900 um was chosen as the calibration target which was attached at the outside wall of the stirred tank. A high speed camera connected to a computer was mounted at a microscope to observe the image of the target from the monitor.

The flow in the stirred tank was illuminated by a light source (18 watts lamp) placed at the other side of the vessel facing the lens of the microscope. In this way, the contrast ratio between the image background and the bubbles was enhanced. The exposure time of the camera was adjusted carefully to avoid over exposure which otherwise would cause severe damage to the camera, and to prevent image distortion due to bubbles' fast motion in the stirred tank. An exposure time of 900 μs was chosen which was found to get better bubble images in the experiments.

The Dantec Dynamics software was used to record the images of this target. The pixel numbers of the calibration target were measured by the image analysis tool in the Dantec Dynamics software.

Since the original pictures captured by the Dantec Dynamics are saved in a 32-bit tiff format, these photos cannot be displayed on computer. The software named Image J was used to convert the 32-bit tiff data into 16-bit jpg files. To get enough data to analyse the mean bubble size, at least 600 images were sampled at each operation condition. These images of bubbles were further processed to increase the contrast ratio between the bubbles and image background, which makes the bubbles' boundaries easier to be identified. The pixel numbers of each bubble's diameter were obtained and analysed in the Bubble Pro software at various operating conditions. Around 40,000 images of bubbles' boundaries were drawn and processed manually in the software.

Since the target pixel numbers (Pix_C) will be changed accordingly when the microscope setting (Mic_S) is adjusted during the measurement, a relationship between the target pixels and the microscope settings can be obtained which will facilitate the measuring process. This relationship is shown in Figure 5.2.

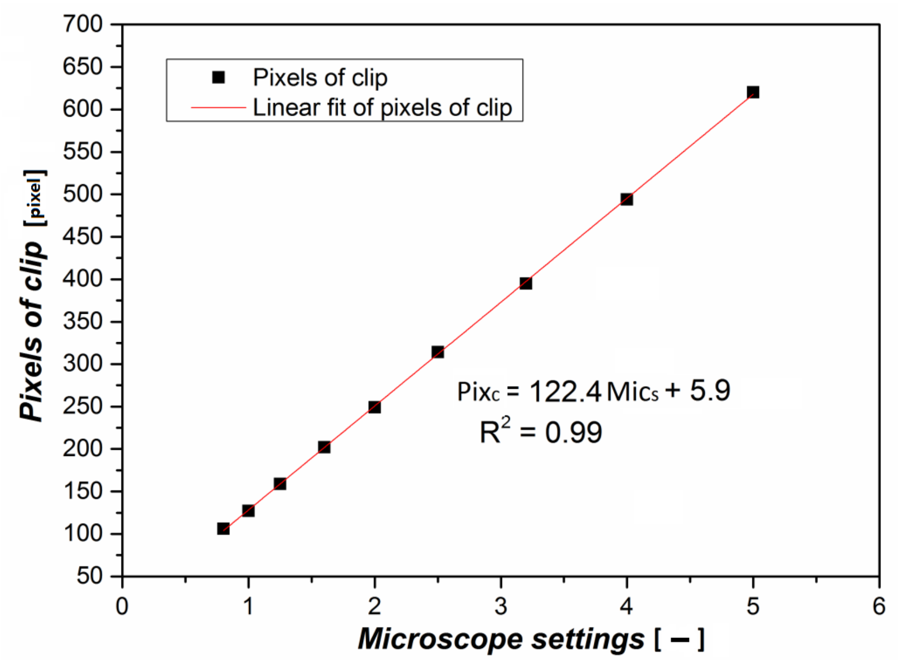

Figure 5.2 Linear fit of the pixels of the target at different microscope settings

A Linear fit of the plotted data from Figure 5.2 can be expressed as following equation:

$$Pix_C = 122.4\ Mic_S + 5.9 \tag{5.1}$$

where the microscope setting (Mic_s) ranges from 0.8 to 5.

Since the diameter of the calibration clip is 900 um, the conversion from 1 pixel to microns is given by the below equation:

$$\text{Microns} = 900/\text{measured pixels} \tag{5.2}$$

Equation 5.1 and 5.2 are embedded in the Bubble Pro software for calculation of the pixel numbers. The bubble size can be calculated by drawing the bubble boundary with hand at the focal plane and analysing the pixel numbers of bubble's diameter.

5.3 Measuring the Physical Property of Ionic Liquid Solutions

In order to carry out the gas-ionic liquid multiphase flow numerical simulations and study the effect of the liquid physical properties on the bubble size in the stirred tank, the physical properties including the viscosity, surface tension and density of 0 wt.%, 1 wt.%, 5 wt.%, 10 wt.%, 30 wt.%, 50 wt.%, 100 wt.% ionic liquid ($BmimBF_4$) aqueous solutions were measured and showed in this section.

The ionic liquid ($BmimBF_4$) used in this investigation was purchased from Cheng Jie (Shanghai, China) chemical company. Table 5.1 shows the information of physical properties of the pure ionic liquid ($BmimBF_4$) used in this study.

Table 5.1 Physical properties of ionic liquid

Name	1-Butyl-3-methylimidazolium tetrafluoroborate
CAS No.	174501-65-6
Molecular formula	$C_8H_{15}N_2BF_4$
Abbreviation	$BMIMBF_4$
Melting point	-82℃
Molecular weight	226.02
Density	1202 kg/m^3
Viscosity	7.0*10^{-2} Pa.s
Surface tension	43.85 mN/m

5.3.1 Viscosity measurement

A rheometer (Malvern Kinexus, UK) was used to test the viscosities of the $BmimBF_4$ aqueous solutions (0 wt.%, 1 wt.%, 5 wt.%, 10 wt.%, 30 wt.%, 50 wt.% and 100 wt.%). In order to test the accuracy of the rheometer, pure water was measured as the testing sample before measuring the $BmimBF_4$ solutions. Samples were placed on the testing platform, and a cone-plate were moved towards the testing platform and contacted with the samples (in Figure 5.3). The cone-plate rotated at various speeds during each measurement. By monitoring the shear forces and shear rates applied to the samples, the viscosities can be obtained (Hill, 2013). The temperature of the platform was controlled at 25℃. The shear rate of the cone-plate was varied from 0.1 to 1000 s^{-1} at each measurement. The dynamic viscosities of the ionic liquid solutions showed constant values under various shear rates after the system was stabilized, which indicates that these ionic liquid solutions are Newtonian fluids.

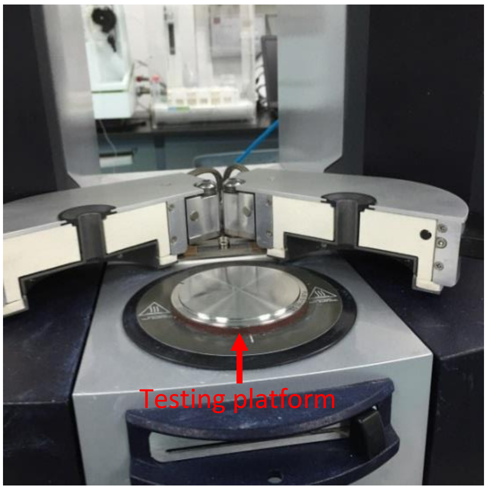

(a) The testing platform

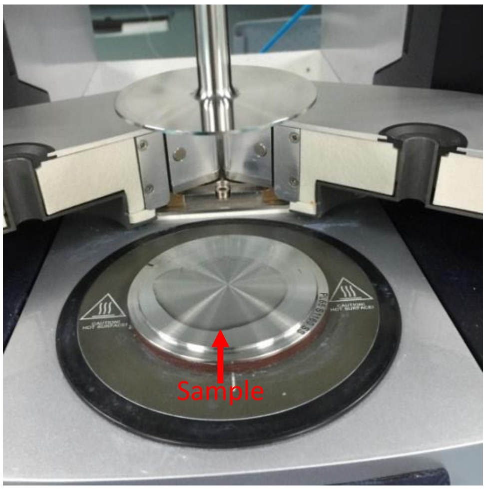

(b) Loading samples

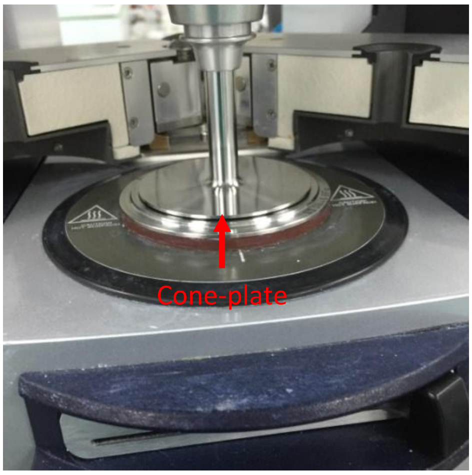

(c) A cone-plate moves towards the testing platform and rotating at different speeds

Figure 5.3 Measurement of the viscosities of BmimBF4 solutions

Figure 5.4 shows the viscosities of different concentrations of $BmimBF_4$ aqueous solutions. As can be seen from this figure, there is very little increase in the liquid viscosity when the concentration of $BmimBF_4$ grows from 0 wt.% to 50 wt.%. However, a sharp growth of liquid viscosity is identified with increasing $BmimBF_4$ concentration from 50 wt.% to 100 wt.%. This trend is very similar to the variation trend reported by Liu et al. (2008), in which all tested ionic liquids showed constant viscosity in dilute solutions and there was a rapid rise of viscosity in concentrated solutions.

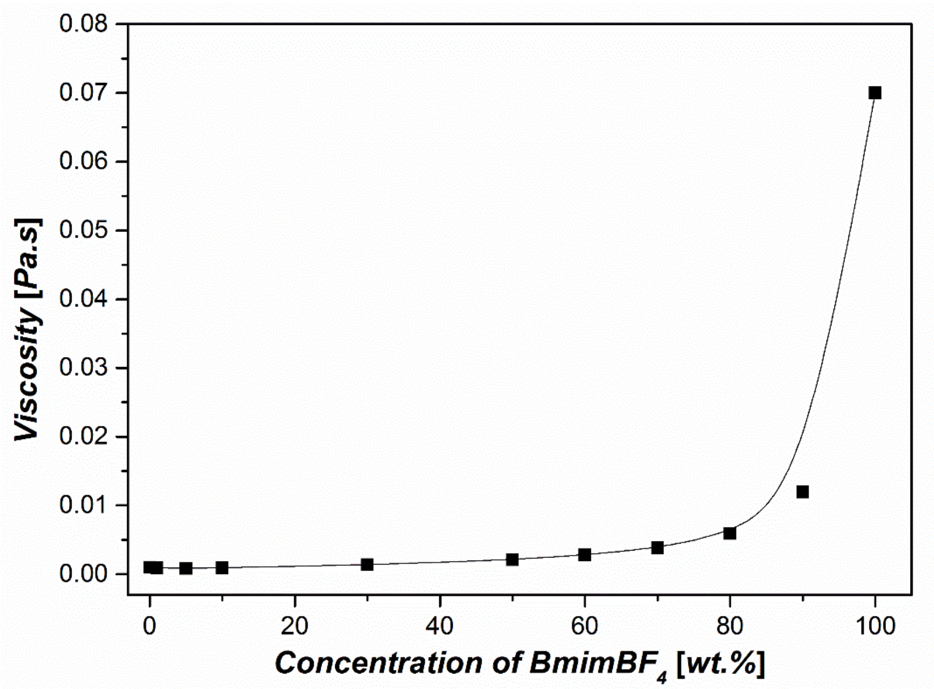

Figure 5.4 Sample viscosities at different concentrations of BmimBF4 solutions

5.3.2 Surface tension measurement

The surface tension data of $Bmimbf_4$ solutions were measured by a surface tension meter (Hengping Instrument, China). During the experiment, around 30 ml of each sample was poured into a beaker placed on a lifting platform at each test. A small platinum loop was used in this measurement which was hung above the lifting platform. This platform can move towards the platinum loop gradually allowing the loop to immerse into the testing sample gently. Afterwards, the platform started to move downward. As the platform moving down, a liquid film was formed between the liquid surface and platinum loop (see Figure 5.5). Finally, this platinum loop was detached from the liquid surface. During this detachment, a peak force that enables the platinum loop to detach from the liquid surface was detected. This peak force was then used to calculate the surface tension force in the software installed in this equipment.

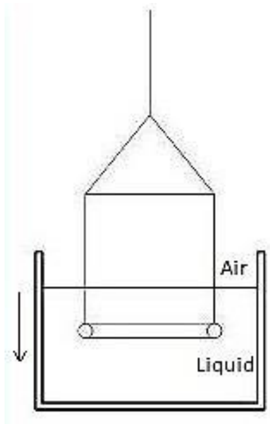

(a) Platinum loop dipped into liquid sample and beaker started to move downwards

(b) Liquid film was formed as the platform moving down

Figure 5.5 Measurement of the surface tensions of BmimBF4 solutions

In order to test the accuracy of the surface tension meter, water was employed as the testing sample first. The measured surface tension of water (at 25℃) is 71.85 mN/m. This value is very close to the reference data (71.97 mN/m) from the reference book of this instrument, which shows good accuracy of this surface tension meter. $BmimBF_4$ solutions (0 wt.%, 1 wt.%, 5 wt.%, 10 wt.%, 30 wt.%, 50 wt.% and 100 wt.%) were tested afterwards. After finishing each measurement, the beaker was washed with cleanser, distilled water and wiped clean for further use. The platinum loop was cleaned by the distilled water and heated by a flame of alcohol lamp for the next measurement.

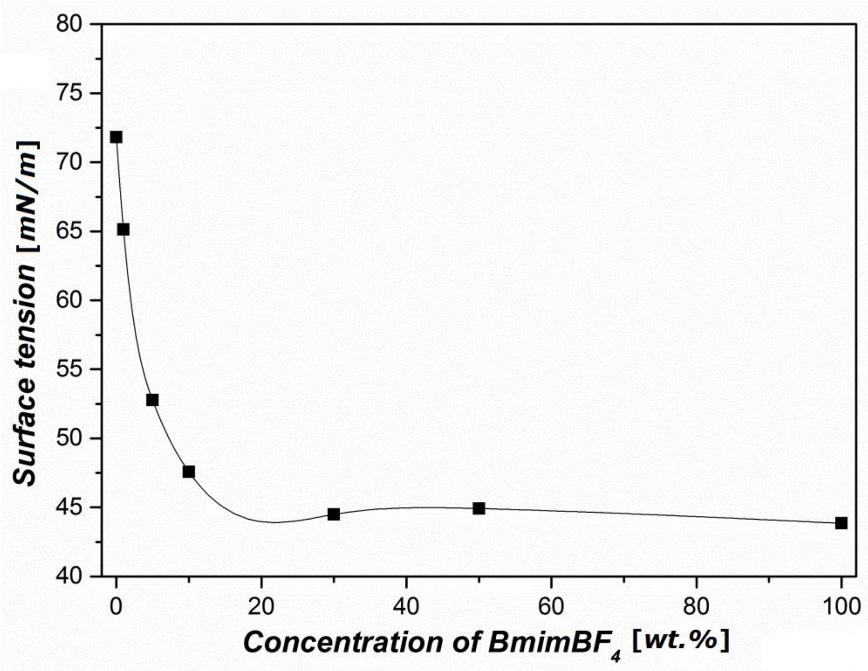

Figure 5.6 Surface tension of different concentration of BmimBF4 solutions

The surface tension data of different concentration of $BmimBF_4$ solutions are plotted in Figure 5.6. As can be observed from this graph, the surface tension of the tested samples decreased sharply in the solutions with concentration increasing from 0% to 10 wt.%. However, surface tension stays almost constant afterward when solutions' concentration increased from 30 wt.% to 100 wt.%. This variation trend is due to the differential surface segregation of cations and anions at different ionic liquid concentrations. At low ionic liquid concentration, the cations are the dominant species at the interface. And with the increasing ionic liquid concentration, anions start to balance their distributions until both cations and anions are evenly presented (Malham et al., 2006, Sung et al., 2005), resulting in almost constant surface tension force at higher concentrations of ionic liquid solutions (from 30 wt.% to 100 wt.%).

5.3.3 Density measurement

Densimeter (DH-300L, China) with a measuring range of 1-99999 kg/m^3 was used to test the density of $BmimBF_4$ solutions at 25℃. The densimeter was calibrated first using standard 100g weight. The pure water was used as the testing sample to test the accuracy of this equipment. The tested water density equals 998 kg/m^3. This value is very close to the reference data of 997 kg/m^3 (at 25℃), which indicates the good measuring accuracy of the densimeter. The ionic liquid solutions were tested afterwards and the measured data are shown in Figure 5.7. As can be seen from this figure, the variation of the densities of ionic liquid solutions is almost in linear relation with the $BmimBF_4$ concentrations. This trend is consistent with the variation trend of the density of ionic liquids aqueous solutions tested by Liu et al. (2008).

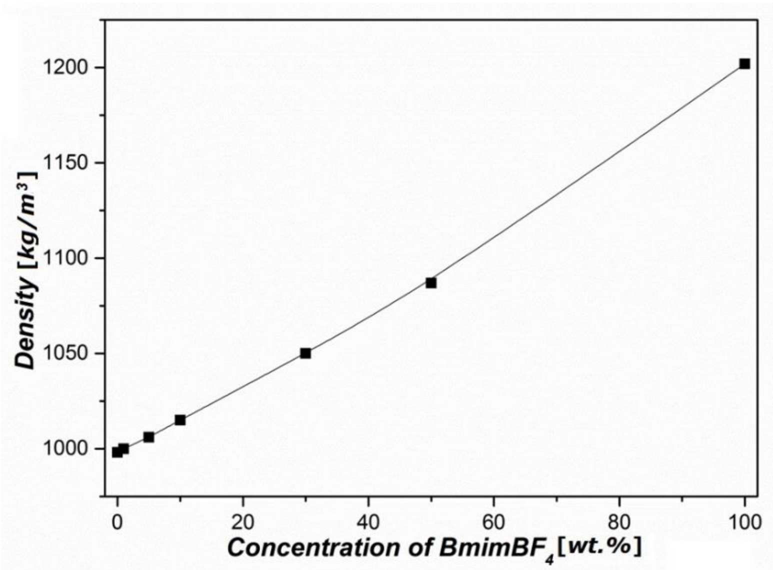

Figure 5.7 Density of different concentrations of BmimBF4 solutions

Table 5.2 summarised the detailed physical properties of the $BmimBF_4$ solutions including viscosity, surface tension and density. These data are critical parameters for modelling the ionic liquid flow in the stirred tank.

Table 5.2 Physical properties of BmimBF4 solutions

Physical properties / Concentration (wt.%)	Viscosity (Pa.s)	Surface tension (mN/m)	Density (kg/m^3)
0	$9.7*10^{-4}$	71.82	998
1	$9.5*10^{-4}$	65.13	1000
5	$8.5*10^{-4}$	52.76	1006
10	$9.6*10^{-4}$	47.56	1015
30	$1.38*10^{-3}$	44.5	1050
50	$2.1*10^{-3}$	44.92	1087
100	$7.0*10^{-2}$	43.85	1202

5.4 Distribution of Bubble Size in Ionic Liquid Solutions at Various Operation Conditions

Based on above measurements, this section experimentally investigate the effects of the impeller speed, gas flow rate and physical properties of ionic liquid solutions on the bubble size in the gas-ionic liquid system in the stirred tank.

In order to analyse the images of bubbles in the gas-liquid stirring system operated in steady state, an optimum stirred tank running time needs to be determined. The minimum running time of 10 minutes for each operation conditions was suggested to ensure the system to operate at the steady state and this running time was used throughout the experiments for this study (Hu et al., 2005a).

The image qualities of bubbles are strongly affected by the light source. In this experiment, it was found that as the number of bubbles increase in the stirred tank by means of increasing the impeller speed or gassing rate, the excessive bubbles blocked the light from the light source, which makes the bubble images at the focal plane were not easy to be identified. The images of bubble are in good quality under the fixed impeller speed of 150 rpm with gassing rates of 0.1 L/min, 0.2 L/min and 0.3 L/min respectively; or under the fixed gassing rate of 0.1 L/min with impeller speeds of 150 rpm, 200 rpm and 250 rpm. Therefore, the information of the bubble size under the above operation conditions is investigated.

5.4.1 The Effect of Impeller Speed on Bubble Size

This section shows the effect of the impeller agitation speed on the bubble size in the stirred tank. Figure 5.8 shows the bubble images in different ionic liquid aqueous solutions under the fixed gassing rate of 0.1 L/min with impeller speeds of 150 rpm, 200 rpm and 250 rpm respectively. As can be seen clearly from Figure 5.8, a decrease of bubble diameter can be observed with increasing impeller speed from 150 rpm to 250 rpm for all ionic liquid solutions due to the fact that the bubble size distribution is a result of dynamics of the bubble breakage and coalescence rates. For the breakage of bubble, the energy input must be high enough to overcome the force that hold it together as a function of surface tension force. The energy needed to break a bubble comes from the surrounding flow field as a form of kinetic energy in the turbulent eddies, shear energy, or as a combination of the two (Stamatoudis and Tavlarides, 1985). And the bubble coalescence occurs when bubbles suspended in a moving fluid, collide with one another. At the time of collision a thin film of liquid between them was formed. If the bubbles contact together for sufficient time, the liquid film will be thin and rupture and thus resulting in coalescence. However, the colliding bubbles will separate instead of coalescence if the contact time is less than the film drainage time (Paul et al., 2004). The increasing impeller speed will result in higher turbulence intensity and shear rate, which will increase bubble breakage frequency (Stamatoudis and Tavlarides, 1985), hence resulting in the smaller bubbles in the stirred tank.

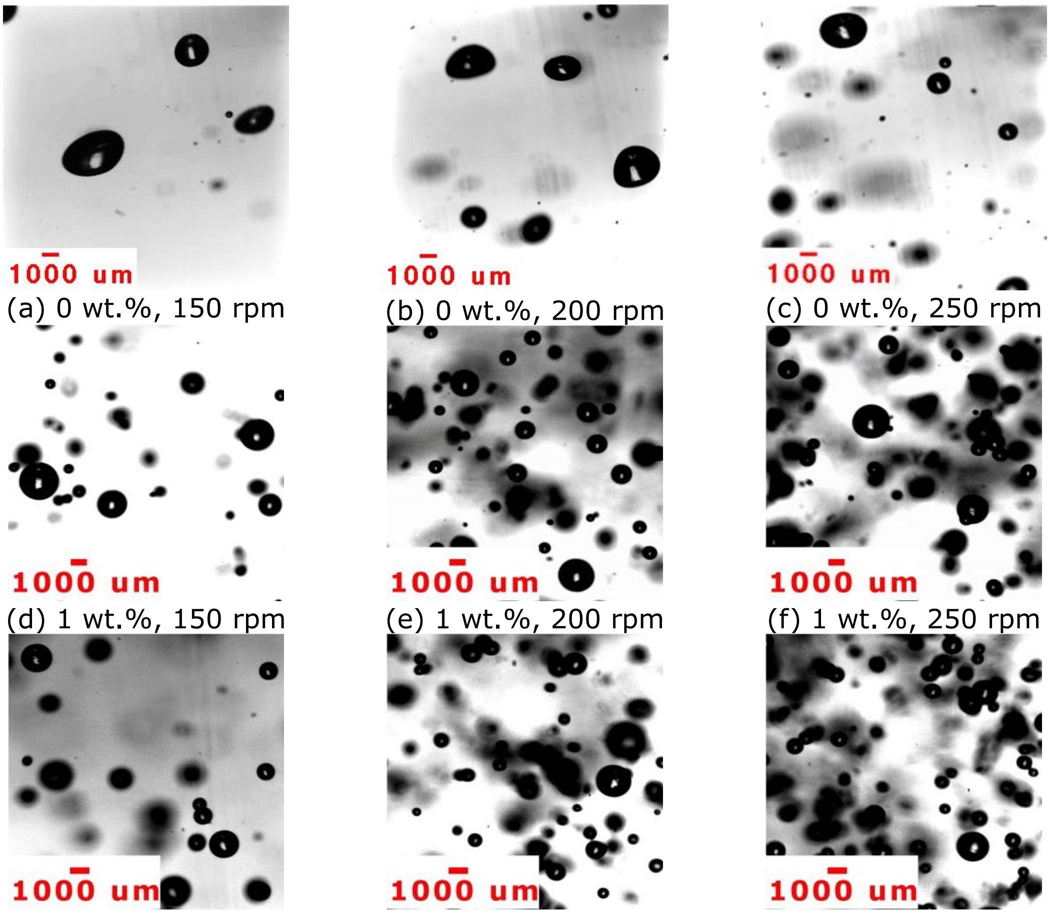

(a) 0 wt.%, 150 rpm (b) 0 wt.%, 200 rpm (c) 0 wt.%, 250 rpm

(d) 1 wt.%, 150 rpm (e) 1 wt.%, 200 rpm (f) 1 wt.%, 250 rpm

(g) 5 wt.%, 150 rpm (h) 5 wt.%, 200 rpm (i) 5 wt.%, 250 rpm,

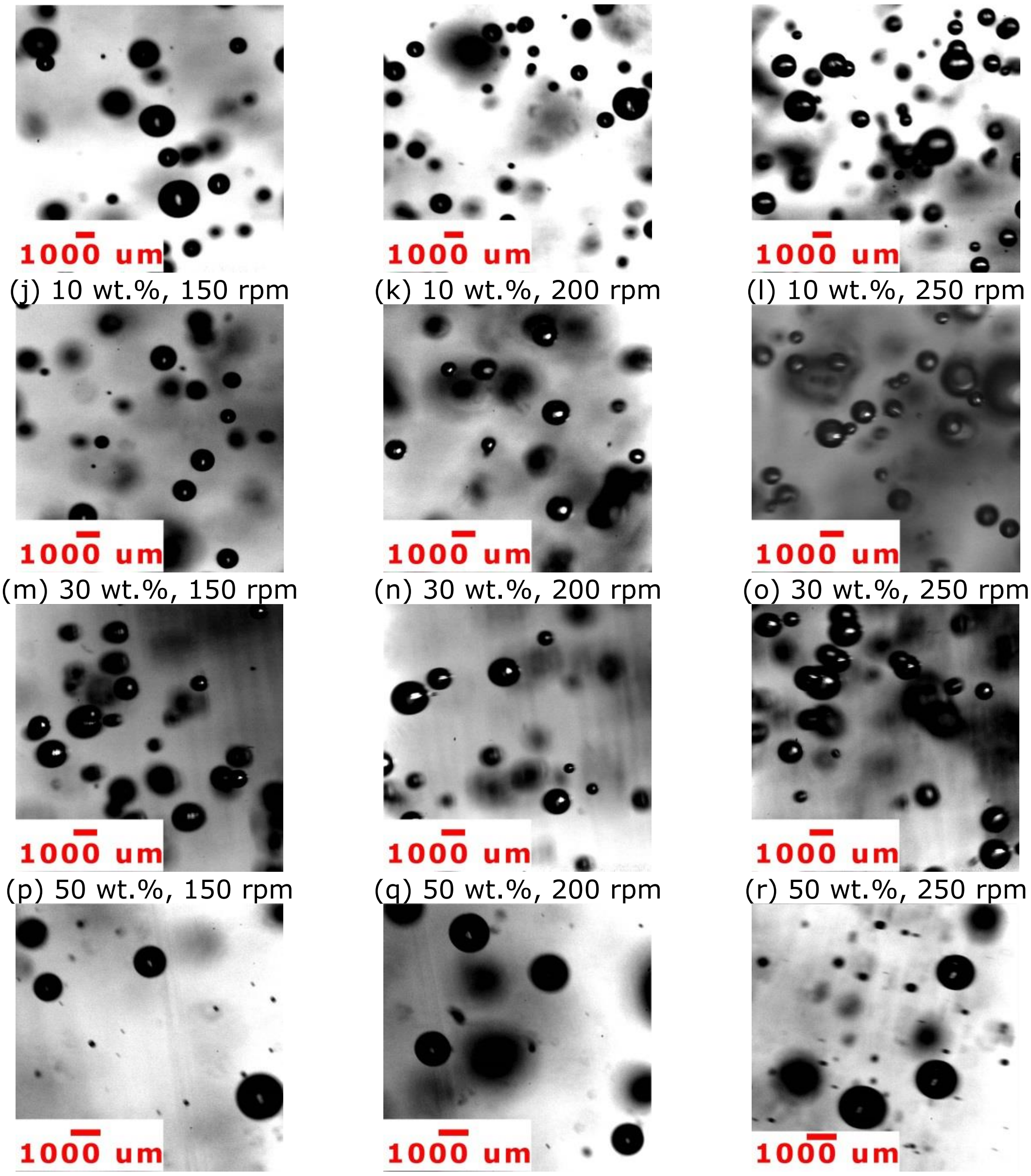

(j) 10 wt.%, 150 rpm (k) 10 wt.%, 200 rpm (l) 10 wt.%, 250 rpm

(m) 30 wt.%, 150 rpm (n) 30 wt.%, 200 rpm (o) 30 wt.%, 250 rpm

(p) 50 wt.%, 150 rpm (q) 50 wt.%, 200 rpm (r) 50 wt.%, 250 rpm

(s) 100 wt.%, 150 rpm (t) 100 wt.%, 200 rpm (u) 100 wt.%, 250 rpm

Figure 5.8 Bubble size in the ionic liquid solutions (Impeller speed: 150 rpm, 200 rpm and 250 rpm; Gassing rate: 0.1 L/min)

The bubbles showed irregular spherical shape in each picture when the pure water (0 wt.% of ionic liquid) is agitated in the stirred tank. At the same operation condition, significant reduction of bubble size can be found when only 1 wt.% of ionic liquid solution is used as the operation liquid. This phenomenon is the result of the high surface tension of pure water, in which bubbles' breakage is restrained and large bubbles are more easily formed in stirred tank during gassing and stirring. The larger bubbles are easier to be deformed in flow, while smaller bubbles are dragged by the flow with little deformation (Paul et al., 2004).

The Sauter mean diameter (d_{32}) is widely used in literatures to characterise the bubble size in the gas-liquid multiphase flow system, as it relates the volume of the dispersed phase to its area consequently the chemical reaction rates and mass transfer. Therefore, the Sauter mean diameter was adopted in this section to characterise the detailed bubble size information in the gas-ionic liquid aqueous solutions in the stirred tank. The Sauter mean diameter is defined as

$$d_{32} = \frac{\sum n_i d_{eqi}^3}{\sum n_i d_{eqi}^2} \tag{5.3}$$

where n_i is the number of bubbles with an equivalent diameter d_{eqi} which is obtained by assuming the bubbles as ellipsoids (Paul et al., 2004). The d_{eqi} is calculated through

$$\mathrm{d_{eqi}} = \sqrt[3]{\mathrm{a}'^2\mathrm{b}'} \tag{5.4}$$

where a' is the horizontal bubble diameter, b' is the vertical bubble diameter as shown in Figure 5.9.

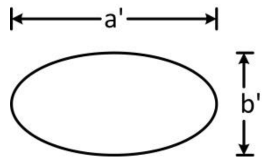

Figure 5.9 The horizontal and vertical diameter of a bubble

Additional two groups of measured data were added into Figure 5.10 to Figure 5.16 to fit the bubble size information by using the power function, in which the impeller agitation speed was kept at 180 rpm and 220 rpm respectively. The detailed values of d_{32} at different impeller agitation speeds and ionic liquid concentrations at gassing rate of 0.1 L/min were plotted from Figure 5.10 to Figure 5.16 respectively. As can be found in those figures, the data of d_{32} is decreasing with the increasing impeller speed for all ionic liquid solutions. Significant reduction of d_{32} is identified when the impeller speed increases from 150 rpm to 200 rpm with pure water and 1 wt.% ionic liquid solution being used as the operation liquid respectively.

The surface tension of pure water and 1 wt.% ionic liquid solution is much higher than other ionic liquid solutions. Larger bubbles are easily formed at low impeller energy power input into the gas-liquid flow system. The large bubbles are easily deformed and broken, while small bubbles are more stable and move with the flow (Martín et al., 2008). Therefore, as can be seen from Figure 5.10 and Figure 5.11, the increase of energy input by means of rising impeller speed from 200 rpm to 250 rpm does not cause great reduction of d_{32} compared with the increase from 150 rpm to 200 rpm. With the increase of ionic liquid concentration from 5 wt.% to

100 wt.% (Figure 5.12 to Figure 5.16), more stable, sphere and smaller bubbles are formed, with the reduction of d_{32} being not remarkable.

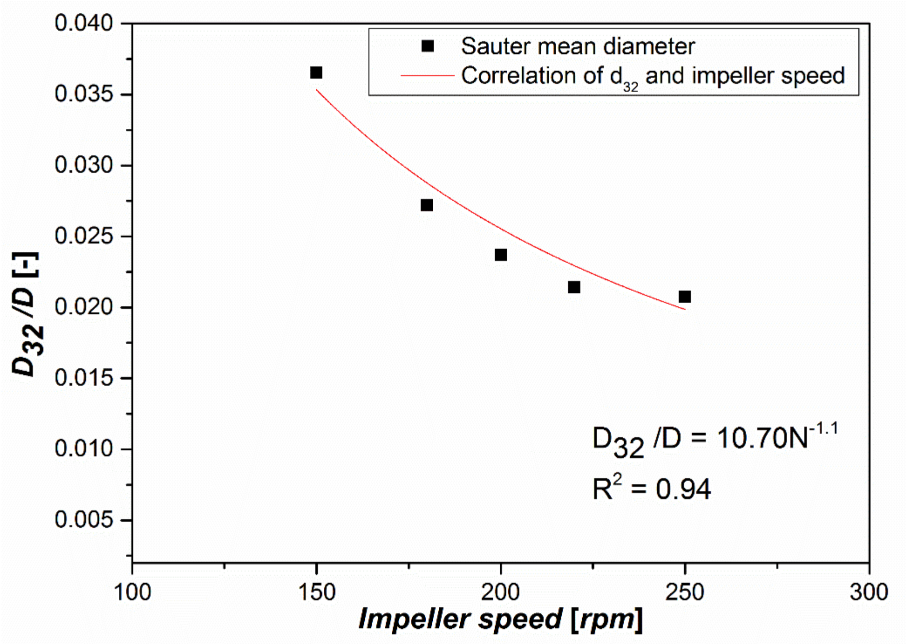

Figure 5.10 Sauter mean diameter at different impeller speeds (0 wt.% ionic liquid solution)

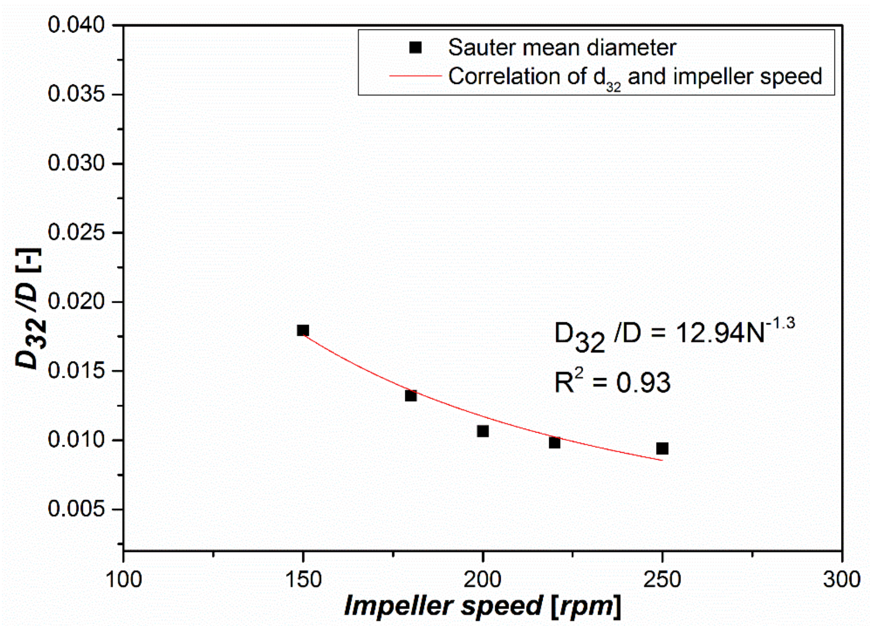

Figure 5.11 Sauter mean diameter at different impeller speeds (1 wt.% ionic liquid solution)

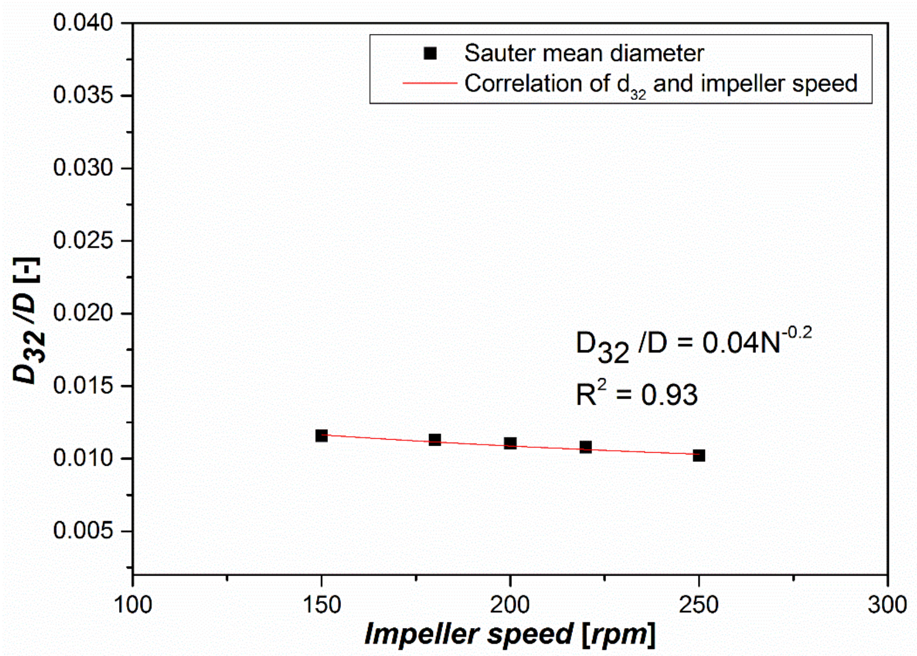

Figure 5.12 Sauter mean diameter at different impeller speeds (5 wt.% ionic liquid solution)

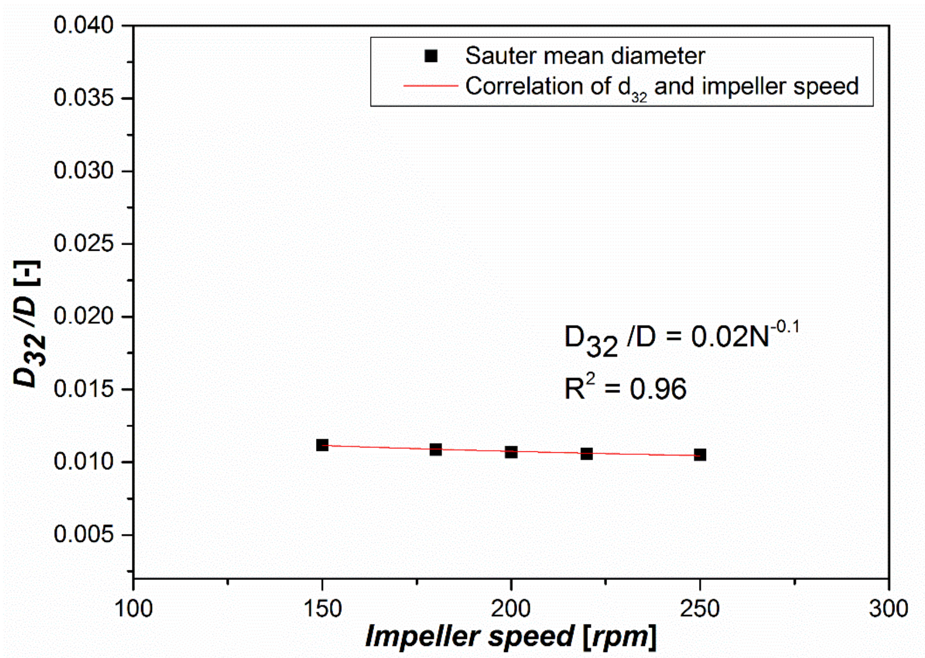

Figure 5.13 Sauter mean diameter at different impeller speeds (10 wt.% ionic liquid solution)

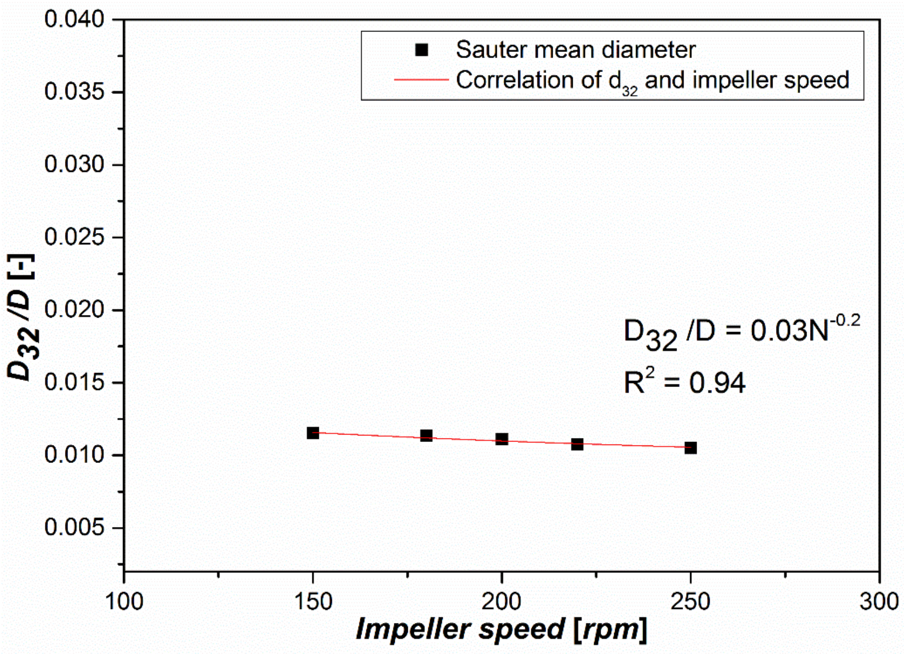

Figure 5.14 Sauter mean diameter at different impeller speeds (30 wt.% ionic liquid solution)

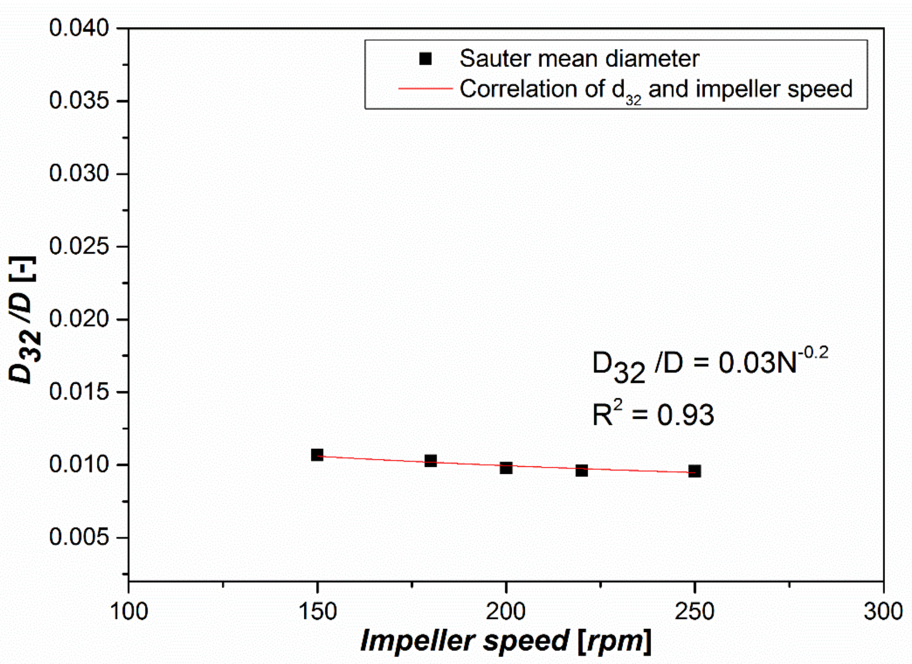

Figure 5.15 Sauter mean diameter at different impeller speeds (50 wt.% ionic liquid solution)

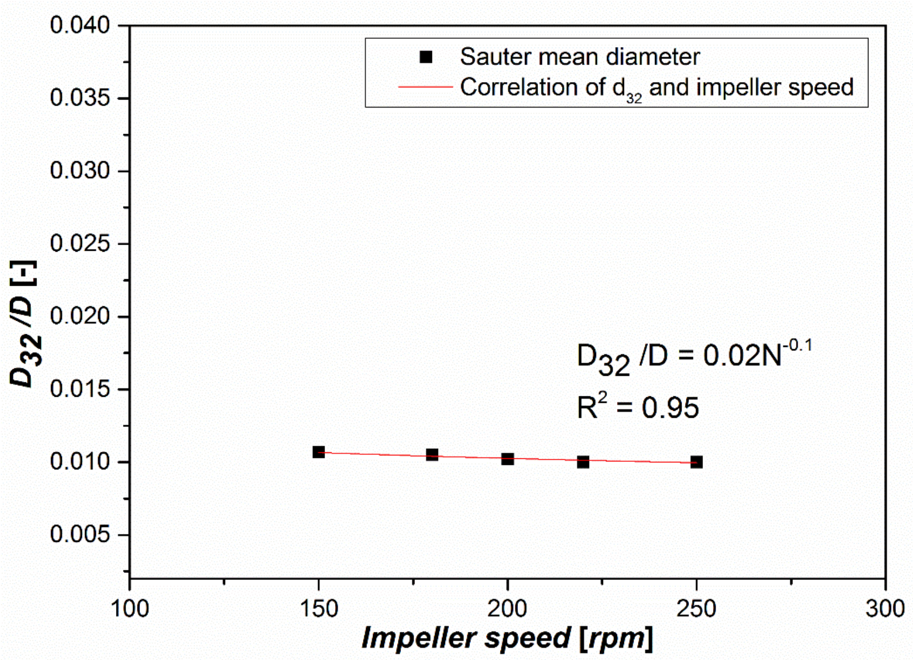

Figure 5.16 Sauter mean diameter at different impeller speeds (100 wt.% ionic liquid solution)

The relationship between the impeller agitation speed and the d_{32} is reported to fit with the following equation proposed by (Pacek et al., 1998):

$$d_{32}/D \propto N^{\alpha'} \tag{5.5}$$

where D is the impeller diameter, N is the impeller rotating speed. In literature, the exponent value of α' is -1.2 when the flow is in turbulent state.

The following equation can be used to correlate the sampled data. This equation assumes that the droplet Sauter mean diameter is proportional to the maximum stable droplet size in the stirred tank in the turbulent flow, and the droplet size is controlled by the breakage processes and the effect of coalescence on affecting the droplet size is insignificant.

$$d_{32}/D = A'N^{\alpha'}$$

(5.6)

The correlations of d_{32} with the impeller speeds using equation 5.6 are summarised in Table 5.3.

Table 5.3 Correlation of d_{32} and impeller speed

Concentration of $BmimBF_4$	A'	α'	R^2 value	*Re*
0 wt.%	10.70	-1.1	0.94	14468-24133
1 wt.%	12.94	-1.3	0.93	14733-24641
5 wt.%	0.04	-0.2	0.93	16511-27549
10 wt.%	0.02	-0.1	0.96	14619-24385
30 wt.%	0.03	-0.2	0.94	10169-16963
50 wt.%	0.03	-0.2	0.93	6683-11147
100 wt.%	0.02	-0.1	0.95	200-334

As can be found in Table 5.3, the coefficient of determination (R^2) is larger than 90% in all cases indicating that the regression line fitted well with the experimental data. The exponential value (α') is -1.1 and -1.3 for 0 wt.% and 1 wt.% ionic liquid solutions respectively, which is close to the theoretical value of -1.2. As the exponential value (α') for 0 wt.% and 1 wt.% ionic liquid solutions fits well with the equation 5.6, it implies that the breakage of the bubbles dominates the process of gas dispersion in 0 wt.% and 1 wt.% ionic liquid solutions (Martín et al., 2008, Pacek et al., 1998).

With the increasing ionic liquid concentration from 5 wt.% to 100 wt.%, the exponential values (α') varied between -0.1 and -0.2. These exponential values are much larger than the theoretical value of being -1.2 indicating that the theoretical equation (equation 5.6) failed to predict the bubble Sauter mean diameter when ionic liquid solutions with larger concentration (more than 5 wt.%) are operated in stirred tank. This also implies that the bubbles behave differently in ionic liquid solutions with larger concentrations compared with conventional solvents. The exponential values (α') varied between -0.1 and -0.2 may indicate that both the bubble breakage and coalescence process determine the bubble size in the ionic liquid solutions with concentration larger than 5 wt.%.

5.4.2 The Effect of Gassing Rate on Bubble Size

The Sauter mean diameter of the bubbles in the pure water, pure ionic liquid and with 10 wt.% concentration of the ionic liquid solution under various gassing rates is shown in Figure 5.17. And Figure 5.18 gives a detailed comparison of the Sauter mean diameters under all conditions investigated. As can be found in these figures, the increasing gas flow rate results in increasing bubble diameter when the pure water or pure ionic liquid is used as the operation liquid. While slight reduction of the bubble size can be observed in the ionic liquids solutions with concentrations from 1 wt.% to 50 wt.%.

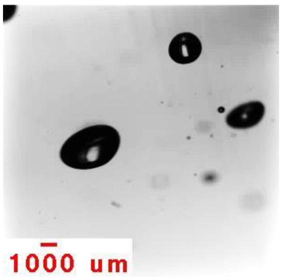

(a) 0 wt.%, 150 rpm, 0.1 L/min

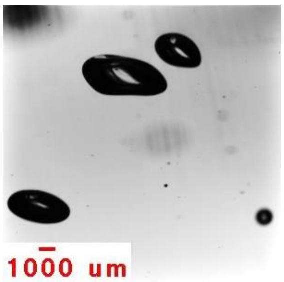

(b) 0 wt.%, 150 rpm, 0.2 L/min

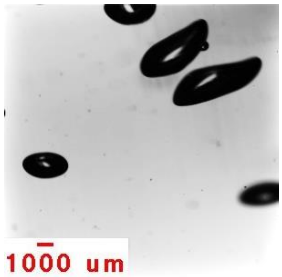

(c) 0 wt.%, 150 rpm, 0.3 L/min

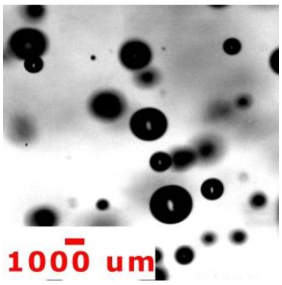

(d) 10 wt.%, 150 rpm, 0.1 L/min

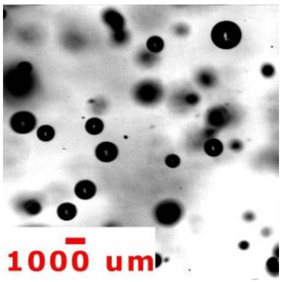

(e) 10 wt.%, 150 rpm, 0.2 L/min

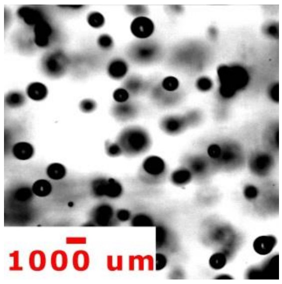

(f) 10 wt.%, 150 rpm, 0.3 L/min

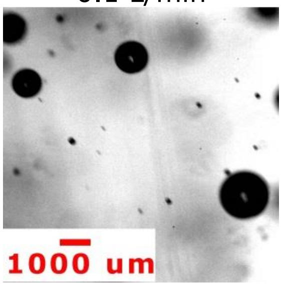

(g) 100 wt.%, 150 rpm, 0.1 L/min

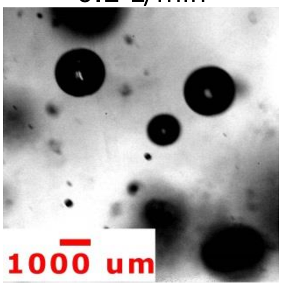

(h) 100 wt.%, 150 rpm, 0.2 L/min

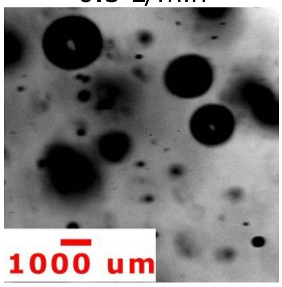

(i) 100 wt.%, 150 rpm, 0.3 L/min

Figure 5.17 Sauter mean diameter of ionic liquid solutions at different gas flow rates

It is reported that the coalescence of bubbles is dependent on the collision rate, as the increasing gassing rate enhances the bubble collision frequency and thus improves bubble coalescence (Paul et al., 2004). The faster is the gas flow rate, the higher is the collision probability. Therefore, the bubble size increases with the increasing gas flow rate in the gas-water multiphase flow system. Same trend is observed in the gas-pure ionic liquid system that the bubbles size increases with the increasing gas flow rate. This attributes to the high viscosity of the ionic liquid which hinders the capability of impeller dispersion of the gas phase and the flows turbulence (Stamatoudis and Tavlarides, 1985), which lead to the decrease of the bubble breakage rate. The collision probability is enhanced with the increasing gas flow rate, which consequently results in forming large bubbles. Therefore, the Sauter mean bubble dimeter is increased with the increasing gas flow rate, which reduces the mass transfer rate of the gas-liquid multiphase flow system.

However, the measured d_{32} of the bubbles in the ionic liquid solutions (from 1 wt.% to 50 wt.%) is contradictory to the above theory on that with the growing gassing rate, the bubble size decreased slightly when these aqueous solutions are served as the operation liquid (in Figure 5.18). Nevertheless, this decreasing trend shown in Figure 5.18 is very similar to the experimental results obtained by Asari and Hormozi (2013) where a decrease of bubble size was identified with an increase in the gas flow rate in a surfactant-water system in a bubble column. The reduction of bubble size may attribute to the drop of the solution surface tension with the increasing concentration of pure ionic liquid. The decrease of solution surface tension means that less energy is required to break the large bubbles consequently smaller bubbles are formed. In addition, the rise of gas flow rate gives rise to higher liquid velocity resulting in the enhancement of the turbulent intensity (Asari and Hormozi, 2013). Thus the bubble breakage is intensified by the greater turbulence and the numbers of small bubbles are increased, which results in smaller mean bubble size.

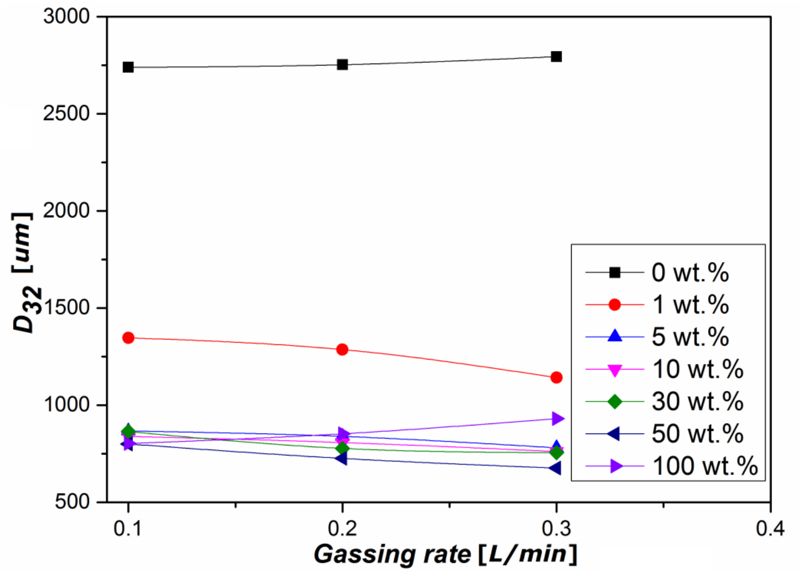

Figure 5.18 Sauter mean diameter at different gassing rates (impeller speed=150 rpm)

5.4.3 The Effect of Liquid Physical Properties on Bubble Size

This section discusses the effect of the liquid physical properties including the viscosity and surface tension on the bubble size in the ionic liquid aqueous solutions in the stirred tank.

There are no unanimous conclusions in terms of the effect of liquid viscosity on the bubble size in the literatures. For example, Martín et al. (2010) and Khurana and Kumar (1969) found that the increased viscosity of operation liquid results in the increase of bubble size in the solutions. Puthli et al. (2005) noted that the increased viscosity dampens turbulent eddies, therefore sufficiently higher energy is required to overcome the resistance of the viscous layer to break the bubbles. As a result, with increasing liquid viscosity, the bubble coalescence is enhanced, the bubble breakage is confined and the bubble size is increased. However, Benzing and Myers (1955) stated that the viscosity of liquid has very slight effect on the bubble size, which can be ignored. Bondarev and Romanov (1973) noted that the bubble size is independent on viscosity of liquids with low viscosity.

As has been shown in Figure 5.4 in section 5.3.1, there was little change in solution viscosities when the concentration of $BmimBF_4$ increased from 0 wt.% to 50wt.%. However, as shown in Figure 5.19, the bubble Sauter mean diameter decreases significantly with the increasing ionic liquid concentration from 0 wt.% to 5 wt.%, and further increase of ionic liquid concentration from 5 wt.% to 100 wt.% does not cause significant change on the bubble size. Therefore, in this investigation, it seems the viscosity of ionic liquid solutions has little effect on the bubble size.

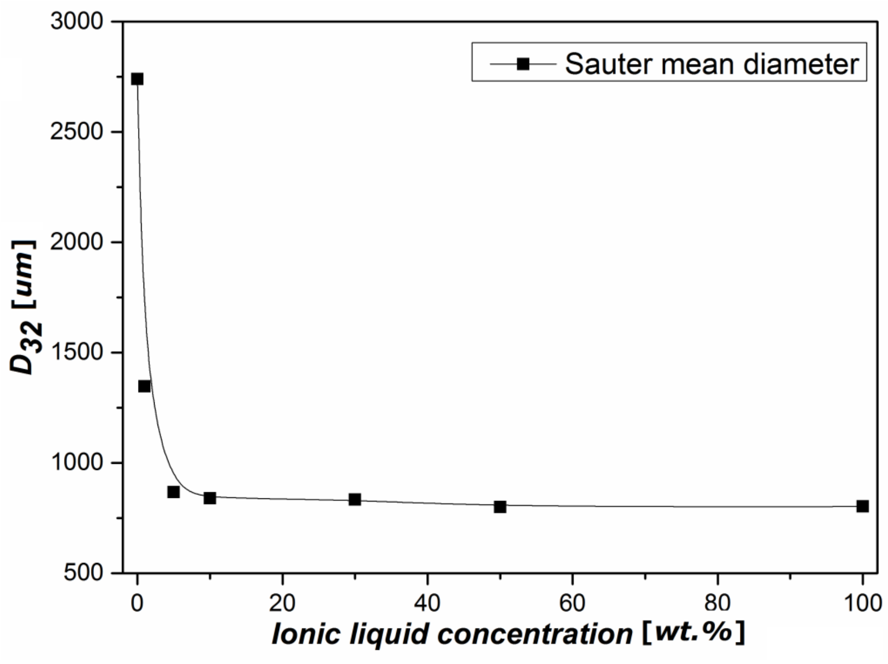

Figure 5.19 Sauter mean diameter at different ionic liquid solutions (impeller speed=150 rpm, gassing rate=0.1 L/min)

Similar to the non-unanimous conclusions on whether the liquid viscosity can decrease or increase the bubble size in the solutions, there are no unanimous conclusions on the effect of ionic liquid surface tension on the bubble size in it in literatures. For example, Schmidt et al. (2006) stated that in order to deform and break large bubbles, the total local shear stress imposed by the continuous phase must overcome the surface tension force and the viscous stress inside the droplets. The decrease of surface tension and disperse phase viscosity will lead to higher bubble breakage probabilities, hence reducing the bubble size. Wang et al. (2010b) studied the bubble size in different ionic liquids in a bubble column. They noted that if the ionic liquids with similar viscosity were used as operation liquids, smaller bubble can be found in ionic liquid with lower surface tension. While other researchers such as Zhang et al. (2012) found that the ionic liquid viscosity plays a leading role in affecting the bubble size in it, while the effect of surface tension seems to be less.

In order to show the effect of solution surface tension on the bubble size, the values of d_{32} in the ionic liquid aqueous solutions is plotted against the corresponding surface tension of the solutions as displayed in Figure 5.20. As can be observed from this figure, generally the bubble size is decreasing sharply with the decreasing ionic liquid surface tension from 71.8 mN/m to 52.8 mN/m, and stays relatively stable afterward with the surface tension ranges from 47.5 mN/m to 43.9 mN/m. Therefore, it may imply that the surface tension of the ionic liquid aqueous solutions plays more important role than the viscosity in determining the bubble size in the ionic liquid aqueous solutions.

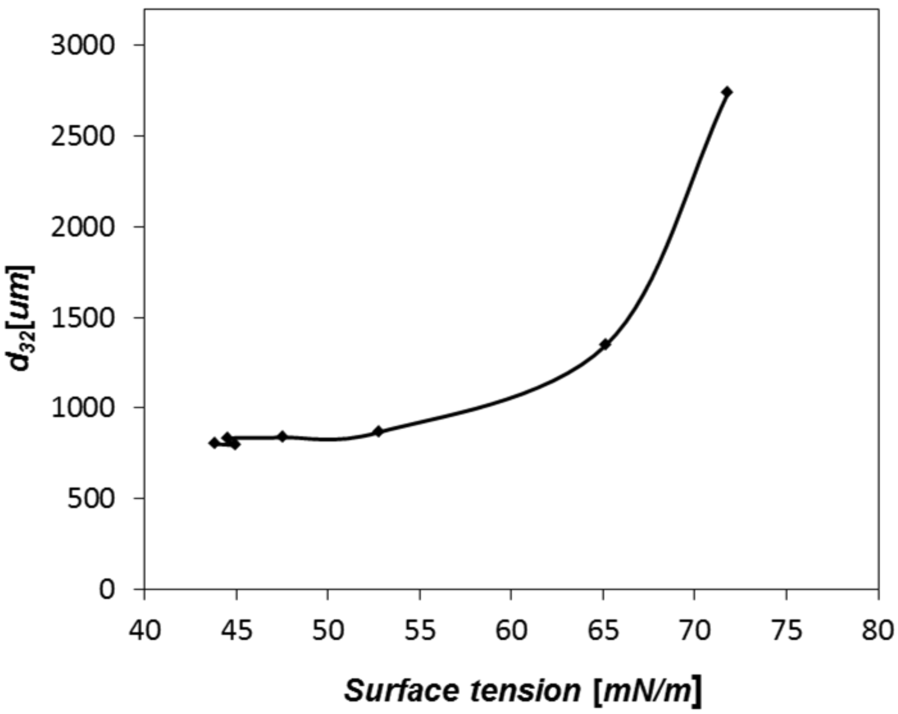

Figure 5.20 Sauter mean diameter at different surface tension of the ionic liquid solutions

5.5 Conclusions

The physical properties such as the viscosity, surface tension and density of ionic liquid $BmimBF_4$ solutions (0 wt.%, 1 wt.%, 5 wt.%, 10 wt.%, 30 wt.%, 50 wt.%, 100 wt.%) were measured at room temperature (25℃). The measurement of viscosity showed that the ionic solutions exhibit Newtonian fluid behaviour. The increase of concentration of $BmimBF_4$ from 0 wt.% to 90 wt.% has little effect on the increase of solutions viscosity, while sharp growth of viscosity was found as the $BmimBF_4$ concentration increased from 90 wt.% to 100 wt.%. The $BmimBF_4$ solutions showed sharp decrease in surface tension as the concentration of $BmimBF_4$ increased from 0 wt.% to 10 wt.%. However further increase of ionic liquid concentration has no significant effect on solutions surface tension.

The density of ionic liquid solutions was almost in linear relationship with the growth of $BmimBF_4$ concentration.

High speed camera was used to study the bubble size in the gas-ionic liquid system in stirred tank. The $BmimBF_4$ was operated at different impeller speeds (150 rpm, 200 rpm and 250 rpm) and gas flow rates (0.1 L/min, 0.2 L/min and 0.3 L/min) respectively. Sauter mean diameter (d_{32}) was used to characterise the bubble size. It showed that more large bubbles were found in the pure water. Stable and small bubbles were identified in $BmimBF_4$ solutions with concentrations range from 1 wt.% to 100 wt.%. With the increasing impeller speed, the bubble size was found to decrease in all $BmimBF_4$ solutions.

The impeller speed was correlated with $d_{32.}$ The correlation showed agreement with theoretical equation at low $BmimBF_4$ concentration (0 wt.% and 1 wt.%), where the theoretical exponential value is -1.2. However with increasing ionic liquid concentration, the theoretical equation failed to estimate the bubble size in the ionic liquid solutions. This equation assumes that the droplet Sauter mean diameter is proportional to the maximum stable droplet size in stirred tank in turbulent flow where the droplet size is controlled by the breakage processes and the effect of the coalescence on affecting the droplet size is insignificant. It can be concluded that the bubble size in the pure water and low $BmimBF_4$ concentration (1 wt.%) is mainly controlled by bubble breakage and the effect of bubble coalescence was not significant. But with increasing ionic liquid concentration, both the bubble breakage and coalescence has significant effect on determining bubble size.

The effect of the gas flow rate on the bubble size in the ionic liquid solutions was studied. It indicated that the increasing gas flow rate caused the increase of bubble size when pure water or pure $BmimBF_4$ were used as the operation liquid. While slight reduction of bubble size was found as the gas flow rate increases in the $BmimBF_4$ solutions with their concentrations ranging from 1 wt.% to 50 wt.%.

The effects of physical properties of ionic liquid solutions such as the viscosity and surface tension on affecting the bubble size in them were analysed. According to this experiment, the surface tension of the ionic liquid aqueous solutions seems to play more important role than the viscosity in determining the bubble size in the ionic liquid aqueous solutions.

CHAPTER 6: MODELLING OF GAS-IONIC LIQUID MULTIPHASE FLOW IN STIRRED TANK

6.1 Introduction

Stirred tanks are widely used for gas dispersion in industrial mixing (Zhang et al., 2009). The main aim of mixing is to improve the mass transfer efficiency of the gas-liquid multiphase flows in the stirred tanks, which is often influenced by the bubble size, volume fraction of dispersed phase, turbulence level, physical properties of operation liquid, and operation conditions such as impeller and vessel design, gassing rate and flow velocity (Sajjadi et al., 2012). The inefficient mixing in the stirred tank will result in poor yields, which require disposal or unproductive downstream processing and excessive costs hence reducing the profitability (Mueller and Dudukovic, 2010). The better understandings of the fluid flows inside the multiphase stirred tank will enable better stirred tank design and process optimization, therefore maximize the stirred tank mixing performance, decrease the wastes result from the inadequate stirred vessel design, and increase the profitability.

Since it is hard to experimentally obtain all parameters involved in the mixing process, the computational fluid dynamics (CFD) can serve as an alternative tool to provide insights into the mixing process, which offers valuable information for optimisation and design of the mixing process (Patel et al., 2010). So far, the CFD modelling of single phase and multiphase flow in the stirred tanks mainly focus on the water being served as the operation liquid. This available knowledge on the gas-water multiphase flow in literatures may not be transferred directly to the hydrodynamics behaviours of the gas-ionic liquid flow in the stirred tank due to the different flow behaviours between the ionic liquids and water when they are agitated. The study on the modelling of gas-ionic liquid multiphase flow in the stirred tanks is still very rare in the literature. To fill this research gap, this chapter therefore attempts to provide knowledge on the hydrodynamics of the gas-ionic liquid multiphase flow in the stirred tank.

6.2 Modelling the Gas-Water Multiphase Flow in a Stirred Tank

In order to verify the multiphase flow modelling approaches and models used in this study, a more commonly used geometry of stirred tank from reference data (Montante et al., 2007) was created, and CFD simulation was carried out based on this tank for verification. Operation conditions such as the gas flow rate, impeller rotating speed and bubble size used in the verification case were the same as used by Montante et al. (2008). The Eulerian-Eulerian multiphase flow modelling approach, the RNG k-ε model, the Sliding Mesh method, Schiller-Naumann drag force coefficient model were used to simulate the gas-water multiphase flow in this tank geometry. The simulated results were compared with the PIV data from Montante et al. (2008). If the proposed multiphase flow simulation approaches and models were verified in modelling the turbulent gas-water flow, they can be then used for the gas-ionic liquid multiphase flow modelling in the stirred tank.

6.2.1 Geometry of Stirred Tank

The geometry of the stirred tank from Montante et al. (2007) for verifying the numerical models is a fully baffled flat bottom tank (T=236 mm) equipped with a Rushton turbine impeller (D=T/3=78.7 mm) placed at the distance C=T/2=118 mm from the tank bottom. The height of the liquid phase (H) before air injection equals to the tank diameter (T). The gas phase was introduced into the stirred tank through a tube fixed below the impeller with a nozzle being C_{spa}=T/4=59 mm from the tank bottom. Figure 6.1 and Figure 6.2 show the detailed geometry dimension of the stirred tank. The operation liquid was water. The impeller speed and gas flow rate were controlled at 450 rpm and 0.02 vvm (gas volume/culture volume/min) respectively, which are the same operation conditions used in the study carried out by Montante et al. (2008). The flow was operated in the fully developed turbulent state.

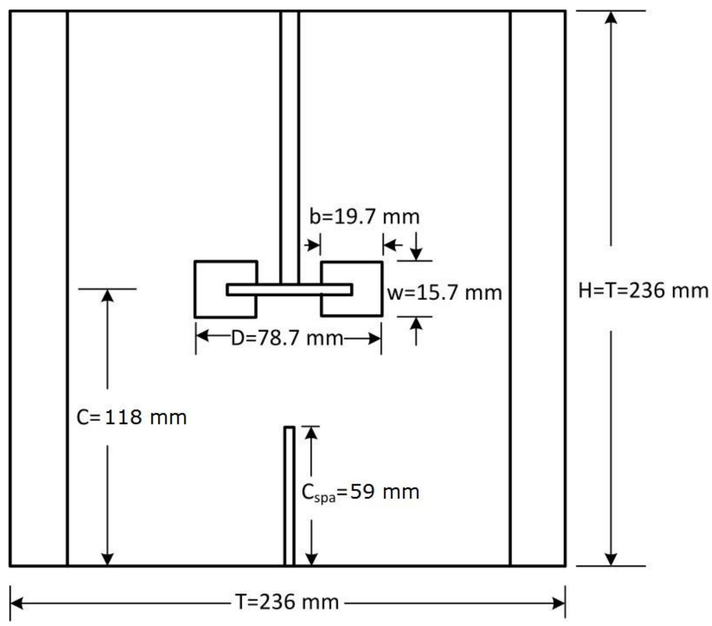

Figure 6.1 Geometry of the stirred tank (side view)

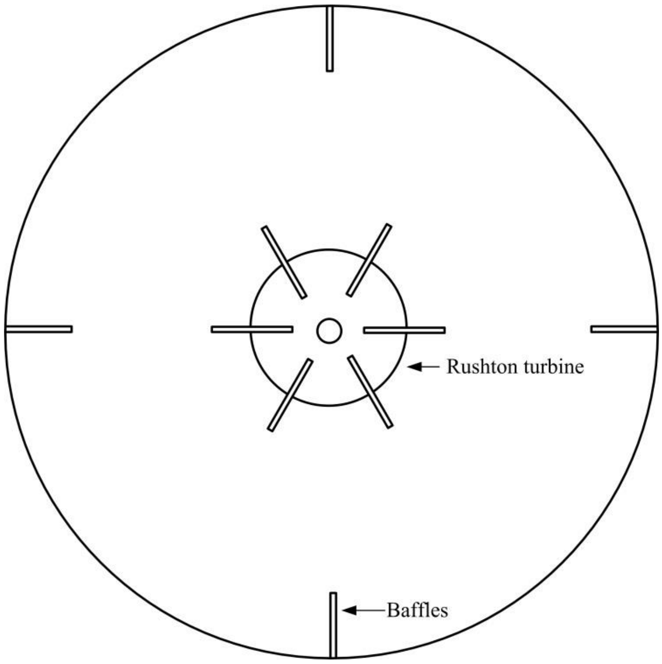

Figure 6.2 Geometry of the stirred tank (top view)

6.2.2 Numerical Modelling Methods

The Eulerian-Eulerian approach was used to simulate the gas-water multiphase flow in the stirred tank, where the flow domain was considered as interpenetrating continua interacting by the interphase transfer terms. The continuity and momentum equations were solved for each phase:

$$\frac{\partial(\alpha_i\rho_i)}{\partial t} + \nabla\cdot(\alpha_i\rho_i\vec{u}_i) = 0 \tag{6.1}$$

$$\frac{\partial(\alpha_i\rho_i\vec{u}_i)}{\partial t} + \nabla\cdot(\alpha_i\rho_i\vec{u}_i\vec{u}_i) = -\nabla\cdot(\alpha_i p) + \nabla\cdot\bar{\bar{\tau}}_{eff,i} + \vec{F}_i + \alpha_i\rho_i\vec{g} \tag{6.2}$$

where ρ is the fluid density, t is the time, $\vec{u}$ is the flow velocity vector. α is the phase volume fraction. The subscript $i = l$ indicates liquid phase and

$i = g$ indicates gas phase. $\vec{F}_i$ is the interphase force, p is the pressure, the modified pressure P' will be used instead. The equation is:

$$P' = p + \frac{2}{3}\mu_{eff}\nabla \cdot \vec{u}_l + \frac{2}{3}\rho_l k_l$$

(6.3)

where μ_{eff} is the effective viscosity of the liquid phase which can be obtained through the RNG *k*-*ε* model. Its equation is showing below:

$$\mu_{eff} = \rho_l C_u \frac{k^2}{\varepsilon} + \rho_l C_{u,b}\alpha_g d_b |\vec{u}_g - \vec{u}_l|$$

(6.4)

where C_u and $C_{u,b}$ are model constants, their values are 0.0845 and 1.0 respectively. d_b is the mean bubble diameter. $\bar{\bar{\tau}}_{eff,i}$ is the Reynolds stresses. The Boussinesq hypothesis which relates the Reynolds stresses to the mean velocity gradients was applied:

$$\bar{\bar{\tau}}_{eff,i} = \alpha_i\left[\mu_{eff}(\nabla\vec{u}_i + \nabla\vec{u}_i^T) - \frac{2}{3}\rho_i k_i \vec{I}\right]$$

(6.5)

where k is the turbulent kinetic energy per unit mass and $\vec{I}$ is the unit vector.

The widely used standard *k*-*ε* model is suitable to simulate the flow in a fully developed turbulence status. The ionic liquid-gas multiphase flow in the stirred tank is operated in the transitional state (240<*Re*<400) in this investigation, therefore the standard *k*-*ε* model may not be applicable here. Since there are insignificant differences among the simulation results in terms of the flow pattern and flow velocities when the standard *k*-*ε* model and the RNG *k*-*ε* model were adopted in the turbulent flow modelling respectively (Aubin et al., 2004, Deglon and Meyer, 2006) and the RNG *k*-*ε* model yields better results than the standard *k*-*ε* model when it was used for modelling the transitional flows (Jaworski et al., 1996), the RNG *k*-*ε* model was used here to closure the RANS equations used in the gas-water and gas ionic liquid multiphase flow simulations as following:

$$\frac{\partial(\rho k)}{\partial t}+\frac{\partial}{\partial x_i}(\rho k\vec{u}_i)==\frac{\partial}{\partial x_j}\left(\sigma_k(\mu+\mu_t)\frac{\partial k}{\partial x_j}\right)+G_k-\rho\varepsilon \tag{6.6}$$

$$\frac{\partial(\rho\varepsilon)}{\partial t}+\frac{\partial}{\partial x_i}(\rho\varepsilon\vec{u}_i)=\frac{\partial}{\partial x_j}\left(\sigma_\varepsilon(\mu+\mu_t)\frac{\partial\varepsilon}{\partial x_j}\right)+C_{\varepsilon1}\frac{\varepsilon}{k}G_k-C^*_{\varepsilon2}\rho\frac{\varepsilon^2}{k} \tag{6.7}$$

where $C^*_{\varepsilon2}=C_{\varepsilon2}+\frac{C_u\eta^3(1-\eta/\eta_0)}{1+\beta\eta^3}$ and $\eta=Sk/\varepsilon$ and $S=(2S_{ij}S_{ij})^{0.5}$. The models constants, $\sigma_k=0.7194$, $\sigma_\varepsilon=0.7149$, $\eta_0=4.38$, $\beta=0.012$, $C_{\varepsilon1}=1.42$ and $C_{\varepsilon2}=1.68$.

The RNG *k*-*ε* mode includes a differential formulation of the turbulent viscosity (μ_t) that is supposed to account for the low Reynolds number effects:

$$d\left(\frac{\rho^2k}{\sqrt{\varepsilon\mu}}\right)=1.72\frac{\hat{v}}{\sqrt{\hat{v}^3-1+C_v}}d\hat{v}$$

(6.8)

where $\hat{\nu} = \frac{\mu+\mu_t}{\mu}$, $C_\nu \approx 100$.

The equation 6.8 is integrated to obtain an accurate expression of how the effective turbulent transport varies with the effective Reynolds number allowing the model to better handle flows at low Reynolds number. In the flows at high Reynolds number, the turbulent viscosity (μ_t) is calculated in the same approach as it is in the standard *k*-*ε* model (ANSYS, 2011a).

The Multiple Reference Frame (MRF) and Sliding Mesh (SM) method was used to model the rotational impeller in the steady state and transient simulation respectively.

As has been reviewed and discussed in the chapter 2, the drag force is the dominant force among the interphase forces. The drag force coefficient (C_D) model proposed by Schiller and Naumanna (1935), which showed excellent agreements with the experimental measured drag force coefficient in different flow regimes ($0.1 \leq Re_r \leq 10000$) (Marshall and Li, 2014), was adopted here.

$$C_D = \begin{cases} \dfrac{24\left(1 + 0.15{Re_r}^{0.687}\right)}{Re_r} & Re_r \leq 1000 \\ 0.44 & Re_r > 1000 \end{cases}$$

(6.9)

where Re_r is the relative Reynolds number is defined as $Re_r = \frac{d_b \rho_l |u_g - u_l|}{\mu_l}$.

In order to speed up the convergence and save the simulation time, the single phase water flow steady state modelling was carried out first to get the initial water flow condition. The gas phase was then introduced from the sparger and transient simulation was employed. The velocity inlet boundary condition was adopted at the nozzle of the sparger. Degassing boundary condition was applied to the tank cover, where only the gas phase can escape from the liquid surface. The bubble size was set as 1 mm in diameter according to the experimental study carried out by Montante et al. (2008).

6.2.3 Model Verifications

Figure 6.3 shows the water phase velocity vectors at a vertical plane passing through two adjacent baffles in the stirred tank. The water phase flow vectors show the typical flow pattern stirred by a Rushton turbine in the stirred tank, which is characterised by a classic double-loop structure in the region above and below the impeller. Compared with the single phase water flow vectors in Figure 6.4, the presence of gas at this gassing rate (0.02 vvm) does not cause significant change of the liquid phase flow pattern. The result is very similar to the PIV result obtained by Montante et al. (2007).

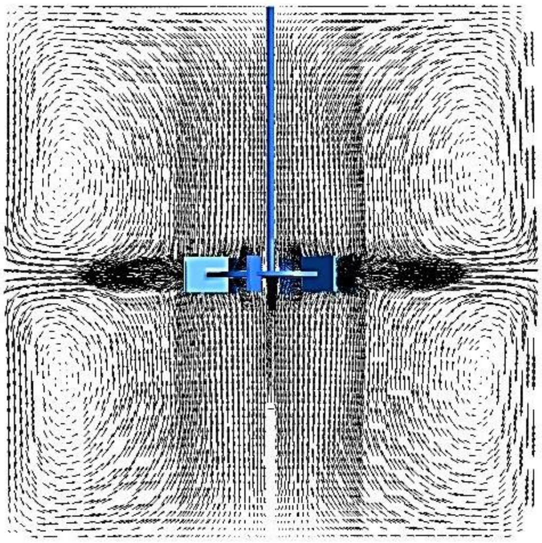

Figure 6.3 Flow vectors of the water phase (two-phase)

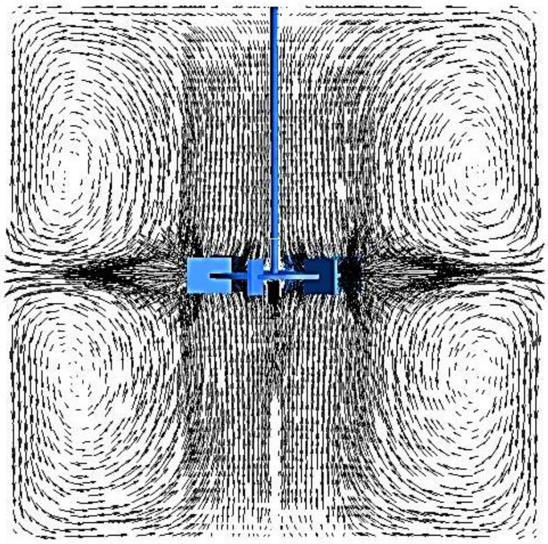

Figure 6.4 Flow vectors of the water (single phase)

However, obvious differences can be identified between gas phase and water phase. As shown in Figure 6.5, compared with the vectors of water phase in the multiphase flow (in Figure 6.3), the intensity of the gas phase downward circulation loops has reduced a lot. As the length of the vector is proportional to the velocity magnitude, Figure 6.5 indicates that there is little gas circulated in the region below the impeller disk.

Compared with upper region, the gas dispersion is poor below the impeller under current operation conditions.

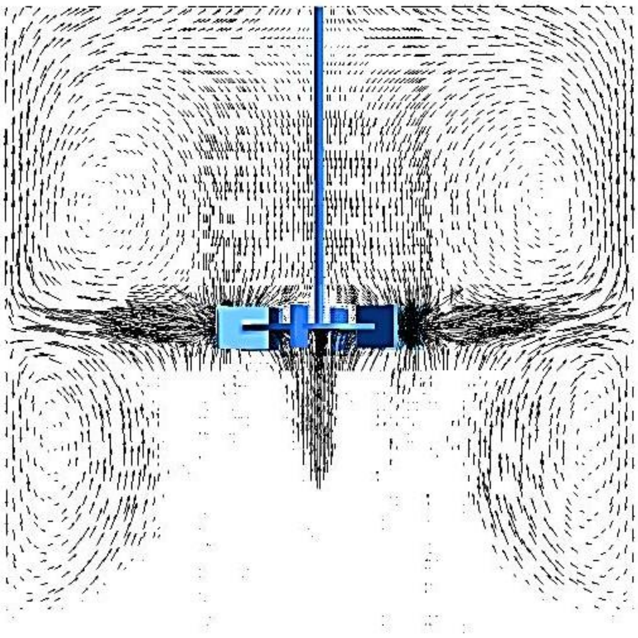

Figure 6.5 Flow vectors of the gas phase

The volume fraction of gas phase in the stirred tank is shown in Figure 6.6. As can be observed from this figure, more gas is distributed in the upper circulation regions. Due to the low pressure regions at the back side of the Rushton turbine impeller blades, high volume fraction of gas phase can be identified around the impeller blades. Compared with the upper circulation regions, except for the location where the gas is introduced, the gas volume fraction is very low in the lower circulation areas. Only a little gas is accumulated in the vortex cores of the lower circulation loops due to the low pressure regions here. This feature of gas hold-up is very similar to the experiment results carried out by Montante et al. (2008).

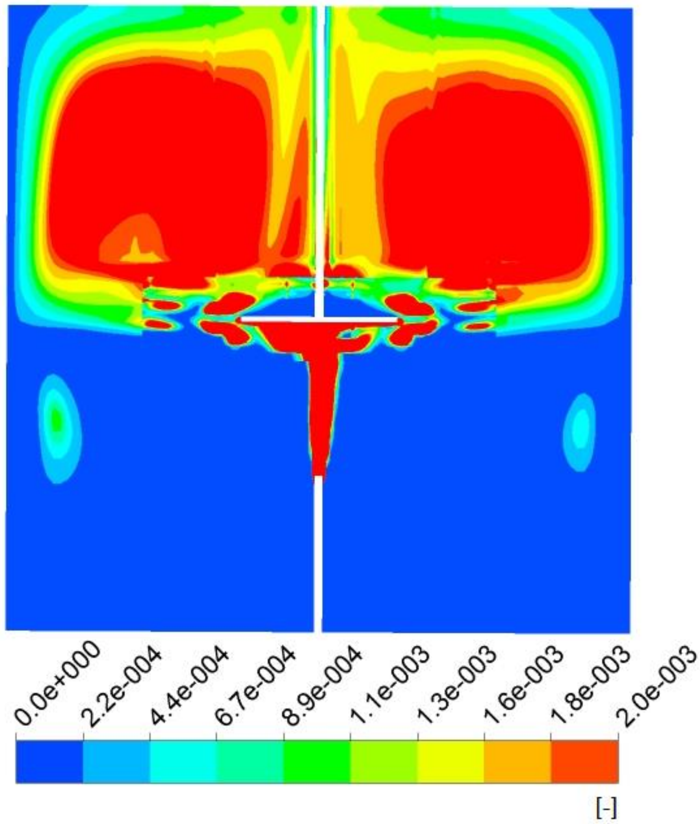

Figure 6.6 Contours of gas volume fraction distributions

The simulated mean axial and radial velocity profiles of liquid and gas phase were compared respectively with the PIV data from Montante et al. (2007) at selected locations (r/T=0.26). Figure 6.7 and Figure 6.8 show the liquid phase axial and radial velocity profiles in the axial direction, from the tank bottom to the tank top, at radial distance r=0.26T. Both the radial and axial velocities are normalized by the impeller tip velocity U_{tip}=1.85 m/s.

As can be found in Figure 6.7, the predicted liquid radial velocities show similar trend with the PIV data from Montante et al. (2007). The radial velocity profiles, especially in the impeller discharge region, are well predicted. The peak radial velocity predicted by the CFD modelling is 0.45U_{tip} which is very close to the PIV data of about 0.41U_{tip}. The simulated radial velocity profiles are a little higher than the PIV data in the region close to the tank bottom and tank top. Generally, the overall variation trend is very similar.

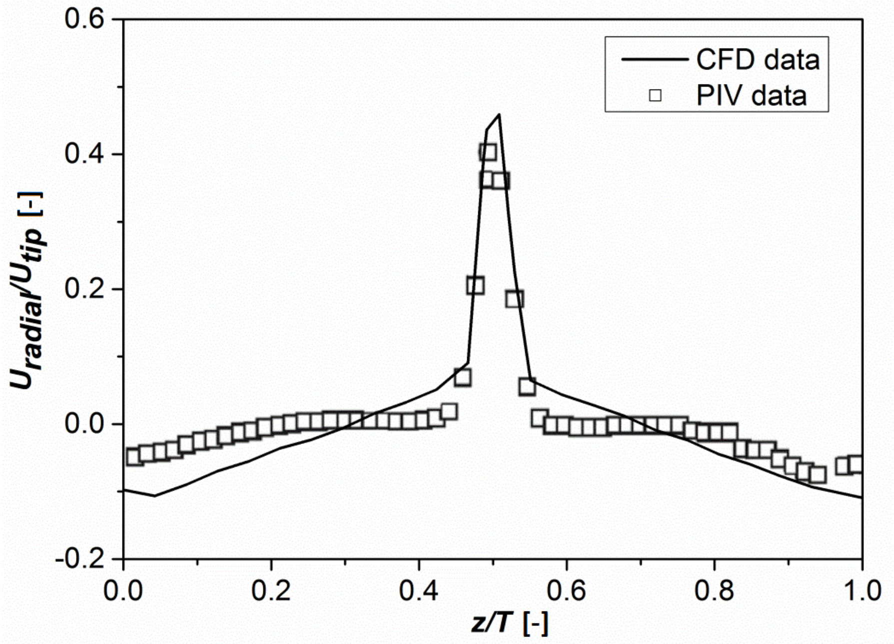

Figure 6.7 Mean radial velocity profiles (liquid phase)

Figure 6.8 shows the liquid axial velocity profiles in the axial direction at the radial location *r/T*=0.26. The experimental and CFD results show good agreement except that slight differences can be found in regions above and below the radial jet flow from the impeller (0.3≤z/T≤0.45 and 0.55≤z/T≤0.65). Figure 6.8 indicates that the axial velocity distributions at this sampling area are well predicted by the CFD modelling.

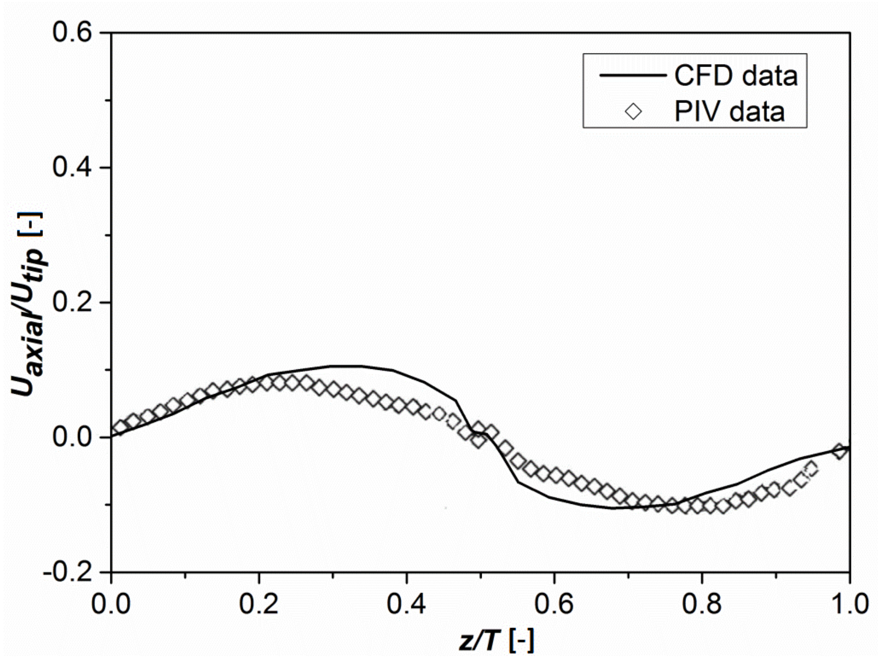

Figure 6.8 Mean axial velocity profiles (liquid phase)

The air entrainment from the liquid surface, the very strong intensity of reflected laser light from the liquid surface and from the tank bottom can affect the accuracy of the PIV measurement near these regions (Montante et al., 2008). Therefore, discrepancies between CFD and PIV results are identified in these areas. In addition, the turbulent flow in stirred tank especially in impeller discharge region is highly anisotropic (Ge et al., 2014). However, the isotropic assumption of the *k*-*ε* model would underestimate the velocity profiles in the impeller discharge regions (Lane, 2006).

The mono-sized bubble assumption employed in the multiphase modelling is not the main reason results in the discrepancy between the CFD and PIV data of the liquid phase flow velocities. Montante et al. (2008) suggested that the mono-sized bubble assumption has no significant effect on the CFD accuracy of the liquid phase flow modelling. In the study of Montante et al. (2008), they adopted both the mono-sized bubble assumption approach and the Population Balance Model (PBM) to simulate the gas-liquid flow in a stirred tank. By adopting the PBM approach, the bubbles were divided into 16 classes based on the range of their bubble size. Compared with their mono-sized bubble modelling, there was no significant improvement in predicting the liquid radial and axial velocities than when the Population Balance Model was used.

Figure 6.9 and Figure 6.10 describe the mean radial and axial gas velocities in the axial direction from the tank bottom to the liquid surface at the radial distance *r*=0.26*T*. As can be observed from Figure 6.9, the simulated gas peak radial velocity is 0.46U_{tip} which is very close to the measured value of about 0.44U_{tip}. The predicted mean gas radial velocities are in good agreement with the PIV data from Montante et al. (2008).

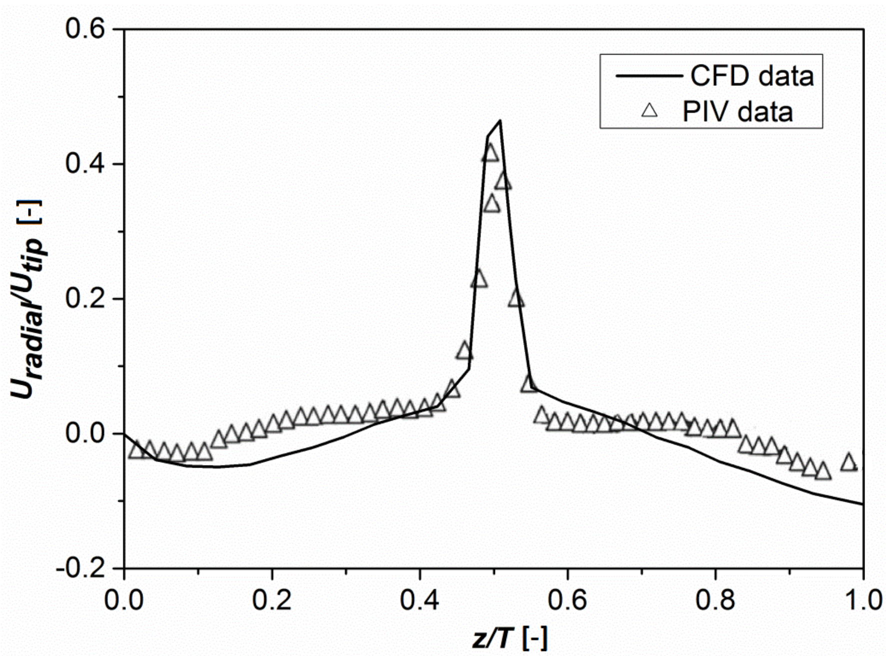

Figure 6.9 Mean radial velocity profiles (gas phase)

Figure 6.10 shows the simulated and measured mean axial velocity profiles of gas phase. As can be seen from this figure, the simulated gas axial velocities agree well with the PIV data in the impeller discharge region except that there is slight difference between CFD and PIV data in the area close to the tank bottom. The discrepancy found in gas flow modelling might be caused by the mono-sized bubble assumption used in this gas-liquid multiphase simulation. Since the bubble coalescence is apparent near the tank bottom when the downward gas flow encounters the rising bubbles, the bubbles size near tank bottom are larger than the mean bubble size used in this modelling. Whereas, due to the strong shear effect of rotating impeller blades in the impeller discharge region, the bubble size in this area is usually smaller than the mean bubble size in the stirred tank. Since the larger bubbles rise faster than the smaller ones in liquid flows (Kulkarni and Joshi, 2005), the predicted gas axial velocities in impeller discharge region are slightly higher than the PIV data and the simulated gas axial velocities near tank bottom are larger than the PIV results.

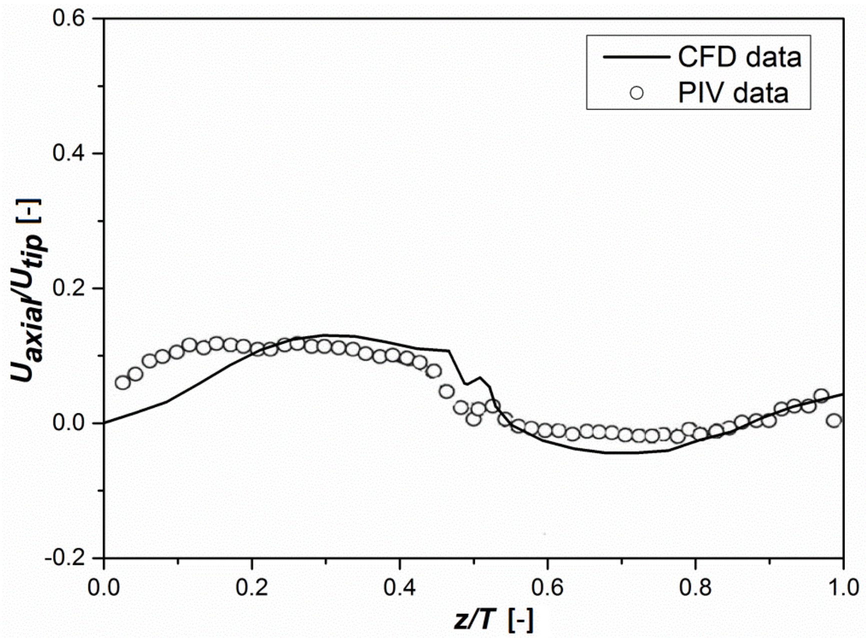

Figure 6.10 Mean axial velocity profiles (gas phase)

Based on the above discussions, the simulated results obtained by the current CFD models were compared with the PIV data from Montante et al. (2008) and showed good agreement. The Eulerian-Eulerian simulation approach, the RNG k-ε model, the MRF or SM method, the mono-sized bubble assumption and the drag force model etc. were verified and therefore can be used for further gas-ionic liquid multiphase flow modelling.

6.3 Modelling the Gas-ionic Liquid Multiphase Flow in the Stirred Tank

Since the single phase flow patterns in the DBD tank and DBB tank were very similar when the pure ionic liquid was agitated in these vessels, the gas-ionic liquid flow modelling was only carry out in the DBD tank. The pure ionic liquid ($BmimBF_4$) was chosen as the operation liquid and gas phase (hydrogen) was injected into the stirred tank through a sparger fixed below the impeller. The liquid phase and gas phase flow fields and the gas holdup, which relates to the mass transfer, at various impeller agitation speeds and gassing rates were numerically studied. The simulation results of the gas-ionic liquid multiphase flow were compared with the broadly studied gas-water turbulent flow in the stirred tanks, which provide knowledge for design and optimization of the gas-ionic liquid system in lab scale and industry.

6.3.1 Geometry of the Stirred Tank

The detailed dimension of the DBD tank is shown in Figure 6.11. This stirred tank is equipped with four baffles on the tank wall, and a Rushton turbine impeller is fixed in the tank centre. The baffles reach to the edge of the dished bottom. A gas tube is fixed below the impeller with the nozzle being C_{spa}=T/4=37.5 mm from the tank bottom.

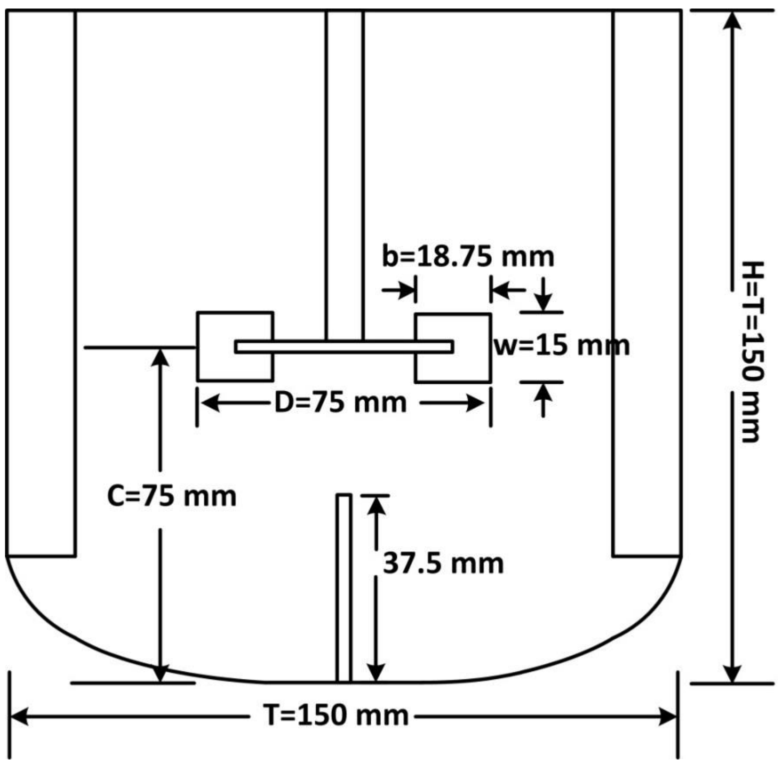

Figure 6.11 Geometry of the gas-liquid stirred tank

6.3.2 Numerical Modelling Methods

The Eulerian-Eulerian approach was used to simulate the gas-ionic liquid multiphase flow in the stirred tank, the continuity and momentum equations used here have been introduced in section 6.2.2. As the RNG *k*-*ε* model (showed in section 6.2.2) yields better results than the standard *k*-*ε* model when it was used for modelling the transitional flows (Jaworski et al., 1996), it was used here to close the governing equations.

In order to save the computation time and speed up the convergence of simulation, the steady state single phase simulation of the ionic liquid

($BmimBF_4$) was carried out first. The MRF method was used to model the rotating impeller. The steady state of the single phase flow was achieved when the residuals values of flow variables such as velocities, continuity, k and ε in numerical models dropped below 10^{-4}.

After the steady state of single phase flow modelling was achieved, the gas phase was then introduced from the sparger by adopting the velocity inlet boundary condition at the top surface of the sparger and the transient simulation was activated. The Sliding Mesh (SM) method was adopted to model the transient motion of the impeller in the stirred tank. The gassing rate of 0.1 L/min corresponding to 0.53 m/s gas inlet velocity at the sparger was used in simulation. The direction of the gas velocity was set normal to the gas inlet boundary and the gas volume fraction was specified as one here. The degassing boundary condition was applied to the liquid surface, which is treated as a stationary and flat frictionless wall where only the gas phase is allowed to escape from the liquid surface and the liquid phase will stay in the tank.

6.3.3 Judging Convergence

The time step (Δt) adopted in the transient simulation needs to be carefully selected. Longer time step at the start of the simulation will cause instability of the calculation and convergence difficulty. Very small time step will prolong the simulation time. Therefore, the following rules were considered to determine the time step used here (ANSYS, 2011b):

- The time step should be set at least one order of magnitude smaller than the smallest time constant in the system being modelled.

- Observe the number of iterations needed for convergence at each time step. The suggested number of iterations at each time step is around 5-10.
- For model contains rotor and stator, around 20 time steps are needed between each blade passing.

Based on the above rules, a time step of 0.002 s was used in this transient gas-ionic liquid simulation which would ensure accuracy of the solution. By applying this time step, about 9 iterations were identified at each time step and less than 30 time steps were performed at each blade passing.

The residual curves for velocity components, continuity, k, ε and gas phase volume fraction at the end of each time step showed three orders smaller than that at the beginning of the time step, which implies a good level of convergence (ANSYS, 2011b, Hartmann et al., 2004). In this case, the gas-ionic liquid multiphase flow simulation was running at a steady state by monitoring the residuals values dropped below 10^{-4} at each time step. In addition, the gas mass flow rate at the gas inlet and outlet were monitored and found almost identical indicating a good convergence. The simulation of the transient multiphase flow is very time consuming and each case costs about 60 days to complete corresponding to 130 s of impeller rotating time to achieve its steady state.

6.3.4 Flow Patterns in Conditions with and without the Gas Phase

The flow pattern of the liquid phase has significant influence on the bubbles behaviours in stirred vessels (Lane et al., 2002). And the gas flow pattern controls the degree of gas recirculation and back-mixing of the gas phase hence determining the concentration of driving force for mass transfer in gas-liquid flow in stirred tanks. The gas flow pattern also affects the liquid phase macro circulation and homogeneous mixing (Paul et al., 2004). Therefore, the ionic liquid phase flow pattern in conditions with and without gas, and the gas flow pattern were simulated and compared in this section.

6.3.4.1 Flow Vectors of the Liquid Phase and the Gas Phase

A vertical plane passing through the midway between two adjacent baffles was selected to show the multiphase flow fields. The flow filed velocity vectors of each phase were displayed at this plane.

The single phase ionic liquid flow field in the stirred tank has already been introduced in the chapter 4 and will not describe here. Figure 6.12 and Figure 6.13 show the vectors of the ionic liquid phase under conditions with and without gas injection respectively. As can be found in Figure 6.12 and Figure 6.13, the flow pattern of the liquid phase does change significantly due to the presence of gas phase. Both the lower and upper circulation loops are not able to drive the liquid near tank bottom and top, generating stagnant zones in these areas. Similar flow structures can be found when highly viscous fluid is agitated in stirred tanks (Bakker et al., 1997, Sungkorn et al., 2012).

Despite the similar flow patterns of ionic liquid phase in conditions with and without gas injection, slight different flow pattern can be observed in the region close to tank bottom. In the condition without gas injection, the ionic liquid moves at a low velocity near tank bottom, while when the gas is injected, the magnitude of the liquid phase velocity vectors in this region is further decreased. This phenomenon is caused by the large pressure difference between the front side and back side of the impeller blades, where bubbles accumulate in the low pressure regions behind the impeller blades. The accumulation of the bubbles behind impeller blades, which obstructs the liquid discharge from the impeller and reduces the impeller pumping ability and the intensity of flow circulations in the stirred tank (Lane et al., 2002, Paul et al., 2004).

The gas phase (in Figure 6.14) shows very similar flow pattern to the liquid phase. Figure 6.13 and Figure 6.14 shows that the velocity magnitudes of both phases are almost zero near the vessel bottom and dead zone is formed here due to the reduction of impeller pumping ability.

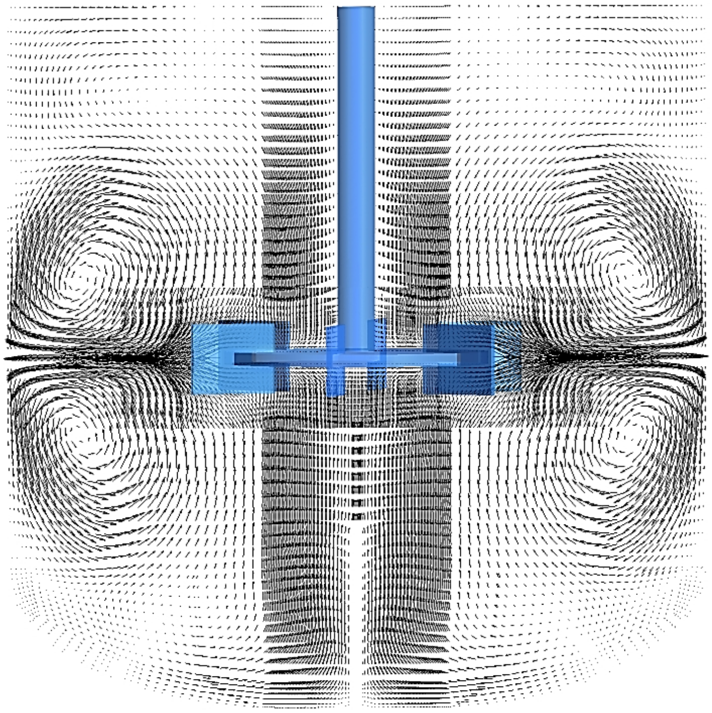

Figure 6.12 Flow vectors of the ungassed liquid phase (Impeller speed: 150 rpm)

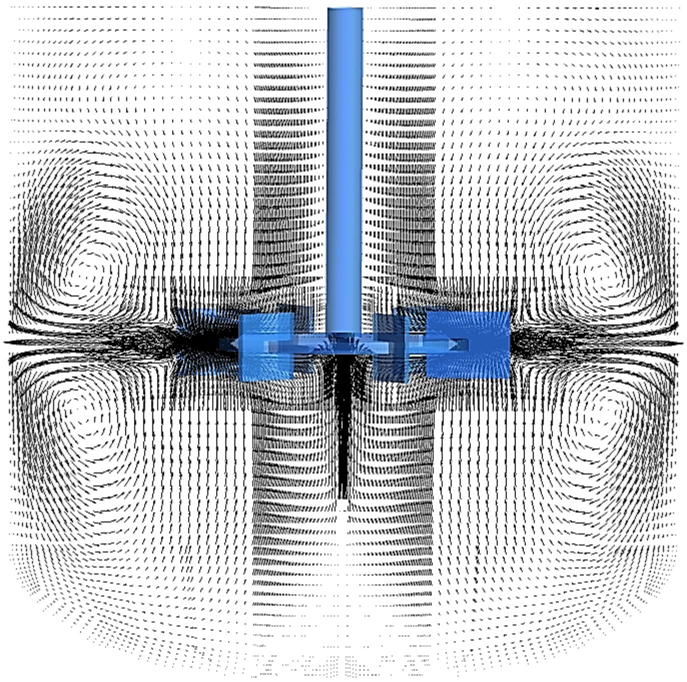

Figure 6.13 Flow vectors of the gassed ionic liquid phase (Impeller speed: 150 rpm; gassing rate: 0.1 L/min)

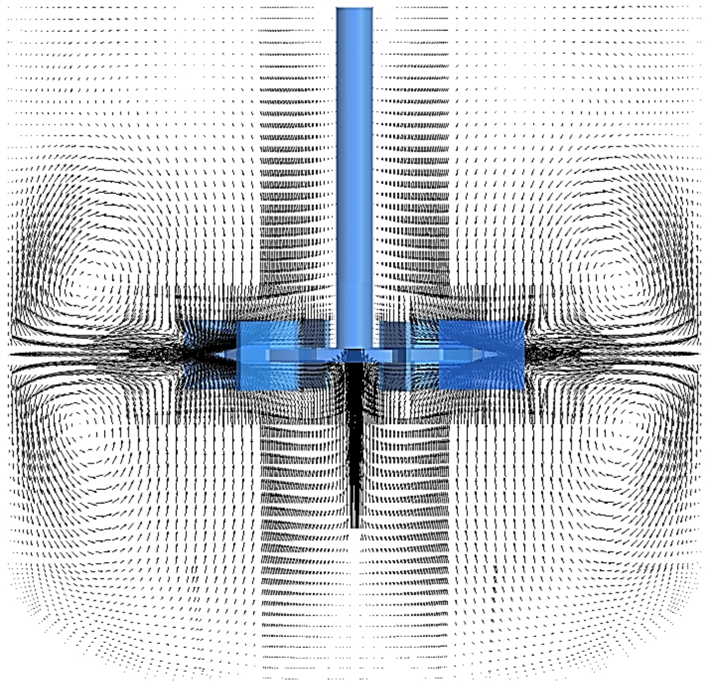

Figure 6.14 Flow vectors of the gas phase (Impeller speed: 150 rpm; gassing rate: 0.1 L/min)

Compared with the gas-water multiphase turbulent flow in the stirred tank, the gas phase in the ionic liquid (in Figure 6.14) shows different flow pattern.

As can be noticed in the flow vectors of the gas phase in the gas-water turbulent flow shown in Figure 6.5 in section 6.2.3, due to the effect of rising of bubbles, the gas phase radial jet flows from the impeller are slightly inclined upward after being thrust by the rotating impeller blades. Whereas the gas jet flows found in the gas-ionic liquid system flow almost radially towards the tank wall, which forms similar intensity of the upward and downward circulation loops. In addition, there is limited gas circulated in the downward circulation loops in the gas-water multiphase flow system. However, the gas in the gas-ionic liquid system follows well with the ionic liquid phase, which allows the gas to circulate well in the tank hence increasing the degree of homogeneous mixing and the mass transfer in the stirred tank.

6.3.4.2 Velocities of the Ionic Liquid with and without the Gas

In order to show the more detailed information of the presence of the gas phase on the liquid phase in the gas-ionic liquid multiphase flow fields in the stirred tank, the contours and the velocity profiles of the liquid phase flow fields at gassed and ungassed conditions were showed in this section.

The contours of the velocity magnitude of the ionic liquid flow at conditions with and without the gas injection are shown in Figure 6.15 and Figure 6.16. As can be observed from these two figures, the dead zone areas can be found near the corners of the tank top and tank bottom where the fluids are almost still in these regions. Figure 6.16 and Figure 6.17 show that both the gas phase and ionic liquid phase show similar velocity fields. Compared with the water turbulent flow in DBD tank (Figure 3.21), the dead zone area below the impeller disk has reduced a lot when the gas phase is introduced into the stirred tank.

The dead zone regions near the tank corners are mainly caused by the high viscosity of the ionic liquid agitated in stirred tank, which exerts higher resistance to the moving fluids (Doolittle, 1952). The radial jet flows from the impeller hit the vessel wall and separates into the flows into upward and downward directions. Due to the high resistance of surrounding liquids, both the upward and downward flows cannot reach to the tank bottom and tank wall. Consequently, stagnation regions are formed in the flow field and dead zones are developed. In addition, the presence of the gas phase causes the accumulation of bubbles behind the impeller blades, resulting in the reduction of the impeller energy input into the surrounding liquid phase. As a consequence, the intensity of the circulation loops has further decreased due to the introduction of the gas into the stirred tank.

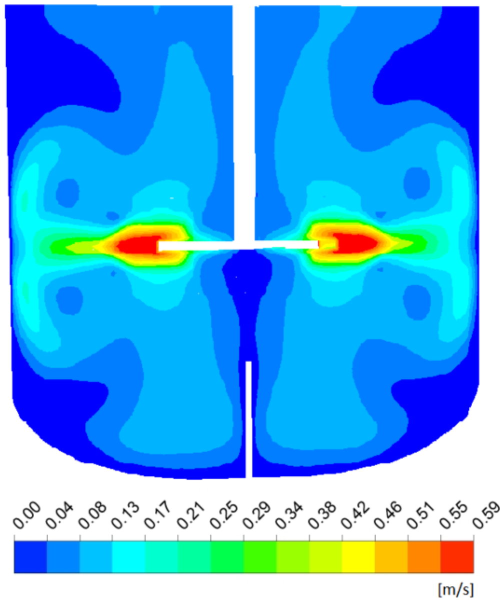

Figure 6.15 Contours of the ionic liquid velocity magnitude at ungassed condition (Impeller speed: 150 rpm)

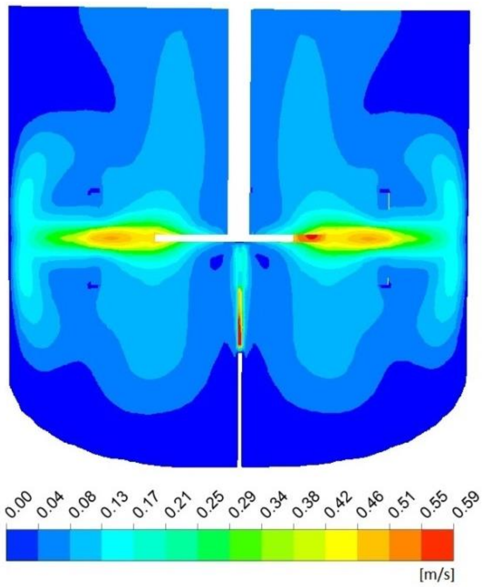

Figure 6.16 Contours of the ionic liquid velocity magnitude at gassed condition (Impeller speed: 150 rpm; Gassing rate: 0.1 L/min)

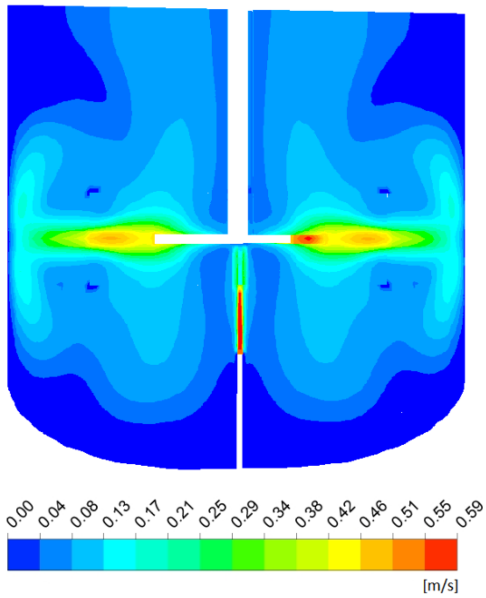

Figure 6.17 Contours of the gas velocity magnitude (Impeller speed: 150 rpm; Gassing rate: 0.1 L/min)

In order to carry out quantitative assessment of the ionic liquid flow field with and without gas injection, detailed comparisons of the mean ionic liquid velocity components with and without gas phase were made at selected regions in the stirred tank (in Figure 6.18). Focuses were paid in four horizontal planes: the impeller discharge region (z/H=0.5), the midway between the impeller and the tank bottom (z/H=0.27), the midway between the impeller and the tank top (z/H=0.73), and the region passing through the dead zone near the tank bottom (z/H=0.1). Simulation data were shown in the radial direction from the vessel centric line to the wall.

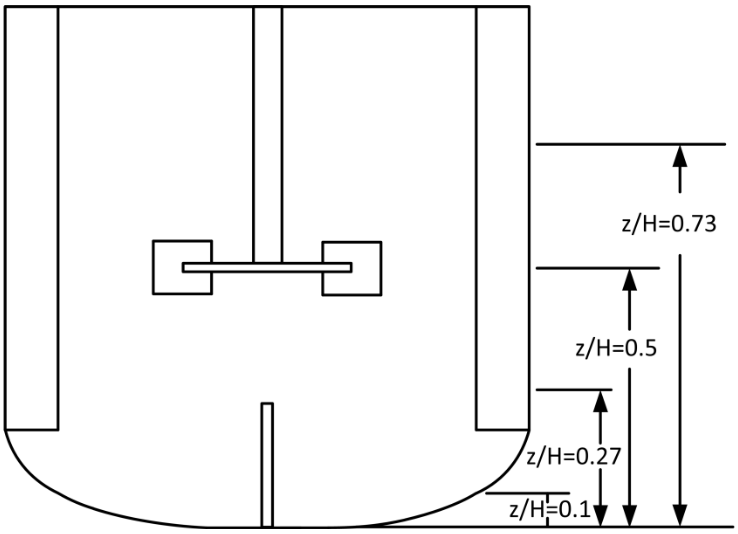

Figure 6.18 Data sampling regions in the stirred tank

Figure 6.19 to Figure 6.21 display the radial, axial and tangential velocity components of ionic liquid flow field at the horizontal plane between impeller discharge region and tank top (z/H=0.73). The liquids in this area start to flow back to the impeller, therefore the negative radial velocities at this plane and opposite axial flows can be found in Figure 6.19 and Figure 6.20 respectively. In Figure 6.20, due to the high shear caused by the rotating impeller, the tangential velocities are relative high in regions above the impeller ($0.03R \leq r \leq 0.5R$). As can be found in these figures, the velocity components of the ionic liquid with and without the presence of gas are almost identical at this plane. The presence of gas phase does not cause significant change on ionic liquid flow pattern.

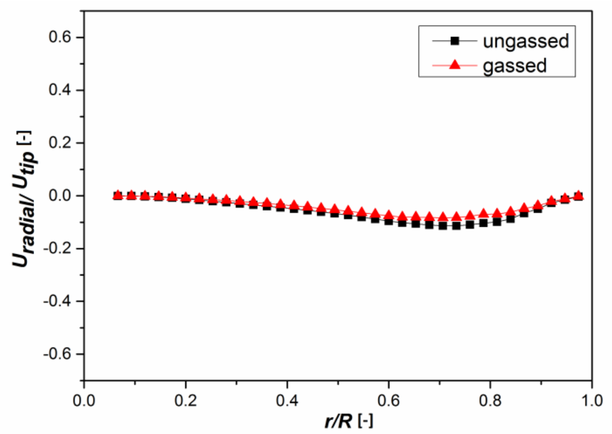

Figure 6.19 Ionic liquid radial velocities at the gassed and ungassed conditions (at *z/H*=0.73)

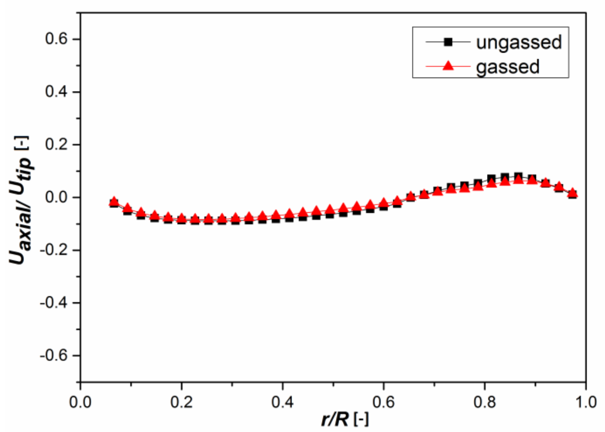

Figure 6.20 Ionic liquid axial velocities at the gassed and ungassed conditions (at *z/H*=0.73)

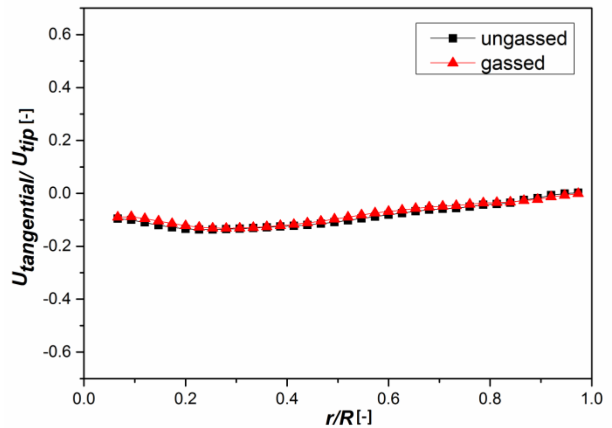

Figure 6.21 Ionic liquid tangential velocities at the gassed and ungassed conditions (at *z/H*=0.73)

Figure 6.22 to Figure 6.24 show the velocity components at the impeller discharge region (z/H=0.5) where the ionic Liquid in this region flows radially and tangentially. As shown in Figure 6.22 and Figure 6.24, high level of radial and tangential velocity can be noticed near the impeller blade tips for both conditions with and without gas injection. However, compared with the condition without the gas, slight reduction in radial and tangential velocities can be seen near the impeller blades in the condition with gas injection. The velocity profiles are almost consistent in the region away from this area. The reduction of radial and tangential velocities close to the impeller is mainly caused by the reduction of the impeller power input due to the presence of gas phase which hinders the impeller pumping ability. In addition, the gas inlet velocity is much lower than the liquid velocity agitated by the rotating impeller, so the lower gas velocity will decrease the magnitude of the liquid jet flows discharged from the impeller (Gorji et al., 2007).

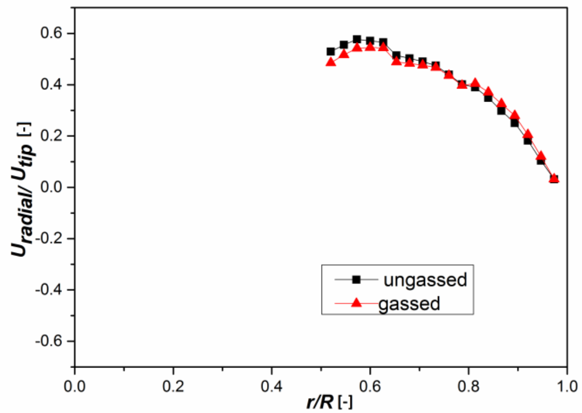

Figure 6.22 Ionic liquid radial velocities at the gassed and ungassed conditions (at z/H=0.5)

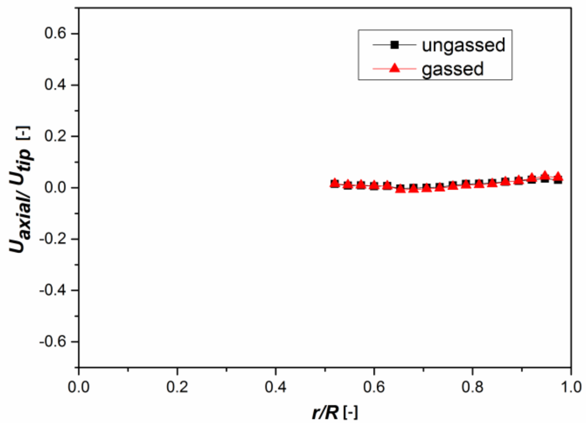

Figure 6.23 Ionic liquid axial velocities at the gassed and ungassed conditions (at z/H=0.5)

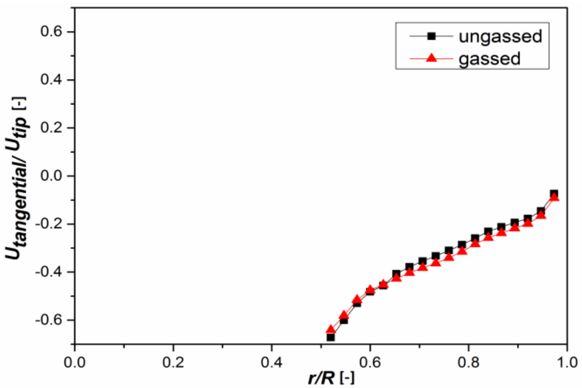

Figure 6.24 Ionic liquid tangential velocities at the gassed and ungassed conditions (at z/H=0.5)

The velocity components at location between impeller discharge region and tank bottom (z/H=0.27) were shown from Figure 6.25 to Figure 6.27. This plane passes through the lower circulation loop, therefore negative radial and axial velocities are identified close to the baffles ($0.6R \leq r \leq 0.9R$) in Figure 6.25 and Figure 6.26 respectively. As can be observed from these figures, the presence of the gas phase does not cause significant change of velocity components in the majority region of this plane. Only a slight reduction of the axial velocities of the ionic liquid at the radial distance of around 0.15R in the stirred tank, due to the reduced impeller pumping ability and the decreased intensity of the downward circulation loops when the gas is introduced into the stirred tank.

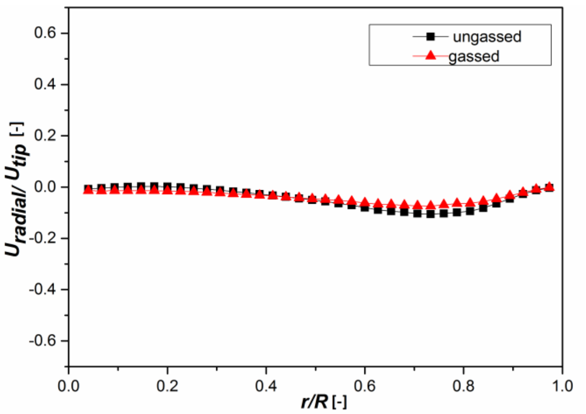

Figure 6.25 Ionic liquid radial velocities at the gassed and ungassed conditions (at z/H=0.27)

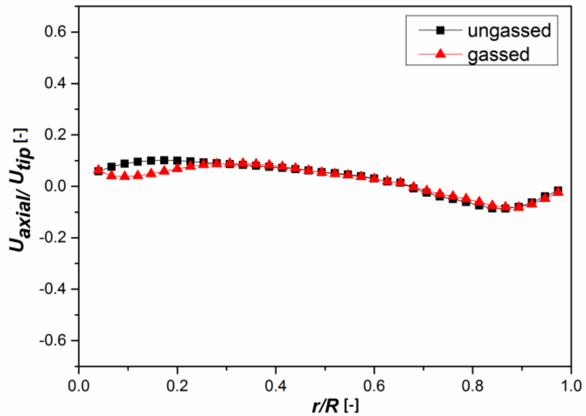

Figure 6.26 Ionic liquid axial velocities at the gassed and ungassed conditions (at z/H=0.27)

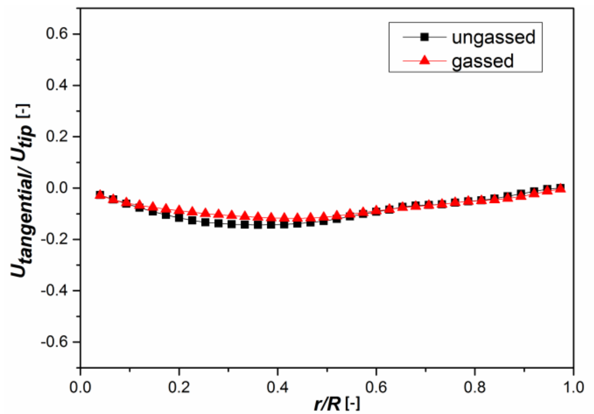

Figure 6.27 Ionic liquid tangential velocities at the gassed and ungassed conditions (at z/H=0.27)

Figure 6.28 to Figure 6.30 display the ionic liquid velocity components at a horizontal plane close to tank bottom (z/H=0.1) under conditions with and without gas injection. This plane passes through the dead zone region near tank bottom. As shown in Figure 6.28, the radial velocities of the ionic liquid at conditions with and without gas are almost zero at this plane indicating that the downward circulation loops have little effect on circulating liquids along the tank bottom.

However, the presence of the gas has more obvious effect on axial and tangential velocities of the ionic liquid at this plane. As can be observed in Figure 6.29, with the introduction of gas, a reduction of axial velocities can be found in the region below the impeller ($0.03R \leq r \leq 0.3R$). In addition, significant decreases of the tangential velocities are identified at this whole plane (in Figure 6.30). At condition without gas injection, the ionic liquid near the tank bottom rotates at a low speed due to the motion of the spinning impeller. With the presence of gas phase, the ionic liquid tangential motion in the tank bottom are weakened resulting in almost zero velocities and a poor mixing dead zone area near the tank bottom. The dead zone region will decrease the mixing efficiency of the stirred tank, the mass transfer and reaction rate hence increasing the overall cost of the mixing process.

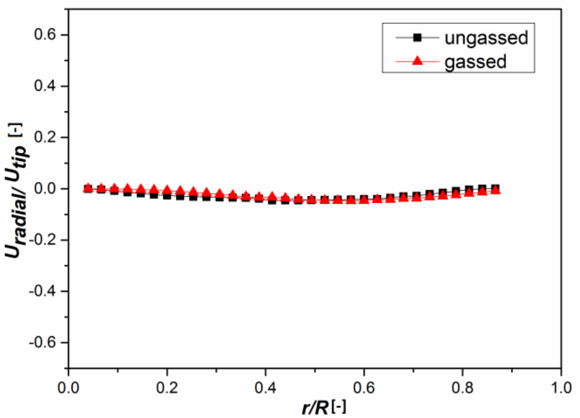

Figure 6.28 Ionic liquid radial velocity at the gassed and ungassed conditions (at *z*/*H*=0.1)

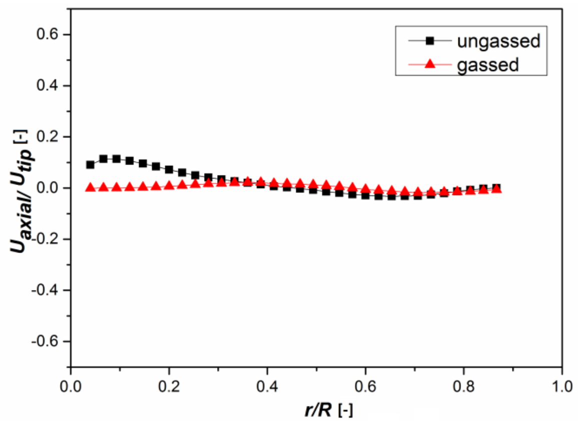

Figure 6.29 Ionic liquid axial velocity at the gassed and ungassed conditions (at *z*/*H*=0.1)

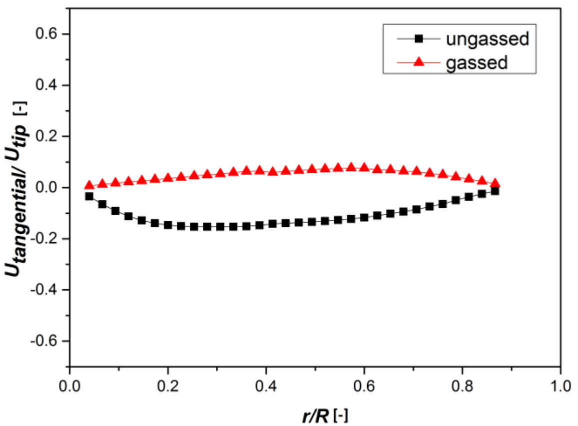

Figure 6.30 Ionic liquid tangential velocity at the gassed and ungassed conditions (at *z*/*H*=0.1)

6.3.4.3 Velocities of the Gas Phase and the Ionic Liquid Phase

As the bubbles circulating in the stirred tank under the effect of liquid flow, a balance between drag and buoyancy forces acting on bubbles determines their velocities relative to the liquid phase (Lane et al., 2002). The relative velocity between the bubble and the liquid is known as the slip velocity (Paul et al., 2004). This slip velocity essentially controls the rate of rise of bubbles and the proportion of recirculated bubbles in the stirred vessels (Lane et al., 2002), hence significant affecting the gas holdup and mass transfer in the stirred tanks. In order to investigate the features of the gas phase in the gas-ionic liquid multiphase flow field and the slip velocity, the velocity components of the gas phase together with the ionic liquid phase were displayed at four horizontal planes as indicated in Figure 6.18. Since the liquid phase and the gas phase is almost still near the tank bottom, data in this region (z/H=0.1) will not show here.

Figure 6.31 to Figure 6.33 show the gas and liquid phase velocities at a horizontal plane in the midway between the impeller and the tank top. As can be observed from these figures, the velocity components of the gas and ionic liquid phase are almost identical. The reason is that, for the small relative Reynolds number in this investigation, the majority of the drag force acting on a single bubble results from the viscous shear stress applied by the surrounding liquid (Marshall and Li, 2014). The viscous shear stress at the bubble surface will be high when the small bubbles move in the ionic liquid due to the high viscosity of the ionic liquid. High level of the viscous shear stress will cause high residence to the moving bubbles in the ionic liquid. Therefore, the gas phase faithfully follows with the ionic liquid phase, and the bubbles recirculated in the stirred tank, hence increasing the volume fraction of the gas phase and the mass transfer in the stirred tank.

This phenomenon mentioned above is different from the gas behaviours in the gas-water turbulent flow in the stirred tank, where a significant reduction of the gas velocity can be found above the impeller near the impeller shaft (Scargiali et al., 2007). In the gas-water multiphase flow modelling carried out by Scargiali et al. (2007), the water in the region above the impeller near the impeller shaft mainly flow axially toward the impeller, and the gas flow affected by the buoyance force has the tendency of moving upward towards the liquid surface. Therefore, significant increase of slip velocities between two phases can be found in this region and there are fewer bubbles circulated back to the impeller resulting in the decreased gas holdup and mass transfer in the stirred tank.

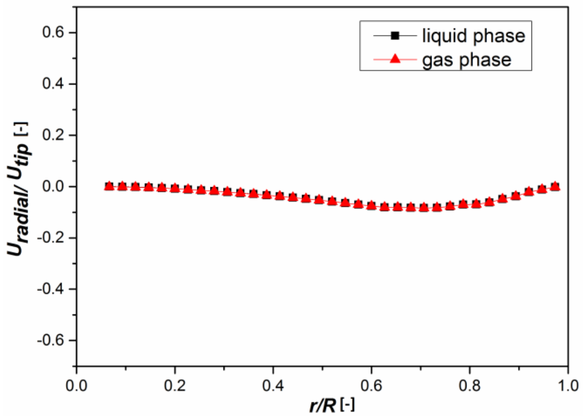

Figure 6.31 Liquid and gas phase radial velocities (at *z*/*H*=0.73)

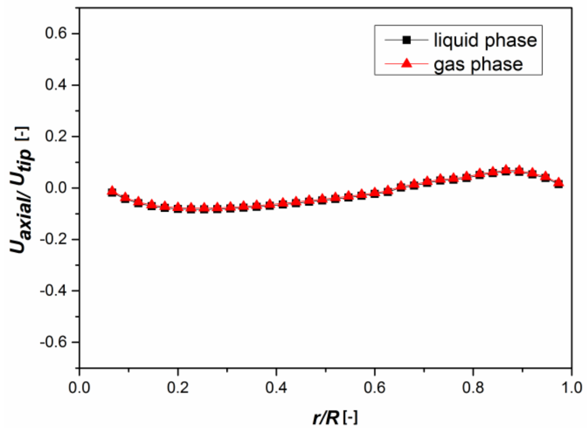

Figure 6.32 Liquid and gas phase axial velocities (at *z*/*H*=0.73)

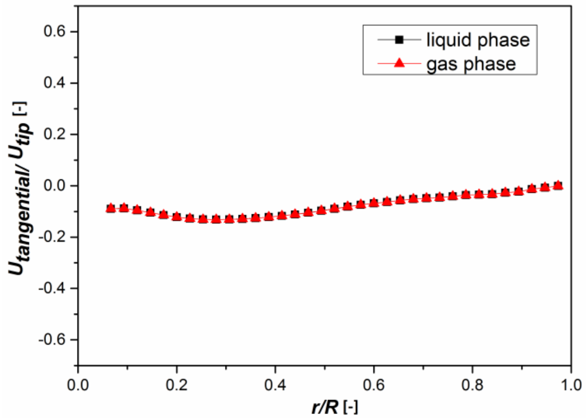

Figure 6.33 Liquid and gas phase tangential velocities (at *z*/*H*=0.73)

Figure 6.34 to Figure 6.36 illustrate the gas and liquid phase velocity components at a horizontal plane in the impeller discharge region (*z/H*=0.5). Figure 6.34 to Figure 6.36 show that, due to the rotating impeller, high shear stress is applied to its surrounding liquid and bubbles resulting in large radial and tangential velocities for both gas and ionic phase in the region close to impeller blades (*r*=0.5*R*). The gas phase well follows with the liquid phase resulting in good gas dispersion in this area. The axial velocities are almost zero for both phases (in Figure 6.35). This trend is different from the gas-water turbulent flow in the stirred tank where the gas phase moves faster than the water phase in the axial direction in the impeller discharge region (Montante et al., 2007) hence decreasing the proportion of recirculated bubbles and reducing the gas holdup in the stirred tank.

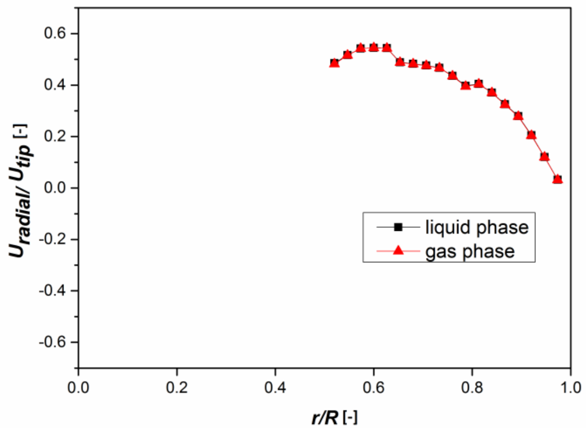

Figure 6.34 Liquid and gas phase radial velocities (at *z*/*H*=0.5)

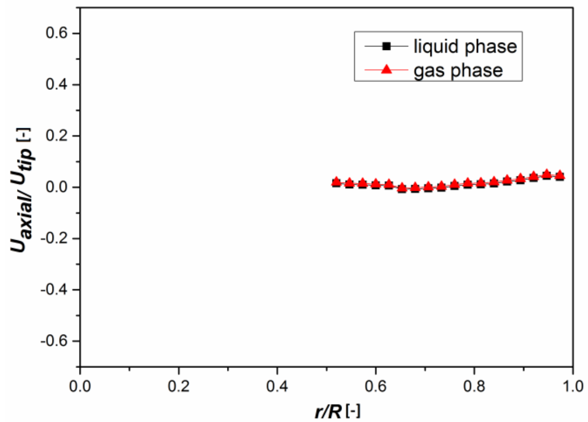

Figure 6.35 Liquid and gas phase axial velocities (at *z*/*H*=0.5)

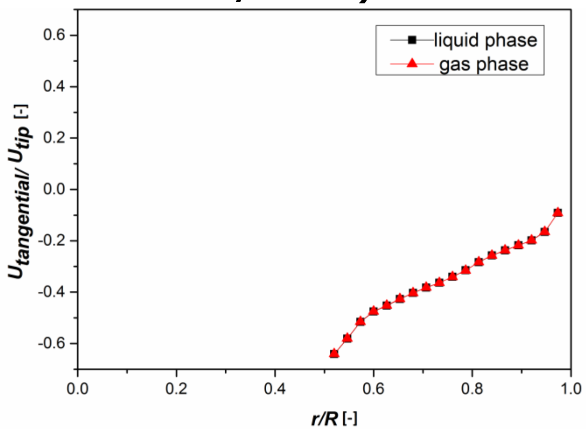

Figure 6.36 Liquid and gas phase tangential velocities (at *z*/*H*=0.5)

Figure 6.37 to Figure 6.39 show the velocity components of the ionic liquid and gas phase at a horizontal plane in the midway between impeller and tank bottom (z/H=0.27). These figures demonstrate that there are no significant differences between the gas phase and liquid at this area. This is also different from the phenomenon in the gas-water turbulent flow at the corresponding region where the bubble's motion in axial direction is decelerated causing obvious slip velocities between the two phases (Montante et al., 2008). The high slip velocity in gas-water multiphase flow system implies that the reduced proportion of the circulated bubbles and decreased the gas holdup and mass transfer in this area.

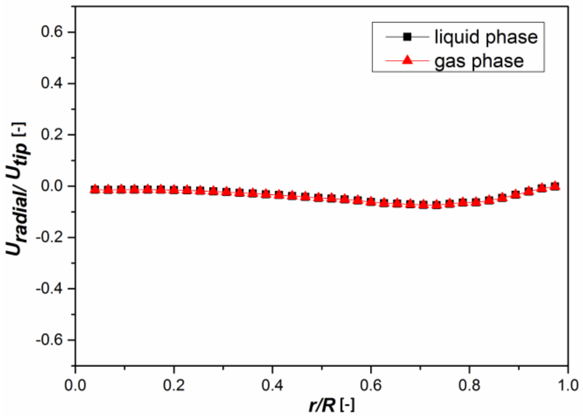

Figure 6.37 Liquid and gas phase radial velocities (at *z/H*=0.27)

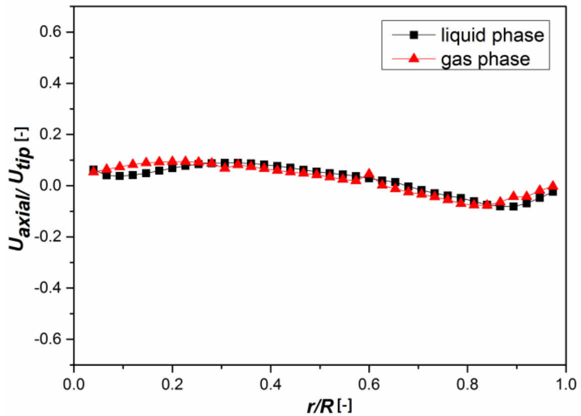

Figure 6.38 Liquid and gas phase axial velocities (at *z/H*=0.27)

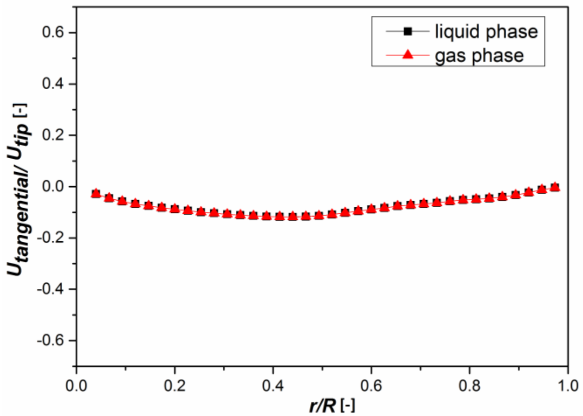

Figure 6.39 Liquid and gas phase tangential velocities (at *z/H*=0.27)

6.3.5 Effect of the Impeller Speed on the Flow Field

The impeller rotation speed plays a key role on flow circulation, thus enhancing the mixing efficiency in the stirred tanks (Wang et al., 2014). It has been also found that the dead zone in the single phase flow can be significantly reduced by increasing the impeller speed (Bakker et al., 1997, Sungkorn et al., 2012). The study in section 6.3.4.2 identified a dead zone region near the tank bottom when the gas is introduced into the ionic liquid flow in the stirred tank, which will cause poor mixing in that region. This section therefore attempts to investigate the effect of the impeller agitation speed on the gas-ionic liquid multiphase flow field and the dead zone area in the gas-ionic liquid multiphase flow in the stirred tank. The flow was modelled at different impeller rotating speeds (150 rpm, 200 rpm and 250 rpm) and various gassing rates (0.1 L/min, 0.2 L/min and 0.3 L/min). The gas-ionic liquid multiphase flow was in the transitional flow state under these operation conditions.

The flow vectors of the ionic liquid phase and the gas phase are shown from Figure 6.40 to Figure 6.43. Compared with the gas and ionic liquid flow vectors in Figure 6.13 and Figure 6.14 in section 6.3.4.1, the intensity of the circulations near the tank bottom is enhanced as the impeller speed increased from 150 rpm to 200 rpm in the gas-ionic liquid system. The flow pattern of the gas phase and the ionic liquid phase is very similar at the investigated operation conditions. The dead zone region found in Figure 6.13 and Figure 6.14 has almost disappeared in Figure 6.40 to Figure 6.43 as the impeller rotation speed increases from

150 rpm to 200 rpm and 250 rpm respectively resulting in the enhancement of mixing efficiency near the tank bottom.

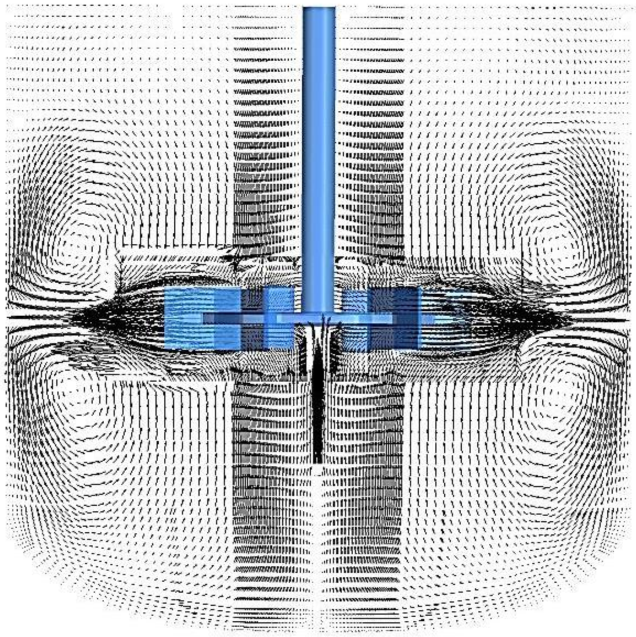

Figure 6.40 Flow vectors of the liquid phase (200 rpm)

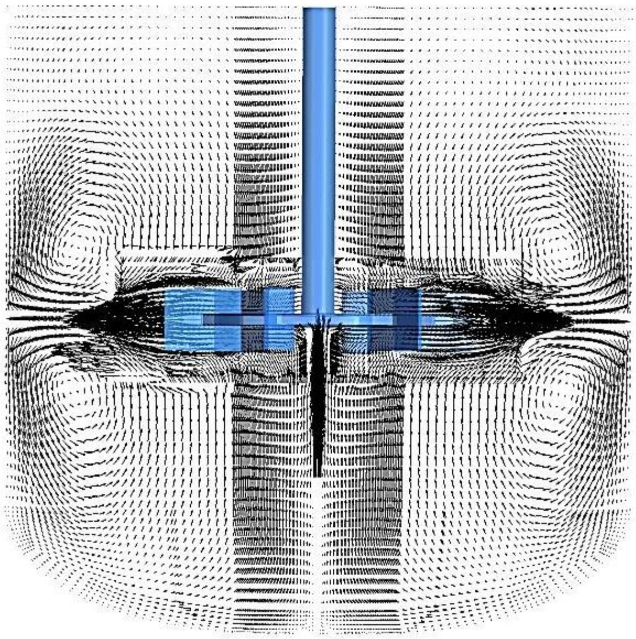

Figure 6.41 Flow vectors of the gas phase (200 rpm)

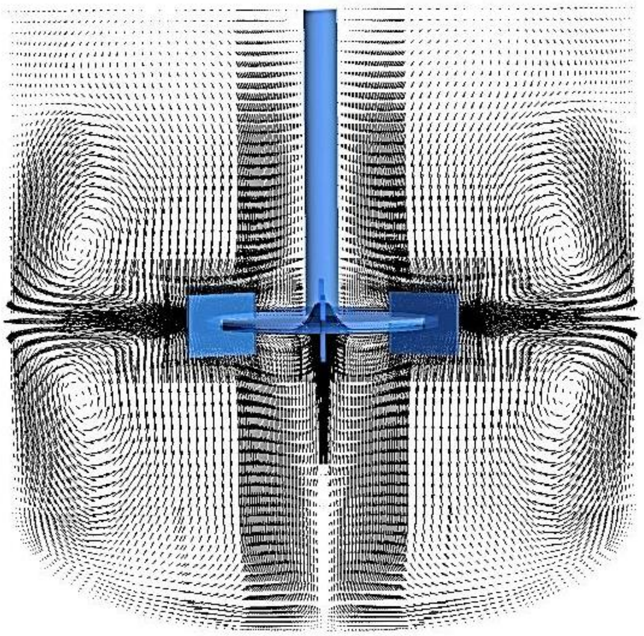

Figure 6.42 Flow vectors of the liquid phase (250 rpm)

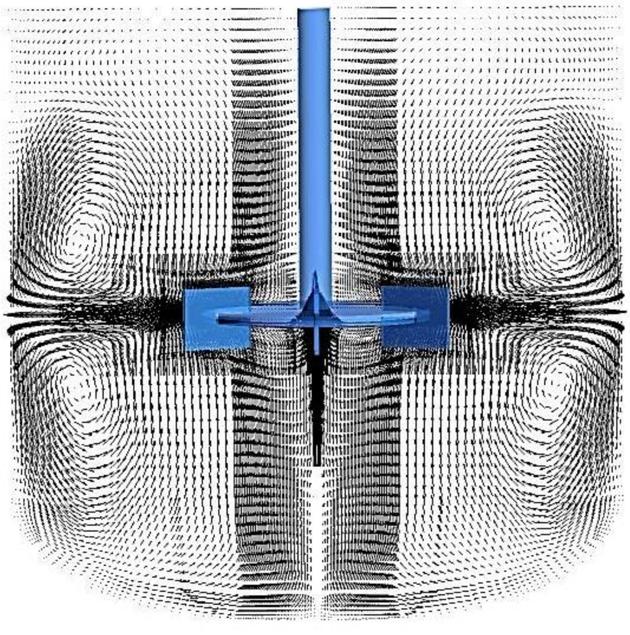

Figure 6.43 Flow vectors of the gas phase (250 rpm)

The contours of the time-averaged velocity magnitude of the liquid phase and gas phase at the different impeller agitation speeds are shown from Figure 6.44 to Figure 6.47. The contours of the liquid phase and the gas phase are very similar showing that the gas phase follows faithfully with the liquid phase. Compared with ionic liquid and gas velocity contour shown in Figure 6.16 and Figure 6.17 in section 6.3.4.1, with the increasing impeller speed from 150 rpm to 200 rpm and 250 rpm, there is no significant change of stagnant zone near the corners of the tank top and the edge of the dished bottom, however, there is a significant reduction of the dead zone area near the tank bottom. Both the gas phase and ionic liquid phase circulate in this region increasing the gas holdup in the stirred tank.

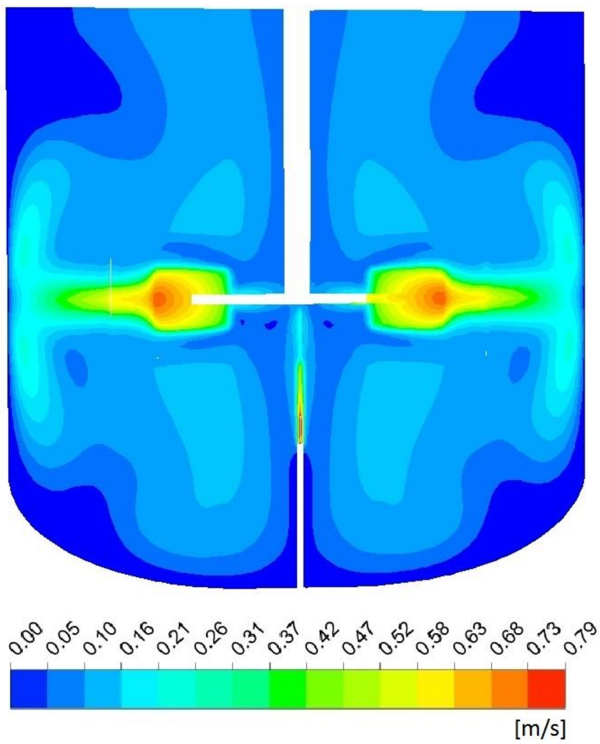

Figure 6.44 Contours of the ionic liquid phase (200 rpm)

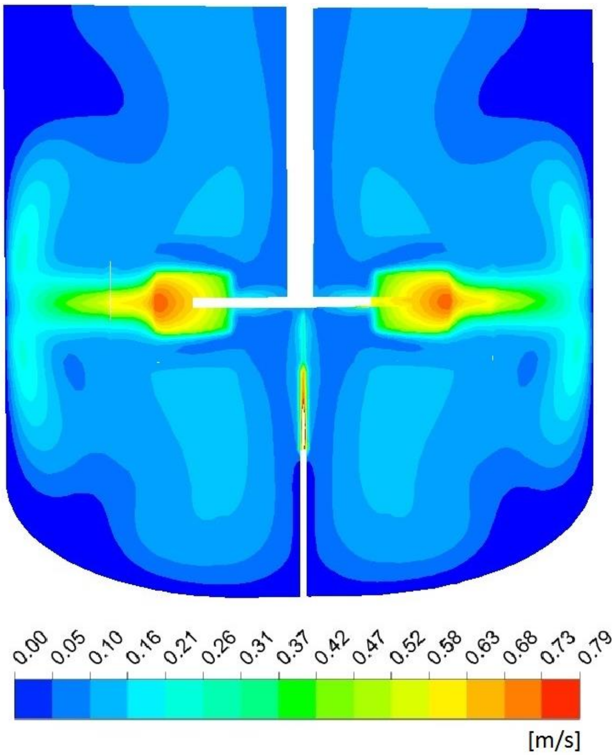

Figure 6.45 Contours of the gas phase (200 rpm)

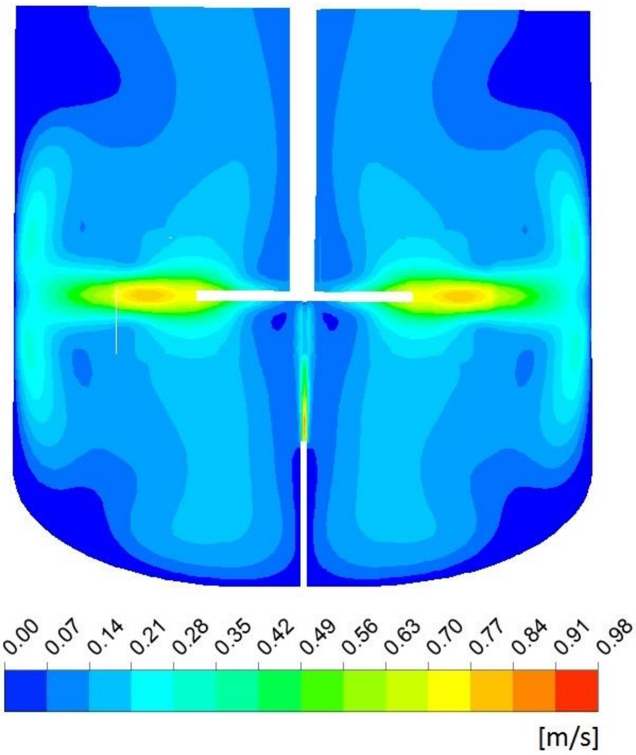

Figure 6.46 Contours of the ionic liquid phase (250 rpm)

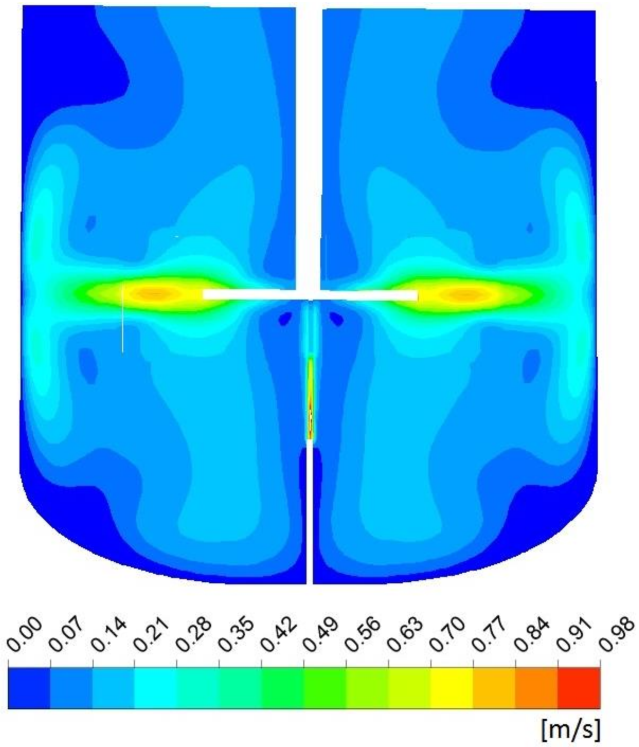

Figure 6.47 Contours of the gas phase (250 rpm)

Figure 6.48 to Figure 6.50 show a more detailed effect of the increasing impeller speed on the flow field with simulated velocity components were plotted at a horizontal plane (z/H=0.1) passing through the dead zone region. Since the gas phase faithfully follows the liquid phase, only the data of the liquid phase were plotted and displayed.

As can be observed in Figure 6.48, the radial velocity components of the ionic liquid for the three impeller speeds are all around zero close to tank bottom indicating that the increased intensity of the downward circulation loops by means of the increasing impeller agitation speed dose not has a significant effect on circulating the flows in the radial direction near the tank bottom.

Figure 6.49 shows the ionic liquid axial velocity components for various impeller rotating speeds. As can be observed from this figure, the increasing impeller speed from 150 rpm to 250 rpm has caused a clear increase of the axial velocity near the sparger ($0.01R \leq r \leq 0.1R$). However, the axial velocity is still almost zero away from it. As showed in Figure 6.50, the increase of impeller speed from 150 rpm to 200 rpm has given rise to a clear increase of the tangential velocity of ionic liquid. However further increase of the impeller speed from 200 rpm to 250 rpm does not have significant on increasing the circulation of flows near tank bottom. Since the impeller is rotating at the clock-wise direction and this direction opposites to tangential direction of the coordinate, the minus value of tangential velocities in this plane indicate that the ionic liquid flow is almost rotating at the same direction with the impeller.

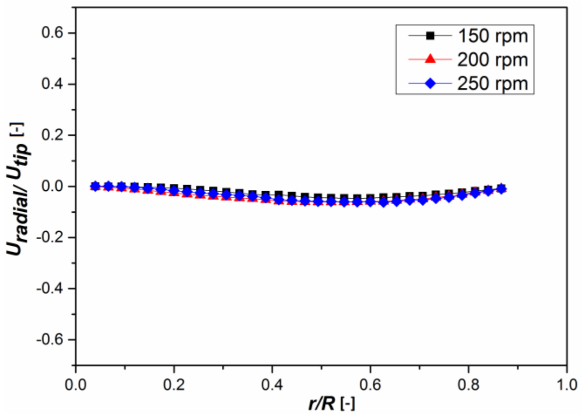

Figure 6.48 Liquid radial velocity component at different impeller speed (at z/H=0.1)

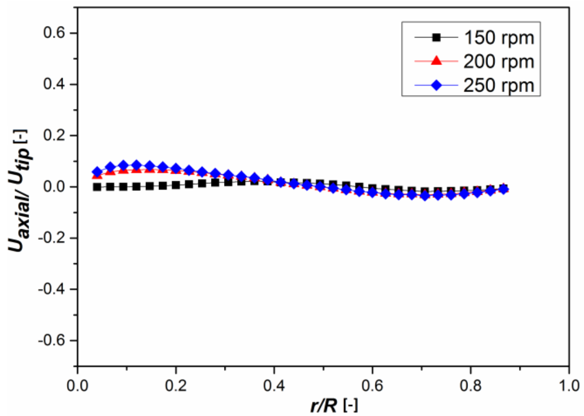

Figure 6.49 Liquid axial velocity component at different impeller speed (at z/H=0.1)

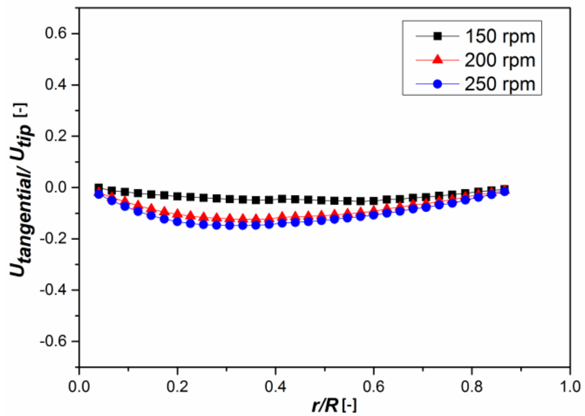

Figure 6.50 Liquid tangential velocity component at different impeller speed (at z/H=0.1)

The flow behaviours mentioned above are different from the gas-water turbulent flow system agitated by the rotating impeller. In the gas-water turbulent flow in a stirred tank, there are strong gas-liquid circulations in the region near the tank bottom. However, the simulation work suggests that these gas-liquid circulations near the tank bottom are very weak due to the high viscosity of ionic liquid and the presence of the gas phase when the gas-ionic liquid system is under operation. The poor circulations in this region will reduce the degree of the homogeneous mixing and mixing efficiency in the stirred tank hence increasing the overall cost of the mixing process and decrease the quality of the final products (Wang et al., 2014). The increase of impeller speed from 150 rpm to 200 rpm greatly reduced the dead zone near the tank bottom. However, it does not have significant effect on the reduction of dead zone regions close to the edge of dished bottom and the corners of the tank top. In addition, further increase of impeller speed from 200 rpm to 250 rpm has less effect on the reducing of the dead zone region at the tank bottom compared to the increase of impeller speed from 150 rpm to 200 rpm.

It has been mentioned in the literature that the change of Reynolds number does not cause noticeable variations of normalized flow variables such as velocity components if the flow is operated in fully developed turbulent state (Li et al., 2011, Montante et al., 2001b). As can be found in Figure 6.49 and Figure 6.50, the increase of the impeller speed hence increasing the Reynolds number has obvious effect on the normalized velocity components when the flow is operated at the transitional state. This simulation work somehow proofed that the above theory mentioned by Li et al., (2011) and Montante et al. (2001) is only applicable to the fully turbulent flows but not the transitional flows in the stirred tanks.

6.3.6 Effect of the Gassing Rate on the Flow Field

This section explores the effect of the gassing rate on the gas-ionic liquid flow field. Figure 6.51 to Figure 6.54 show the contours of the velocity magnitude of the ionic liquid and the gas phase operated at fixed impeller speed of 150 rpm and gassing rates of 0.2 L/min and 0.3 L/min respectively. The contours of the ionic liquid and the gas phase under the operation condition of 150 rpm and 0.1 L/min is shown in Figure 6.16 and Figure 6.17 in section 6.3.4.2. It can be observed from these figures that both the gas phase and liquid phase show similar flow field for each operation conditions. The increasing gassing rate from 0.1 L/min to 0.3 L/min does not seem to have significant effect on the flow pattern in the upper bulk regions. However, compared with Figure 6.16 and Figure 6.17, an obvious increasing of the dead zone can be observed near tank bottom in Figure 6.51 and Figure 6.52 when the gassing rate increased to 0.2 L/min. And further increase of the dead zone region near the tank bottom can be observed in Figure 6.53 and Figure 6.54 as the gassing rate increased from 0.2 L/min to 0.3 L/min. The reason is due to the excessive accumulation of the bubbles behind the impeller blades causing the reduction of the impeller gas dispersion ability and the liquid pumping capability in the stirred tank (Paul et al., 2004). Therefore, the further increase of gas flow rate in the gas-ionic liquid flow will enlarged the dead zone region near the tank bottom leading to poor mixing area.

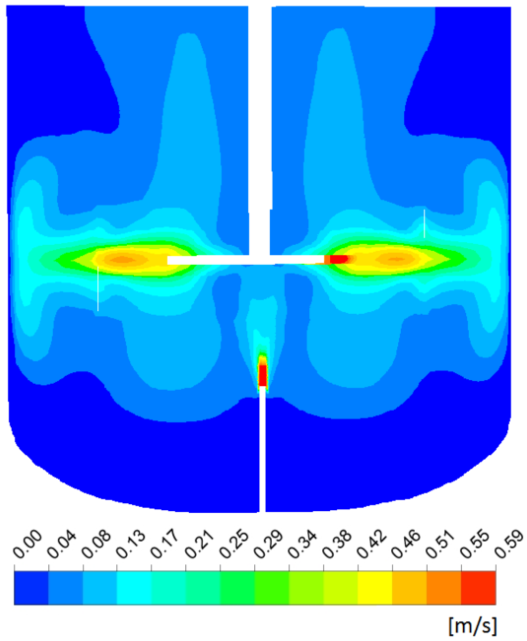

Figure 6.51 Contours of the liquid phase (gassing rate: 0.2 L/min)

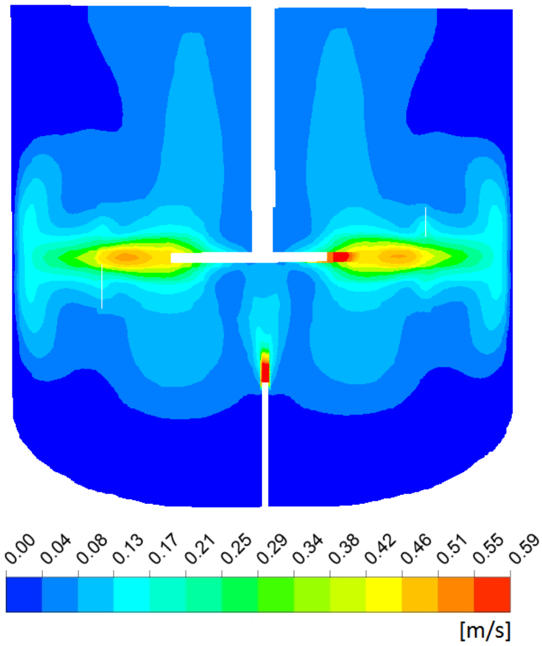

Figure 6.52 Contours of the gas phase (gassing rate: 0.2 L/min)

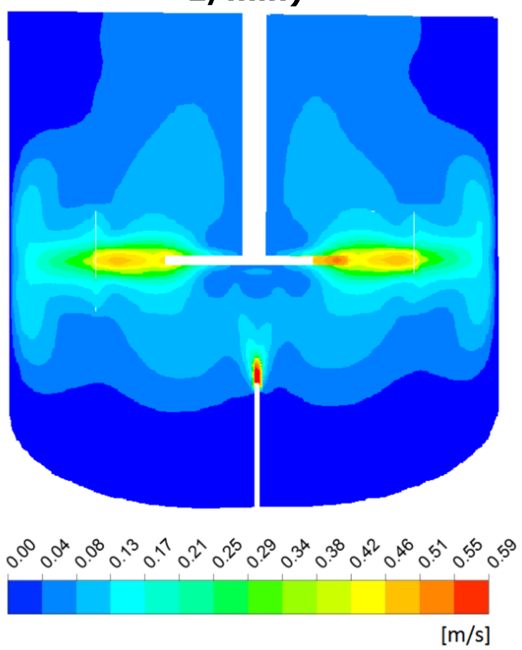

Figure 6.53 Contours of the liquid phase (gassing rate: 0.3 L/min)

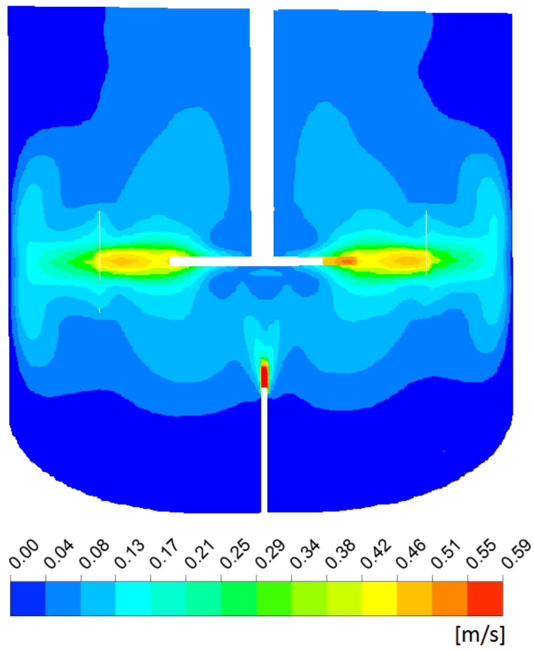

Figure 6.54 Contours of the gas phase (gassing rate: 0.3 L/min)

6.3.7 Gas Holdup of Gas-ionic Liquid Flow in the Stirred Tank

The major concern in the design of gas-sparged stirred tank is to create large interfacial area by a combination of sufficiently fine bubbles and sufficiently high gas holdup (Lane, 2006). Since the gas holdup and the number of fine bubbles determine the contact area between gas and liquid phase, it is considered as the most important hydrodynamic parameter of gas-liquid system (Wang et al., 2014). In this section, the volume-averaged gas holdup was simulated and analysed under different impeller agitation speed and gas flow rate in the stirred tank.

Table 6.1 displays the simulated volume-averaged gas holdup under fixed gassing rate of 0.1 L/min and various impeller speeds of 150 rpm, 200 rpm and 250 rpm respectively. As can be observed from this table, the value of the gas holdup is around 3% at current operation conditions which shows slight increase with the increasing impeller speed.

Table 6.1 Volume-averaged gas holdup at various impeller speeds

Impeller speed	volume-averaged gas holdup
150 rpm	2.9%
200 rpm	3.0%
250 rpm	3.1%

Table 6.2 shows the predicted volume-averaged gas holdup under fixed impeller rotating speed of 150 rpm and various gassing rates of 0.1 L/min, 0.2 L/min and 0.3 L/min respectively. It demonstrates that under the fixed impeller speed, the gas holdup increases greatly with the increasing gassing rate. Compared with Table 6.1, the increase in inlet gas flow rate

has more obvious effect than the increase in the impeller agitation speed on the growth of the gas holdup in the stirred tank. For example, under the fixed gassing rate of 0.1L/min, as the impeller speed increased from 150 rpm to 250 rpm, the corresponding gas holdup increases from 2.9% to 3.1%. However, under fixed impeller speed, when the gassing rate grows from 0.1 L/min to 0.3 L/min the gas holdup rises sharply from 2.9% to 7.1%. This phenomenon is very similar to the trend can be observed in the gas-water turbulent flow that the increase in inlet gas velocity has more obvious effect on the overall gas holdup in stirred tank than the increase of impeller speed (Liu et al., 2011).

Table 6.2 Volume-averaged gas holdup at various gassing rate

Impeller speed	volume-averaged gas holdup
0.1 L/min	2.9%
0.2 L/min	4.9%
0.3 L/min	7.1%

In order to show the detailed instantaneous distributions of the gas holdup in the stirred tank, the contours of the gas holdup at different time step (0 s, 5 s, 10 s, 20 s, 50 s, 80 s, 100 s and 130 s respectively) are shown in the midway between two adjacent baffles (in Figure 6.55). The contours were obtained in the condition with the impeller speed of 150 rpm and a gassing rate of 0.1 L/min.

As can be observed from Figure 6.55, high level of gas holdup can always be found in the area above the sparger where the gas is introduced into the stirred tank. After the gas reaches to the impeller disk, it accumulates below the impeller disk and disperses into the bulk region by the rotating impeller. Compared with the upper bulk region, more gas is circulated in the lower bulk region. The gas flow in the lower bulk region reaches to its steady state first. At around 100 s of system running time, the gas holdup in the stirred tank is almost in the steady state. With the increasing agitating time, a steady dispersion of the gas phase is achieved and the bubbles circulate well inside the stirred tank. The gas phase is uniformly distributed in the ionic liquid, which indicates a good gas dispersion and mass transfer in the stirred tank.

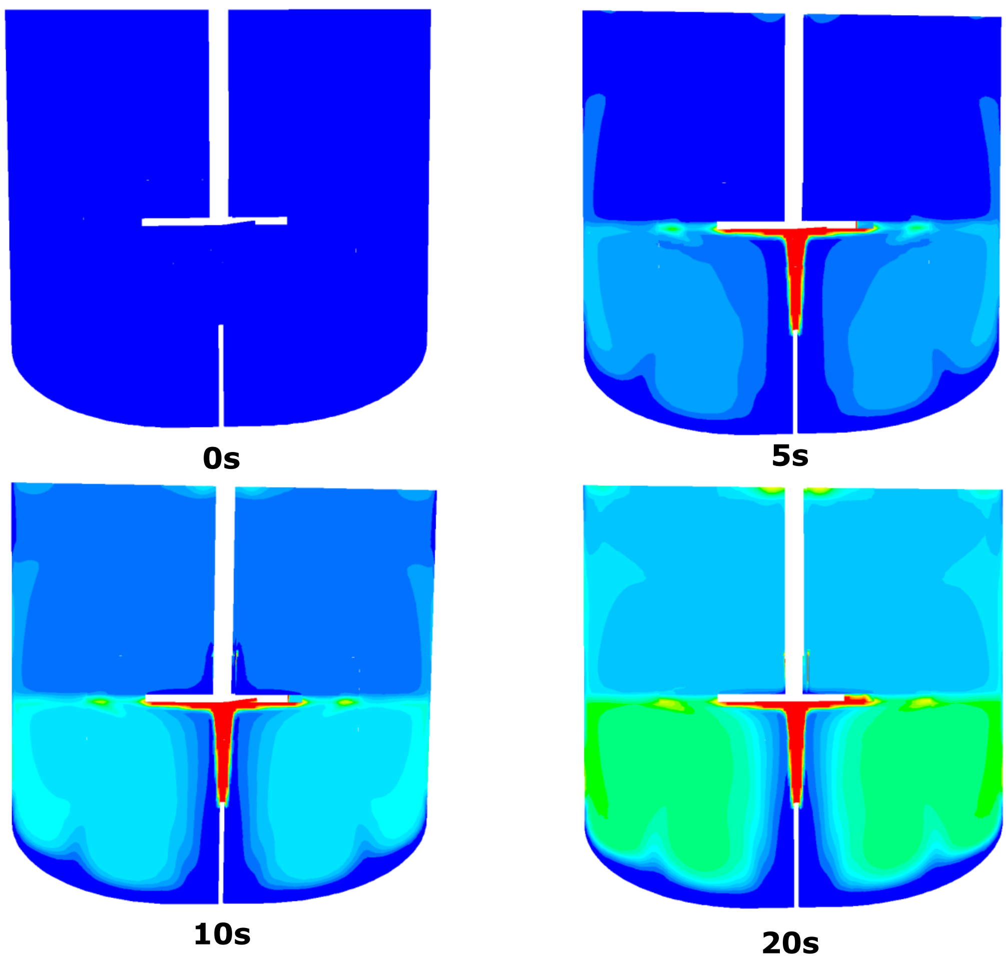

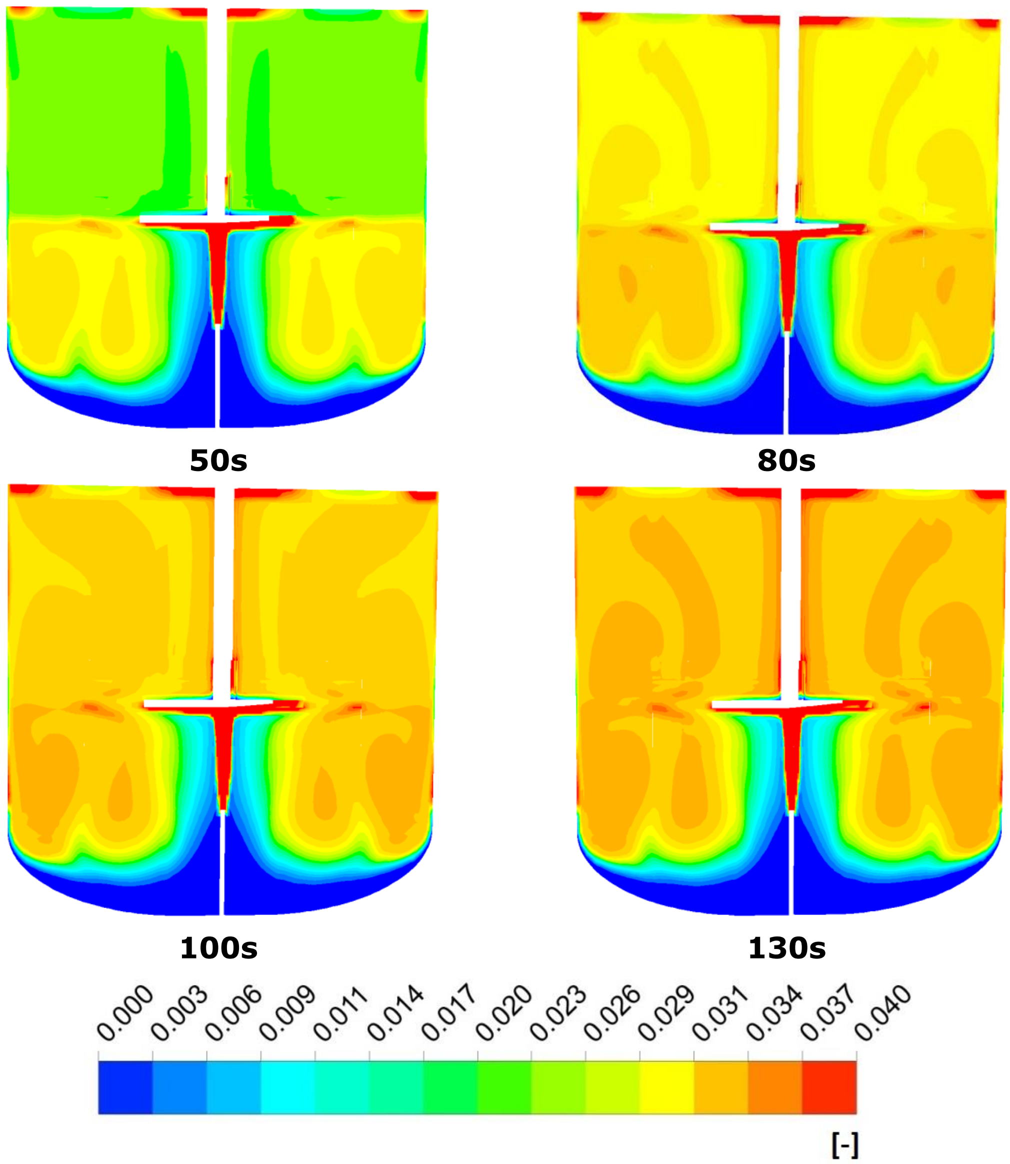

Figure 6.55 Instantaneous gas holdup in the stirred tank

With the purpose of showing the gas holdup at the different heights of the stirred tank when the gas-ionic liquid flow is operating at the steady state, the contours of the gas holdup at different horizontal planes of the stirred tank are displayed in Figure 6.56. As can be observed from Figure 6.56, at the height level of z/H=0.1, due to the existence of baffles above this region, bubbles are brought to these areas. The value of gas holdup is almost zero away from these areas affected by the baffles. At the height of z/H=0.27, the low local gas holdup regions are located around the sparger, which is mainly due to the less intensive lower circulation loops bringing fewer bubbles to this area when the ionic liquid is served as the operation liquid. At the height of z/H=0.5, due to the high pressure region at the front side and low pressure region at the back side of the impeller blades, more gas is accumulated at the rear of the impeller blades after the gas is released from the sparger. With the increase in the tank height from z/H=0.5 to z/H=0.73, the gas holdup in stirred tank is getting more uniform indicating a homogenous mixing and good gas dispersion in these areas.

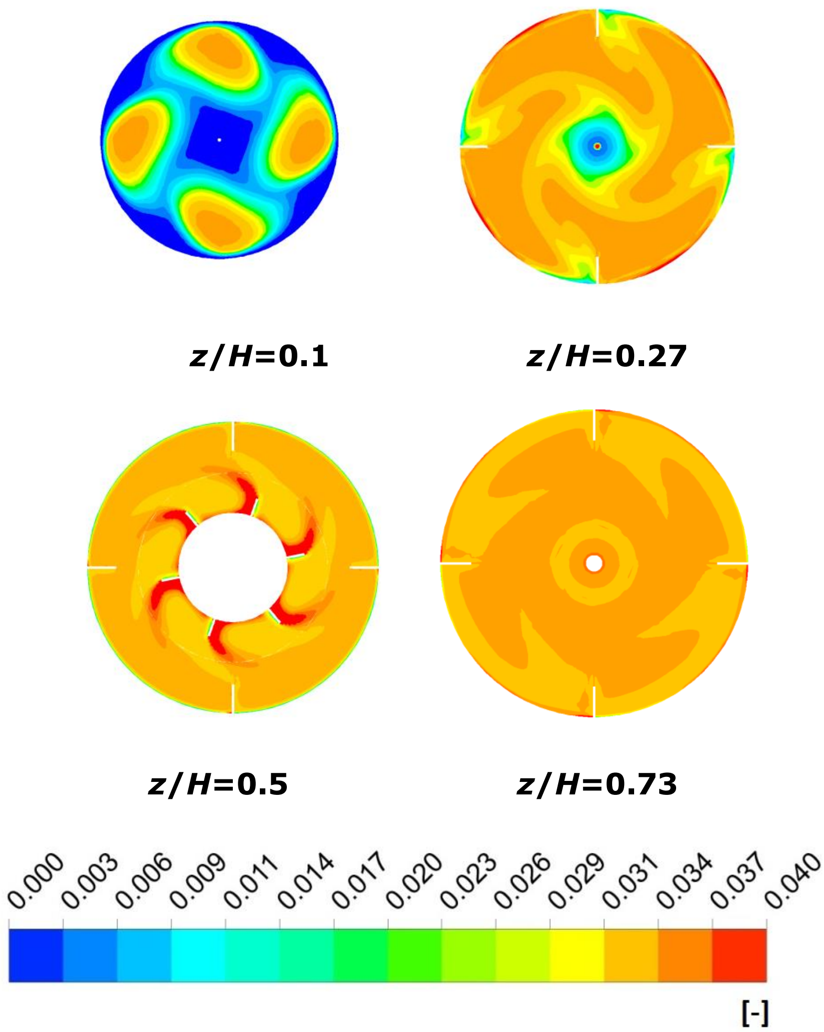

Figure 6.56 Gas holdup at different heights in the stirred tank

Generally, in the gas-ionic liquid multiphase flow in the stirred tank, the high viscosity of the ionic liquid gives rise to a significant reduction of the rising velocity of bubbles in the ionic liquid, hence the bubbles flowing faithfully with the liquid (Hua and Lou, 2007). Therefore, more uniform gas holdup in gas-ionic liquid flow stirred tank is achieved.

Compared with the gas holdup distributions in the gas-water turbulent flow obtained by Montante et al. (2008), the gas holdup distributions in the ionic liquid demonstrate some different characteristics. For example, when water is served as the operation liquid, due to the balance between the drag force and buoyancy force, only small portion of the bubbles are circulated in the downward circulation loops and the majority of the gas is circulated in the upper bulk region near the impeller and sparger (Montante et al., 2008). In addition, in the lower bulk region, the bubbles are not uniformly distributed and they are mainly accumulated at the cores of the downward circulation loops (Scargiali et al., 2007). Therefore, in the gas-water turbulent system, the gas phase is not homogeneous dispersed and insufficient mixing inside the vessel.

In order to provide more detailed information of the effect of the impeller agitation speed on the gas holdup distributions in the stirred tank, the gas holdup values are displayed at different heights of the stirred vessel. The flows were operated at the fixed gassing rate of 0.1 L/min and various impeller speeds of 150 rpm, 200 rpm and 250 rpm. Figure 6.57 to Figure 6.60 show the gas holdup values at different heights in the stirred tank: near tank bottom (z/H=0.1), midway between impeller and tank bottom (z/H=0.27), impeller discharge region (z/H=0.5) and midway between impeller and tank cover (z/H=0.73).

As can be observed from Figure 6.57 and Figure 6.58, the local gas holdup at planes *z*/*H*=0.1 and *z*/*H*=0.27 undergoes a sharp increase from the tank centre to the radial distance at about *r*=0.25*R*. In Figure 6.57, a sharp decrease of local gas holdup is identified from radial distance of 0.7*R* to the tank wall. While in Figure 6.58, the local gas holdup is almost constant with the increasing radial distance afterward. The phenomenon of the uneven gas holdup distributions in Figure 6.57 and Figure 6.58 are probably due to the dead zones in the regions near sparger, tank bottom and edge of dished bottom at condition with air injection, where liquid is almost still and bubbles are hard to be brought to these areas under mild impeller rotation speed.

Figure 6.59 and Figure 6.60 show the distributions of the gas holdup at the planes of *z*/*H*=0.5 and *z*/*H*=0.73 respectively. Figure 6.59 and Figure 6.60 show that, with the increasing impeller speed, there is no significant change in the local gas holdup in the upper bulk region in the stirred tank suggesting that the effect of the increasing impeller has little effect on increasing the gas holdup in these areas. However, compared with gas holdup distributions in the lower bulk region (Figure 6.57 and Figure 6.58), the gas holdup distributions are more uniform distributed in the planes of *z/H*=0.5 and *z*/*H*=0.73. The values of the gas holdup at the planes of *z*/*H*=0.5 and *z*/*H*=0.73 are relative high showing a good mass transfer in these areas.

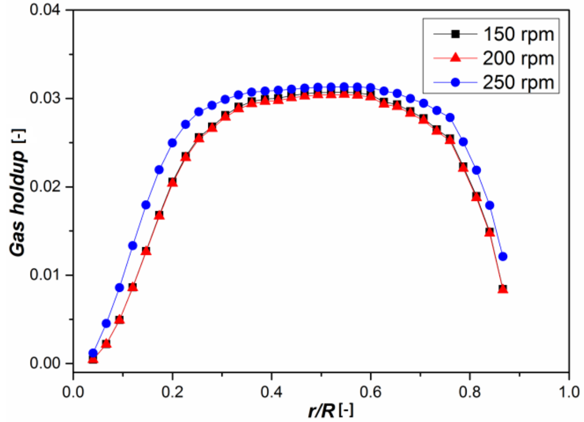

Figure 6.57 Gas holdup at different impeller speeds (gassing rate 0.1L/min, at z/H=0.1)

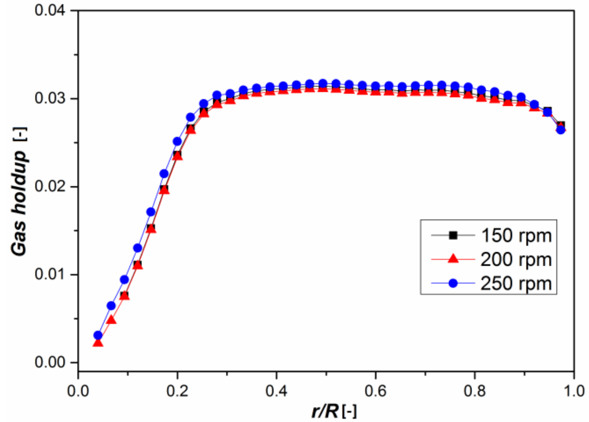

Figure 6.58 Gas holdup at different impeller speeds (gassing rate 0.1 L/min, at z/H=0.27)

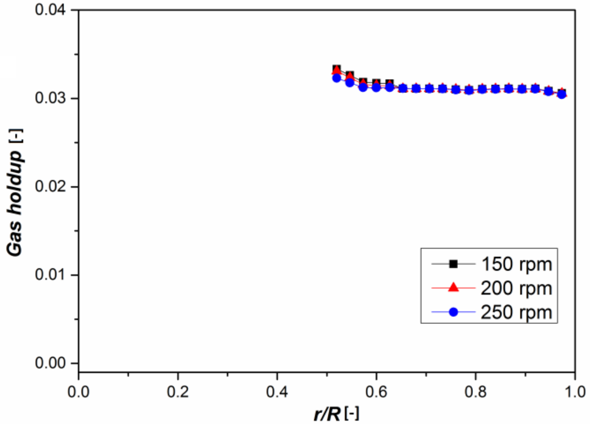

Figure 6.59 Gas holdup at different impeller speeds (gassing rate: 0.1 L/min, at z/H=0.5)

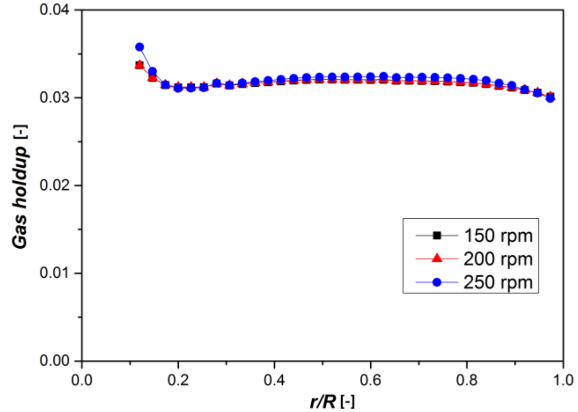

Figure 6.60 Gas holdup at different impeller speeds (gassing rate: 0.1 L/min, at z/H=0.73)

In order to show more detailed information of the effect of the gas flow rate on the gas holdup distributions in the stirred tank, the gas holdup values are displayed at different heights of the stirred vessel. Figure 6.61 to Figure 6.64 show the predicted gas holdup distributions at planes (z/H=0.1, z/H=0.27, z/H=0.5 and z/H=0.73) under fixed impeller rotation speed of 150 rpm and various gassing rates of 0.1 L/min, 0.2 L/min and 0.3 L/min.

Figure 6.61 show the gas holdup distributions at various gassing rates near the tank bottom (z/H=0.1). As can be observed from this figure, the increasing gassing rate significantly reduces the gas holdup in this area. The gas holdup is between 0 % and 3 % with an inlet gas flow rate of 0.1 L/min. However, as the gassing rate reaches to 0.3 L/min, due to the reduction of impeller pumping ability as it was mentioned earlier, the bubbles cannot be brought by the flowing fluids to the tank bottom leading to the decreased gas holdup in this area (around 0% at gassing rate of 0.3 L/min).

Different from the gas holdup distributions at the plane of z/H=0.1, Figure 6.62 to Figure 6.64 show that the growth of inlet gas flow rate has positive effect on increasing the gas holdup above the dished bottom (z/H=0.27, z/H=0.5 and z/H=0.73). Due to the bubbles accumulation behind the impeller blades (r=0.5R), high value of gas holdup is identified near the impeller tips (shown in Figure 6.63). The gas phase is uniformly distributed in upper bulk regions and impeller plane (in Figure 6.63 and Figure 6.64), which provides better degree of homogeneous mixing and mass transfer rate in these areas.

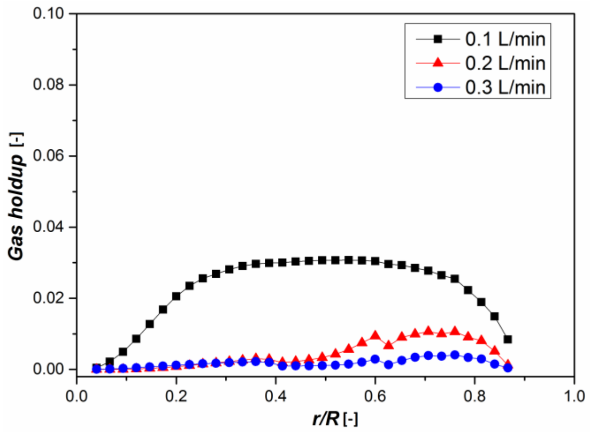

Figure 6.61 Gas holdup at different gassing rates (impeller speed: 150 rpm, at *z/H*=0.1)

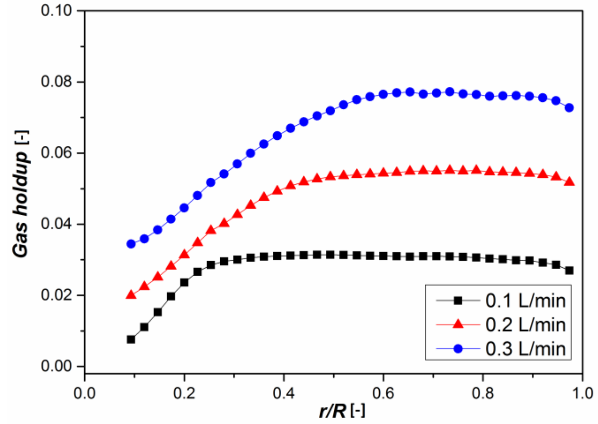

Figure 6.62 Gas holdup at different gassing rates (impeller speed: 150 rpm, at *z/H*=0.27)

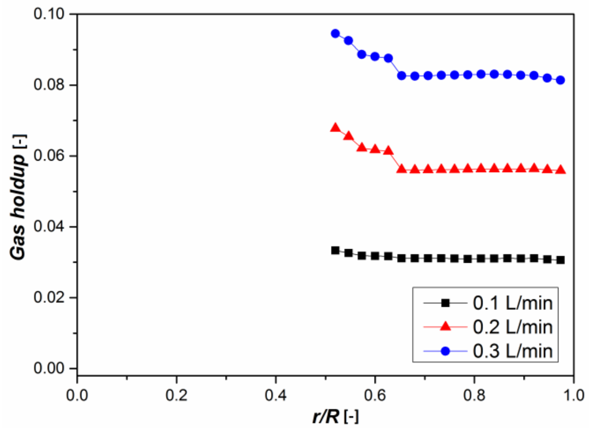

Figure 6.63 Gas holdup at different gassing rates (impeller speed: 150 rpm, at *z/H*=0.5)

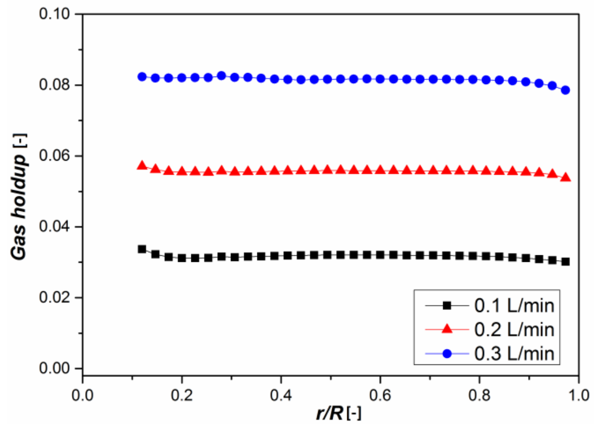

Figure 6.64 Gas holdup at different gassing rates (impeller speed: 150 rpm, at *z/H*=0.73)

6.4 Impeller Power Consumption of the Gas-ionic Liquid Multiphase Flow System

The power consumption under gassed condition provides the curtail information for the gas-liquid multiphase flow stirred tanks scale-up and design. The impeller power consumption in the gas-liquid multiphase flow systems is always lower than that in the ungassed systems due to the formation of gas cavities behind the impeller blades (Gill et al., 2008). Normally, the power consumption of the Rushton turbine impeller in the gassed condition is nearly 50% (or less) than the ungassed situation if the flow is in the fully developed turbulent state. However, the knowledge of the impeller power consumption under ionic liquid transitional flow gassed condition is still very rare in open literatures. This information will offer information for the design and optimization of the gas-ionic liquid multiphase stirred tanks.

Several investigations have been carried out to estimate the power consumption (P_g) in the gas-liquid multiphase flow system in the stirred tanks. The parameters considered in the correlations for the power consumption in the gas-liquid multiphase flow systems in the stirred tanks are ungassed power consumption (P), gassing rate (Q_g), fluid properties such as density (ρ) and viscosity (μ), impeller agitation speed (N) and impeller geometry (Paul et al., 2004). In this investigation, the following equation was proposed to correlate above parameters:

$$\frac{P_g}{P} = K_1 Re^{K_2} \left(\frac{Q_g}{NV_l}\right)^{K_3} \tag{6.10}$$

where K_1, K_2, K_3 are equation variables will be determined by CFD data regression. The data used for regression can refer to Appendix 6.1 Data Used for Regression to Estimate the Impeller Power Consumption of the Gas-ionic Liquid Multiphase Flow System. The regression result is showing as:

$$\frac{P_g}{P} = 2.7Re^{-0.08}\left(\frac{Q_g}{NV_l}\right)^{-0.006} \tag{6.11}$$

The value of R Square is 0.94 which indicates a good accuracy of this correlation, and this equation is applicable to predict the impeller power consumption of the gas-ionic liquid transitional flow in a stirred tank agitated by a Rushton turbine impeller.

6.5 Conclusions

In order to verify the multiphase models and approaches used (Eulerian-Eulerian approach, the RNG *k-ε* model, the mono-size assumption, the sliding mesh method, the Schiller-Naumann drag force coefficient model) in this investigation, the gas-water multiphase flow modelling was carried out based on a vessel with the same geometry and boundary conditions from reference. The multiphase models and approaches applied in this vessel were found to yield results in good agreement with the PIV data in literature. The verified multiphase models were then used to investigate the gas-ionic liquid multiphase flow under various operation conditions in the stirred tank used in this study.

The gas-ionic liquid multiphase simulation found that

- The ionic liquid flow pattern was very similar at condition with and without gas injection. Slight difference can be found in area near tank bottom where dead zone region was formed at condition with gas injection.
- The detailed information of the velocity components of the gas and liquid phase were plotted at different height of the stirred tank. It showed that, unlike the inhomogeneous distributions of bubbles in the gas-water turbulent flow, the bubbles in the gas-ionic liquid system follow well with the ionic liquid and circulate in the most region of stirred tank resulting in the increase of gas holdup in stirred vessel.
- The effect of the impeller speed and gassing rate on the flow field were investigated. The results indicated that the increasing impeller speed can significantly reduce the dead zone area near tank bottom, whereas the growth of gassing rate resulted in the increase of dead zone regions, which decreases the degree of the homogeneous mixing and mass transfer rate of the multiphase flow system.
- The increase of gassing rate is more effective on improving the overall gas holdup in the stirred tank than increasing the impeller speed. At regions above the dished bottom, obvious increase of gas holdup can be observed with increasing gas flow rate. However, in regions close to the tank bottom, the increase of the gassing rate will enlarge the dead zone and reduce the local gas holdup in these regions. As a result, poor mixing areas were formed in the regions near the tank bottom at high gas flow rate. Therefore, higher impeller speed and lower gas flow rate are recommend to operate

the gas-ionic liquid multiphase flow in stirred tank to achieve the homogeneous mixing and improve the mass transfer rate and final products quality.

- A correlation was proposed to predict the impeller power consumption of the gas-ionic liquid transitional flow in a stirred tank agitated by a Rushton turbine impeller.

CHAPTER 7: EXPERIMENTAL VALIDATION OF THE CFD MODELS USING PIV

7.1 Introduction

This chapter focus on the experimental validation of the CFD modelling using the Particle Image Velocimetry (PIV) technique. PIV is a nonintrusive optical flow measurement and visualization technique, that is broadly used to investigate the flow field and the turbulent quantities in the single phase and multiphase flow systems (Paul et al., 2004). The PIV system can directly measure the instantaneous velocity for an entire plane of a flow field, which makes it have obvious advantages over the point wise measurement such as the capillary suction probe and Laser Doppler Anemometry for measuring the flows in the stirred tanks(Oakley et al., 1997). A detailed introduction of the PIV system including its components, measuring principles and measuring process is discussed in section 2.4 in chapter 2.

Since the physical properties of the ionic liquid ($BmimBF_4$) are different from water, a suitable particle tracer needs to be carefully selected to faithfully follow the motion of the ionic liquid. The selection of the particle tracers is introduced at the section 7.2 of this chapter. Afterward, the procedures of the PIV experiments were introduced, where a 2D3C (which measures two dimensions and three velocity components of the flows) PIV system was used to measure the water turbulent flow in a stirred tank and a 2D2C (which measures two dimensions and two velocity components of the flows) PIV system equipped with lens filters were adopted to measure the single phase ionic liquid and gas-ionic liquid multiphase flows in a stirred vessel.

In order to validate the simulation models and approaches used in this investigation, the PIV experimental results including single phase water flow, single phase ionic liquid flow and gas-ionic liquid multiphase flow in a stirred tank were compared with the simulation data in terms of the flow pattern and velocity components in the stirred tank. The PIV and simulation data showed good agreements, which indicates good accuracy of the CFD modelling.

7.2 Selection of Particle Tracer

Since the physical properties of the ionic liquid are very different from water and the tracers listed in the Table 7.1 showed excellent traceability with water (Dantec, 2005), the particle tracer used for the ionic liquids PIV measurement has to be selected carefully. To select the tracers, the Dantec PIV manual (Dantec, 2005) has stated a number of criteria which should be:

- Able to follow the flow
- Good light scatters
- Conveniently generated (and cheap)
- Non-toxic, non-corrosive and non-abrasive
- Non-volatile or slow to evaporate
- Chemically inactive (and clean)

Table 7.1 summarized the available particle tracers provide by the Dantec Company. Among the tracers listed in the Table 7.1, the PSP, HGS and S-

HGS tracers are suitable for the PIV measurement of the single phase flows and the PSP tracer is highly recommendable for the water flow applications (Dynamics, 2017b). The FPP tracer is designed for the PIV measurement of the liquid single phase or the gas-liquid multiphase flows. The FPP tracer is the most expensive one.

Table 7.1 Specifications of the Particle tracer

Tracers / Properties	**PSP** Polyamide Seeding Particles	**HGS** Hollow Glass Spheres	**S-HGS** Silver Coated Hollow Glass	**FPP** Fluorescent Polymer Particles
Price	167,00 euro/bottle	75,00 euro/bottle	228,00 euro/bottle	1.843,00 euro/bottle
Mean diameter (μm)	5,20,50	10	10	10,30,75
Size distribution (μm)	1-10 5-35 30-70	2-20	2-20	1-20 20-40 50-100
Particle shape	Non-spherical but round	spherical	spherical	spherical
Density (kg/m^3)	1030	1100	1400	1500
Melting point (℃)	175	740	740	250
Refractive index	1.5	1.52	-	1.68
Material	Polyamid 12	Borosilicate glass	Borosilicate glass	Melamine resin based polymer

The Stokes number (*St*) is widely accepted as traceability indicator for the particle tracers where proper tracer should have the Stokes number $St \ll 1$, and a $St \leq 10^{-3}$ is preferred as in this condition that the experiment deviations caused by the particle tracer are negligible (Tropea, 2007, Hamdi et al., 2014). The Stokes number (St) can be calculated using the equation below:

$$St = \frac{\tau_p}{\tau_f}$$

(7.1)

where τ_p is the relaxation time of the particle tracer. τ_f is the characteristic time of the carrier fluid, which is Kolmogorov time scale here. τ_p and τ_f is obtained through the below equation 7.2 and 7.3:

$$\tau_p = d_p^2 \frac{\rho_p}{18\mu}$$

(7.2)

$$\tau_f = (\frac{\nu}{\varepsilon_{avg}})^{1/2}$$

(7.3)

where d_p is the tracer diameter. ρ_p is the density of tracer. μ is the viscosity of ionic liquid which equals 0.07 Pa.s. ν is the kinematic viscosity, which is the ratio of the liquid dynamic viscosity (μ) and density (1210 kg/m^3). ε_{avg} is the mean energy dissipation rate of the fluids calculated by the following equation:

$$\varepsilon_{avg} = \frac{\rho_l N^2 D^5 P_0}{\rho_l V}$$

(7.4)

where ρ_l is the density of ionic liquid. *N* is the impeller speed which equals 2.5 rps or 7.3 rps, *D* is the impeller diameter which equals to 0.075 m, P_0 is the power number which is 3.4. V is the volume of liquid in the stirred tank, which equals 2.5×10^{-3} m^3.

According to equations 7.1 to 7.4, the calculated *St* at impeller speed of 7.3 rps is 1.7×10^{-5} for the PSP tracer, and 4.7×10^{-6}, 6.0×10^{-6}, and 5.8×10^{-5} for the HGS, S-HGS and FPP tracer respectively. The calculated *St* at impeller speed of 2.5 rps is 6.1×10^{-6} for the PSP tracer, and 1.6×10^{-6}, 8.2×10^{-6}, and 1.7×10^{-5} for the HGS, S-HGS and FPP tracer respectively. Since the proper tracer should have the Stokes number *St* $\ll$1, and a *St* $\leq10^{-3}$ is preferred as in this condition the experiment deviations caused by the tracer particle are negligible, the calculation shows that all the tracers listed in Table 7.1 have good traceability for the flows of ionic liquid.

In addition to the traceability indicator of *St*, in order to track the smallest turbulence structures of the turbulence flow, the particle tracer should be smaller than the Kolmogorov length scale of the turbulence. The below equation can be used to calculate the Kolmogorov length scale:

$$\eta_l = (\frac{\nu^3}{\epsilon})^{1/4}$$

(7.5)

The Kolmogorov length scale of the turbulence in the stirred tank was calculated according to the equation 7.5, and the Kolmogorov length scale was found to be 0.001 m and 0.002 m at the impeller speed of 7.3 rps and 2.5 rps respectively. As can be shown in Table 7.1, all the tracers are smaller than the Kolmogorov length scale of the turbulence. Therefore, they all can track the smallest turbulence structures of the flow of the ionic liquid.

In general, the tracking ability of the suspended tracers is influenced by the particle shape, particle diameter, particle density and fluid density (Melling, 1997). However, these are based on the condition that the particle concentration is low and the particles are homogeneously dispersed in the fluid. Therefore, it is important to make sure that there is little interactions between the particles (Melling, 1997). The concentration of the tracers seeded in the flow should be very low so that the particles are generally separated from each other by several equivalent particle diameters. Besides, the ionic liquid $BmimBF_4$ is hydrophilic (Opallo and Lesniewski, 2011) and the hydrophilic tracer will be suitable. The tracers listed in Table 7.1 have good ability of homogeneous dispersion in water (DantecDynamics, 2013). Therefore, the tracers list in the Table 7.1 can be well dispersed in the ionic liquid and the interaction between the particle tracers can be ignored in the PIV measurement.

In addition, the accuracy of the PIV is also influenced by the light scattering ability of the tracers. The light scattering ability of the tracers is directly related to the tracer diameter. Larger particles scatter more light than the smaller ones do, which therefore enhances the signal strength for the camera (Dantec, 2005). However, if the tracer size is larger than the Kolmogorov length scale, the detailed information of the turbulence cannot be captured and may also cause problem of the traceability of particle. In this study, a Nd:YAG pulsed laser with a wavelength of 532 nm was used in the PIV system, and the range of the tracer diameter within 0.1-50 um would be appropriate for this laser (Dantec, 2005). Thus, the particle tracers listed in Table 7.1 with diameter less than 50 um can be used in this investigation.

Based on the above discussion, the PSP tracer (with a mean diameter of 20 μm) due to its excellent traceability of the flows of water, was used for the PIV measurement of single phase water flow in the stirred tank. The FPP tracer (with a mean diameter of 30 μm), due to its application on the PIV measurement of the liquid single phase and gas-liquid multiphase flows, was used in the single phase ionic liquid and multiphase flows PIV experiment.

7.3 The Experimental Techniques

7.3.1 Experimental Rig Setup

The Dantec PIV (laser model: Litron NANO TRL 425-10) was used in this study. Figure 7.1 illustrates the key components of the experimental rig including the PIV system and the stirred tank. The Nd: YAG Pulsed Laser is served as the laser source which emits a laser beam with a wavelength of 532 nm. A laser sheet probe equipped with a prism lens was fixed at the end of the laser arm to transform the laser beam into a fan-shaped light sheet. The traverse control system was used to control the position of the cameras which are fixed on the traverse. A synchronizer is used to accurately control the time between each pulse of the laser and the placement of the laser beam in the testing area to the camera's timing. The images are captured by two Imperx cameras (2048×2048 pixels CCD). The impeller agitation speed was controlled by an operation platform.

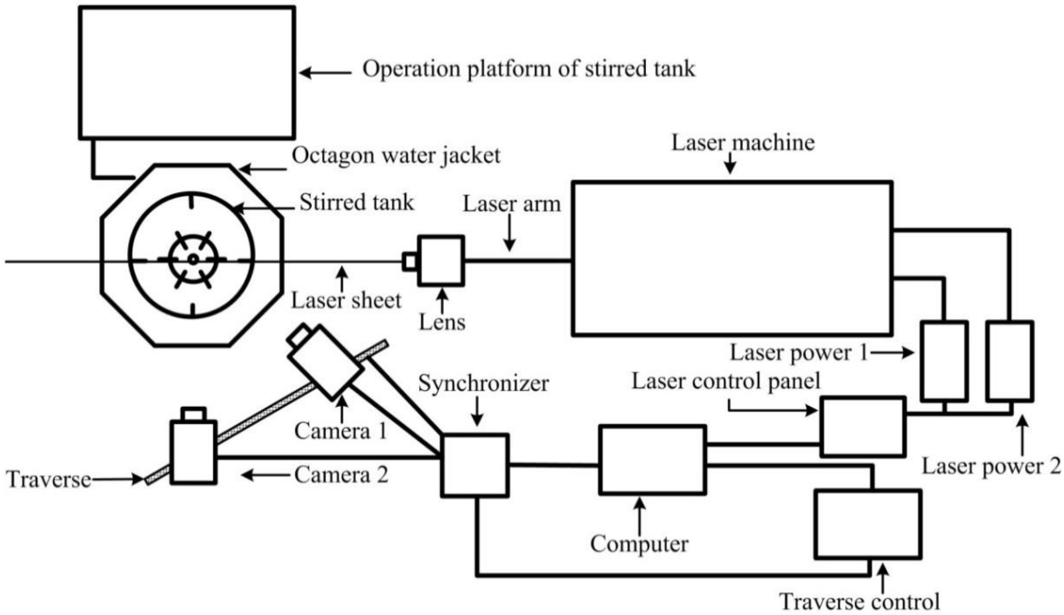

Figure 7.1 The experimental rig

The flows are operated in a dished bottom stirred tank with baffles reaching to the edge of dish (DBD tank). In order to minimise the optical refraction, the stirred tank was placed in an octagon glass tank filled with water. The water in the stirred tank was seeded with the PSP particle tracer with 20 μm in diameter and density of 1030 kg/m^3. The laser, cameras, synchronizer, data acquisition and processing were controlled and operated by the “Dynamic Studio” software installed on a computer.

With the purpose of avoiding the strong reflect light when laser reaches the metal components in the measuring area, which would cause severe damage to the cameras, all the metal components such as the baffles, impeller and shaft in the stirred tank were coated with matte Teflon.

7.3.2 General Procedure of the PIV Measurement

In this investigation, the general procedure of the flow field measurement using PIV is as below:

- The first step is to identify the intended measuring target and align the laser sheet to the measuring target (a plane for two-dimensional PIV measurements) (Figure 7.2a).

- The camera calibration is very important for accurate PIV measurement. To calibrate the camera, a calibration target, which contains calibration markers in known positions on the target surface, was placed at the intended measuring plane (Figure 7.2c).

- Record the images of the calibration target at the intended measuring plane using cameras (Figure 7.2d and Figure 7.2e). By comparing the known markers positions with the corresponding markers positions on each camera image, the cameras are calibrated and the coordinate system of the measuring plane is established by the "Dynamic Studio" software.

- After the calibration, turn on the laser and record the particle images in the flow using the cameras to measure the flow field (Figure 7.2f).
- Afterward, convert the signals of the particle images to the vectors of flow field.
- Finally, post-process the particle images and create the vectors map of the flow in the intended measuring area.

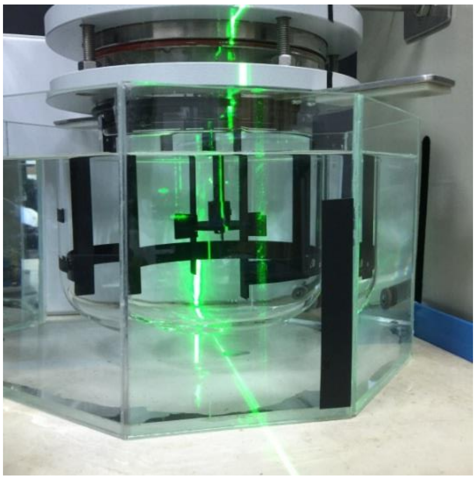

(a) Identify the measuring plane

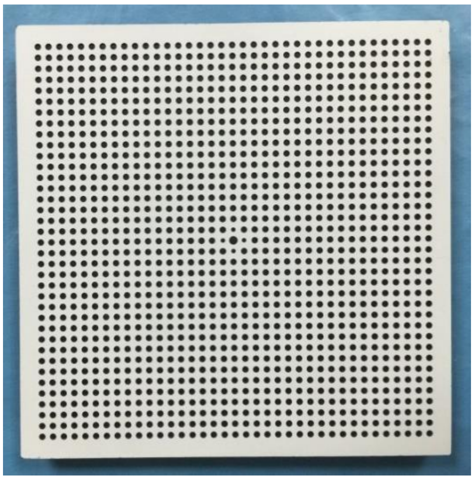

(b) The calibration target

(c) Place the calibration target at the testing area

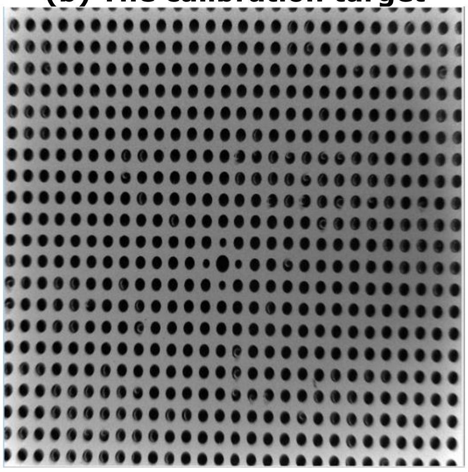

(d) The view of the calibration target from the right camera

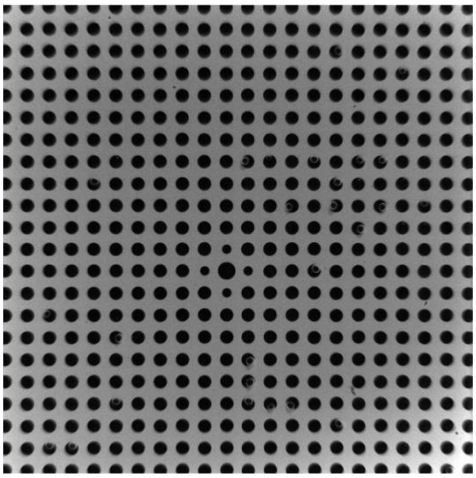

(e) The view of the calibration target from the left camera

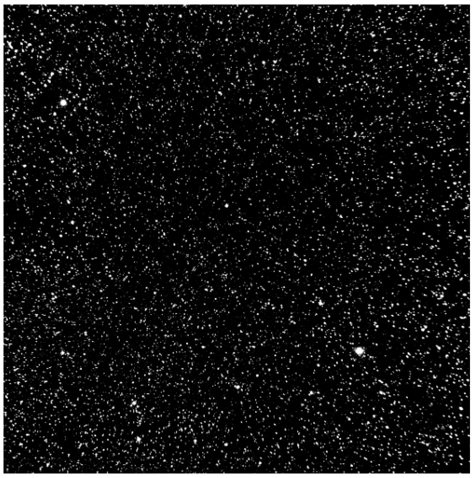

(f) The image of the particle tracers captured by the cameras

Figure 7.2 General procedure of PIV experiment

7.3.3 PIV Measurement Procedure in the Single Phase Water Flow in a Stirred Tank

Followed by the general PIV measurement procedure introduced in section 7.3.2, the PIV system was used to measure the single phase water flow in the stirred tank. The PIV measurements were carried out at a vertical laser plane passing through the centre of the impeller as shown in Figure 7.1. In order to validate the previous CFD results, the PIV experimental data were sampled at the same flow regions as the areas where the CFD modelling results obtained.

The water in the stirred tank was seeded with the PSP tracers. Two telecentric lenses were adopted to measure the 2D3C water turbulent flow field in the stirred tank, where the velocity components in the x and y directions were obtained by analysing the tracers' images illumined by the pulsed laser and the velocity component in the z direction was derived by using two cameras in the stereoscopic arrangement (Dynamics, 2017a).

Due to the feature of the telecentric lens, the angle of view from this lens is detailed and the testing area is small (in Figure 7.3).

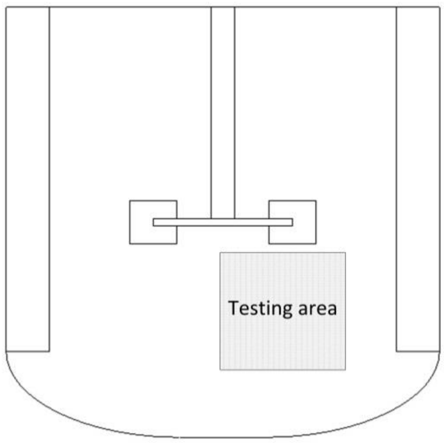

Figure 7.3 Testing area of the single phase water flow in the stirred tank

In the process of the PIV measurement of the single phase water flow in the stirred tank, a pair of tracer images illumined by a sequence of two light pulses is recorded by two cameras and the images are divided into subsections called interrogation areas. The interrogation areas are next correlated pixel by pixel. The correlation produces a signal peak identifying the common particle displacement (Dynamics, 2017a). This displacement can then be used to construct a 2D vector map. In this study, the time interval between two laser pulses was set 1500 μs, which makes sure that the move distance of the tracers in the gird cells plotted by the software is about a quarter to a half of the cell side length when the tracer images were sampled. By doing this, the image processing programme can accurately track the trajectories of the tracers. The cross correlation of the image pairs was processed on a grid with 50% overlap between adjacent cells and the images were divided into several 64×64 pixels interrogation areas, which produces more detailed velocity vectors when the images were processed. After that, the removal of the velocity outliers, interpolation calculation and velocity field smoothing were carried out, which all enhance the accuracy of the PIV measurement results.

In order to get the time-averaged variables of the flow field, the number of the required images sampled in the PIV measurement in the intended measuring area should be identified. To accurately measure the velocity magnitude of a single point in the intersection of the height 40 mm above the tank bottom and radial distance of 10 mm away from the axial centre, a number of 50, 100, 150, 200 pair of images were collected and processed respectively to determine the proper sampling number. The velocity magnitudes of this point at various numbers of samples were shown in Figure 7.4. As can been seen from Figure 7.4, the measured data shows almost constant value when the number of sampled images is larger than 100. Therefore, the PIV data were obtained from 150 tracer images and these data were used to validate the CFD results of single phase water and ionic liquid flows.

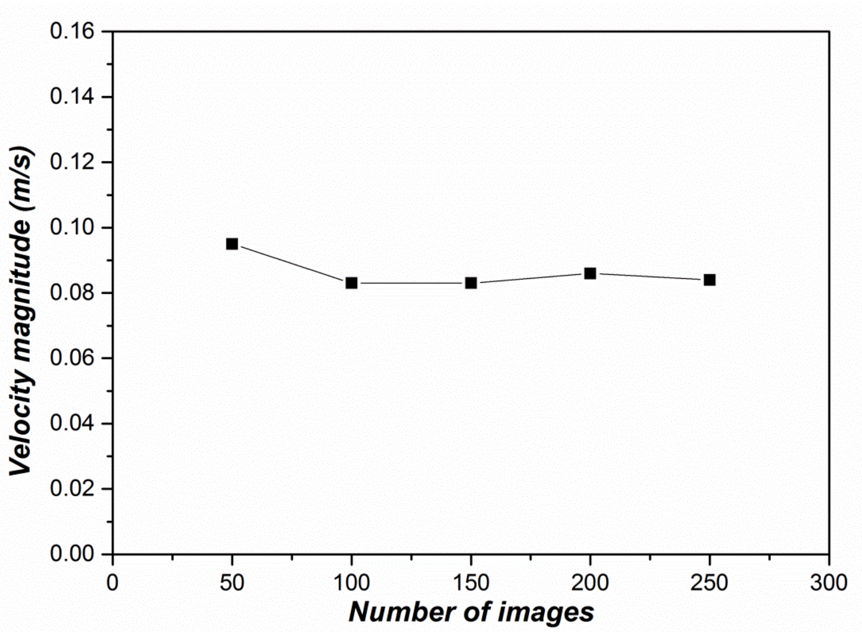

Figure 7.4 Velocity magnitudes at sampling point

7.3.4 PIV Experiment Procedure in the Gas-ionic Liquid and the Ionic Liquid Flows in a Stirred Tank

There is limited amount of ionic liquid in this investigation. And it is found that the FPP tracer can be used in the single phase and multiphase flow PIV measurement applications. In addition, the ionic liquid is hard to reuse in the multiphase flow PIV measurement if it was already seeded with other tracers such as the PSP and HGS tracer for single phase flow PIV measurement. Due to the above reasons, the FPP tracer was used for the single phase ionic liquid flow and gas-ionic liquid multiphase flow PIV measurements.

Due to the large size of the telecentric lenses, they cannot be fixed behind the spectroscope which is used to separate the scattered laser light of the FPP tracers and bubbles from the laser illuminated area in the gas-liquid flow domain. Two small-sized prime lenses provided by the Dantec

Company were fixed behind the spectroscope. It was found that, as showed in Figure 7.5, the angle of view of the prime lens is much larger than that of the telecentric lens used in the single phase water flow PIV measurement.

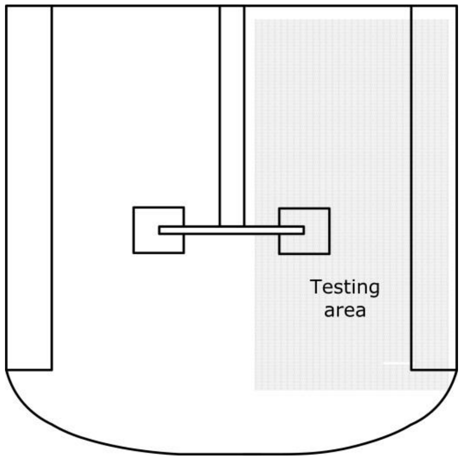

Figure 7.5 Testing area of the ionic liquid and the gas-ionic liquid flows

There are two cameras installed with two different colours of light filters to capture the tracers' images in the liquid phase and the gas phase separately. The orange light filter was installed at the lens of one camera, which allows the passage of the scattered light (wavelength of 600 nm) from the fluorescent particles in the liquid while blocking the scattered light from the bubbles. By doing this, only the images of the tracers in the liquid phase can be captured by one camera and the velocities of the liquid phase can be measured by analysing the FPP tracers' images. The bubbles in the stirred tank were served as the tracers for the gas phase. The gas phase velocities were determined by equipping a green filter on another camera, which only permits the passage of the laser scattered by the bubbles and meanwhile blocks the light scattered from the FPP tracers.

The velocities of the gas phase can be obtained by analysing the bubbles' images in the multiphase flow domain.

In the process of the single phase ionic liquid flow PIV measurement, the camera equipped with the orange light filter which allows the passage of the scattered light by the fluorescent particles was used to record the images of tracers in the ionic liquid. Meanwhile, another camera equipped with the green light filter was not used by covering a lens cap. In this way, only the images of the illuminated fluorescent tracers were recorded and analysed to visualize the single phase flow field. Whilst, both cameras were used in the gas-ionic liquid multiphase flow PIV experiment.

The time interval between two laser pulses was set at 1200 μs in both single phase ionic liquid and multiphase flows PIV measurement, which makes sure that the move distance of tracers in the gird cells plotted by the software is about a quarter to a half of the cell side length and thus resulting in good experimental results.

With the purpose of getting accurate time-averaged multiphase flow fields in the PIV measurements, the numbers of the tracer images to be collected should be identified beforehand. The time-averaged velocity magnitudes of the liquid phase and the gas phase at a point close to the impeller blade were obtained by analysing various numbers of tracer images. The velocity magnitudes of the gas phase and the liquid phase at this single point are calculated from the different number of images and are plotted in Figure 7.6.

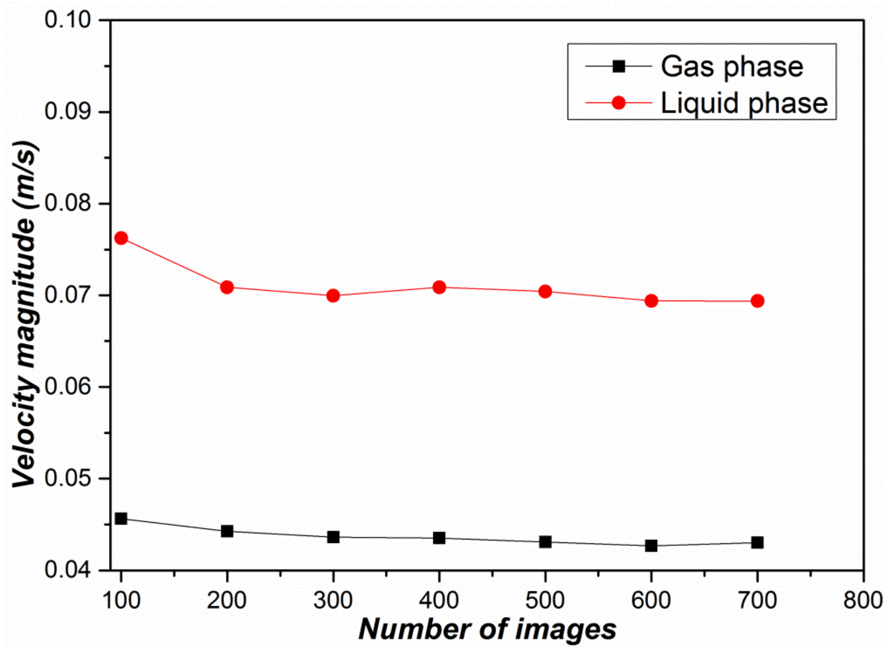

Figure 7.6 Velocity magnitudes at a sampling point

As can be seen from Figure 7.6, the velocity magnitudes of gas phase and the liquid phase show almost constant value when the amount of the sampled images are more than 200. Therefore, it is decided that at least 300 tracer images of liquid phase and gas phase should be recorded and analysed during the PIV measurement of the gas-ionic liquid multiphase flow.

7.4 Single Phase Flow PIV Validation

7.4.1 Single Phase Water Flow PIV Validation

Since the CFD results of the velocity components predicted by the standard *k-ε* model and LES were almost identical, only the simulation results obtained from the standard *k-ε* model were displayed and compared with the PIV data.

The PIV and simulation data were sampled in a dished bottom stirred tank with baffles reaching to the edge of dish (DBD tank). The sampling area was as shown in Figure 7.3. The vectors of the flow field predicted by the CFD and measured by the PIV at the measuring area are shown in Figure 7.7 and Figure 7.8 respectively. As displayed in Figure 7.7 and Figure 7.8, both the CFD and PIV data show similar flow field, where the shape of downward circulation loop is identified successfully. These two figures show that the jet flow from the impeller hits the tank wall and flows axially towards the tank bottom. After the axial flow reaches to the tank bottom, it axially moves towards the impeller. Both Figure 7.7 and Figure 7.8 show the very low liquid velocity below the impeller, which indicates that a dead zone is formed in this area.

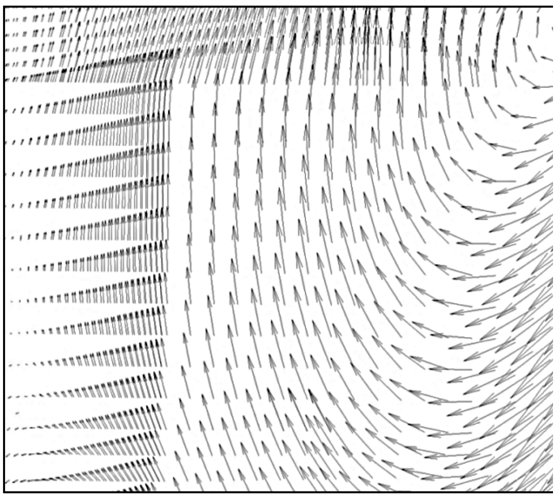

Figure 7.7 Vectors of flow field in the sampling area (CFD results)

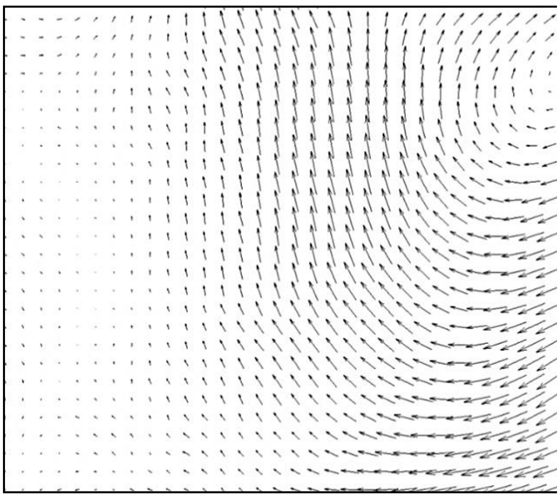

Figure 7.8 Vectors of flow field in the sampling area (PIV results)

In order to provide more detailed information of the water flow field, the PIV and simulation data are plotted at a horizontal plane 40 mm (z/H=0.27) above the tank bottom from the axial centre (r/R=0) towards the tank wall (r/R=1.0). The values of the velocity components were normalized by the impeller tip velocity (U_{tip}=0.59 m/s). The radial distance was normalized by the radius of the stirred tank (R=0.075 m).

Figure 7.9 shows the measured and predicted radial velocity profiles at this horizontal plane. Since this plane passes through the downward circulation loop where the flows are mainly axial, liquid velocities are quite low in the radial direction. As can be observed in Figure 7.9, in generally, the CFD data of the radial velocity component fit well with the PIV results showing very low radial velocity distributions at this plane.

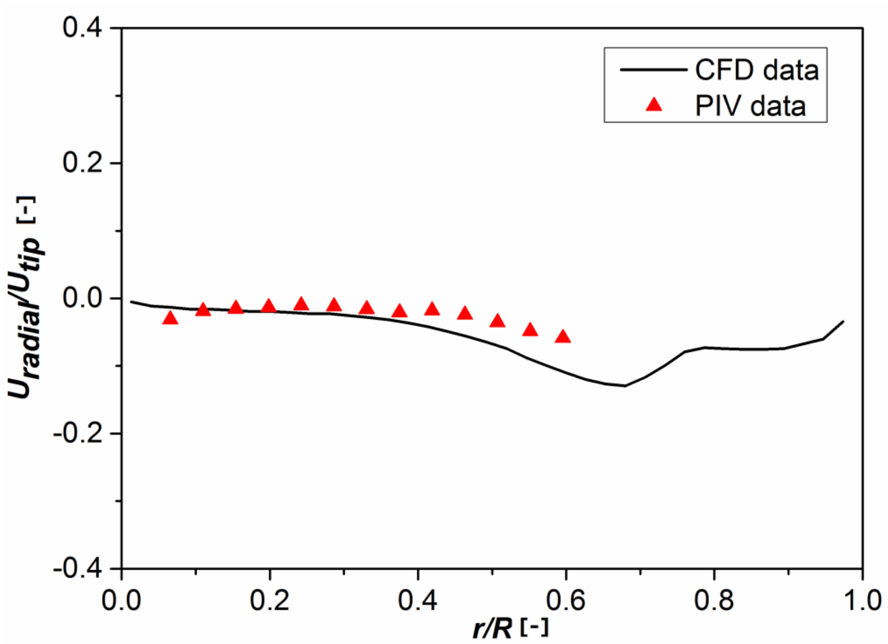

Figure 7.9 Radial Velocity profiles obtained by PIV and CFD (at *z/H*=0.27)

Figure 7.10 illustrates the tangential velocity profiles at this sampling plane. According to Figure 7.10, both the PIV and CFD data show a peak value at radial distance around 0.3R below the impeller. As was mentioned in the chapter 3, this indicates that a forced vortex is formed in this area. Liquid in this forced vortex area is rotating like a rigid body without efficient mixing in the axial direction, which leads to poor mixing in this area.

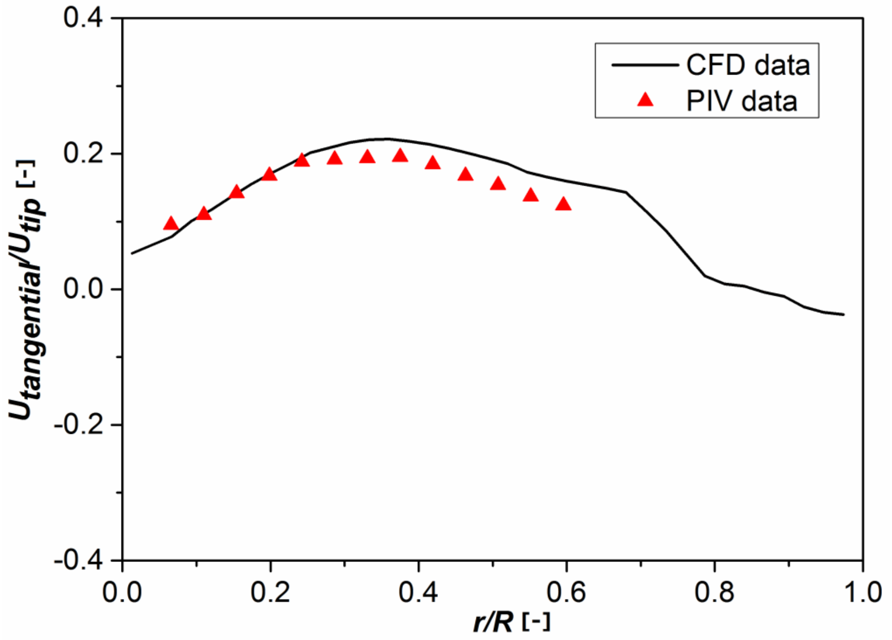

Figure 7.10 Tangential velocity profiles obtained by PIV and CFD (at z/H=0.27)

Figure 7.11 compares the axial velocity profiles at the plane obtained by the PIV and CFD respectively. The PIV results and the CFD data indicate the nearly zero axial velocities at this plane centre, implying that the liquid mixing at the axial direction below the impeller is poor which will cause problems of suspending solid particles and increase the liquids mixing time in the stirred tank.

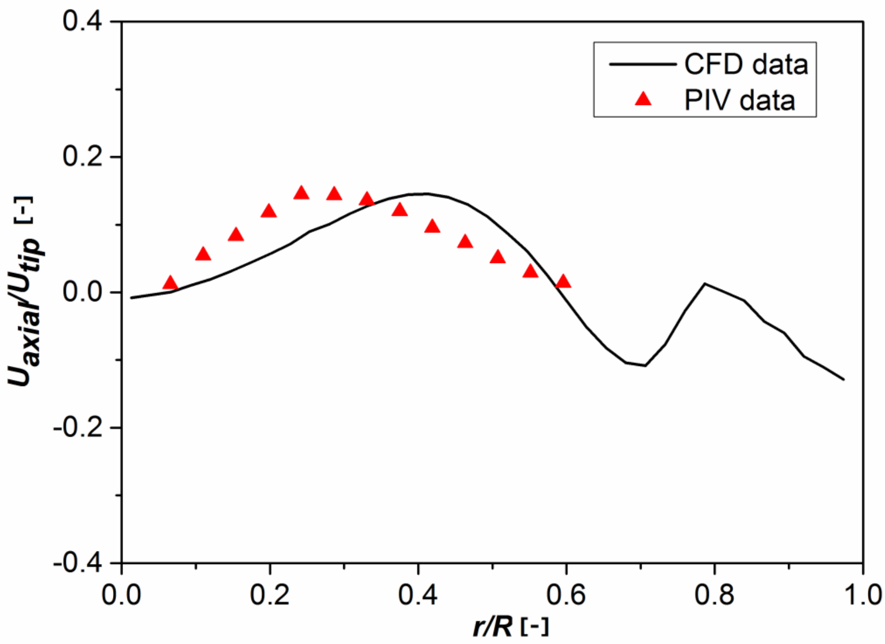

Figure 7.11 Axial Velocity profiles obtained by PIV and CFD (at z/H=0.27)

Generally, the existence of the dead zone area numerically identified in the DBD tank below the impeller disk is experimentally validated by the PIV experiment. The CFD data showed good agreement with the PIV results, especially for the velocity components in the radial and tangential directions. Differences can be observed in the axial velocity components, which may attribute to the below factors. Firstly, the four metal baffles are made by hand and are connected by the metal strips. The baffles are not perfect perpendicular to the horizontal plane when they are fixed inside the stirred tank. Since the position of the baffles have significant effect on the turbulent flow in the axial direction in a stirred tank (Karcz and Major, 1998), the slight geometry difference between the CFD and the position of the baffles in the real tank may give rise to the difference between the CFD and PIV data as shown in the Figure 7.11. Secondly, the glass stirred tank is a handmade vessel, so the inner wall and the dished bottom are not as universally smooth and flat as the model geometry created by the computer software, which may cause discrepancies between the simulated data and PIV measured results. Third, the Rushton turbine impeller is mounted on a shaft with a shaft's end extended about 1 cm below the impeller disk. This shaft is not perfectly coaxial with the motor which drives the shaft. The extended shaft below the impeller may disturb the core of the forced vortex below the impeller and cause the discrepancies between the CFD and PIV results.

7.4.2 Single Phase Ionic Liquid Flow PIV Validation

The single phase ionic liquid flow simulation results obtained by the LES were displayed and compared with the PIV data in this section. The PIV and simulation data were sampled at the same position in the stirred tank, which is shown in Figure 7.5 with a focus being on the region below the impeller. The vectors of the flow field in the measuring area obtained by the CFD and PIV are compared in Figure 7.12 and Figure 7.13 respectively. As displayed in Figure 7.12 and Figure 7.13, both the CFD and PIV data show the similar flow pattern where the rotating impeller pushes the surrounding liquids flow radially towards the tank wall. After the radial jet flows reach the tank wall, downward circulation loops are formed below the radial jet flows. Unlike the downward circulation loops in the water turbulent flow, the downward circulation loop in the ionic liquid does not reach to the tank bottom but starts flowing back to the impeller in the midway between the impeller and vessel bottom. The intensity of the circulation loops have reduced a lot compared to that in the turbulent water flow (Figure 7.8) in the stirred tank, which can result in poor mixing efficiency of the stirred tank (Zhang et al., 2013).

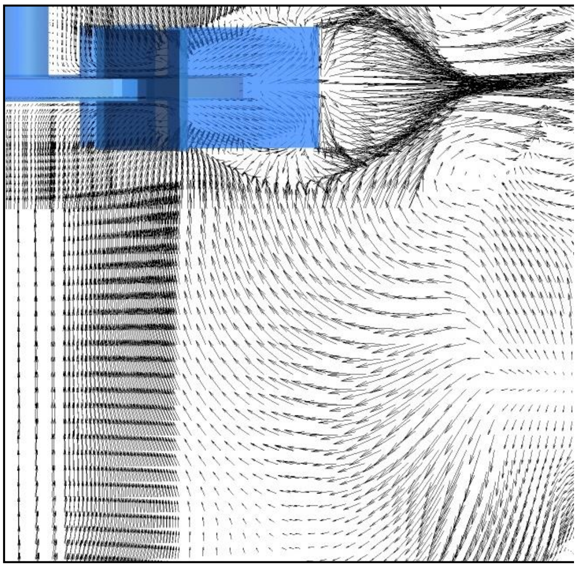

Figure 7.12 Vectors of the ionic liquid flow field in the sampling area (CFD)

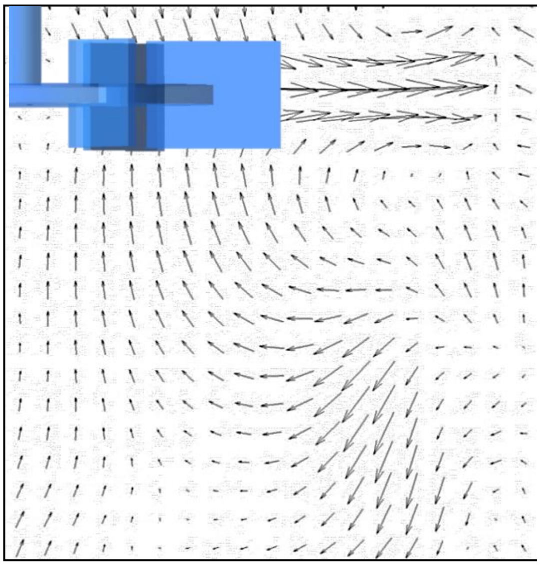

Figure 7.13 Vectors of ionic liquid flow field in sampling area (PIV)

The ionic liquid flow in the axial direction below the impeller disk (in Figure 7.12 and Figure 7.13) implies that the dead zone area found in the water turbulent flow (Figure 3.21) is minimized when the ionic liquid flow is operated in the transitional state.

In order to show the more detailed information of the flows in the region below the impeller, the PIV and CFD data of the single phase ionic liquid flow were plotted at a horizontal plane 40 mm above the tank bottom (z/H=0.27) from axial centre (r/R=0) towards the vessel wall (r/R=1.0) with the ionic liquid flow being operated in the transitional state in the stirred tank. The values of the velocity components were normalized by the impeller tip velocity (U_{tip}=1.73 m/s). The radial distance was normalized by the radius of the stirred tank (*R*=0.075 m). Since the current PIV rig can only measure the flow in the radial and axial direction, only the velocity components of the radial and axial velocities obtained by the PIV were compared with the corresponding CFD data.

Figure 7.14 shows the radial velocity profiles obtained by CFD and PIV respectively at this sampling plane. As can be found in Figure 7.14, in the ionic liquid transitional flow, the radial velocity component shows negative value away from axial centre (*r*/*R*=0), which indicates that the intensity of the downward circulation loop has reduced and the fluids begin to flow towards the impeller before reaching the bottom of stirred vessel.

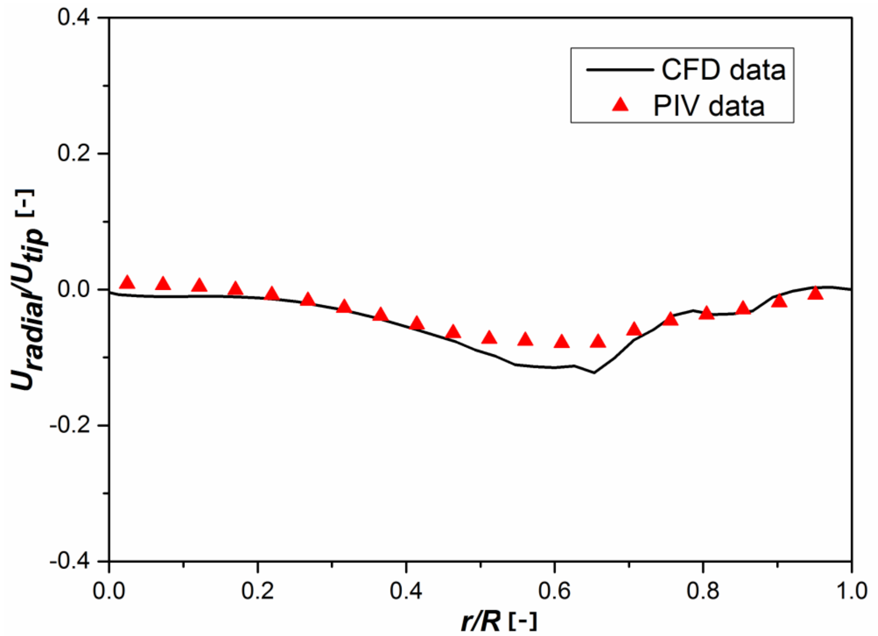

Figure 7.14 Ionic liquid radial velocity profiles obtained by PIV and CFD (at *z*/*H*=0.27)

Figure 7.15 illustrates the axial velocity profiles obtained by CFD and PIV respectively at this sampling area. As can be observed from this figure, there is strong effect of flow regime on the axial velocity profiles. In the water turbulent flow (shown in Figure 7.11), the velocity in axial direction at the centre of this plane is almost zero, whilst the axial velocity of the ionic liquid is around $0.06U_{tip}$ at the corresponding region. Therefore, compared with water turbulent flow in the DBD tank, the mixing in axial direction below the impeller disk has slightly increased when the ionic liquid is used as operation liquid in the DBD tank.

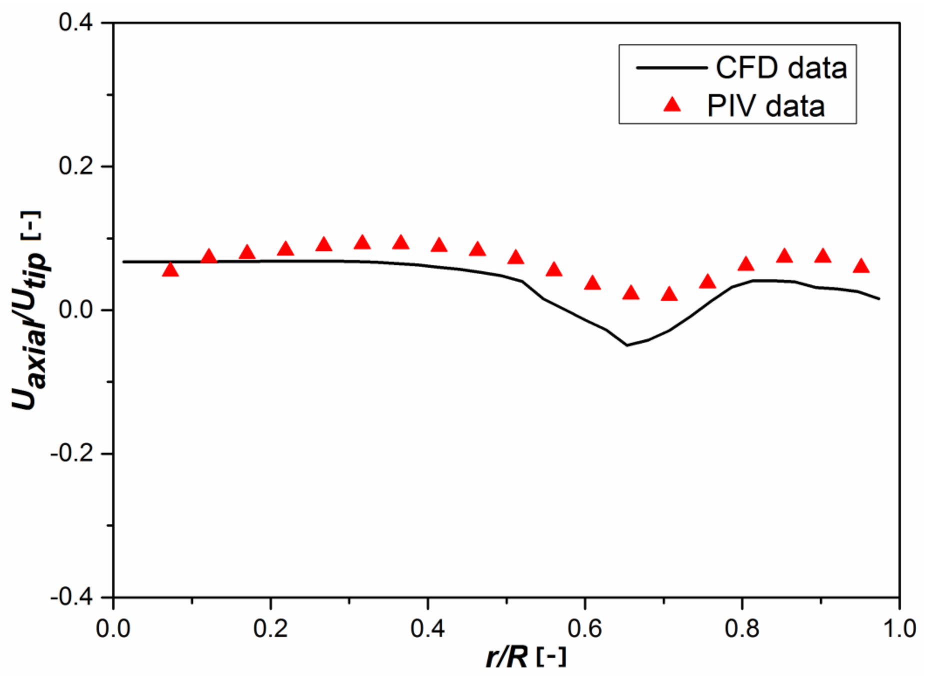

Figure 7.15 Ionic liquid axial velocity profiles obtained by PIV and CFD (at *z*/*H*=0.27)

The PIV measurements validate the CFD models that the short baffles in the DBD tank has a slight effect on generating the dead zone area below the impeller disk when the flow is in the transitional status, whereas, a large and clear dead zone area is identified in the water turbulent flow. The PIV data of the ionic liquid transitional flow in the stirred tank showed agreement with the CFD results, which proves the accuracy of the simulation models used in this investigation.

7.5 Gas-ionic Liquid Multiphase Flow PIV Validation

This section concerns the validation of the gas-ionic liquid multiphase flow modelling in the stirred tank using PIV. The ionic liquid in the stirred tank was seeded with the FPP tracers. Two cameras with the orange and green filters were used to record the tracer images of the liquid phase and the gas phase in stirred vessel respectively. Only the axial and radial velocity components predicted by CFD were compared and validated due to the limitation of the current PIV rig. Since the volume fraction of the gas below the impeller is very high and the strong reflected laser light from the dished bottom will cause severe damage to the cameras, the flow in regions below the impeller shaft and dished bottom area were not measured to protect the PIV system.

The gas-ionic liquid multiphase flow was measured at an impeller speed of 150 rpm and a gassing rate of 0.1 L/min, which are the same operation conditions with the CFD modelling. Figure 7.16 and Figure 7.17 show the vectors of the liquid phase and gas phase respectively measured by PIV. These two figures indicate that the gas phase and liquid phase show very similar flow pattern implying that the presence of the gas phase does not cause significant change of flow pattern at current operation conditions. Compared with the gas-water turbulent flow in the stirred tank showed in the chapter 6, the intensity of the downward and upward circulation loops has greatly reduced when the ionic liquid is agitated in the stirred tank.

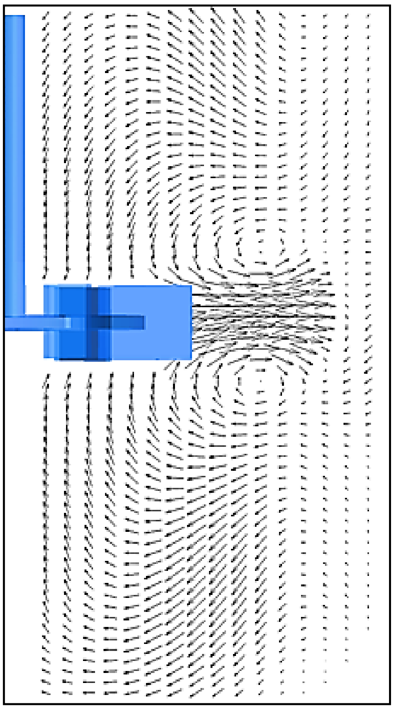

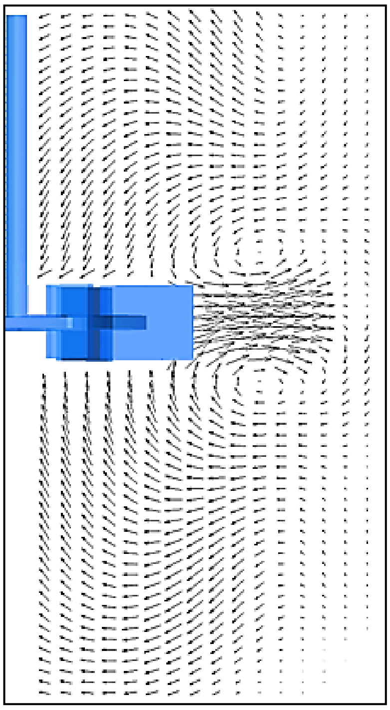

Figure 7.16 PIV measured vectors of the flow field (liquid phase)

Figure 7.17 PIV measured vectors of the flow field (gas phase)

The vectors of the liquid and gas flow fields predict by the CFD are shown in Figure 7.18 and Figure 7.19 respectively at a vertical plane in front of one baffle with this plane being almost identical as the laser plane in PIV measurement. The predicted liquid and gas flow patterns show good agreement with the PIV results, which indicates the accuracy of the CFD modelling.

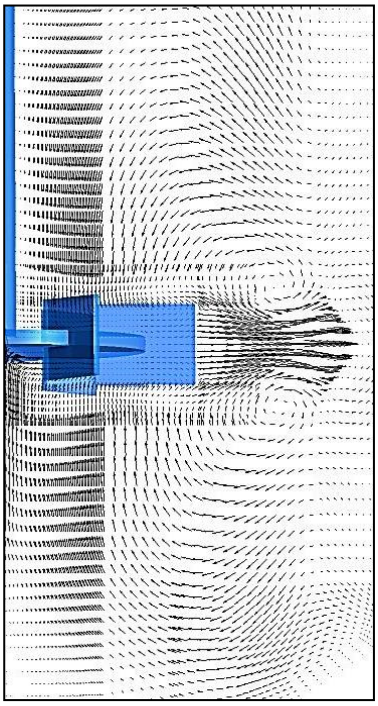

Figure 7.18 CFD simulated vectors of the flow field (liquid phase)

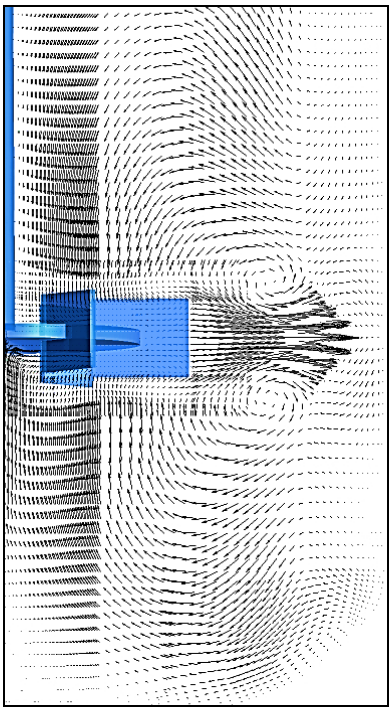

Figure 7.19 CFD simulated vectors of flow field (gas phase)

Figure 7.20 to Figure 7.23 compare the radial and axial velocity components of the gas and liquid phase predicted by the CFD with measured ones by PIV at the plane of z/H=0.5. As can be observed from Figure 7.20 and Figure 7.21, due to the rotating impeller, high level of the radial velocity of the liquid and gas phase can be identified close to the impeller blades. With the increasing radial distance from the impeller blade to tank wall, a sharp decrease of the radial velocity can be observed for both phases. Figure 7.22 and Figure 7.23 show that the axial velocity for gas and liquid phase are almost zero in this area since this data sampling plane is in the impeller jet flow region.

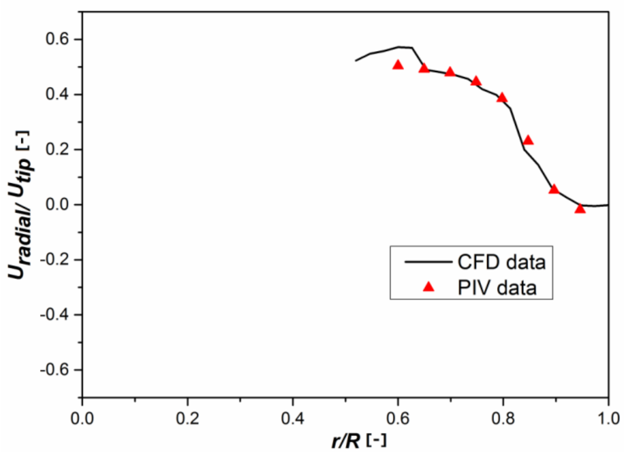

Figure 7.20 Radial velocity profiles at z/H=0.5 obtained by PIV and CFD (liquid phase)

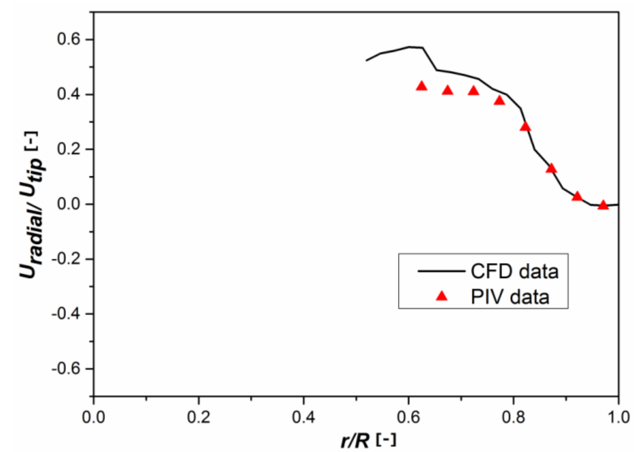

Figure 7.21 Radial velocity profiles at z/H=0.5 obtained by PIV and CFD (gas phase)

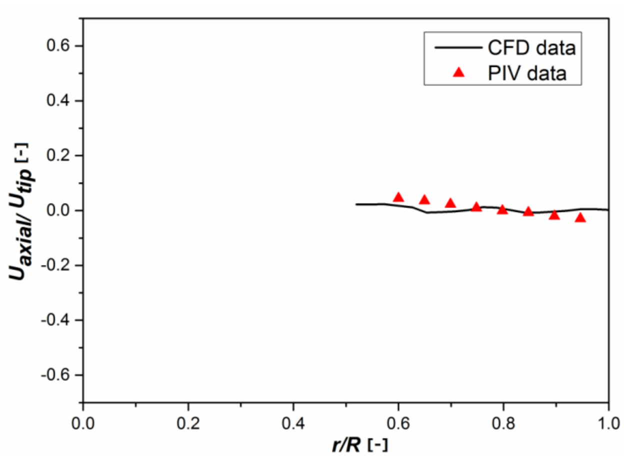

Figure 7.22 Axial velocity profiles at z/H=0.5 obtained by PIV and CFD (liquid phase)

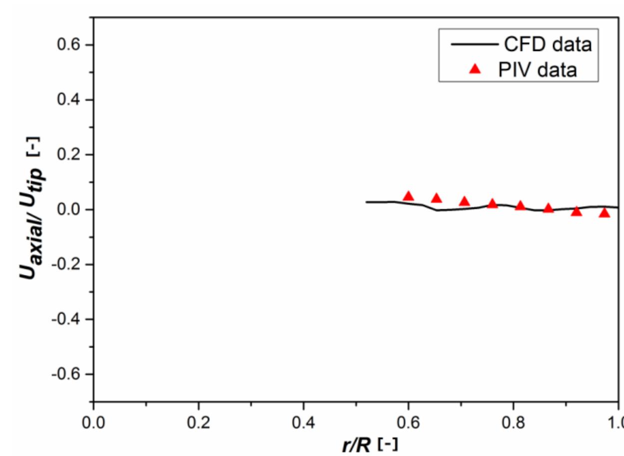

Figure 7.23 Axial velocity profiles at z/H=0.5 obtained by PIV and CFD (gas phase)

Comparing the CFD prediction with the PIV measurements, a slight difference can be found in the radial velocities in the region near the impeller blade, where the simulation slightly over predicts the radial velocity of gas phase and liquid phase. Similar over prediction of the gas and liquid velocities close to the impeller blade can also be observed in investigations carried out by Deen et al. (2002) and Montante et al. (2008) who mentioned that the grid resolutions and bubble size near the impeller blades would cause this discrepancy. Due to the high velocity gradient near impeller blade, the flow velocity profiles can be well predicted if a very fine grid resolution is used in this area (Deglon and Meyer, 2006). However, the use of very grid will give rise to extensive computational demand and convergence difficulties. In addition, when gas is introduced into the stirred tank, various sizes of bubble exist near the impeller blades. The mono-sized bubble assumption used in this investigation, which assumes uniform size of bubbles, will give rise to slight discrepancy between CFD and PIV data in flow velocity close to impeller blade (Montante et al., 2008). Besides, the high concentration of bubbles near the impeller blades will refract strong laser light and cause distortions of the image hence affect the accuracy of the PIV measurement near the impeller blades region (Dias and Reithmuller, 2000).

Despite of the slight discrepancy, the CFD and PIV data showed similar trend at this sampling plane. Good agreement between CFD and PIV data can be found in the regions away from the impeller blades.

Figure 7.24 to Figure 7.27 show the comparison of the predicted liquid and gas phase radial and axial velocities at plane of z/H=0.27 with the corresponding PIV data. At this horizontal plane, both phases were mainly moving axially towards the impeller or tank bottom resulting in very low radial velocities. As can be found from these figures, the velocity distributions of the gas and liquid phase are very similar at this sampling plane, which indicates that the bubbles followed well with the liquid phase, hence increasing the gas holdup and interphase mass transfer in this area. The PIV data show very good agreement with the CFD results.

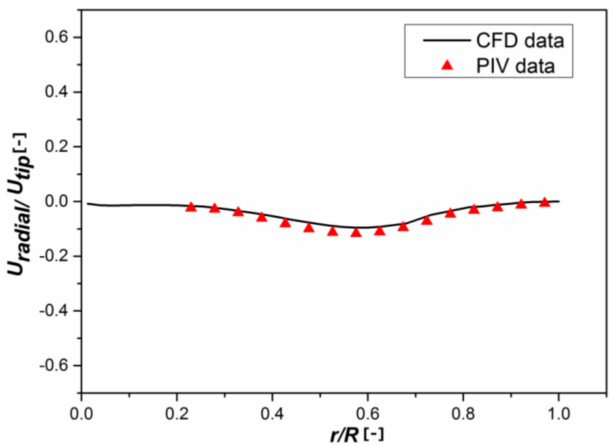

Figure 7.24 Radial velocity profiles at z/H=0.27 obtained by PIV and CFD (liquid phase)

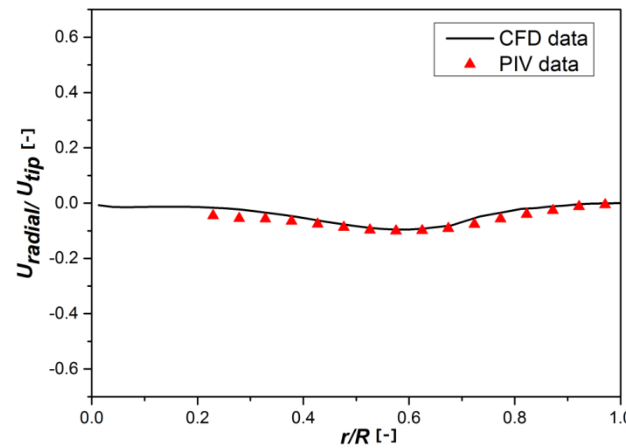

Figure 7.25 Radial velocity profiles at z/H=0.27 obtained by PIV and CFD (gas phase)

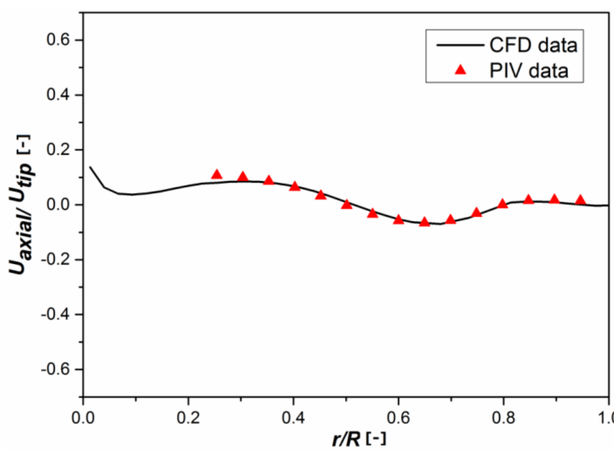

Figure 7.26 Axial velocity profiles at z/H=0.27 obtained by PIV and CFD (liquid phase)

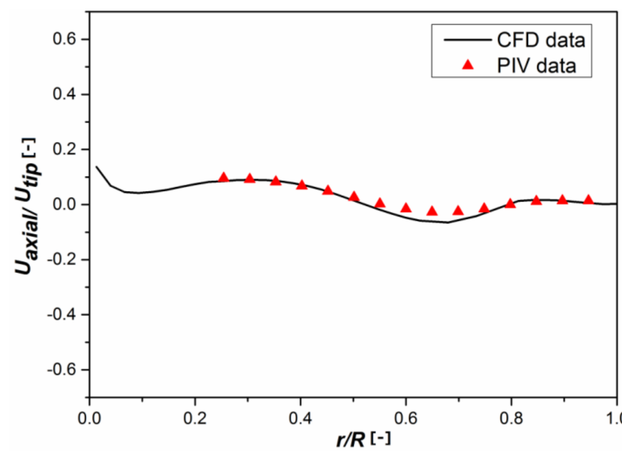

Figure 7.27 Axial velocity profiles at z/H=0.27 obtained by PIV and CFD (gas phase)

Figure 7.28 to Figure 7.31 show the radial and axial velocity component distributions of the liquid and gas phase at plane of z/H=0.73 obtained by CFD and PIV. The figures show great agreement between CFD and PIV results. As can be observed from these figures, the gas phase and liquid phase show similar trend and distributions, which indicate that the bubble faithfully follow the liquid phase and bubble residence time is increased in the liquid phase. Therefore, the overall mass trensfer processes of the gas-ionic liquid multipahse flow system has improved a lot (Oliveira et al., 2003).

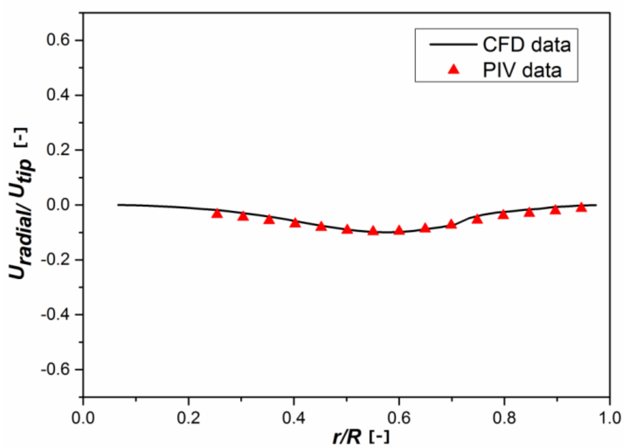

Figure 7.28 Radial velocity profiles at z/H=0.73 obtained by PIV and CFD (liquid phase)

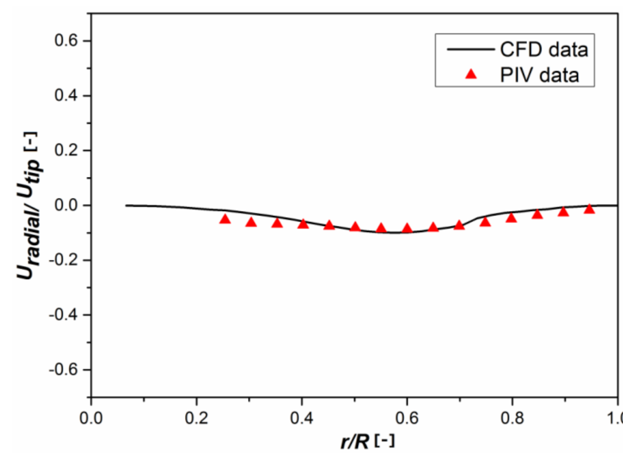

Figure 7.29 Radial velocity profiles at z/H=0.73 obtained by PIV and CFD (gas phase)

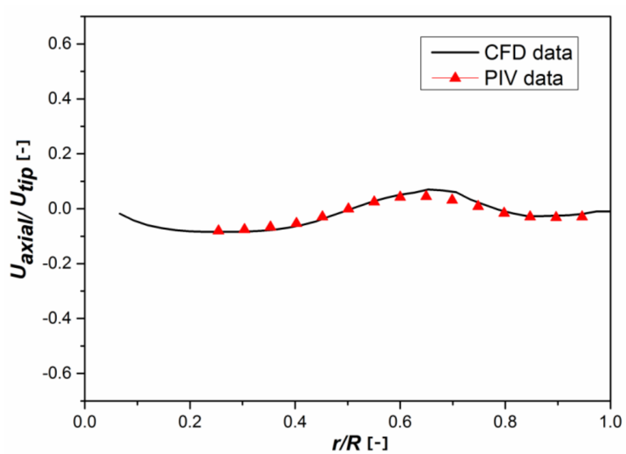

Figure 7.30 Axial velocity profiles at z/H=0.73 obtained by PIV and CFD (liquid phase)

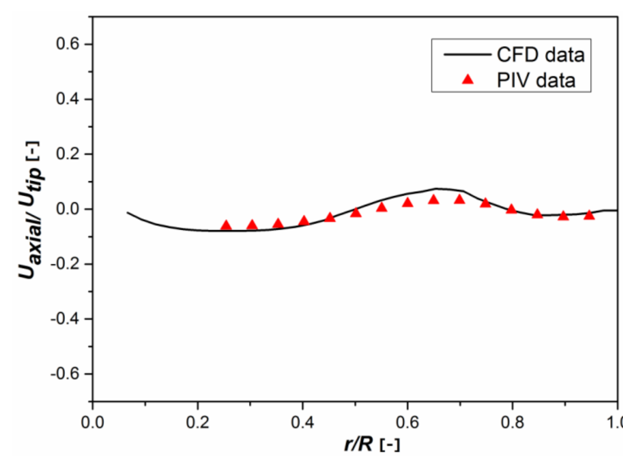

Figure 7.31 Axial velocity profiles at z/H=0.73 obtained by PIV and CFD (gas phase)

7.6 Conclusions

The CFD data indicated that when water was agitated in the DBD tank, a dead zone was formed below the impeller disk where the liquid in this region was rotating tangentially without fully mixing in the axial direction, which can reduce the stirred tank mixing efficiency in this area. In section 7.4.1, the PIV measurements also identified the existence of the dead zone region which successfully validated the CFD models and approaches used in the single phase water turbulent flow modelling in the stirred tank.

When ionic liquid was served as the operation liquid, the flow was in the transitional state. Probably due to the secondary circulations below the downward circulation loops and high shear stress imposed by the rotating impeller blade, compared with the water turbulent flow, the predicted magnitude of the dead zone has reduced a lot. This variation of the magnitude of the dead zone has also been captured by the PIV measurements as it shows good agreement with CFD prediction in terms of flow pattern and flow velocities. The PIV measurements indicate the accuracy of the simulation models used in modelling the ionic liquid transitional flow in the stirred tank.

The PIV measurements of the gas-ionic liquid flow confirmed that CFD prediction that the bubbles followed well with the ionic liquid showing similar flow pattern and velocity distributions at the sampling planes. Therefore, it will result in the increase of gas holdup and mass transfer in the stirred tank. However, slight discrepancy can be found in the region near the blade tips where the CFD tends to over predict the gas and liquid radial velocities. This over prediction may attribute to the mono-sized bubbles assumption used in the multiphase flow modelling, the number of the nodes used in simulation and the high concentration of bubbles near the impeller blades. Despite of the slight discrepancy, the PIV measurements have validated the CFD models and approaches used in modelling the gas-ionic liquid multiphase flow in the stirred tank.

Generally, the CFD results of the single phase water turbulent flow, single phase ionic liquid transitional flow and gas-ionic liquid transitional flow were validated by the PIV experiment. Good agreements were found between the CFD and PIV data for all stirred tank operation conditions, which suggest that the simulation models and methods used in this investigation such as the turbulent model, Euler-Euler multiphase flow model, drag force model, MRF and SM method, and mono-sized bubble assumption are applicable in simulating the single phase water and ionic liquid and gas-ionic liquid multiphase flows in the stirred tank. Thus, the computational models and approaches presented in this investigation are reliable and practical as a useful tool for design and optimisation of the chemical processes containing ionic liquids in the stirred tanks.

CHAPTER 8: CONCLUSIONS AND FUTURE WORK

8.1 Conclusions

The aim of this research is to numerically and experimentally study the hydrodynamics of single phase water, ionic liquid and gas-ionic liquid multiphase flows in the stirred tank to provide insights into design and optimization of the stirred tanks for chemical process involving ionic liquids. A comprehensive literature review was covered on the simulation models and methods to simulate the single phase and multiphase flow in the stirred tank, and advanced visualization and measurements techniques in flow fields. Based on this, numerical studies were carried out to investigate the turbulent single phase water flow, single phase ionic liquid transitional flow, gas-water multiphase turbulent flow and gas-ionic liquid multiphase transitional flow in the stirred tanks. The simulation results were compared with the reference or PIV experimental data and showed good agreements, which validates the accuracy of current CFD models and methods used in this study. Based on the numerical and experimental study, the following conclusions can be drawn from this investigation.

8.1.1 The Effect of Baffle Length and Bottom Shape on the Water Turbulent Flow Parameters

- A series of water turbulent flow modelling adopting RANS modelling were carried out in the stirred tanks equipped with different length of baffles and bottom shapes. The short baffles slightly were found to reduce the impeller power number and flow number when water was operated in the fully developed turbulent state in the stirred tank, whilst the effect of the bottom shape is almost negligible.

- Both the bottom shape and baffles' length has little effect on trailing vortex behaviour behind the impeller blades.
- The CFD results indicated that the distributions of k and ε were very similar near the impeller tips in the FB and DBB tank, while slightly reduction of k and ε can be found close to impeller in the DBD tank. The simulation results suggest that the FB and DBB tank provide better mixing performance than the DBD tank in mixing the flow in the turbulent state hence requiring less energy consumption at the same condition compared with the DBD tank.
- Both the bottom shape and baffles' length have significant effect on the flows in the region below the impeller. A large dead zone area starting from the impeller disk to the tank bottom was discovered in the DBD tank when water was served as the operation liquid and operated in the turbulent state. By extending the baffles' length to the tank bottom, a clear reduction of dead zone was identified, which can improve the mixing efficiency in the dished bottom stirred tank.

8.1.2 Large Eddy Simulation of Single Phase Water and Ionic Liquid Flows in the Stirred Tanks

- The LES of turbulent water flow showed good agreement with the RANS modelling as they both identified the formation of a large dead zone area in the DBD tank.
- When ionic liquid $BmimBF_4$ was served as the operation liquid in all three tanks, the intensity of the upward and downward circulation loops generated by the rotating impeller were reduced and secondary

circulation loops were formed near them, resulting in the requirement of longer mixing time in the stirred tanks. In addition, the liquid velocities in the near wall region were low, which reduced the mixing efficiency in the region close to the tank wall.

- Compared with the dead zone of water in the DBD tank, the dead zone of ionic liquid formed below the impeller disk reduced a lot in the DBD tank.
- Despite of a larger dead zone of water turbulent flow in the DBD tank than in the DBB tank, a rather similar flow pattern and velocity components of ionic liquid were identified in both the DBD and DBB tank below the impeller, which showed decreased dead zone region. Therefore, the disadvantage of the DBD tank in mixing performance has reduced when the ionic liquid was mixed in the transitional state in this vessel.

8.1.3 Experimental Investigation on the Effects of Mixing Parameters and Physical Properties of Ionic Liquid on the Bubble Size in a Stirred Tank

- The viscosity measurement experiment showed that the ionic liquid ($BmimBF_4$) aqueous solutions demonstrate Newtonian fluid behaviour.
- When the concentration of the $BmimBF_4$ increased form 0 wt.% to 50 wt.%, the viscosity of the ionic liquid aqueous solutions is almost constant. While a sharp growth of viscosity was found when the $BmimBF_4$ concentration increased from 90 wt.% to 100 wt.%.
- The $BmimBF_4$ solutions showed sharp decrease in surface tension when the concentration of $BmimBF_4$ increased from 0 wt.% to 10 wt.%,

however further increase of the ionic liquid concentration has no significant on the solutions surface tension.

- The density of ionic liquid solutions was almost in linear relationship with the growth of $BmimBF_4$ concentration.
- Under the investigated operation conditions, more larger bubbles were found in 0 wt.% and 1 wt.% $BmimBF_4$ solutions. Whilst more stable and smaller bubbles were identified in the $BmimBF_4$ solutions with concentration ranges from 5 wt.% to 100 wt.%.
- The impeller speed showed an exponential correlation with the bubble Sauter mean diameter (d_{32}) in the ionic liquid aqueous solutions. The correlation showed agreement with the theoretical value of the exponential value being -1.2 at low $BmimBF_4$ concentrations (0 wt.% and 1 wt.%). However, discrepancies with theoretical value were found with the increasing ionic liquid concentration. It is suggested that the bubble size in the pure water and low $BmimBF_4$ concentration (1 wt.%) was mainly controlled by the bubble breakage and the effect of the bubble coalescence was not significant. However, with the increasing ionic liquid concentration, both the bubble breakage and coalescence showed significant effect on determining the bubble size.
- The increasing gas flow rate gave rise to the increase of bubble size when pure water and pure $BmimBF_4$ were used as the operation liquids. However, slight reduction of bubble size was found in $BmimBF_4$ solutions when the gas flow rate increased from 1 wt.% to 50 wt.%.
- The experiments showed that the effect of surface tension has more significant effect than liquid viscosity on affecting bubble size in the $BmimBF_4$ solutions.

8.1.4 Modelling of Gas-Ionic Liquid/water Multiphase Flows in the Stirred Tank

- In the gas-water multiphase flow, the presence of gas did not have significant effect on changing the flow of water phase under the operation conditions used in this modelling. The intensity of the lower circulation loops of gas phase was much lower than that of the upper circulation loops, which will cause poor gas dispersion in this area.
- In the gas-water multiphase flow, high volume of gas was accumulated in the upper circulation regions, while there was little gas circulated in the lower circulation loops. The gas dispersion and mass transfer was poor in the lower bulk regions.
- In the gas-ionic liquid multiphase flow, the presence of the gas phase has little effect on the ionic liquid flow pattern, and the ionic liquid flow pattern was very similar in conditions with and without gas. However, slight difference can be found near the tank bottom, where the appearance of the gas phase caused dead zone region in this area.
- The gas phase followed well with the liquid phase and circulated in most region of the stirred tank, which results in the increase of the gas holdup in the stirred tank.
- The increasing impeller speed can significantly reduce the dead zone area near tank bottom, whereas the growth of gassing rate resulted in the increase of dead zone regions. As a result, the gas holdup and the mass transfer near tank bottom have reduced with the increasing gassing rate.
- The rise of inlet gas velocity has more pronounced effect than the growth of impeller speed on increasing the mean gas holdup in the stirred tank.

8.1.5 PIV Validation

- The selection of particle tracers was justified. The PSP and FPP tracers were selected as the tracers in water and ionic liquid flow PIV measurement.
- The PIV experiment results showed agreement with CFD data of the water turbulent flow and the ionic liquid transitional flow in the stirred tank, which validated the existence of the dead zone region below the impeller in the DBD tank.
- The PIV data revealed that the bubbles followed well with the ionic liquid and showed similar flow pattern and velocity distributions with the liquid phase at the data sampling planes in the stirred tank. The bubbles from the sparger were circulated together with the liquid phase, which results in the increase of gas holdup and mass transfer in the stirred tank. Generally, the CFD and PIV results showed good agreements.
- The experimental validation suggested that the simulation models and methods used in this investigation such as the turbulent model, Euler-Euler multiphase model, drag force model, MRF and SM method, and mono-sized bubble assumption are applicable and accurate in simulating the single phase water and ionic liquid, gas-water and gas-ionic liquid multiphase flows in stirred tank.

8.2 Contribution to Knowledge

This thesis contributes to the knowledge in that:

- A comprehensive literature review on numerical and experimental studies on flow hydrodynamics in stirred tanks were carried out including RANS and LES modelling in stirred vessel, turbulence and transitional flow modelling, methods to model the rotating impeller, boundary conditions, models for simulating the multiphase flow, interphase forces and flow measurement techniques etc.

- The study found that the baffles' length and the shape of tank bottom affect the flow variables such as the power number, flow number, turbulent kinetic energy and its dissipation rate, and flow pattern in the turbulent flow in the stirred tank. A large dead zone region was identified below the impeller in the DBD tank when water was operated in turbulent state. Liquid in this region is rotating without fully mixing in the axial direction. By extending the baffles to the tank bottom (DBB tank), the magnitude of the dead zone has greatly reduced and the mixing efficiency can be improved a lot.
- The ionic liquid ($BmimBF_4$) transitional flows in the stirred tanks were numerically investigated. Different from that in the turbulent water flows, the baffles' extension has little effect on reducing the size of the dead zone area. The study shows that the ionic liquid transitional flow in the stirred tank is not very sensitive to the bottom shape and the extension of baffles.
- This study carried out measurement of bubble size in the gas-ionic liquid multiphase flow system in the stirred tank where the effects of impeller agitation speed, the gassing rate and the ionic liquid physical properties on bubble size were determined. Correlations between the bubble size and the impeller agitation speed were established, which provides knowledge for predicting the bubble size in the gas-ionic liquid system in the lab scale and industry at similar operation conditions.

- The gas-ionic liquid multiphase flow in a stirred tank was numerically studied. It reveals that, compared with the water turbulent flow, the gas phase in the gas-ionic system was more uniformly distributed in the stirred tank. Except the region close to the tank bottom, the presence of gas phase did not give rise to significant effect on the ionic liquid flow pattern. The study shows that the gas flow rate has more pronounced effect than the impeller speed on increasing the gas holdup, which improves the mass transfer in the stirred tank. However, in regions close to the tank bottom, the increase of the gassing rate would enlarge the dead zone and reduced the local gas holdup in these regions. Therefore, higher impeller speed and lower gas flow rate was recommended to operate the gas-ionic liquid multiphase flow in the stirred tank to achieve the homogeneous mixing and improve the mass transfer rate and final products quality. A correlation was proposed to predict the impeller power consumption of the gas-ionic liquid transitional flow in a stirred tank agitated by a Rushton turbine impeller.
- The flow patterns and velocities of single phase ionic liquid and gas-ionic liquid multiphase flows in a stirred tank were experimentally visualized and measured employing the PIV. The PIV results showed agreement with the CFD data, which implies that the CFD models and methods used in this investigation can be applied in the relevant investigations. This numerical and experimental study provides insights into the design and optimization of the stirred tanks for chemical process involving ionic liquids.

8.3 Future Work

8.3.1 CFD Simulation

This section gives recommendations for future research in order to further advance the present research.

- In the current simulation work, only the geometry of Rushton turbine impeller with the diameter of D/T=0.5 fixed in the middle of a stirred tank was used. Impellers with different D/T ratios and locations in stirred tank and geometries are recommend to use in future investigation to evaluate the effect of impeller configurations on dead regions found in the dished bottom stirred tanks.
- In this study, the LES was only used to model the single phase water and ionic liquid flows in the stirred tanks due to the high computational costs for LES multiphase modelling. With the development of computer technology, the LES should be considered for the gas-water and gas-ionic liquid multiphase modelling.
- Due to the high computational demand by using of the Population Balance Model (PBM), the mono-sized bubble assumption was used in the gas-liquid multiphase flow modelling where the bubble break-up and coalescence were not considered in the simulation. With the increase of computing capacity, PBM can be considered to account the effects of bubble break-up and coalescence thus the bubble size distributions in the stirred tanks can be predicted and flow velocity profiles near the impeller tips may be simulated with improved accuracy.

8.3.2 Experimental Work

- It has been found that with the increasing number of bubbles in the stirred tank, the bubble image become blurry and the bubble boundaries cannot be distinguished from the background colour of the image, which affected the analysis of the bubble size. Due to this limitation, the bubble sizes in the ionic liquid solutions were only measured at selected operation conditions in this investigation. The use of a stronger light source may increase the image contrast between the background colour and the bubble images, hence facilitating the bubble size analysing under more operation conditions.
- In the experiment, the view of the horizontal liquid level was blocked by an iron hoop which was used to fix the baffles in the stirred tank. Therefore, the difference of horizontal liquid level before and after gassing cannot be observed and measured. The simulated gas holdup in the stirred tank was therefore not validated by the experiment in this study. A higher stirred tank equipped with longer baffles should be designed in the future to detect the change of liquid level with and without gas phase, which enables experimentally measuring the gas holdup in the stirred tank.
- For safety concerns, the shaft of the impeller is enclosed in a protective case in the location from the motor to the tank cover. Therefore, there was not enough space to install a shaft encoder with which the detailed behaviour of the trailing vortex can be measured by PIV. A better design of a stirred tank with enough space to fix the shaft encoder can facilitate the investigation of the trailing vortex behaviour behind the impeller blades.

REFERENCES

AHMAD, F. 2012. VOLCANOZ. *PITOT TUBE* [Online]. Available from: http://nonideal2.blogspot.com/2012/04/pitot-tube.html 2012].

AHMED, J. & ALAM UZZAL, R. U. 2012. Fluid Flow and Pump Selection. *Handbook of Food Process Design.* Wiley-Blackwell.

AMINI, N. & HASSAN, Y. A. 2014. Experimental study of bypass flow in near wall gaps of a pebble bed reactor using hot wire anemometry technique. *Annals of Nuclear Energy,* 65**,** 60-71.

ANSYS 2011a. ANSYS FLUENT Theory Guide. Pennsylvania: ANSYS Ltd.

ANSYS 2011b. ANSYS FLUENT User's Guide. Pennsylvania: ANSYS Ltd.

ANSYS 2013. ANSYS CFX-Pre User's Guide. Pennsylvania: ANSYS Ltd.

ARMENANTE, P. M., NAGAMINE, E. U. & SUSANTO, J. 1998. Determination of correlations to predict the minimum agitation speed for complete solid suspension in agitated vessels. *The Canadian Journal of Chemical Engineering,* 76**,** 413-419.

ASARI, M. & HORMOZI, F. 2013. Effects of Surfactant on Bubble Size Distribution and Gas Hold-up in a Bubble Column. *American Journal of Chemical Engineering,* 1**,** 50-58.

AUBIN, J., FLETCHER, D. F. & XUEREB, C. 2004. Modeling turbulent flow in stirred tanks with CFD: the influence of the modeling approach, turbulence model and numerical scheme. *Experimental Thermal and Fluid Science,* 28**,** 431-445.

BAKKER, A., LAROCHE, R. D., WANG, M. H. & CALABRESE, R. V. 1997. Sliding Mesh Simulation of Laminar Flow in Stirred Reactors. *Chemical Engineering Research and Design,* 75**,** 42-44.

BAKKER, A., MYERS, K. J., WARD, R. W. & LEE, C. K. 1996. The Laminar and Turbulent Flow Pattern of A Pitched Blade Turbine. *Chemical Engineering,* 74.

BAKKER, A. & OSHINOWO, L. M. 2004. Modelling of Turbulence in Stirred Vessels Using Large Eddy Simulation. *Chemical Engineering Research and Design,* 82**,** 1169-1178.

BAKKER, A., OSHINOWO, L. M. & MARSHALL, E. M. 2000. The Use of Large Eddy Simulation to Study Stirred Vessel Hydrodynamics. *In:* AKKER, H. E. A. V. D. & DERKSEN, J. J. (eds.) *10th European Conference on Mixing.* Amsterdam: Elsevier Science.

BAKKER, A. & VAN DEN AKKER, H. E. A. 1994a. Gas-liquid contacting with axial flow impellers. *Chemical Engineering Research and Design,* 72**,** 573-582.

BAKKER, A. & VAN DEN AKKER, H. E. A. 1994b. Single-phase flow in stirred reactors. *Chemical Engineering Research and Design,* 72**,** 583-593.

BARIGOU, M. & GREAVES, M. 1992. Bubble-size distributions in a mechanically agitated gas—liquid contactor. *Chemical Engineering Science,* 47**,** 2009-2025.

BASHIRI, H., HENICHE, M., BERTRAND, F. & CHAOUKI, J. 2014. Compartmental modelling of turbulent fluid flow for the scale-up of stirred tanks. *The Canadian Journal of Chemical Engineering,* 92**,** 1070-1081.

BENZING, R. J. & MYERS, J. E. 1955. Low Frequency Bubble Formation at Horizontal Circular Orifices. *Industrial & Engineering Chemistry,* 47**,** 2087-2090.

BITTORF, K. J. & KRESTA, S. M. 2000. Active volume of mean circulation for stirred tanks agitated with axial impellers. *Chemical Engineering Science,* 55**,** 1325-1335.

BONDAREV, G. S. & ROMANOV, V. F. 1973. Formation of gas bubbles in viscous liquids at low gas flow rates. *Chemistry and Technology of Fuels and Oils,* 9**,** 133-136.

BRENNEN, C. E. 2005. Fundamentals of Multiphase Flows. U.S: Cambridge University Press.

BRISCOE, B., LUCKHAM, P. & ZHU, S. 2000. The effects of hydrogen bonding upon the viscosity of aqueous poly(vinyl alcohol) solutions. *Polymer,* 41**,** 3851-3860.

BRUCATO, A., CIOFALO, M., GRISAFI, F. & MICALE, G. 1998. Numerical prediction of flow fields in baffled stirred vessels: A comparison of alternative modelling approaches. *Chemical Engineering Science,* 53**,** 3653-3684.

BUSCIGLIO, A., CAPUTO, G. & SCARGIALI, F. 2013. Free-surface shape in unbaffled stirred vessels: Experimental study via digital image analysis. *Chemical Engineering Science,* 104**,** 868-880.

BUWA, V., DEWAN, A., NASSAR, A. F. & DURST, F. 2006. Fluid dynamics and mixing of single-phase flow in a stirred vessel with a grid disc impeller: Experimental and numerical investigations. *Chemical Engineering Science,* 61**,** 2815-2822.

CHAPPLE, D., KRESTA, S. M., WALL, A. & AFACAN, A. 2002. The Effect of Impeller and Tank Geometry on Power Number for a Pitched Blade Turbine. *Chemical Engineering Research and Design,* 80**,** 364-372.

CHEVULA, S., SANZ-ANDRES, Á. & FRANCHINI, S. 2015. Estimation of the correction term of pitot tube measurements in unsteady (gusty) flows. *Flow Measurement and Instrumentation,* 46, Part A**,** 179-188.

CHTOUROU, W., AMMAR, M., DRISS, Z. & ABID, M. S. 2014. CFD Prediction of the Turbulent Flow Generated in Stirred Square Tank by a Rushton Turbine. *Energy and Power Engineering,* Vol.06No.05**,** 6.

CLIFT, R., GRACE, J. R. & WEBER, M. E. 2005. *Bubbles, Drops, and Particles*, Dover Publications.

COOK, T. L. & HARLOW, F. H. 1984. Virtual mass in multiphase flow. *International Journal of Multiphase Flow,* 10**,** 691-696.

COSTES, J. & COUDERC, J. P. 1988. Study by laser Doppler anemometry of the turbulent flow induced by a Rushton turbine in a stirred tank: Influence of the size of the units—I. Mean flow and turbulence. *Chemical Engineering Science,* 43**,** 2751-2764.

DANTEC 2005. 2D PIV Reference Manual. Skovlunde, Denmark.

DANTECDYNAMICS. 2013. *Seeding Materials* [Online]. Skovlunde, Denmark.

DEEN, N. G., SOLBERG, T. & HJERTAGER, B. H. 2002. Flow Generated by an Aerated Rushton Impeller: Two-phase PIV Experiments and Numerical Simulations. *The Canadian Journal of Chemical Engineering,* 80**,** 1-15.

DEGLON, D. A. & MEYER, C. J. 2006. CFD modelling of stirred tanks: Numerical considerations. *Minerals Engineering,* 19**,** 1059-1068.

DELAFOSSE, A., COLLIGNON, M.-L., CRINE, M. & TOYE, D. 2011. Estimation of the turbulent kinetic energy dissipation rate from 2D-PIV measurements in a vessel stirred by an axial Mixel TTP impeller. *Chemical Engineering Science,* 66**,** 1728-1737.

DELAFOSSE, A., LINE, A., MORCHAIN, J. & GUIRAUD, P. 2008. LES and URANS simulations of hydrodynamics in mixing tank: Comparison to PIV experiments. *Chemical Engineering Research and Design,* 86**,** 1322-1330.

DELNOIJ, E., LAMMERS, F. A., KUIPERS, J. A. M. & VAN SWAAIJ, W. P. M. 1997. Dynamic simulation of dispersed gas-liquid two-phase flow using a discrete bubble model. *Chemical Engineering Science,* 52**,** 1429-1458.

DERKSEN, J. & VAN DEN AKKER, H. E. A. 1999. Large eddy simulations on the flow driven by a Rushton turbine. *AIChE Journal,* 45**,** 209-221.

DIAS, I. & REITHMULLER, M. L. 2000. PIV in Two-Phase Flows: Simultaneous Bubble Sizing and Liquid Velocity Measurements. *In:* ADRIAN, R. J., DUR O, D. F. G., DURST, F., HEITOR, M. V., MAEDA, M. & WHITELAW, J. H. (eds.) *Laser Techniques Applied to Fluid Mechanics: Selected Papers from the 9th International Symposium Lisbon, Portugal, July 13–16, 1998.* Berlin, Heidelberg: Springer Berlin Heidelberg.

DODA, B. 2008. *LDV - Laser Doppler Velocimetry* [Online]. India. Available: http://www.velocimetry.net/ldv_principles.htm.

DONG, H., WANG, X., LIU, L., ZHANG, X. & ZHANG, S. 2010. The rise and deformation of a single bubble in ionic liquids. *Chemical Engineering Science,* 65**,** 3240-3248.

DOOLITTLE, A. K. 1952. Studies in Newtonian Flow. III. The Dependence of the Viscosity of Liquids on Molecular Weight and Free Space (in Homologous Series). *Journal of Applied Physics,* 23**,** 236-239.

DRUZHININ, O. A. & ELGHOBASHI, S. 1998. Direct numerical simulations of bubble-laden turbulent flows using the two-fluid formulation. *Physics of Fluids,* 10**,** 685-697.

DUMITRIU, G., LUCESCU, L., BICU, E. & BELEIA, D. 2010. New Phenothiazine Derivatives with Ionic Liquid Structure. *ACTA CHEMICA IASI,* 18.

DYNAMICS, D. 2013. *Measurement Principles of PIV* [Online]. Skovlunde, Denmark. Available: http://www.dantecdynamics.com/measurement-principles-of-piv.

DYNAMICS, D. 2017a. *Measurement Principles of PIV* [Online]. Available: https://www.dantecdynamics.com/measurement-principles-of-piv.

DYNAMICS, D. 2017b. *PSP, Polyamid Seeding Particles* [Online]. Available: https://www.dantecdynamics.com/psp-polyamid-seeding-particles.

EARLE MARTYN, J. & SEDDON KENNETH, R. 2000. Ionic liquids. Green solvents for the future. *Pure and Applied Chemistry.*

EARLE, M. J. & SEDDON, K. R. 2000. Ionic liquids, Green solvents for the future. *Pure and Applied Chemistry,* 72**,** 1391-1398.

EGGELS, J. G. M. 1996. Direct and large-eddy simulation of turbulent fluid flow using the lattice-Boltzmann scheme. *International Journal of Heat and Fluid Flow,* 17**,** 307-323.

FAN, J., WANG, Y. & FEI, W. 2007. Large Eddy Simulations of Flow Instabilities in a Stirred Tank Generated by a Rushton Turbine. *Chinese Journal of Chemical Engineering,* 15**,** 200-208.

FREEMANTLE, M. 1998. DESIGNER SOLVENTS. *Chemical & Engineering News Archive,* 76**,** 32-37.

GABRIEL, S. & WEINER, J. 1888. Ueber einige Abkömmlinge des Propylamins. *Chemische Berichte,* 21.

GABRIELE, A., NIENOW, A. W. & SIMMONS, M. J. H. 2009. Use of angle resolved PIV to estimate local specific energy dissipation rates for up- and down-pumping pitched blade agitators in a stirred tank. *Chemical Engineering Science,* 64**,** 126-143.

GE, C.-Y., WANG, J.-J., GU, X.-P. & FENG, L.-F. 2014. CFD simulation and PIV measurement of the flow field generated by modified pitched blade turbine impellers. *Chemical Engineering Research and Design,* 92**,** 1027-1036.

GERMANO, M., PIOMELLI, U., MOIN, P. & CABOT, W. H. 1991. A dynamic subgrid-scale eddy viscosity model. *Physics of Fluids A,* 3**,** 1760-1765.

GILL, N. K., APPLETON, M., BAGANZ, F. & LYE, G. J. 2008. Quantification of power consumption and oxygen transfer characteristics of a stirred miniature bioreactor for predictive fermentation scale-up. *Biotechnology and Bioengineering,* 100**,** 1144-1155.

GIMBUN, J., RIELLY, C. D. & NAGY, Z. K. 2009. Modelling of mass transfer in gas–liquid stirred tanks agitated by Rushton turbine and CD-6 impeller: A scale-up study. *Chemical Engineering Research and Design,* 87**,** 437-451.

GIMBUN, J., RIELLY, C. D., NAGY, Z. K. & DERKSEN, J. J. 2012. Detached eddy simulation on the turbulent flow in a stirred tank. *AIChE Journal,* 58**,** 3224-3241.

GORJI, M., BOZORGMEHRY BOOZARJOMEHRY, R. & KAZEMEINI, M. 2007. CFD Modeling of Gas-Liquid Hydrodynamics in a Stirred Tank Reactor. *Iranian Journal of Chemistry and Chemical Engineering (IJCCE),* 26**,** 85-96.

GREAVES, M. & BARIGOU, M. 1988. The internal structure of gas-liquid dispersion in a stirred reactor. *Proceedings of the Sixth European Conference on Mixing.* Pavia, Italy: BHRA Fluid Engineering.

HAMDI, M., HAVET, M., ROUAUD, O. & TARLET, D. 2014. Comparison of different tracers for PIV measurements in EHD airflow. *Experiments in Fluids,* 55**,** 1-12.

HAQUE, J. N., MAHMUD, T., ROBERTS, K. J., LIANG, J. K., WHITE, G., WILKINSON, D. & RHODES, D. 2011. Free-surface turbulent flow induced by a Rushton turbine in an unbaffled dish-bottom stirred tank reactor: LDV measurements and CFD simulations. *The Canadian Journal of Chemical Engineering,* 89**,** 745-753.

HARTMANN, H., DERKSEN, J. J., MONTAVON, C., PEARSON, J., HAMILL, I. S. & VAN DEN AKKER, H. E. A. 2004. Assessment of large eddy and RANS stirred tank simulations by means of LDA. *Chemical Engineering Science,* 59**,** 2419-2432.

HARVEY, P. S. & GREAVES, M. G. 1982. Turbulent Flow in an Agitated Vessel Part-I: A Predictive Model. *Chemical engineering research and design,* 60**,** 195-200.

HILL, A. 2013. RHEOLOGY BASICS: INTRODUCING THE MALVERN KINEXUS A PRACTICAL MEASUREMENT PERSPECTIVE.

HINZE, J. O. 1975. *Turbulence,* New York, McGraw-Hill Publishing Co.

HONKANEN, M. & SAARENRINNE, P. 2002. Turbulent bubbly flow measurements in a mixing vessel with PIV. *Proceedings of the 11th International Symposium on Applications of Laser Techniques to Fluid Mechanics.* Lisboa.

HU, B., NIENOW, A. W., HUGH STITT, E. & PACEK, A. W. 2006. Bubble sizes in agitated solvent/reactant mixtures used in heterogeneous catalytic hydrogenation of 2-butyne-1,4-diol. *Chemical Engineering Science,* 61**,** 6765-6774.

HU, B., NIENOW, A. W. & PACEK, A. W. 2003. The effect of sodium caseinate concentration and processing conditions on bubble sizes and their break-up and coalescence in turbulent, batch air/aqueous dispersions at atmospheric and elevated pressures. *Colloids and Surfaces B: Biointerfaces,* 31**,** 3-11.

HU, B., PACEK, A. W., STITT, E. H. & NIENOW, A. W. 2005a. Bubble sizes in agitated air–alcohol systems with and without particles: Turbulent and transitional flow. *Chemical Engineering Science,* 60**,** 6371-6377.

HU, B. J., PACEK, A. W. & NIENOW, A. W. 2005b. Break-up and Coalescence of Bubbles in Agitated Protein Solutions at High Air Volume Fraction. *In:* DICKINSON, E. (ed.) *Food Colloids: Interactions, Microstructure and Processing.* The Royal Society of Chemistry.

HUA, J. & LOU, J. 2007. Numerical simulation of bubble rising in viscous liquid. *Journal of Computational Physics,* 222**,** 769-795.

ISHII, M. & ZUBER, N. 1979. Drag coefficient and relative velocity in bubbly, droplet or particulate flows. *AIChE Journal,* 25**,** 843-855.

JAWORSKI, Z. & FOŘT, I. 1991. Energy dissipation rate in a baffled vessel with pitched blade turbine impeller. *Collect. Czech. Chem. Commun.,* 56**,** 1856-1867.

JAWORSKI, Z., WYSZYNSKI, M. L., BADHAM, R. S., DYSTER, K. N., MOORE, I. P. T., OZCAN-TASKIN, N. G., NIENOW, A. W. & MCKEMMIE, J. 1996. Sliding Mesh Simulation of Transitional, Non-Newtonian Flow in a Baffled, Stirred Tank. *In:* DEVILLE, M., GAVRILAKIS, S. & RYHMING, I. (eds.) *Computation of Three-Dimensional Complex Flows.* Vieweg+Teubner Verlag.

JAWORSKI, Z. & ZAKRZEWSKA, B. 2002. Modelling of the Turbulent Wall Jet Generated by a Pitched Blade Turbine Impeller: The Effect of Turbulence Model. *Chemical Engineering Research and Design,* 80**,** 846-854.

JOSHI, J. B., NERE, N. K., RANE, C. V., MURTHY, B. N., MATHPATI, C. S., PATWARDHAN, A. W. & RANADE, V. V. 2011. CFD SIMULATION OF STIRRED TANKS: COMPARISON OF TURBULENCE MODELS. PART I: RADIAL FLOW IMPELLERS. *Canadian Journal of Chemical Engineering,* 89**,** 23-82.

KARCZ, J. & MAJOR, M. 1998. An Effect of a Baffle Length on the Power Consumption in an Agitated Vessel. *Chemical Engineering and Processing: Process Intensification,* 37**,** 249-256.

KELLY, W. & GIGAS, B. 2003. Using CFD to predict the behavior of power law fluids near axial-flow impellers operating in the transitional flow regime. *Chemical Engineering Science,* 58**,** 2141-2152.

KHOPKAR, A. R. & RANADE, V. V. 2006. CFD simulation of gas–liquid stirred vessel: VC, S33, and L33 flow regimes. *AIChE Journal,* 52**,** 1654-1672.

KHURANA, A. K. & KUMAR, R. 1969. Studies in bubble formation — III. *Chemical Engineering Science,* 24**,** 1711-1723.

KOJI TAKAHASHI & NIENOW, A. 1993. BUBBLE SIZES AND COALESCENCE RATES IN AN AERATED VESSEL AGITATED BY A RUSHTON TURBINE. *JOURNAL OF CHEMICAL ENGINEERING OF JAPAN,* 26**,** 536-542.

KOLBECK, K., LEHMANN, J., LOVELOCK, K. R. J., CREMER, T., PAAPE, N., WASSERSCHEID, P., FROBA, A. P., MAIER, F. & STEINRUCK, H. P. 2010. Density and Surface Tension of Ionic Liquids. *J. Phys. Chem.,* 114.

KULKARNI, A. A. & JOSHI, J. B. 2005. Bubble Formation and Bubble Rise Velocity in Gas−Liquid Systems: A Review. *Industrial & Engineering Chemistry Research,* 44**,** 5873-5931.

KUMARESAN, T. & JOSHI, J. B. 2006. Effect of impeller design on the flow pattern and mixing in stirred tanks. *Chemical Engineering Journal,* 115**,** 173-193.

LAMARQUE, N., ZOPP , B., LEBAIGUE, O., DOLIAS, Y., BERTRAND, M. & DUCROS, F. 2010. Large-eddy simulation of the turbulent free-surface flow in an unbaffled stirred tank reactor. *Chemical Engineering Science,* 65**,** 4307-4322.

LAMB, H. 1994. Hydrodynamics (6th ed.). Cambridge University Press.

LAMBERTO, D. J., ALVAREZ, M. M. & MUZZIO, F. J. 1999. Experimental and computational investigation of the laminar flow structure in a stirred tank. *Chemical Engineering Science,* 54**,** 919-942.

LANCE, M. & NACIRI, A. 1991. Lift and added mass coefficient for a single bubble. *First European Fluid Mechanics Conference.* Cambridge, U.K.

LANE, G. L. 2006. *Computational Modelling of Gas-Liquid Flow in Stirred Tank.* PhD, The University of Newcastle.

LANE, G. L., SCHWARZ, M. P. & EVANS, G. M. 2000. Comparison of CFD Methods for Modelling of Stirred Tanks. *10th European Conference on Mixing, Delft, Netherlands*.

LANE, G. L., SCHWARZ, M. P. & EVANS, G. M. 2002. Predicting gas–liquid flow in a mechanically stirred tank. *Applied Mathematical Modelling,* 26**,** 223-235.

LANEA, G. L., SCHWARZA, M. P. & EVANSB, G. M. 2005. Numerical modelling of gas-liquid flow in stirred tanks. *chemical Engineering Science,* 60**,** 2203-2214.

LAPIN, A. & L BBERT, A. 1994. Numerical simulation of the dynamics of two phase gas–liquid flows in bubble columns. *Chem. Eng. Sci,* 49.

LI, Z., BAO, Y. & GAO, Z. 2011. PIV experiments and large eddy simulations of single-loop flow fields in Rushton turbine stirred tanks. *Chemical Engineering Science,* 66**,** 1219-1231.

LI, Z., SONG, G., BAO, Y. & GAO, Z. 2013. Stereo-PIV experiments and large eddy simulations of flow fields in stirred tanks with Rushton and curved-Blade turbines. *AIChE Journal,* 59**,** 3986-4003.

LILLY, D. K. 1966. On the Application of the Eddy Viscosity Concept in the Inertial Sub-range of Turbulence. *NCAR Manuscript 123*.

LILLY, D. K. 1992. A proposed modification of the Germano subgrid-scale closure method. *Physics of Fluids A: Fluid Dynamics (1989-1993),* 4**,** 633-635.

LIU, W., CHENG, L., ZHANG, Y., WANG, H. & YU, M. 2008. The physical properties of aqueous solution of room-temperature ionic liquids based on imidazolium: Database and evaluation. *Journal of Molecular Liquids,* 140**,** 68-72.

LIU, Y.-J., LI, W., HAN, L.-C., CAO, Y., LUO, H.-A., AL-DAHHAN, M. & DUDUKOVIC, M. P. 2011. γ-CT measurement and CFD simulation of cross section gas holdup distribution in a gas–liquid stirred standard Rushton tank. *Chemical Engineering Science,* 66**,** 3721-3731.

LU, W.-M., WU, H.-Z. & JU, M.-Y. 1997. Effects of baffle design on the liquid mixing in an aerated stirred tank with standard Rushton turbine impellers. *Chemical Engineering Science,* 52**,** 3843-3851.

LUO, J. Y., ISSA, R. I. & GOSMAN, A. D. 1994a. Prediction of impeller-induced flows in mixing vessels using multiple frames of reference. *IChemE Symp.*

LUO, J. Y., ISSA, R. I. & GOSMAN, A. D. 1994b. Prediction of impeller induced flows in mixing vessels using multiple frames of reference. *Inst. Chem. Eng. Symp. Ser,* 136**,** 549-556.

MALHAM, I. B., LETELLIER, P. & TURMINE, M. 2006. Evidence of a Phase Transition in Water−1-Butyl-3-methylimidazolium Tetrafluoroborate and Water−1-Butyl-2,3-dimethylimidazolium Tetrafluoroborate Mixtures at 298 K: Determination of the Surface Thermal Coefficient, bT,P. *The Journal of Physical Chemistry B,* 110**,** 14212-14214.

MARKOPOULOS, J., BABALONA, E. & TSILIOPOULOU, E. 2004. Power Consumption in Agitated Vessels with Dual Rushton Turbines: Baffle Length and Impeller Spacing Effects. *Chemical Engineering & Technology,* 27**,** 1212-1215.

MARS, B. D. G. 2015. Schematic of a hot-wire anemometer. *Schematic of a hot-wire anemometer.* France.

MARSHALL, J. S. & LI, S. 2014. *Adhesive Particle Flow A Discrete-Element Approach*, Cambridge University Press.

MART N, M., MONTES, F. J. & GAL N, M. A. 2008. Bubbling process in stirred tank reactors I: Agitator effect on bubble size, formation and rising. *Chemical Engineering Science,* 63**,** 3212-3222.

MART N, M., MONTES, F. J. & GAL N, M. A. 2010. Mass transfer rates from bubbles in stirred tanks operating with viscous fluids. *Chemical Engineering Science,* 65**,** 3814-3824.

MARTIN, M. N. 2011. *CFD Modelling of the Mixing Process in a Stirred Tank.* Master, Glyndwr University.

MAT, M. D. & KAPLAN, Y. 2001. Numerical study of hydrogen absorption in an Lm−Ni5 hydride reactor. *International Journal of Hydrogen Energy,* 26**,** 957-963.

MAVROS, P. 2001. Flow Visualization in Stirred Vessels: A Review of Experimental Techniques. *Chemical Engineering Research and Design,* 79**,** 113-127.

MELLING, A. 1997. Tracer particles and seeding for particle image velocimetr. *Measurement science & technology***,** 1406-1416.

MOILANEN, P. 2009. *Modelling gas-liquid flow and local mass transfer in stirred tanks.* Doctorial degree, Helsinki University of Technology.

MONTANTE, G., HORN, D. & PAGLIANTI, A. 2008. Gas-liquid flow and bubble size distribution in stirred tanks. *Chemical Engineering Science,* 63**,** 2107-2118.

MONTANTE, G., LEE, K. C., BRUCATO, A. & YIANNESKIS, M. 2001a. Experiments and predictions of the transition of the flow pattern with impeller clearance in stirred tanks. *Computers & Chemical Engineering,* 25**,** 729-735.

MONTANTE, G., LEE, K. C., BRUCATO, A. & YIANNESKIS, M. 2001b. Numerical simulations of the dependency of flow pattern on impeller clearance in stirred vessels. *Chemical Engineering Science,* 56**,** 3751-3770.

MONTANTE, G., PAGLIANTI, A. & MAGELLI, F. 2007. Experimental analysis and computational modelling of gas-liquid stirred vessels. *Chemical Engineering Research & Design,* 85**,** 647-653.

MORUD, K. E. & HJERTAGER, B. H. 1996. LDA measurements and CFD modelling of gas-liquid flow in a stirred vessel. *Chemical Engineering Science,* 51**,** 233-249.

MUELLER, S. G. & DUDUKOVIC, M. P. 2010. Gas Holdup in Gas−Liquid Stirred Tanks. *Industrial & Engineering Chemistry Research,* 49**,** 10744-10750.

MURTHY SHEKHAR, S. & JAYANTI, S. 2002. CFD Study of Power and Mixing Time for Paddle Mixing in Unbaffled Vessels. *Chemical Engineering Research and Design,* 80**,** 482-498.

NG, K. & YIANNESKIS, M. 2000. Observations on the Distribution of Energy Dissipation in Stirred Vessels. *Chemical Engineering Research and Design,* 78**,** 334-341.

NIENOW, A. W. & WISDOM, D. J. 1974. Flow over disc turbine blades. *Chemical Engineering Science,* 29**,** 1994-1997.

NIENOW, A. W., WISDOM, D. J., SOLOMON, J., MACHON, V. & VLCEK, J. 1983. THE EFFECT OF RHEOLOGICAL COMPLEXITIES ON POWER-CONSUMPTION IN AN AERATED, AGITATED VESSEL. *Chemical Engineering Communications,* 19**,** 273-293.

OAKLEY, T. R., LOTH, E. & ADRIAN, R. J. 1997. A two-phase cinematic PIV method for bubbly flows. *Journal of Fluids Engineering, Transactions of the ASME,* 119**,** 707-712.

OHNO, H. 2005. Electrochemical Aspects of Ionic Liquids. Japan: Wiley Interscience.

OLIVEIRA, M. S. N., FITCH, A. W. & NI, X. 2003. A Study of Bubble Velocity and Bubble Residence Time in a Gassed Oscillatory Baffled Column. *Chemical Engineering Research and Design,* 81**,** 233-242.

OLIVIER-BOURBIGOU, H., MAGNA, L. & MORVAN, D. 2010. Ionic liquids and catalysis: Recent progress from knowledge to applications. *Applied Catalysis A: General,* 373**,** 1-56.

OPALLO, M. & LESNIEWSKI, A. 2011. A review on electrodes modified with ionic liquids. *Journal of Electroanalytical Chemistry,* 656**,** 2-16.

PACEK, A. W., MAN, C. C. & NIENOW, A. W. 1998. On the Sauter mean diameter and size distributions in turbulent liquid/liquid dispersions in a stirred vessel. *Chemical Engineering Science,* 53**,** 2005-2011.

PATEL, H., EIN-MOZAFFARI, F. & DHIB, R. 2010. CFD analysis of mixing in thermal polymerization of styrene. *Computers & Chemical Engineering,* 34**,** 421-429.

PATWARDHAN, A. W. 2001. Prediction of Flow Characteristics and Energy Balance for a Variety of Downflow Impellers. *Industrial & Engineering Chemistry Research,* 40**,** 3806-3816.

PAUL, E. L., ATIEMO-OBENG, V. A. & KRESTA, S. M. 2004. HANDBOOK OF INDUSTRIAL MIXING SCIENCE AND PRACTICE. Canada: John Wiley & Sons, Inc.

PERICLEOUS, K. A. & PATEL, M. K. 1987. The Modelling of Tangential and Axial Agitators in Chemical Reactors *Physico. Chem. Hydrodyn,* 8**,** 105-123.

PETERS, D. C. 1992. Dynamics of emulsification. *Mixing in the Process Industries (Second Edition).* Oxford: Butterworth-Heinemann.

PETITTI, M., VANNI, M., MARCHISIO, D. L., BUFFO, A. & PODENZANI, F. 2013. Simulation of coalescence, break-up and mass transfer in a gas–liquid stirred tank with CQMOM. *Chemical Engineering Journal*.

PETROSKY, B. J., LOWE, K. T., BARDET, P. M., TIEMSIN, P. I., WOHL, C. J., DANEHY, P. M. & ANDRE, M. 2015. Particle Image Velocimetry Applications Using Fluorescent Dye-doped Particles. *53rd AIAA Aerospace Sciences Meeting.* American Institute of Aeronautics and Astronautics.

PLECHKOVAA, N. V. & SEDDON, K. R. 2008. Applications of ionic liquids in the chemical industry. *Chemical Society Reviews,* 37.

PUTHLI, M. S., RATHOD, V. K. & PANDIT, A. B. 2005. Gas–liquid mass transfer studies with triple impeller system on a laboratory scale bioreactor. *Biochemical Engineering Journal,* 23**,** 25-30.

QI, N., WANG, H., ZHANG, K. & ZHANG, H. 2010. Numerical simulation of fluid dynamics in the stirred tank by the SSG Reynolds Stress Model. *Frontiers of Chemical Engineering in China,* 4**,** 506-514.

QI, N., ZHANG, H., ZHANG, K., XU, G. & YANG, Y. 2012. CFD simulation of particle suspension in a stirred tank. *Particuology*.

RANADE, V. V. 1997. An efficient computational model for simulating flow in stirred vessels: a case of Rushton turbine. *Chemical Engineering Science,* 52**,** 4473-4484.

RANADE, V. V. & DOMMETI, S. M. S. 1996. Computational snapshot of flow generated by axial impeller in baffled stirred vessels. *Chemical Engineering Research & Design,* 74**,** 476-484.

RANADE, V. V. & JOSHI, J. B. 1990. Flow Generated by a Disc Turbine: Part II Mathematical Modelling and Comparison with Experimental Data. *Chemical engineering research and design,* 68A**,** 34-43.

RANADE, V. V., PERRARD, M., LE SAUZE, N., XUEREB, C. & BERTRAND, J. 2001a. Trailing Vortices of Rushton Turbine: PIV Measurements and CFD Simulations with Snapshot Approach. *Chemical Engineering Research and Design,* 79**,** 3-12.

RANADE, V. V., PERRARD, M., XUEREB, C., LE SAUZE, N. & BERTRAND, J. 2001b. Influence of Gas Flow Rate on the Structure of Trailing Vortices of a Rushton Turbine: PIV Measurements and CFD Simulations. *Chemical Engineering Research and Design,* 79**,** 957-964.

ROY, S., ACHARYA, S. & CLOETER, M. D. 2010. Flow structure and the effect of macro-instabilities in a pitched-blade stirred tank. *Chemical Engineering Science,* 65**,** 3009-3024.

RUTHERFORD, K., MAHMOUDI, S. M. S., LEE, K. C. & YIANNESKIS, M. 1996. The Influence of Rushton on the Mixing Characteristics of Stirred Vessels. *Chemical engineering research & design,* 74**,** 369-378.

SAJJADI, B., RAMAN, A. A. A., IBRAHIM, S. & SHAH, R. S. S. R. E. 2012. Review on gas-liquid mixing analysis in multiscale stirred vessel using CFD. *Reviews in Chemical Engineering,* 28**,** 171-189.

SANO, Y. & USUI, H. 1985. INTERRELATIONS AMONG MIXING TIME, POWER NUMBER AND DISCHARGE FLOW RATE NUMBER IN BAFFLED MIXING VESSELS. *Journal of Chemical Engineering of Japan,* 18**,** 47-52.

SAWAMURA, S., YOSHIMURA, Y., KITAMURA, K. & TANIGUCHI, Y. 1992. Effects of pressure, temperature, and concentration on the viscosity of an aqueous solution of sodium chloride. *J. Phys. Chem.,* 96.

SCARGIALI, F., D'ORAZIO, A., GRISAFI, F. & BRUCATO, A. 2007. Modelling and Simulation of Gas–Liquid Hydrodynamics in Mechanically Stirred Tanks. *Chemical Engineering Research and Design,* 85**,** 637-646.

SCH FER, M., H FKEN, M. & DURST, F. 1997. Detailed LDV Measurements for Visualization of the Flow Field Within a Stirred-Tank Reactor Equipped with a Rushton Turbine. *Chemical Engineering Research and Design,* 75**,** 729-736.

SCHILLER, L. & NAUMANNA, Z. 1935. A drag coefficient correlation. *Z.Ver.Deutsch.Ing.,* 77.

SCHMIDT, S. A., SIMON, M., ATTARAKIH, M. M., LAGAR G, L. & BART, H.-J. 2006. Droplet population balance modelling—hydrodynamics and mass transfer. *Chemical Engineering Science,* 61**,** 246-256.

SCHWARZKOPF., J. D., SOMMERFELD., M. & TSUJI., Y. 2012. Multiphase Flows with Droplets and Particles. U.S: CRC Press.

SHAW, C. T. 1992. *Using Computational Fluid Dynamics,* New York: Prentice Hall.

SHERIF, S. A. 1998. Hot-wire/film anemometry measurements in flows with heat transfer and signal correction. *ISA Transactions,* 37**,** 141-146.

SHINNAR, R. 1961. On Behavior of Liquid Dispersions in Mixing Vessels. *Journal of Fluid Mechanics,* 10**,** 259 - 275.

SHIROTA, H. & FUKAZAWA, H. 2011. Atom substitution effects in ionic liquids a microscopic view by femtosecond raman induced kerr effect spectroscopy. Japan: Chiba University.

SHUR, M. L., SPALART, P. R., STRELETS, M. K. & TRAVIN, A. K. 2008. A hybrid RANS-LES approach with delayed-DES and wall-modelled LES capabilities. *International Journal of Heat and Fluid Flow,* 29**,** 1638-1649.

SMAGORINSKY, J. 1963. GENERAL CIRCULATION EXPERIMENTS WITH THE PRIMITIVE EQUATIONS. *Monthly Weather Review,* 91**,** 99-164.

SOKOLICHIN, A., EIGENBERGER, G., LAPIN, A. & L BERT, A. 1997. Dynamic numerical simulation of gas-liquid two-phase flows Euler/Euler versus Euler/Lagrange. *Chemical Engineering Science,* 52**,** 611-626.

SOSSA-ECHEVERRIA, J. & TAGHIPOUR, F. 2015. Computational simulation of mixing flow of shear thinning non-Newtonian fluids with various impellers in a stirred tank. *Chemical Engineering and Processing: Process Intensification,* 93**,** 66-78.

STAMATOUDIS, M. & TAVLARIDES, L. L. 1985. Effect of continuous-phase viscosity on the drop sizes of liquid-liquid dispersions in agitated vessels. *Industrial & Engineering Chemistry Process Design and Development,* 24**,** 1175-1181.

STOOTS, C. M. & CALABRESE, R. V. 1995. Mean velocity field relative to a Rushton turbine blade. *AIChE Journal,* 41**,** 1-11.

SUN, S. C., MOTE, C. D. & SKINNER, H. B. 1992. Use of hot wire anemometry to measure velocity of the limb during human movement. *Journal of Biomedical Engineering,* 14**,** 435-439.

SUNG, J., JEON, Y., KIM, D., IWAHASHI, T., IIMORI, T., SEKI, K. & OUCHI, Y. 2005. Air–liquid interface of ionic liquid + H2O binary system studied by surface tension measurement and sum-frequency generation spectroscopy. *Chemical Physics Letters,* 406**,** 495-500.

SUNGKORN, R., DERKSEN, J. J. & KHINAST, J. G. 2012. Modeling of aerated stirred tanks with shear-thinning power law liquids. *International Journal of Heat and Fluid Flow,* 36**,** 153-166.

TABOR, G., GOSMAN, A. D. & ISSA, R. I. Numerical simulation of the flow in a mixing vessel stirred by a Rushton turbine. 1996. 25-34.

TROPEA, C., YARIN, ALEXANDER L., FOSS, JOHN F 2007. Springer Handbook of Experimental Fluid Mechanics. Berlin: Springer-Verlag Berlin Heidelberg.

VERSTEEG, H. K. & MALALASEKERA, W. 2007. An Introduction to Computational Fluid Dynamics The Finite Volume Method. Pearson Education Ltd.

WANG, H., JIA, X., WANG, X., ZHOU, Z., WEN, J. & ZHANG, J. 2014. CFD modeling of hydrodynamic characteristics of a gas–liquid two-phase stirred tank. *Applied Mathematical Modelling,* 38**,** 63-92.

WANG, X., DONG, H., ZHANG, X., XU, Y. & ZHANG, S. 2010a. Numerical Simulation of Absorbing CO2 with Ionic Liquids. *Chemical Engineering & Technology,* 33**,** 1615-1624.

WANG, X., DONG, H., ZHANG, X., YU, L., ZHANG, S. & XU, Y. 2010b. Numerical simulation of single bubble motion in ionic liquids. *Chemical Engineering Science,* 65**,** 6036-6047.

WANG, X. & QIAN, N. 1989. Turbulence characteristics of sedimentladen flow. *J Hydr Eng,* 115**,** 781-800.

WU, H. & PATTERSON, G. K. 1989. Laser-Doppler measurements of turbulent-flow parameters in a stirred mixer. *Chemical Engineering Science,* 44**,** 2207-2221.

XU, Y. & MCGRATH, G. 1996. CFD Predictions in Stirred Tank Flows. *Chemical engineering research and design,* 74.

XUEREB, C. & BERTRAND, J. 1996. 3-D hydrodynamics in a tank stirred by a double-propeller system and filled with a liquid having evolving rheological properties. *Chemical Engineering Science,* 51**,** 1725-1734.

YANG, Z. & PAN, W. 2005. Ionic liquids: Green solvents for nonaqueous biocatalysis. *Enzyme and Microbial Technology,* 37**,** 19-28.

YUE, C., FANG, D., LIU, L. & YI, T.-F. 2011. Synthesis and application of task-specific ionic liquids used as catalysts and/or solvents in organic unit reactions. *Journal of Molecular Liquids,* 163**,** 99-121.

ZADGHAFFARI, R., MOGHADDAS, J. S. & REVSTEDT, J. 2010. Large-eddy simulation of turbulent flow in a stirred tank driven by a Rushton turbine. *Computers & Fluids,* 39**,** 1183-1190.

ZHANG, M., HU, Y., WANG, W., SHAO, T. & CHENG, Y. 2013. Intensification of viscous fluid mixing in eccentric stirred tank systems. *Chemical Engineering and Processing: Process Intensification,* 66**,** 36-43.

ZHANG, S., SUN, N., HE, X., LU, X. & LU, X. 2006. Physical Properties of Ionic Liquids: Database and Evaluation. *J. Phys. Chem. Ref. Data,* 35.

ZHANG, X., DONG, H., HUANG, Y., LI, C. & ZHANG, X. 2012. Experimental study on gas holdup and bubble behavior in carbon capture systems with ionic liquid. *Chemical Engineering Journal,* 209**,** 607-615.

ZHANG, X., HUO, F., LIU, X., DONG, K., HE, H., YAO, X. & ZHANG, S. 2015. Influence of Microstructure and Interaction on Viscosity of Ionic Liquids. *Industrial & Engineering Chemistry Research,* 54**,** 3505-3514.

ZHANG, Y., YONG, Y., MAO, Z.-S., YANG, C., SUN, H. & WANG, H. 2009. Numerical Simulation of Gas-Liquid Flow in a Stirred Tank with Swirl Modification. *Chemical Engineering & Technology,* 32**,** 1266-1273.

ZHAO, J., GAO, Z. & BAO, Y. 2011. Effects of the Blade Shape on the Trailing Vortices in Liquid Flow Generated by Disc Turbines. *Chinese Journal of Chemical Engineering,* 19**,** 232-242.

APPENDICES

Appendix 2.1 Velocity Magnitudes Predicted by Different SGS Models

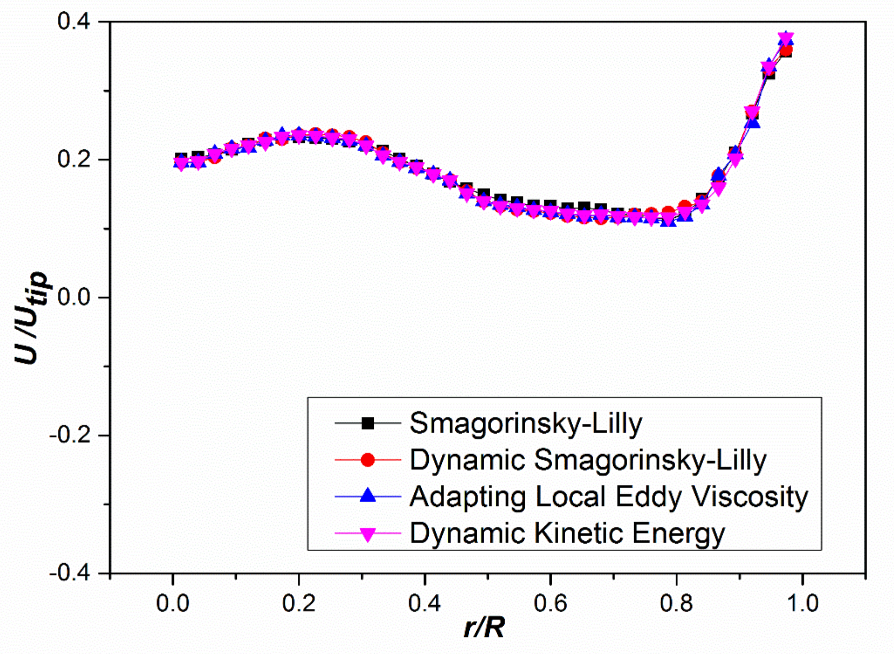

Figure A2.1.1 Velocity magnitude distributions predicted by different SGS models at a horizontal plane 40 mm above the tank bottom in FB tank

Appendix 3.1 Mesh Independence Tests of the Grids of Stirred Tanks

The mesh independence test is to determine an optimum number of nodes of the computational domain, where a fairly accurate solution for the problem is found at the expense of the least computational resources (Mat and Kaplan, 2001).

The coarse grids with nodes number of 440 k, 650 k and 660 k were used for the initial flow modelling in FB tank, DBD tank and DBB tank respectively. The velocity magnitudes at a horizontal plane 40 mm above the tank bottom were monitored in each simulation. As can be noticed from the Figure A3.1.1 to Figure A3.1.3, the simulated velocity magnitudes does not significantly change as the grids number increased to 920 k, 860 k and 880 k for the FB tank, DBD tank and DBB tank respectively. And the solutions can be considered mesh independent for the three stirred tanks.

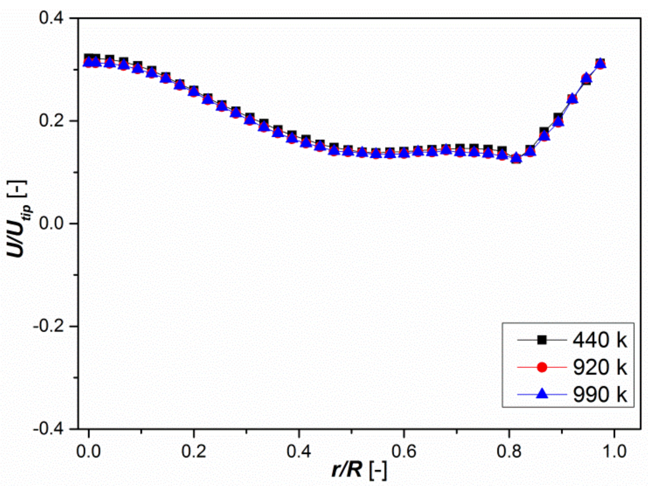

Figure A3.1.1 Velocity magnitude distributions at a horizontal plane 40 mm above the tank bottom in FB tank

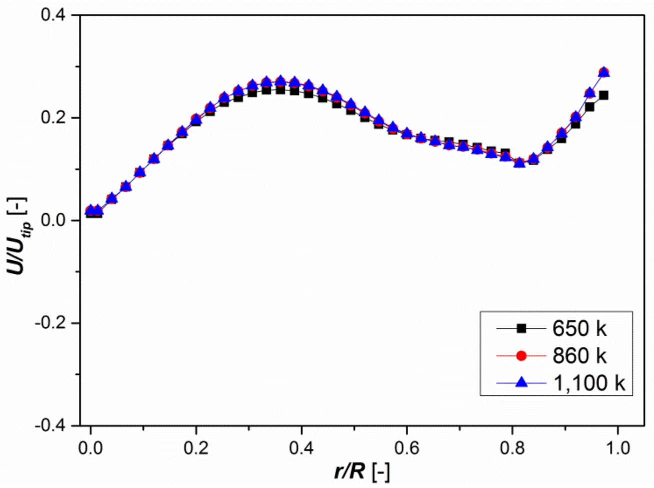

Figure A3.1.2 Velocity magnitude distributions at a horizontal plane 40 mm above the tank bottom in DBD tank

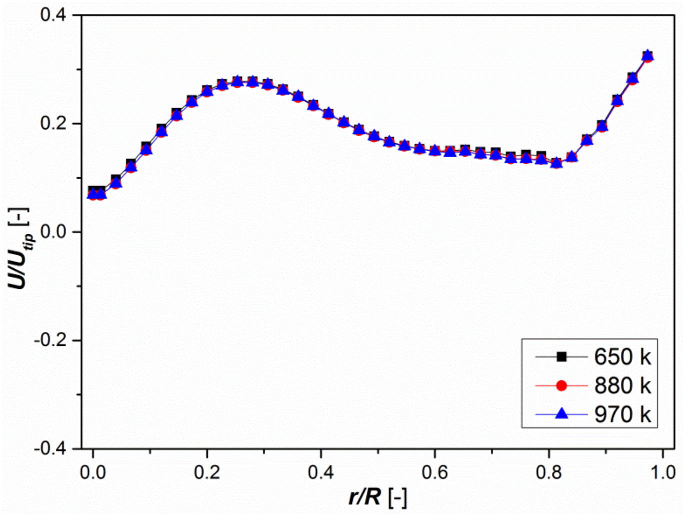

Figure A3.1.3 Velocity magnitude distributions at a horizontal plane 40 mm above the tank bottom in DBB tank

Appendix 6.1 Data Used for Regression to Estimate the Impeller Power Consumption of the Gas-ionic Liquid Multiphase Flow System

Table A6.1.1 Data Used for regression to Estimate the Impeller Power Consumption of the Gas-ionic Liquid Multiphase Flow System

Impeller speed (rpm)	Gassing rate (L/min)	P_g (-)	P (-)	Fr (-)	Fl (-)	T/D (-)	Q_g (m/s)
150	0.1	3.1	3.2	0.0478	0.53	2	1.67E-06
150	0.2	3.1	3.2	0.0478	0.53	2	3.30E-06
150	0.3	3.1	3.2	0.0478	0.53	2	5.01E-06
200	0.1	3.1	3.2	0.08	0.56	2	1.67E-06
200	0.2	3	3.2	0.08	0.56	2	3.30E-06
200	0.3	3	3.1	0.08	0.56	2	5.01E-06
250	0.1	3	3.1	0.13	0.59	2	1.67E-06
250	0.2	2.9	3.1	0.13	0.59	2	3.30E-06
250	0.3	2.9	3.1	0.13	0.59	2	5.01E-06

Appendix 7.1 PIV Validation of the Gas-Ionic Liquid Multiphase Flow in the Stirred Tank

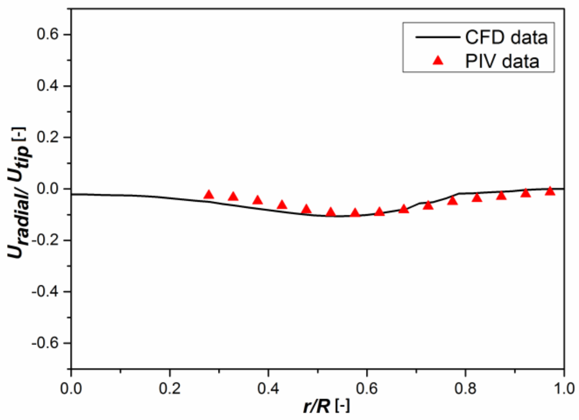

Figure A7.1.1 Liquid phase radial velocity profiles at z/H=0.27 obtained by PIV and CFD (N=150 rpm, Qg=0.2 L/min)

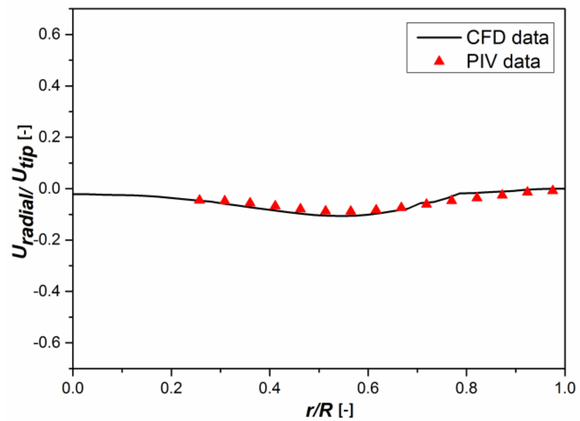

Figure A7.1.2 Gas phase radial velocity profiles at z/H=0.27 obtained by PIV and CFD (N=150 rpm, Qg=0.2 L/min)

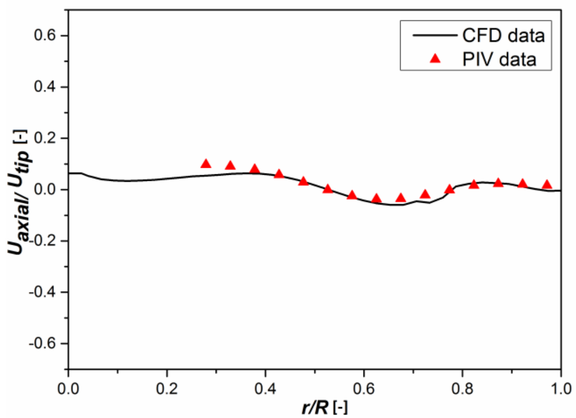

Figure A7.1.3 Liquid phase axial velocity profiles at z/H =0.27 obtained by PIV and CFD (N=150 rpm, Qg=0.2 L/min)

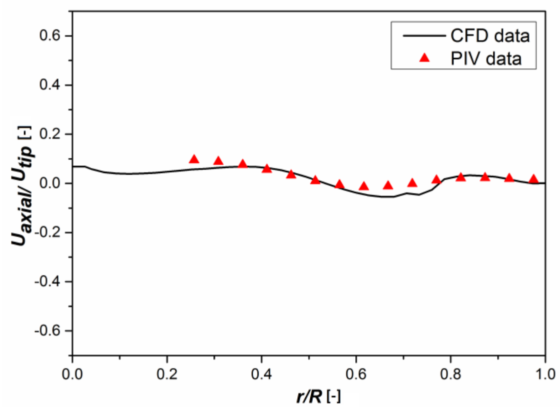

Figure A7.1.4 Gas phase axial velocity profiles at z/H =0.27 obtained by PIV and CFD (N=150 rpm, Q_g=0.2 L/min)

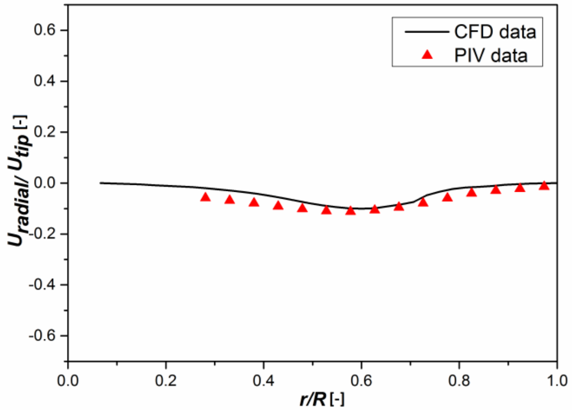

Figure A7.1.5 Liquid phase radial velocity profiles at z/H =0.73 obtained by PIV and CFD (N=150 rpm, Qg=0.2 L/min)

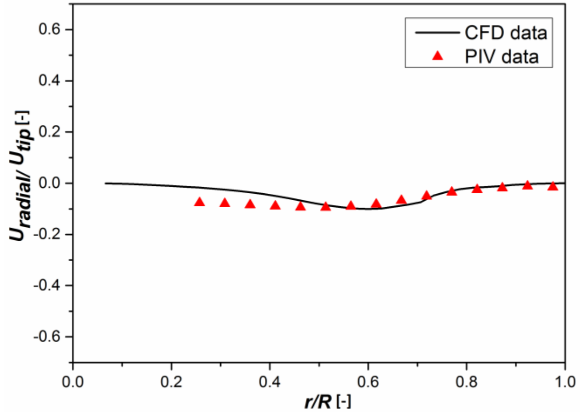

Figure A7.1.6 Gas phase radial velocity profiles at z/H =0.73 obtained by PIV and CFD (N=150 rpm, Qg=0.2 L/min)

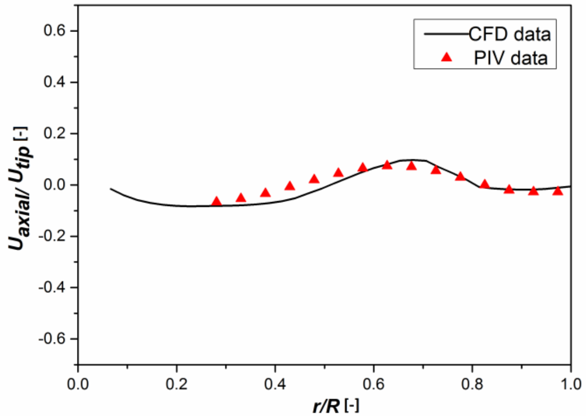

Figure A7.1.7 Liquid phase axial velocity profiles at z/H =0.73 obtained by PIV and CFD (N=150 rpm, Qg=0.2 L/min)

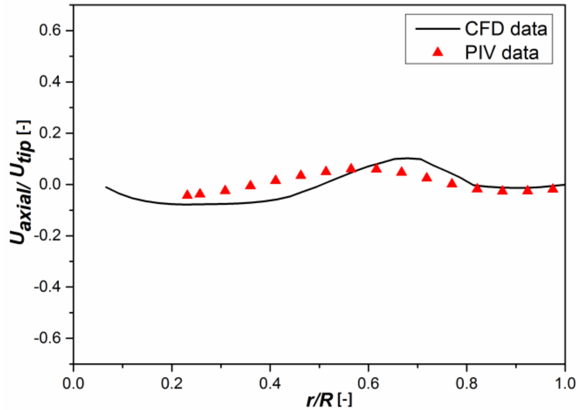

Figure A7.1.8 Gas phase axial velocity profiles at z/H =0.73 obtained by PIV and CFD (N=150 rpm, Qg=0.2 L/min)

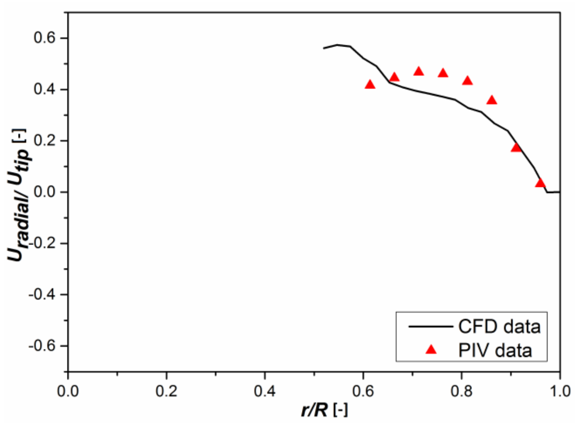

Figure A7.1.9 Liquid phase radial velocity profiles at z/H =0.5 obtained by PIV and CFD (N=150 rpm, Q_g=0.2 L/min)

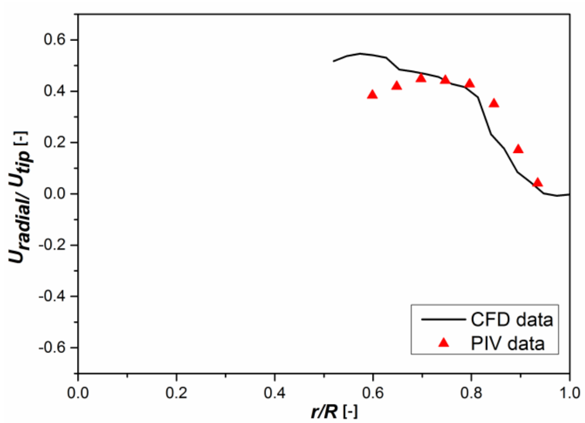

Figure A7.1.10 Gas phase radial velocity profiles at z/H =0.5 obtained by PIV and CFD (N=150 rpm, Qg=0.2 L/min)

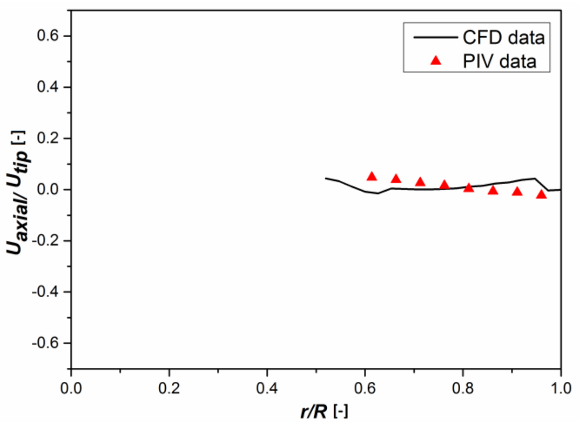

Figure A7.1.11 Liquid phase axial velocity profiles at z/H =0.5 obtained by PIV and CFD (N=150 rpm, Qg=0.2 L/min)

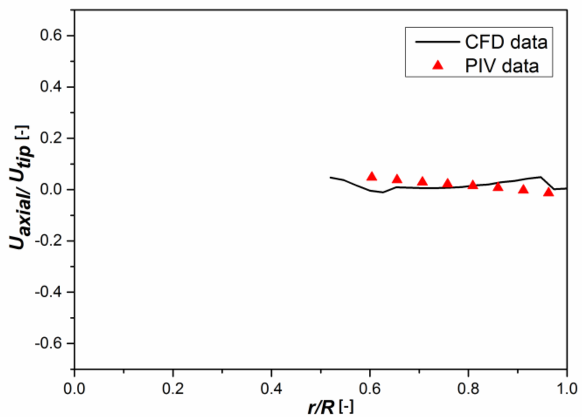

Figure A7.1.12 Gas phase axial velocity profiles at z/H =0.5 obtained by PIV and CFD (N=150 rpm, Qg=0.2 L/min)

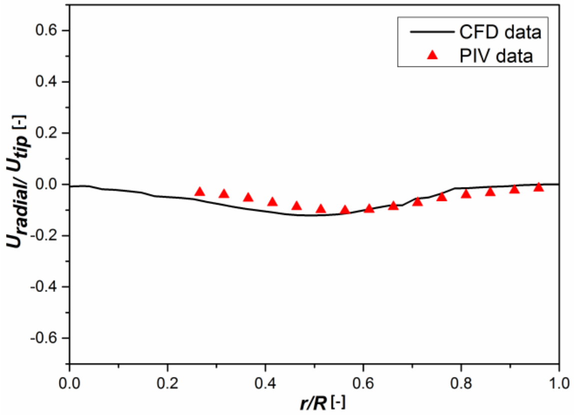

Figure A7.1.13 Liquid phase radial velocity profiles at z/H =0.27 obtained by PIV and CFD (N=150 rpm, Qg=0.3 L/min)

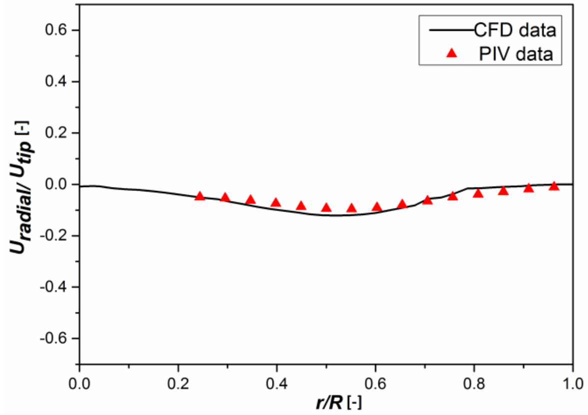

Figure A7.1.14 Gas phase radial velocity profiles at z/H =0.27 obtained by PIV and CFD (N=150 rpm, Qg=0.3 L/min)

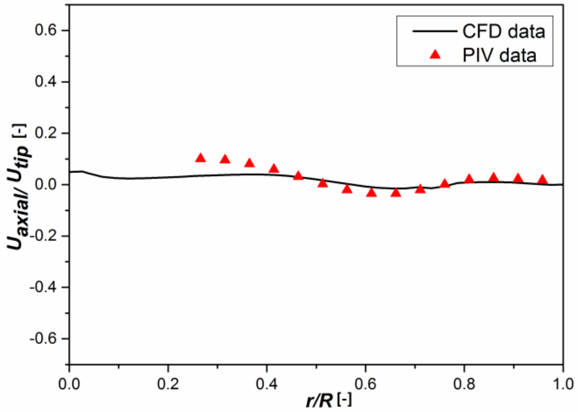

Figure A7.1.15 Liquid phase axial velocity profiles at z/H =0.27 obtained by PIV and CFD (N=150 rpm, Qg=0.3 L/min)

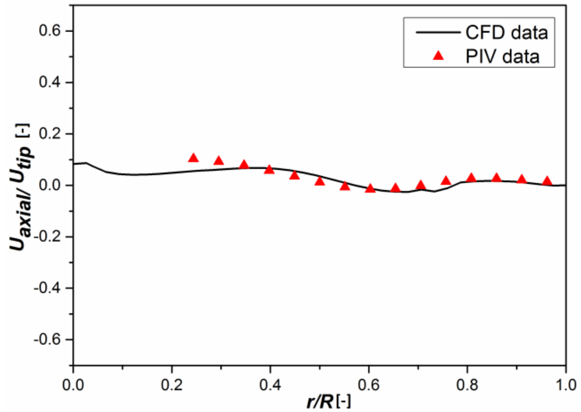

Figure A7.1.16 Gas phase axial velocity profiles at z/H =0.27 obtained by PIV and CFD (N=150 rpm, Qg=0.3 L/min)

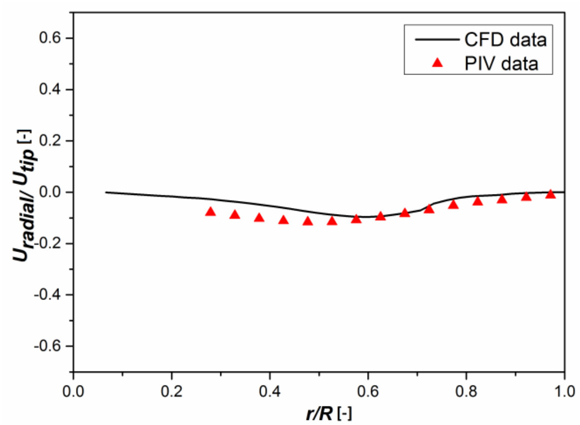

Figure A7.1.17 Liquid phase radial velocity profiles at z/H =0.73 obtained by PIV and CFD (N=150 rpm, Qg=0.3 L/min)

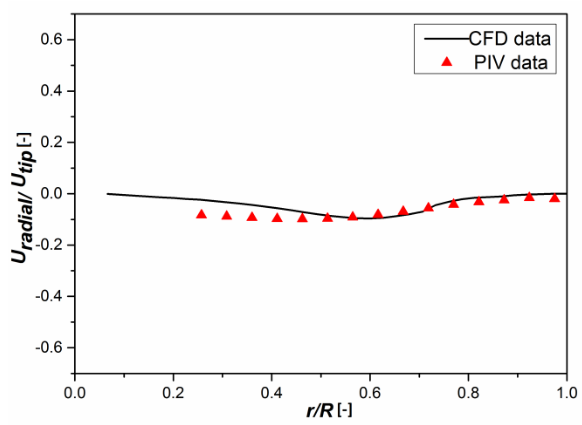

Figure A7.1.18 Gas phase radial velocity profiles at z/H =0.73 obtained by PIV and CFD (N=150 rpm, Qg=0.3 L/min)

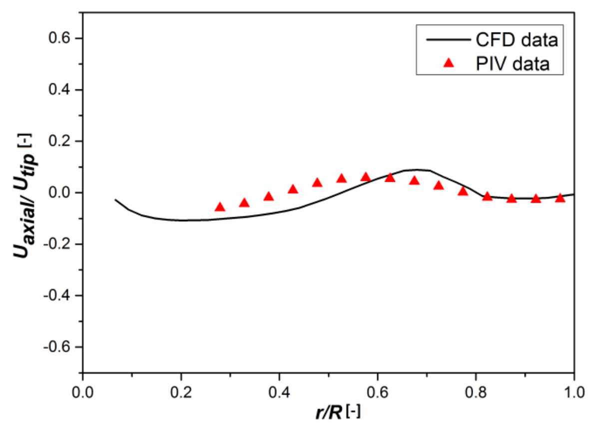

Figure A7.1.19 Liquid phase axial velocity profiles at z/H =0.73 obtained by PIV and CFD (N=150 rpm, Qg=0.3 L/min)

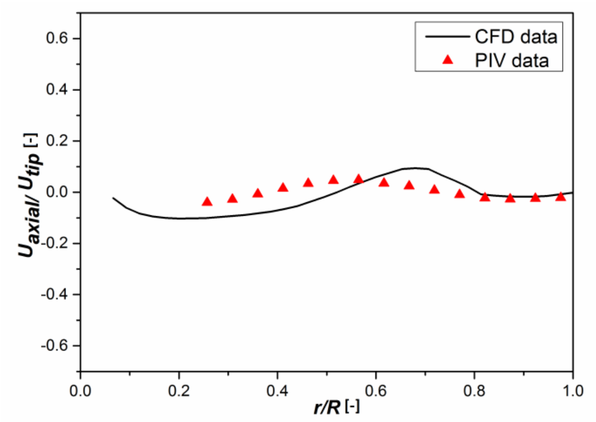

Figure A7.1.20 Gas phase axial velocity profiles at z/H =0.73 obtained by PIV and CFD (N=150 rpm, Qg=0.3 L/min)

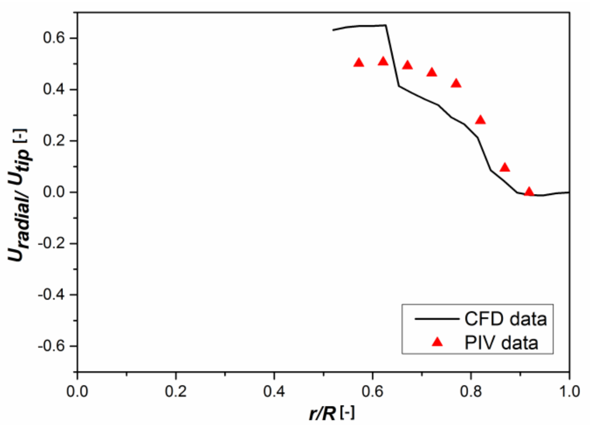

Figure A7.1.21 Liquid phase radial velocity profiles at z/H =0.5 obtained by PIV and CFD (N=150 rpm, Qg=0.3 L/min)

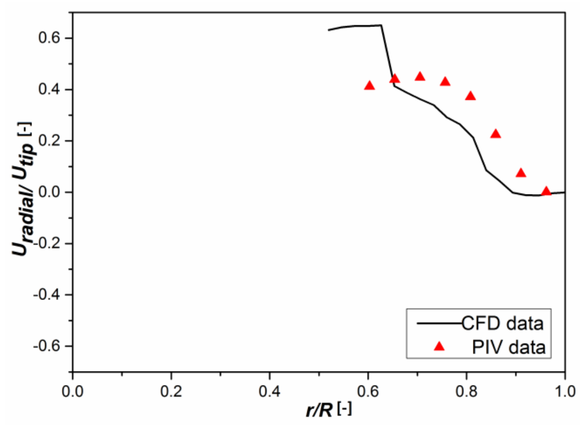

Figure A7.1.22 Gas phase radial velocity profiles at z/H =0.5 obtained by PIV and CFD (N=150 rpm, Qg=0.3 L/min)

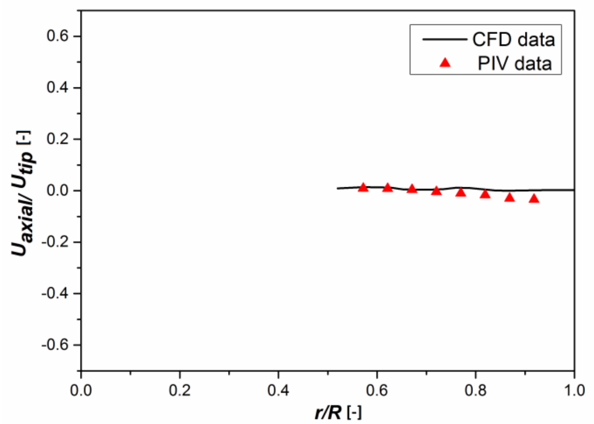

Figure A7.1.23 Liquid phase axial velocity profiles at z/H =0.5 obtained by PIV and CFD (N=150 rpm, Qg=0.3 L/min)

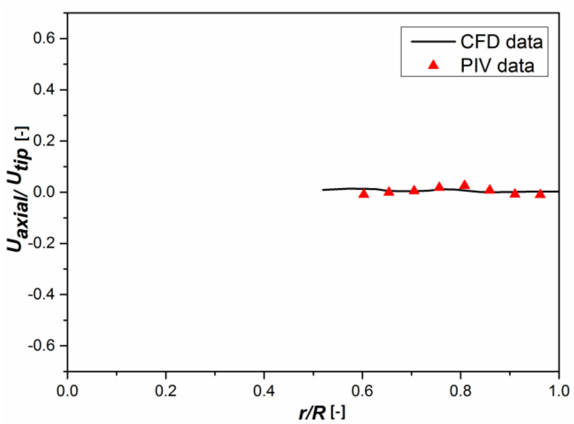

Figure A7.1.24 Gas phase axial velocity profiles at z/H =0.5 obtained by PIV and CFD (N=150 rpm, Qg=0.3 L/min)

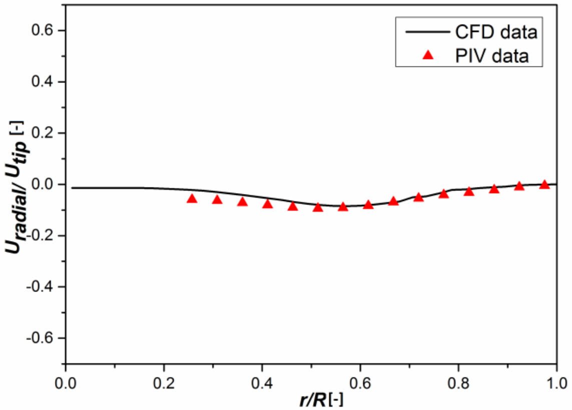

Figure A7.1.25 Liquid phase radial velocity profiles at z/H =0.27 obtained by PIV and CFD (N=200 rpm, Qg=0.1 L/min)

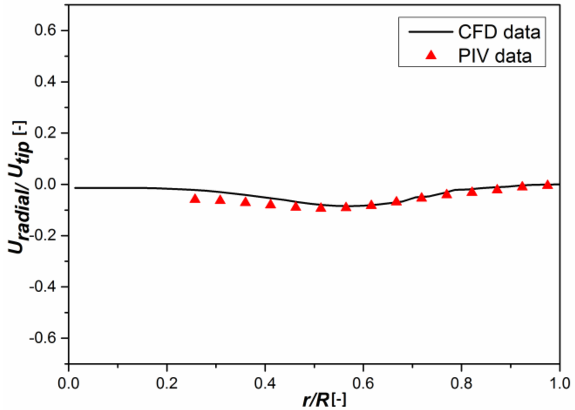

Figure A7.1.26 Gas phase radial velocity profiles at z/H =0.27 obtained by PIV and CFD (N=200 rpm, Qg=0.1 L/min)

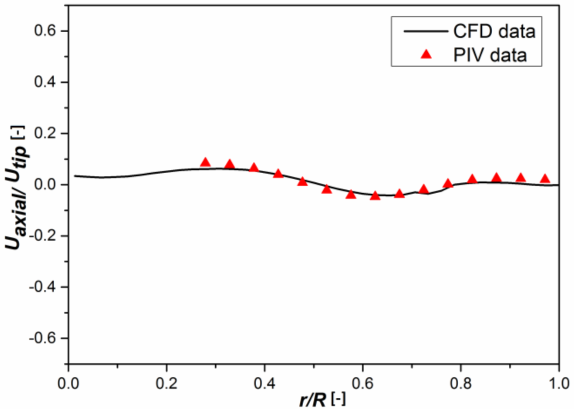

Figure A7.1.27 Liquid phase axial velocity profiles at z/H =0.27 obtained by PIV and CFD (N=200 rpm, Qg=0.1 L/min)

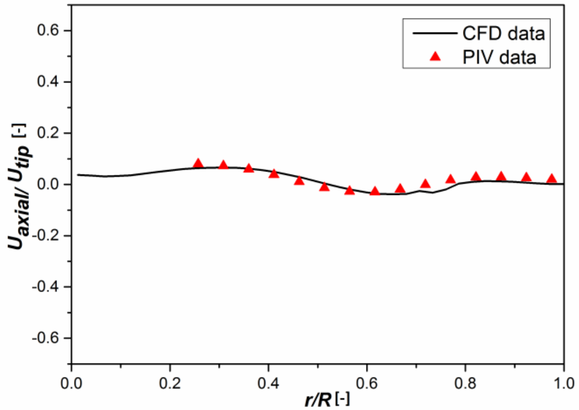

Figure A7.1.28 Gas phase axial velocity profiles at z/H =0.27 obtained by PIV and CFD (N=200 rpm, Qg=0.1 L/min)

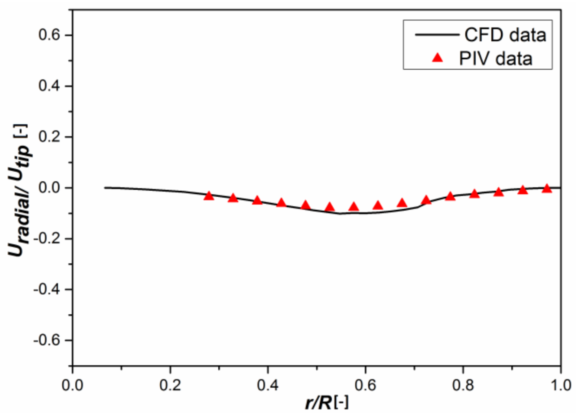

Figure A7.1.29 Liquid phase raidal velocity profiles at z/H =0.73 obtained by PIV and CFD (N=200 rpm, Qg=0.1 L/min)

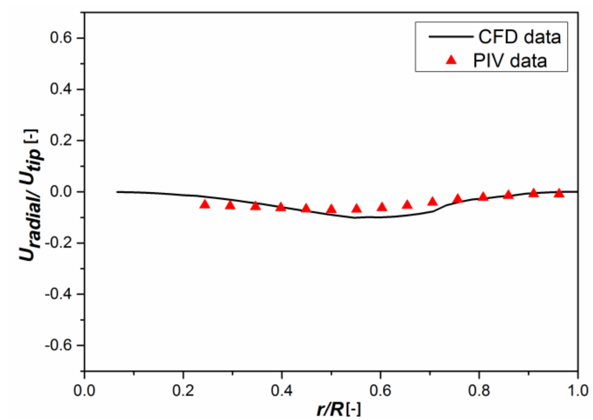

Figure A7.1.30 Gas phase radial velocity profiles at z/H =0.73 obtained by PIV and CFD (N=200 rpm, Qg=0.1 L/min)

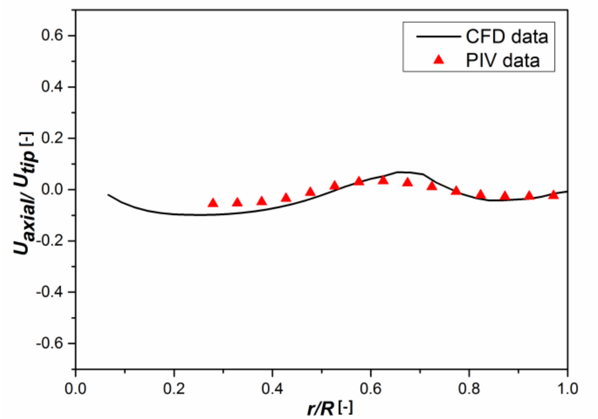

Figure A7.1.31 Liquid phase axial velocity profiles at z/H =0.73 obtained by PIV and CFD (N=200 rpm, Qg=0.1 L/min)

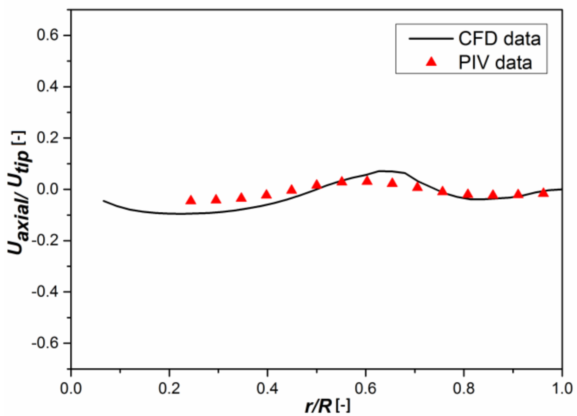

Figure A7.1.32 Gas phase axial velocity profiles at z/H =0.73 obtained by PIV and CFD (N=200 rpm, Qg=0.1 L/min)

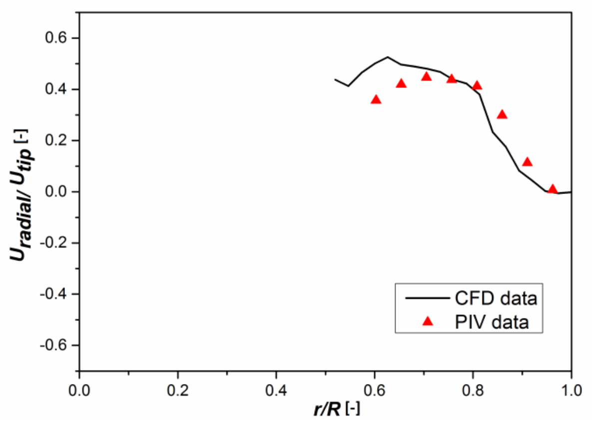

Figure A7.1.33 Liquid phase radial velocity profiles at z/H =0.5 obtained by PIV and CFD (N=200 rpm, Q_g=0.1 L/min)

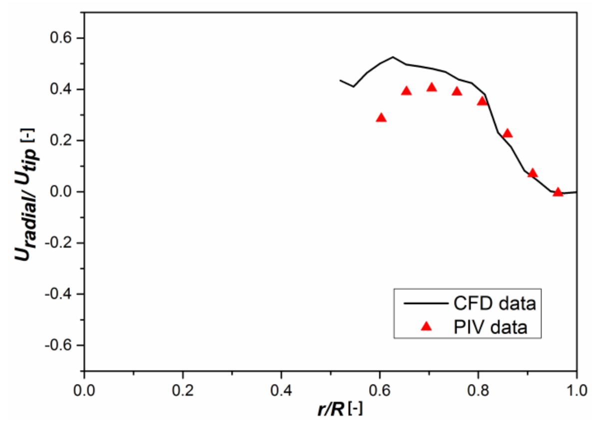

Figure A7.1.34 Gas phase radial velocity profiles at z/H =0.5 obtained by PIV and CFD (N=200 rpm, Qg=0.1 L/min)

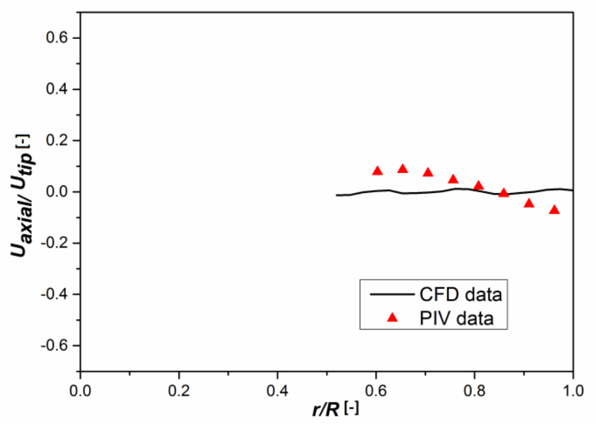

Figure A7.1.35 Liquid phase axial velocity profiles at z/H =0.5 obtained by PIV and CFD (N=200 rpm, Qg=0.1 L/min)

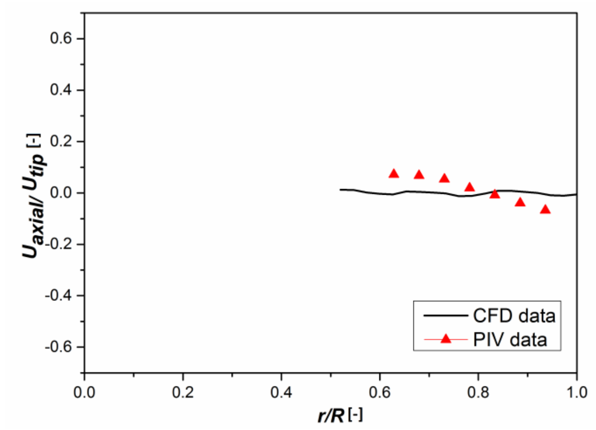

Figure A7.1.36 Gas phase axial velocity profiles at z/H =0.5 obtained by PIV and CFD (N=200 rpm, Qg=0.1 L/min)

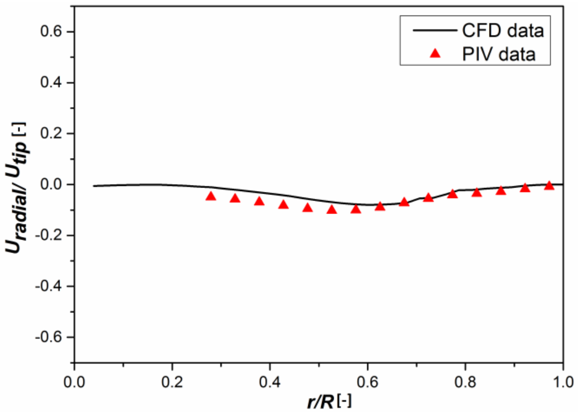

Figure A7.1.37 Liquid phase radial velocity profiles at z/H =0.27 obtained by PIV and CFD (N=250 rpm, Q_g=0.1 L/min)

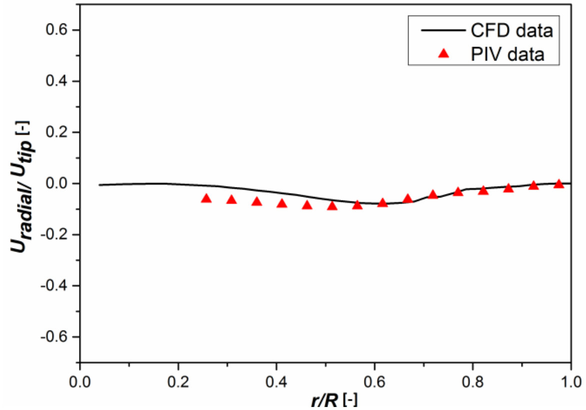

Figure A7.1.38 Gas phase radial velocity profiles at z/H =0.27 obtained by PIV and CFD (N=250 rpm, Q_g=0.1 L/min)

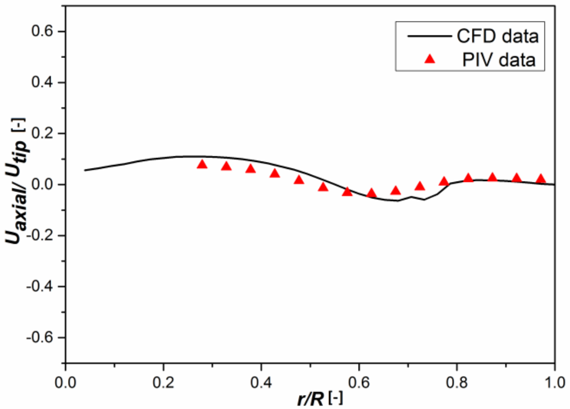

Figure A7.1.39 Liquid phase axial velocity profiles at z/H =0.27 obtained by PIV and CFD (N=250 rpm, Q_g=0.1 L/min)

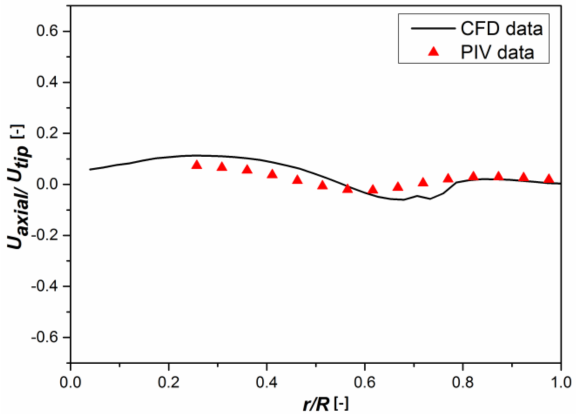

Figure A7.1.40 Gas phase axial velocity profiles at z/H =0.27 obtained by PIV and CFD (N=250 rpm, Q_g=0.1 L/min)

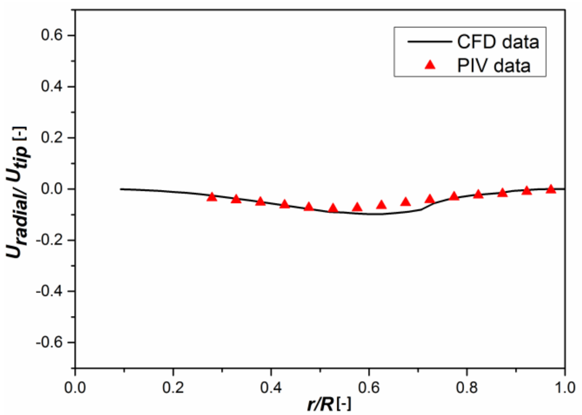

Figure A7.1.41 Liquid phase radial velocity profiles at z/H=0.73 obtained by PIV and CFD (N=250 rpm, Qg=0.1 L/min)

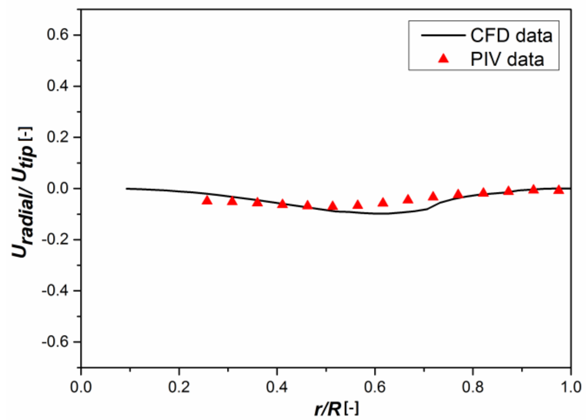

Figure A7.1.42 Gas phase radial velocity profiles at z/H=0.73 obtained by PIV and CFD (N=250 rpm, Qg=0.1 L/min)

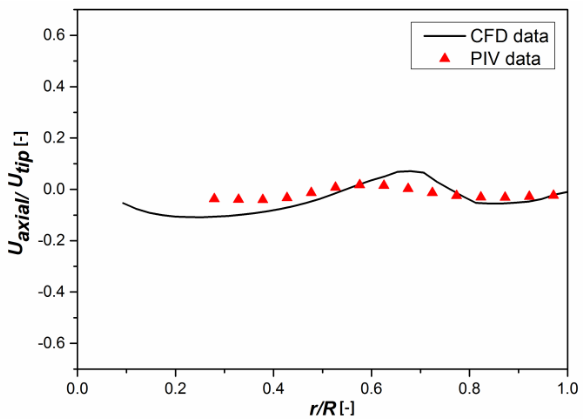

Figure A7.1.43 Liquid phase axial velocity profiles at Z/H=0.73 obtained by PIV and CFD (N=250 rpm, Q_g=0.1 L/min)

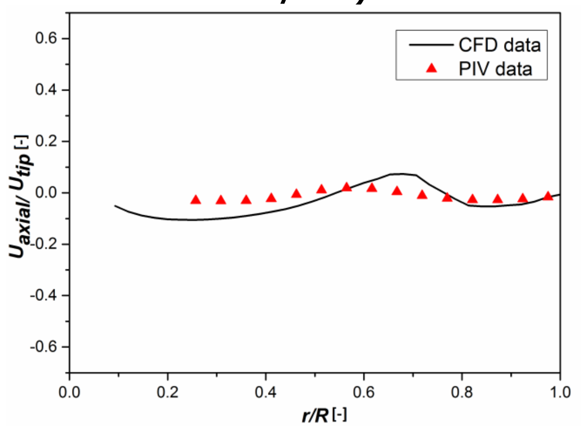

Figure A7.1.44 Gas phase axial velocity profiles at Z/H=0.73 obtained by PIV and CFD (N=250 rpm, Q_g=0.1 L/min)

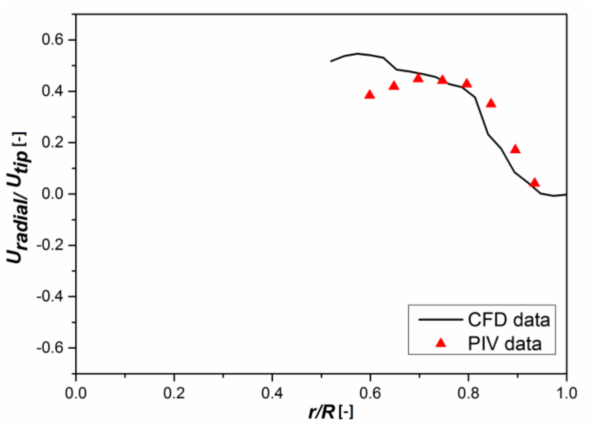

Figure A7.1.45 Liquid phase radial velocity profiles at z/H=0.5 obtained by PIV and CFD (N=250 rpm, Qg=0.1 L/min)

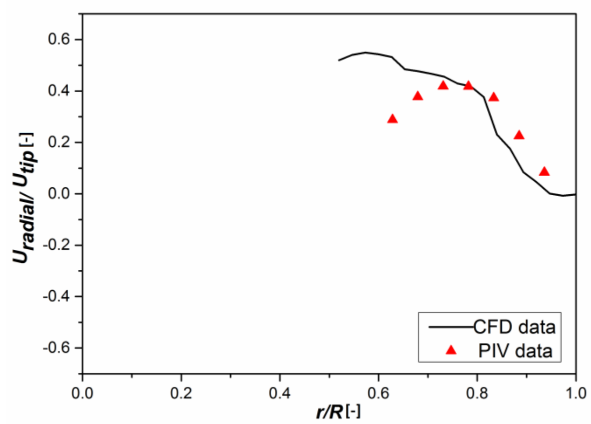

Figure A7.1.46 Gas phase radial velocity profiles at z/H=0.5 obtained by PIV and CFD (N=250 rpm, Qg=0.1 L/min)

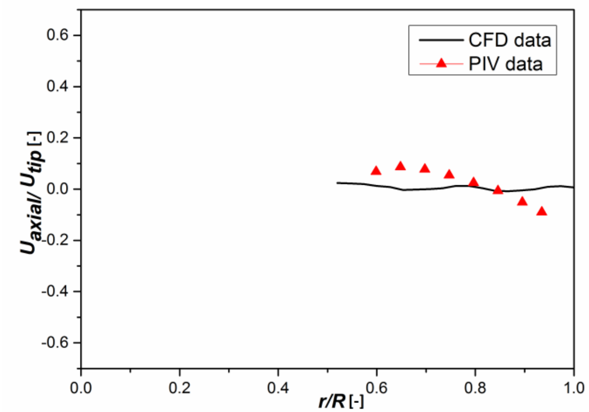

Figure A7.1.47 Liquid phase axial velocity profiles at z/H=0.5 obtained by PIV and CFD (N=250 rpm, Qg=0.1 L/min)

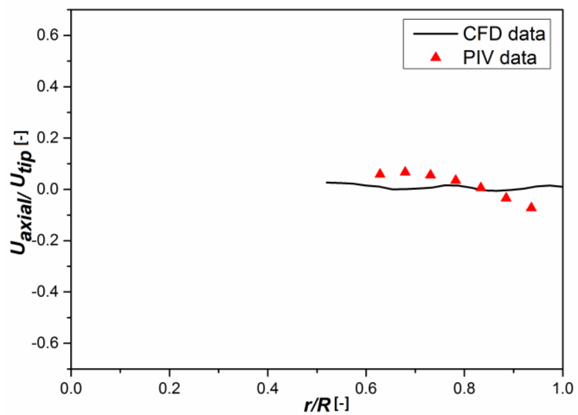

Figure A7.1.48 Gas phase axial velocity profiles at z/H=0.5 obtained by PIV and CFD (N=250 rpm, Qg=0.1 L/min)